Shrunken heads begin the journey home p. 919

Virtual reality for locusts forces a rethink of swarming pp. 924 & 995

Racing to make a radioactive metal sandwich p. 974

Science

$15
28 FEBRUARY 2025
science.org

AAAS

MOLLUSK MENAGERIE

Reconstructing a mysterious family tree p. 1001

QUALITY CONTENT FOR THE GLOBAL SCIENTIFIC COMMUNITY

Multiple ways to stay informed on issues related to your research

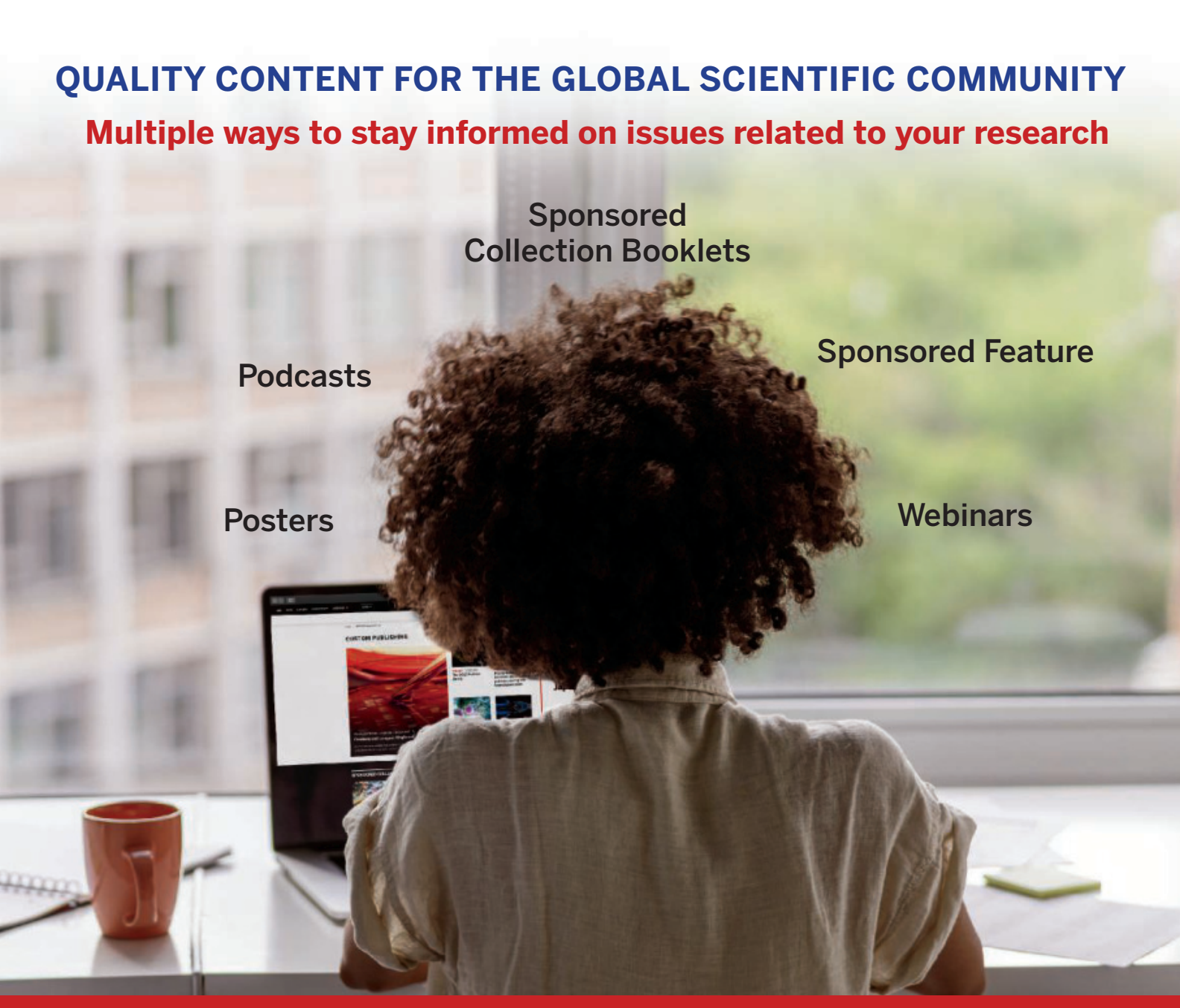

Science
AAAS

Scan the code and start exploring the latest advances in science and technology innovation!

Science.org/custom-publishing

Brought to you by the *Science*/AAAS Custom Publishing Office.

Posters | **Podcasts** | **Sponsored Collection Booklets** | **Sponsored Feature** | **Webinars**

CONTENTS

28 FEBRUARY 2025 • VOLUME 387 • ISSUE 6737

924 & 995

NEWS

IN BRIEF

IN DEPTH

925 & 978

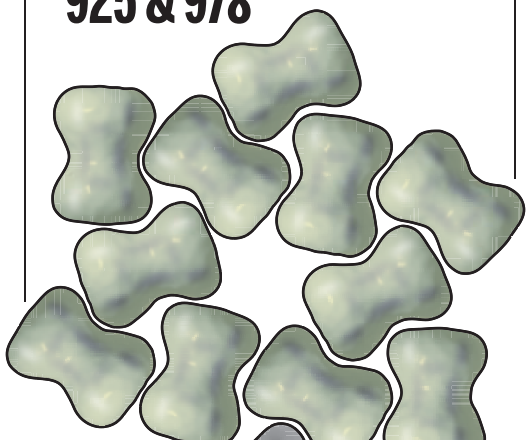

FEATURES

INSIGHTS

PERSPECTIVES

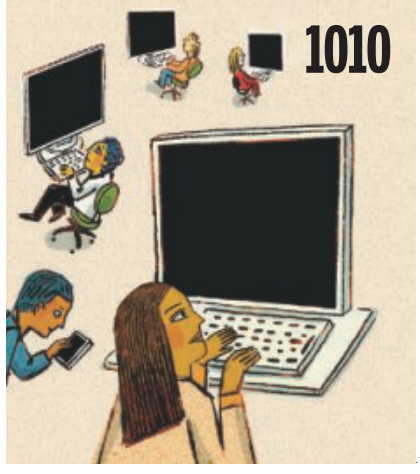

ON THE COVER

An oval squid (*Sepioteuthis lessoniana*) hovers in a nighttime sea, displaying its natural iridescence. This species is among those informing new insights into molluscan evolution. The extreme diversity in the phylum Mollusca—which includes squids, chitons, snails, clams, and others—has long puzzled scientists. Sequencing previously uncharacterized genomes helps to resolve the molluscan family tree. See page 1001. *Photo: Magnus Lundgren/Minden*

SCIENCE (ISSN 0036-8075) is published weekly on Friday, except last week in December, by the American Association for the Advancement of Science, 1200 New York Avenue, NW, Washington, DC 20005. Periodicals mail postage (publication No. 484460) paid at Washington, DC, and additional mailing offices. Domestic individual membership, including subscription (12 months): $165 ($74 allocated to subscription). Domestic institutional subscription (51 issues): $2865; Foreign postage extra: Air assist delivery: $135. First class, airmail, student, and emeritus rates on request. Canadian rates with GST available upon request, GST #125488122. Publications Mail Agreement Number 1069624. **Printed in the U.S.A.**
Change of address: Allow 4 weeks, giving old and new addresses and 8-digit account number. **Postmaster:** Send change of address to AAAS, P.O. Box 96178, Washington, DC 20090–6178. **Single-copy sales:** $15 each plus shipping and handling available from backissues.science.org; bulk rate on request. **Authorization to reproduce** material for internal or personal use under circumstances not falling within the fair use provisions of the Copyright Act can be obtained through the Copyright Clearance Center (CCC), www.copyright.com. The identification code for *Science* is 0036-8075. *Science* is indexed in the *Reader's Guide to Periodical Literature* and in several specialized indexes.

ILLUSTRATION: ROBERT NEUBECKER

EDITORIAL

Come together, right now

H. Holden Thorp
Editor-in-Chief,
Science journals.
hthorp@aaas.org

The chaos, conflicting information, firings, and hurtful rhetoric of the Trump administration's approach to science over the past month are causing anxiety, grief, and concern for the scientific community in the United States. The dramatic events are reverberating around the globe, especially among international scientific collaborators. Not surprisingly, scientists in the US and around the world do not agree on the best approach to preserve science during this onslaught. A diversity of thought has always been a strength of the scientific enterprise but at the same time, there are principles around which all scientists unite—those of evidence, independence, process, and inclusion. These common values must now propel everyone in the scientific community to work together as never before to stand up for science.

The unprecedented events have pushed some universities and associations to sue the federal government to block executive orders and other actions that are harming science—and nearly all are working behind the scenes in Washington, DC, to protect the scientific community. The chief executive officer of the American Association for the Advancement of Science (AAAS, the publisher of *Science*), Sudip Parikh, forcefully objected to the appointment of Robert F. Kennedy Jr. as the Secretary of Health and Human Services (HHS); the Association of American Medical Colleges spoke out against the firings in HHS; and the Association of American Universities objected to arbitrary cuts to indirect costs in grants from the National Institutes of Health (NIH). Presidents of universities, including some in Republican states, have made strong statements about the damage to public health in their states that will arise from cuts to NIH funding. At George Washington University, where I am a faculty member, President Ellen Granberg described the situation to me as a tragedy that risks "destroying a scientific enterprise that is the envy of the world, one that has saved countless lives and produced innovations that help fuel our economy." But she also stressed, "We are watching the legal proceedings carefully and, while we will always in the end comply with the law, we will do everything possible to preserve the principles we have always followed and protect the people of our community."

> **"The weeks ahead may be the greatest test that the US scientific community has ever faced."**

Many scientists and faculty members at universities still do not see the actions of science leaders as sufficient. My plea to my academic colleagues in this time is to trust that science's leaders are making the best judgments they can about how to proceed, remembering that timing can be everything. The vast majority of university presidents appreciate that this is an existential moment requiring careful and consistent action to preserve the values and ambitions of science. Anxious faculty and students will need to be continually apprised by university leadership on potential changes to views and strategies. Although that may be uncomfortable, actions in the name of unity are worth taking the risk.

Those in the scientific community who enjoy the protections of academic and other freedoms afforded by the US Constitution's First Amendment should do and say more. Some will march in the streets, some will send messages to Congress, and some will focus on their research, students, and trainees. And just as leaders deserve some leeway to decide when to speak out most effectively, they should support their constituencies by not trying to squelch or steer more strident voices.

As for the *Science* family of journals, we will continue to uphold the highest standards of scientific integrity while publishing groundbreaking research, provocative commentary, and news that is unencumbered by interference. We will not change the principles and processes by which we serve the scientific community. The *Science* journals stand in solidarity with similar comments made by our colleagues at the Journal of the American Medical Association and the Public Library of Science.

The weeks ahead may be the greatest test that the US scientific community has ever faced. In time, the dust will settle, and the new challenges confronting the enterprise will be clear. It will then be time to take stock and learn how to prosper in a new era. To prepare for that, we need unity and support for each other now. Regardless of style and tactics, everyone in the American scientific community must hold to the principles of independence, peer evaluation, and inclusion. These have enabled the country's success in science and technology for at least a century. We will not turn our backs on them now.*

–H. Holden Thorp

PHOTO: CAMERON DAVIDSON

*A longer version of this piece can be found at https://www.science.org/doi/10.1126/science.adw9972.

10.1126/science.adw9972

NEWS

> “Nobody voted to halt cancer research. Nobody voted to cut lifesaving treatments for heart disease.”

Ph.D. student Emilya Ventriglia, who has conducted research at the U.S. National Institutes of Health, at a rally this week in Washington, D.C., protesting the Trump administration’s cuts to science.

At a rally last week, Jenna McGrew protested cuts at NIH, saying they could harm her brother, who has been receiving treatment there for the past year.

IN BRIEF

Edited by **Jeffrey Brainard**

TRUMP TRACKER

Confusion, woe deepen over White House’s science squeeze

MORE NIH JOB CUTS President Donald Trump’s administration told the 27 directors of the U.S. National Institutes of Health to expect to cut staffing back to 2019 levels, or at least 10% below NIH’s 2024 tally, sources told *Science* last week. That could lead to more terminations beyond the 1200 employees—just over 5% of the biomedical research giant’s 20,000 staff—let go so far this month as part of the governmentwide firings of “probationary” employees, who generally had less than 1 or 2 years in their current position.

PROBATIONARY REDEFINED When the National Science Foundation (NSF) last week fired 168 employees, or 10% of its workforce, about half had probationary status. But several of the fired probationary scientists told *Science* that NSF reclassified them from permanent just days before. NSF has historically made employees permanent after 1 year of service. NSF officials told the reclassified employees the agency had made a mistake and that their probationary period should have lasted 2 years, *Wired* reported. The change enlarged the pool eligible to be dismissed.

FELLOWS AXED At least 15 of 21 fellows in the Centers for Disease Control and Prevention’s (CDC’s) Laboratory Leadership Service were axed this month. The highly competitive, 2-year program trains Ph.D. scientists in the intricacies of public health laboratory work and sends them to states and municipalities that ask for help with local outbreaks. A CDC staffer who works with the program calls the trainees “very successful, service-minded people,” and adds, “Who would want to come in and work in public health after this?”

FIRED, REHIRED After firing scores of scientists, administration officials scrambled to rehire some it decided after the fact were important to retain. Among those called back were at least 15 of 28 probationary employees let go at the National Bio and Agro-Defense Facility in Kansas. Those laid off included some working on the outbreak of highly pathogenic avian flu that is driving up egg prices across the country. Separately, the U.S. Department of Agriculture hired back a plant breeder who had been leading an effort to improve the utility of its “gene banks”—vast collections of seeds and living crops mined by researchers and private seed companies. And dozens of workers dismissed from the Food and Drug Administration’s (FDA’s) medical devices division were rehired, *The New York Times* reported. Their dismissals last week drew criticism because their remit includes evaluating applications filed by Neuralink, which is developing a controversial brain-computer interface

PHOTO: A. ROBLES GIL LUNA/*SCIENCE*

device. The company is owned by billionaire Elon Musk, who has led governmentwide firings on behalf of Trump. Medical device manufacturers whose products need FDA vetting had pushed for those rehires, noting they—not taxpayers—funded the positions with required fees.

DEI AWARDS CANCELED The Chan Zuckerberg Initiative (CZI) science philanthropy canceled its Science Diversity Leadership awards after one round. The program had offered $1.15 million over 5 years to biomedical researchers with a record of promoting diversity, equity, and inclusion (DEI) in their scientific communities. CZI attributed changes to its DEI programs to "the shifting regulatory and legal landscape," *The Guardian* reported. Last month, Trump issued an executive order that demands the end of DEI and other "illegal discrimination" by wealthy foundations, universities, and corporations.

FIVE THINGS YOU DID U.S. science agencies and staff researchers were left confused after the administration's personnel office asked all federal workers in a 22 February email to detail five things they accomplished in the previous week. Musk posted on social media that workers who did not comply within 2 days faced firing, although the email did not include that legally questionable threat. An Interior Department official emailed staff there that they should reply and copy managers; some managers in the National Oceanic and Atmospheric Administration told employees to craft replies but not to send them yet, *The Washington Post* reported. "To be treated the way that somebody in an entry level job might be is shocking," an NIH scientist told *Science*. A biologist at a U.S. cancer center offered a tongue-in-cheek list of accomplishments in a social media post that he dedicated to all his "fantastic colleagues at NIH, NSF, and CDC." Adapted from the lyrics of a famed 1987 pop song by Rick Astley, it began: "Monday: Never gave you up. Tuesday: Never let you down."

PHOTO: PALEONTOLOGICAL RESEARCH INSTITUTION

An Ithaca, New York, museum hosts Antarctic fossils such as these Cretaceous period ones from Seymour Island.

PALEONTOLOGY

Famed fossil museum may close because of money shortfall

The Paleontological Research Institution (PRI), home to one of the most extensive invertebrate fossil collections in North America, is facing imminent closure after its major donor could not make good on a pledge. The museum is now in danger of defaulting on its mortgage. Founded in 1932, the institution in Ithaca, New York, houses more than 7 million specimens, including the largest collections anywhere of fossils from Antarctica, Venezuela, and the Dominican Republic, which draw researchers from around the world. A single, anonymous donor gave it more than $20 million from 2000 to 2023 but has since run into financial hardship. Cornell University, also in Ithaca, told *Science* it cannot provide PRI the needed funds. If it closes, its collections may be divvied up among other institutions or lost.

Petawatt electron pulses debut

ACCELERATOR PHYSICS | For decades, researchers have squeezed laser light into pulses so short that, for just an instant, they pack 1 million gigawatts of power. Now, physicists have matched that feat by producing petawatt pulses of electrons, a paper in press at *Physical Review Letters* reports. Researchers at SLAC National Accelerator Laboratory used a laser to manipulate a millimeter-long bunch of electrons emerging from a linear accelerator, with lower energy particles preceding higher energy ones—a so-called chirp. The laser added another chirp to the bunch, which the team then ran through other accelerating chambers and magnetic bends designed to let higher energy electrons catch up to lower energy ones. The effect was to crowd electrons in the middle of the bunch into an ultraintense pulse only 0.3 micrometers long. Such petawatt electron beams could be used to generate plasmas resembling those in cosmic settings such as gamma ray bursts, and someday might even rip particles out of empty space, as theory predicts is possible.

'Passing' as white extended lives

HEALTH DISPARITIES | Black men in the United States who "passed" as white to skirt segregation and discrimination in the 20th century lived 9.4 months longer, on average, than their siblings who continued to publicly identify as Black, a study has found. The research, which relied on census records collected between 1880 to 1940 and Social Security data from 1975 to 2005, provides an unusual glimpse of the effect of inequalities on health outcomes. The extra longevity represents about 36% of the total longevity gap between all Black and white people at the time, which was about 2.15 years, according to the working paper, published by the National Bureau of Economic Research. On average, Black people who passed as white had 2.2 more years of education than their nonpassing siblings, which the authors estimate accounted for nearly all of the increase in their longevity.

Fusion scientist to lead UKRI

LEADERSHIP | Ian Chapman has been picked as the next chief executive of UK Research and Innovation (UKRI), the country's national science funding agency with an annual budget of £9 billion, starting in June. In 2016, months after the United Kingdom voted to leave the European Union, he was appointed CEO of the UK Atomic Energy Authority, where he oversaw the shuttering of the EU-backed Joint European Torus fusion research facility and refocused the U.K.'s fusion program to build the country's own prototype power reactor. UKRI faces possible flat funding as the government tries to trim its budget.

Students and postdocs fear an even more brutally competitive job market.

PHOTO: STÍGUR MÁR KARLSSON/HEIMSMYNDIR VIA ISTOCK

TRUMP ADMINISTRATION

U.S. early-career scientists struggle amid chaos

Uncertain funding, government firings, and university distress hit the most vulnerable

By **Katie Langin**

For one postdoc, uncertainty about whether the funding for her awarded "diversity" fellowship from the National Institutes of Health (NIH) will come through means she's spending valuable time writing more applications instead of doing research. For another, learning that the "dream job" he'd been offered at the U.S. Department of Agriculture (USDA) was being withdrawn because of the federal hiring freeze has left him clinging to his current position—and $5000 poorer because he already canceled his lease in preparation for moving. And a Ph.D. student whose dream is to one day lead a planetary mission at NASA is "panicking" about her professional future.

These are just a few of the countless researchers reeling after President Donald Trump's administration unleashed a wave of actions over the past month—freezing funds, firing thousands of federal employees, upending programs and research related to gender and diversity, and more. Scientists of all stripes have been affected, but none more so than early-career researchers, a group already struggling with low pay and job insecurity. Now, some wonder how many of those budding researchers will throw in the towel and leave science, or the United States, entirely. "There's going to be a missing age class of researchers that will reverberate for years," one federal scientist fears.

Scores of young researchers were affected after the country's main federal funding agencies, NIH and the National Science Foundation (NSF), canceled programs that were judged to be in violation of Trump's 21 January executive order banning "dangerous, demeaning, and immoral race- and sex-based preferences under the guise of so-called 'diversity, equity, and inclusion' (DEI)." Some were supplements to other grants secured by principal investigators and were meant to support the salaries and career development of trainees from underrepresented groups. Others were awards given directly to graduate students and postdocs who proposed, as part of their research or through outreach, to help broaden the participation of underrepresented groups in science, technology, engineering, and math fields.

"These kinds of shocks are going to lead to a mass exodus … for minorities in particular," says Trajan Hammonds, a Princeton University math Ph.D. student who last year applied for one of the postdoc fellowship programs NSF has since canceled. He expected to hear news about his application this month—but instead he got an automated email notification that the program had been deleted. He's now scrambling to find other postdoc opportunities. "I'm fairly annoyed," he says. "I would've happily applied for the 'regular' [fellowship] … and I would have had a pretty strong application."

Another applicant, a postdoc who asked to remain anonymous, says she's concerned about her own future in science—and about what will come of efforts to ensure the academic community is accessible to people who come from disadvantaged backgrounds. "What part of diversity, equity, and inclusion do you have a problem with?" she asks.

The campaign against DEI could endanger some nondiversity grants to early-career researchers as well. One Ph.D. student, who also wished to remain anonymous, told *Science* she applied for an NIH training grant to support her research on maternal mortality. Her proposal, which had been scheduled to be reviewed in January, mentioned racial disparities and used gender-neutral language such as "birthing people." She fears it may now be

flagged as being in violation of Trump's executive orders.

Young researchers also face the prospect that positions for graduate students and postdocs will dwindle because of broader scale cuts to research funding—for instance, the threatened reduction in the indirect costs that universities charge to carry out research funded through federal grants. As graduate school admission decisions are being made, faculty at several research-intensive universities—including Vanderbilt University and the University of Washington—have been told to reduce the size of their incoming cohorts, the health news site *STAT* reported.

Some prospective students wonder whether they will even accept a slot if offered. Mathew Sarti was hoping to start grad school this fall. Now, he says, "I want to wait and see how departments handle certain things before committing fully to a place," he says. He's holding out for a department that will support students affected by the turmoil, as he was. Sarti, a junior specialist in a lab at the University of California, Santa Cruz, heard from NIH in January that he was being recommended to receive a diversity training grant. But on 5 February he and his supervisor received a follow-up email that said, "I regret to have to inform you that NIH has instructed us not to issue any diversity supplements that are pending." He lost funding to attend conferences, and he can't afford to pay his own way. "I'm first generation in all senses of the word."

Many of the federal scientists fired this month are also early in their careers. "I feel like I was robbed of a career," says one biologist who was terminated from his position at the U.S. Geological Survey on 14 February. Another fired scientist, who had started a position at USDA in 2023 after finishing a 3-year postdoc, says he had "envisioned this being my last job—one I would be in for 20 or more years."

They're now suddenly in an uncertain position, with a new set of financial challenges and anxiety about where they'll be able to find work next. "I'm not optimistic about an already competitive job market that is going to be flooded with qualified scientists," one said.

That leaves those earlier in the career pipeline worried as well, especially as reports start to trickle in about universities slowing hiring of faculty members and postdocs. "What does my future look like?" asks Ashley Walker, a fourth year planetary science Ph.D. student at Howard University who founded #BlackInAstro and dreams about working at NASA someday. "The job market—what it looks like today, will be completely different a year from now, right? And so, what trajectory does that lead me in?" ■

ASTRONOMY

Infrared space telescope will probe 'inflation' after Big Bang

SPHEREx hopes to explain our "boring" uniform universe

By **Daniel Clery**

A modest space telescope with an innovative design is about to search for traces of a key moment in cosmic history: the first tiny fraction of the first second following the Big Bang. The Spectro-Photometer for the History of the Universe, Epoch of Reionization, and Ices Explorer (SPHEREx), an infrared telescope with mirrors no bigger than a dinner plate and a price tag less than 1/20 that of NASA's flagship JWST space observatory, is designed to survey 450 million galaxies and create a vast 3D map. Those data will shed light on galaxy evolution and the chemistry of our Galaxy, but perhaps its most striking use is searching for evidence of cosmic "inflation," a theorized trillion trillionfold ballooning of the universe in its first billionth of a trillionth of a trillionth of a second.

SPHEREx aims to narrow down the possible drivers of that growth. "It's a cool project," says cosmologist Jo Dunkley of Princeton University. "I'm pretty excited we could detect one [of the signatures of inflation] that would tell us more."

The $488 million telescope, scheduled for launch this week into low-Earth orbit, commands a wide field of view, the equivalent of 200 full Moons. During its 2-year mission, this will enable it to map the sky every 6 months, recording the "color" of galaxies in infrared light—a clue to distance, as light from farther objects is redshifted because of the expansion of the universe. "We struggled quite a bit with the design of the optics" to fulfill its varied goals, says SPHEREx principal investigator James Bock of NASA's Jet Propulsion Laboratory.

A series of three aluminum mirrors gathers light from its wide view and onto detectors via so-called linear variable filters. The filters only transmit light around a certain wavelength, which varies along the length of the filter. The entire spacecraft rotates to shift the light across the filter in 102 steps, capturing 102 different colors. The setup is not as precise as a spectrometer, the usual device for analyzing different wavelengths of light, but allows SPHEREx to survey a large area of sky at reasonable cost. Three nested photon shields keep the telescope cold, preserving its sensitivity to incoming infrared signals.

Astronomers hope the resulting data will allow them to probe possible drivers of inflation, a concept developed in the 1970s to get around certain problems thrown up by the cosmic microwave background (CMB) radiation, an all-pervading afterglow of the Big Bang. Dating from just 380,000 years after the Big Bang, the CMB appears now remarkably smooth, suggesting a uniform universe in all directions. But why should conditions at opposite ends of the universe, which could never have communicated because of light's finite speed, look so similar? "This picture of the primordial universe that we have is extremely boring," says astroparticle physicist Lucien Heurtier of King's College London. "It's basically the same everywhere and that was a big surprise."

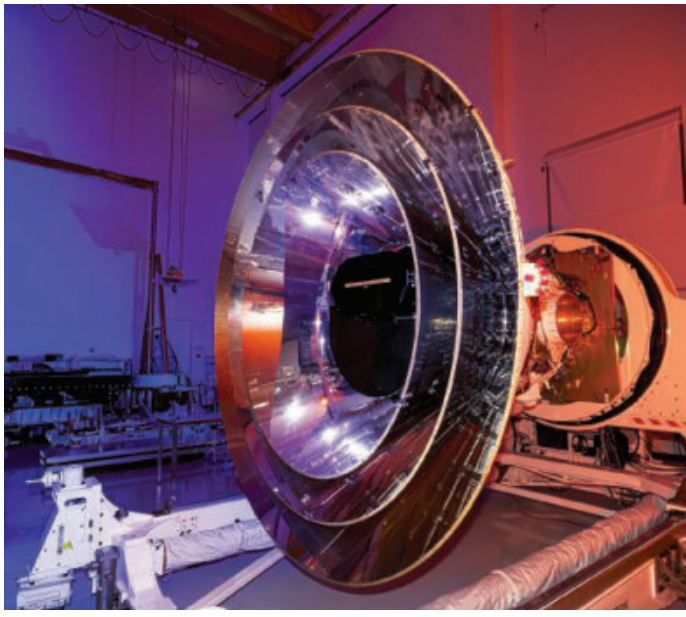

SPHEREx's nested photon shields give it an unusual horn-shaped appearance but are there to keep its telescope cool in space.

PHOTO: JPL-CALTECH/NASA

Its shape is also surprising. According to Albert Einstein's theory of gravity, large masses such as galaxies or black holes add curvature to spacetime, but overall, the universe is utterly "flat," meaning its density is finely balanced between expanding forever and having enough matter to overcome expansion and pull it into a Big Crunch.

That uniformity can be explained if the universe had an early instant of ultrarapid growth, in which it swelled from smaller than a proton to the size of a grapefruit. Its growth then slowed, but the initial burst essentially locked the cosmos into its initial uniform state and stretched out any curvature. Many physicists invoke a new fundamental force with its own field, mediated by a particle called the inflaton, as the driver of this phenomenal growth. But theorists have proposed others, with more fields and more particles. "We cannot pinpoint which theory of cosmic inflation is the correct one yet," Heurtier says.

SPHEREx hopes to narrow down the range of possibilities by measuring the distances between a large number of galaxies. A simple, single-field inflation would produce a universe where the distances between galaxies have a symmetrical distribution called a bell curve. Multifield theories of inflation would deviate from that.

SPHEREx will also study the evolution of galaxies, by looking at the overall glow of space, coming from clouds of gas and isolated stars as well as galaxies. Galaxies began to form when the universe was less than half a billion years old, gradually growing bigger and brighter as they drew in more gas and formed more stars. But after about 4 billion years, star formation began to slow. Today, 13.8 billion years after the Big Bang, galaxies forge few new stars.

One theory attributes the slowdown to stellar winds, outpourings of particles that, when galaxies reached a certain size, became so strong that they broke up the gas clouds. "You need gas to cluster enough in order to then coalesce to form stars," says astronomer Anthony Pullen of New York University. "You don't have that effect if there is wind pressure that's disrupting that process." By analyzing how the intensity of the combined light from galaxies and gas changed over time, SPHEREx investigators hope to test that scenario.

SPHEREx's infrared vision also makes it sensitive to chemical compounds in our own galaxy, including water ice, carbon monoxide and dioxide, and methanol, frozen onto grains of dust—potential building blocks for life. The spacecraft will help reveal how prevalent these materials are and how stars transform them, thanks to its expansive view. "We get the whole sky," Bock says. ■

PUBLIC HEALTH

Tracking the toll of Sudan's forgotten war from afar

Barred from the country, researchers use satellite imagery and models to assess destruction and death

By **Leslie Roberts**

At Yale University's Humanitarian Research Lab, researchers are poring over satellite images and thermal sensing data captured over the Darfur region of Sudan over the past few weeks, looking for telltale signs of recent violence. Where a hospital stood just a few weeks ago, there may only be scarred ruins today. A graveyard on the edge of a town has undergone a sudden expansion. Entire villages have been torched.

The lab, part of Yale's School of Public Health, is one of several groups gauging the devastation caused by Sudan's brutal civil war. The conflict, drowned out in the media by other crises, has resulted in the worst famine in 40 years, disease outbreaks, and the destruction of vital infrastructure, and has driven more than 14 million people from their homes. The recent U.S. freeze on foreign aid, which has provided billions of dollars to Sudan the past 2 years, has deepened the crisis. But assessing the toll, which can guide humanitarian responses and help investigate war crimes, can only be done from afar.

One reason is the intense fighting, which has made large parts of the country inaccessible. But the warring factions are also blocking access. The Sudanese government is "very hostile to data gathering and to having a major humanitarian presence," says Alex de Waal, an expert on food security and Sudan at the World Peace Foundation at Tufts University.

As a result, estimates of how many people have died from fighting and related causes have varied from 20,000 up to 150,000. "We can't responsibly give a number," says Nathaniel Raymond, executive director of the Humanitarian Research Lab. "Many who would do the counting are dead or displaced." But the few data available show that "absolutely more people are dying of starvation and disease than bullets and bombs," says Maha Sulieman, a doctor and director of outreach for the nonprofit Sudanese American Physicians Association (SAPA).

Since April 2023, the government's Sudanese Armed Forces (SAF) have been battling the paramilitary Rapid Support Forces (RSF), an outgrowth of the Janjaweed militia that slaughtered at least 200,000 people in Darfur at the turn of the century. A U.N. fact-finding mission in September 2024 concluded both sides have committed an "appalling range of harrowing human rights violations and international crimes," including mass rape, arbitrary arrests, and torture. They have also destroyed hospitals, schools, communication networks, and water and electricity supplies. The SAF and RSF are both using starvation as a weapon, blocking food, medical supplies, and other aid from reaching many of the estimated 30 million people who desperately need them.

The situation is especially dire in the state of North Darfur, where aid groups are

PHOTOS: 2025 MAXAR TECHNOLOGIES VIA GETTY IMAGES

Satellite images captured in Sudan on 3 February (left) and 10 February (right) reveal that the main market in Zamzam camp in North Darfur was attacked.

largely unable to go, says Leni Kinzli of the United Nations's World Food Programme. In Zamzam camp, home to half a million internally displaced people and under attack from both sides, a child was dying every 2 hours a year ago, Doctors Without Borders (MSF) has estimated. In Tawila, elsewhere in North Darfur, a "staggering" 35% of children were suffering from acute malnutrition, MSF reported in December 2024.

A widely recognized international body that uses scientific criteria to evaluate food security, the Integrated Food Security Phase Classification (IPC), has confirmed that Sudan is starving. In December 2024, its Famine Review Committee, a panel of independent experts, said famine had spread to at least five areas, and five more would face the same fate by May. There was a risk of famine in 17 additional areas—"an unprecedented, deepening, and widening of the … crisis," the committee wrote. But the Sudanese government has dismissed the findings and has withdrawn from the IPC process, says a humanitarian worker who asked not to be named. "A famine declaration shows they are no longer in charge and can't take care of their people," she says.

Outbreaks of infectious diseases, which are especially deadly in malnourished children, have compounded the disaster. A cholera outbreak that has hit 10 states is expected to resurge with the coming rainy season. MSF is seeing more cases of malaria, dengue, measles, acute respiratory infection, and diarrhea, says Melat Haile, the group's medical advisor in Sudan. People with HIV and tuberculosis can't get their drugs, and some with cancer and diabetes are dying for lack of care, says Frank Ross Katambula, MSF's medical coordinator in eastern Sudan.

To assess the toll, the Yale lab collects satellite images and relies on SAPA, which provides humanitarian aid in Sudan, for "ground-truthing"—checking whether hospitals are still functioning, for example. "We are able to get in where the U.N. can't," Sulieman says. "Our work is only possible because we are Sudanese."

In December, the Yale lab reported that nearly half of the hospitals in Khartoum state were damaged. On 5 February, it said the RSF had attacked Zamzam and other camps in January and burned dozens of communities around El-Fasher, the capital of North Darfur. It found many newly dug mounds highly consistent with graves near Zamzam and in Abu Shouk, another camp for the internally displaced. Satellite imagery has also shown the warring factions are burning fields and corrals and attacking water boreholes and reservoirs. "If you want to kill people, deny them the ability to water and graze their animals. We see both," Raymond says.

The Yale researchers don't produce death estimates, but other groups do. The Armed Conflict Location and Event Data (ACLED), an independent nonprofit that monitors conflicts, relies on death estimates from international organizations and other partners, traditional media, and verified Telegram and WhatsApp accounts. In December, it estimated that since the start of the conflict, "at least" 28,700 Sudanese had died from "intentional injuries," including 7500 civilians. That conservative number does not include deaths from war-related malnutrition and disease.

Maysoon Dahab at the London School of Hygiene & Tropical Medicine and colleagues think the toll is far higher. Death estimates often rely on hospital or morgue records, Dahab explains. "But what about people never buried or who never made it to the hospital?" Her team used a modeling technique that compares data from multiple sources, including surveys and obituaries, to estimate that Khartoum state alone had more than 26,000 deaths from intentional injury between April 2023 and June 2024—higher than ACLED's estimate for the entire country during the same period—and more than 61,000 deaths from all causes combined, a 50% increase over the prewar death rate.

Sarah Elizabeth Scales of the University of Nebraska Medical Center and colleagues have adopted another way to estimate the total number of deaths: multiplying the number of direct deaths from violence by a factor based on past experience. In 2008, for example, the secretariat of the Geneva Declaration on Armed Violence and Development estimated, based on 24 small-scale surveys, that there were 2.3 indirect deaths for every direct death from violence during the earlier Darfur genocide. Using that multiplier, Scales and colleagues conservatively estimated total deaths since the start of the current war until October 2024 at 62,000. But calculating these ratios is hard, de Waal says. Based on other armed conflicts around the world, the secretariat has reported that the multiplier ranged from three to 15. Other estimates are lower.

Raymond says such estimates are no substitute for collecting mortality data directly while the war continues. "Since September 2023 we have been screaming at the top of our lungs that international health care organizations and funders should prioritize mortality data collection," he says. But, "They want to wait to do a body count until the conflict is over." He worries things in Sudan will only get worse: "We haven't hit bottom yet." ■

Leslie Roberts is a science journalist in Washington, D.C.

CLIMATE

U.S. cuts support for IPCC report

U.N. climate panel meets without U.S. leadership

By **Paul Voosen**

The world's nations convened this week in Hangzhou, China, to plan the next major international assessment of climate science—but without the United States. Late last week, President Donald Trump's administration denied officials permission to travel to the meeting and cut off a technical support contract for the report, the seventh assessment of the Intergovernmental Panel on Climate Change (IPCC).

The United States has long been a leader of IPCC, which brings volunteer scientists together, unpaid, to produce influential reports every seven or so years. Katherine Calvin, NASA's chief scientist, was set to co-lead IPCC's third working group, on climate mitigation. Former President Joe Biden's administration committed roughly $1.5 million for a technical support unit (TSU) to help with creating graphics and websites, running meetings, and editing the group's report.

NASA leadership decided to end the TSU contract, a source with knowledge of the decision told *Science*. Calvin also did not travel to Hangzhou this week. At the same time, last week the Department of State reportedly told its diplomatic delegation not to attend the meeting, leaving a minimal U.S. presence. "This is really shocking," says Angel Hsu, a climatologist at the University of North Carolina at Chapel Hill who is serving on an upcoming IPCC report on climate change and cities.

As of now, funding for U.S. scientists' travel to IPCC meetings has not been canceled, sources said. Still, Hsu worries her travel expenses won't be reimbursed. "I can still participate, but that can be really challenging if the funding we depend on is cut off," she says.

Even if IPCC figures out how to keep U.S. scientists involved, damage to the reputation of the U.S. has been done, says Robert Kopp, a climate scientist at Rutgers University and former IPCC author. "The U.S. moves are certainly of a piece with other recent moves by the U.S. government to end the United States's long established position of global scientific leadership." ■

A researcher at the Wisconsin National Primate Research Center returns a macaque to its cage.

PHOTO: SCOTT OLSON/GETTY IMAGES

ANIMAL RESEARCH

Fate of millions of research animals at stake in NIH lawsuit

Rodent and monkey facilities imperiled by Trump plan to slash overhead payments to research institutions

By **Meredith Wadman**

The stakes were especially high for one group of scientists last week, as a federal judge in Massachusetts heard arguments on whether she should allow President Donald Trump's administration to slash the overhead costs the National Institutes of Health (NIH) pays to institutions for medical research.

Research associations and 22 states filed two legal challenges to the cut, and on 10 February U.S. District Court Judge Angel Kelley imposed a temporary ban on its implementation. She was set to decide as early as this week on whether to extend that ban while the case is argued on its merits.

Researchers who use tens of millions of rodents and thousands of nonhuman primates each year are especially dependent on NIH's "indirect cost" payments to support major animal research facilities, where complex housing, staffing, medical care, and regulatory requirements push up costs. It's not uncommon for large research universities, for example, to have "mouse houses" that support tens of thousands of rodents.

Indirect cost rates can be relatively high at universities; at Stanford University they are 54%, meaning an NIH grant with direct research costs of $100,000 would come with an additional $54,000 to pay for administration and facility costs. But at animal facilities, the rates can rise above 80%. Although scientists pay per diems to use the animals, they don't cover the cost of running the centers.

That means the steep rate cut NIH has proposed, to 15%, "could have very, very, very bad consequences … for animals," says Paul Locke, an attorney with expertise in laboratory animal law at the Johns Hopkins Bloomberg School of Public Health. (He spoke for himself and not his university.) Some animal facilities, he predicts, will "have to make very, very hard decisions about the animals that they have on site. … It could be extreme." Other observers say institutions might have to euthanize thousands of animals.

At facilities that house primates, "This sort of cut would cause a death spiral," says Deborah Fuller, director of the $30.5 million Washington National Primate Research Center at the University of Washington. The center—one of seven such facilities supported by NIH—would lose $5 million under the policy change, according to the lawsuit filed by 22 state attorneys general. The center's negotiated indirect cost rate is 83.1%, the lawsuit notes. A cut would force it "to reduce or eliminate the 800 nonhuman primates in its care," it states.

At the Jackson Laboratory (JAX), a major supplier of genetically engineered mice to scientists, the policy change would deliver a double blow, both cutting funding to its own large research programs and reducing its revenues by dampening sales of its mice to researchers. The indirect cost rate of the lab's main facility in Bar Harbor, Maine, is 77%.

Gary Friedmann, a member of the Maine House of Representatives whose district includes JAX, wrote to Department of Health and Human Services Secretary Robert F. Kennedy Jr. on 18 February, urging him to withdraw the NIH proposal. Since then, "I've gotten lots of responses from people who are scared about their jobs and, really, about the future of scientific research at the lab," he says. Friedmann estimates that "one-third to almost 40% of the total NIH dollars that are coming to JAX would be at risk." JAX declined to answer questions about its indirect costs, but said the proposed cut "threatens the entire biomedical research community."

At the Washington primate center, Fuller says overhead payments not only help feed and house its 800 macaques, but also support a biosafety level-2 facility for studying infections in the animals. The center employs 179 staff, and the university provides the personnel needed to make sure its work complies with U.S. regulations. "This is a highly sophisticated operation [with] huge infrastructure," Fuller says.

At the Wisconsin National Primate Research Center, interim director Buddy Capuano says a funding cut would not be fatal. "We make contingency plans all the time," he says, adding he would "never" euthanize animals because of budget woes. "Our number one job is to take care of these animals."

Critics of animal research see an opportunity in NIH's plan. Justin Goodman, senior vice president of the White Coat Waste Project, an advocacy group, argued in a recent congressional hearing that "if we're concerned with science and we're concerned about being good stewards of taxpayer dollars … we can end animal testing tomorrow." If NIH cut off "funding for animal testing," he added, researchers are "gonna figure out something else to do."

Locke also believes medical research needs to transition away from using animals. But he says an abrupt cut is a bad idea. Change, he says, needs to come through "aggressive incrementalism and not death by ax." ■

With reporting by Sara Reardon.

ORIGIN OF LIFE

Early life's phosphorus problem solved?

Minerals from volcanic rock could have supplied a key ingredient for biomolecules

By **Robert F. Service**

Be they microbes or monkeys, organisms require phosphorus—and lots of it. It's a key component of DNA and RNA, of the ATP that fuels living cells, and of the lipids that make up cell membranes. The element's centrality has long puzzled researchers trying to understand early life, because phosphorus isn't naturally abundant in most watery environments, the kind of place where life probably began. Now, a trio of new papers supports a recent proposal that volcanic activity around highly alkaline "soda" lakes—and perhaps hot springs—could have enabled phosphorus compounds to accumulate to levels needed for life to start and spread.

Mono Lake, in California, is rich in elements leached from volcanic rock—including high levels of phosphorus.

PHOTO: GALYNA ANDRUSHKO/ALAMY

"This is really a good step forward," says Martina Preiner, an origin-of-life chemist at the Max Planck Institute for Terrestrial Microbiology who was not involved with any of the new research. She cautions that although the new papers offer a plausible route to solving what has long been known as the "phosphorus problem," researchers still need to show that compounds generated under these conditions actually undergo reactions resembling rudimentary biochemistry. Geochemist Matthew Pasek of Rensselaer Polytechnic Institute agrees, but adds: "I think we are much further along than we were before."

The recognition that phosphorus availability was a likely bottleneck on the road to life dates as far back as 1955, to a paper by American biochemist Addison Gulick. The origin of life would probably have required high concentrations of compounds such as phosphate—a phosphorus atom surrounded by four oxygens. In oceans, rivers, and most lakes the phosphate concentration is typically 10,000 times too low.

Early Earth was different, though. Phosphorus is present in volcanic lavas, and the young planet had a lot more volcanic activity than today. In a series of lab studies reported in September 2024 in *Communications Earth & Environment*, Pasek and his colleagues found that reactions between iron-rich volcanic rocks and water at high temperatures—like those found in a hot spring, or hydrothermal, environment on land—convert phosphorus to a range of different phosphates. If the hot spring periodically dried up, it might concentrate phosphates enough to promote vital biochemical reactions.

Soda lakes are another place that could happen, as University of Washington earth scientists David Catling and Jonathan Toner first proposed in the *Proceedings of the National Academy of Sciences* in 2020. Such lakes also form in volcanic environments, in closed basins filled by runoff that has weathered sodium and carbonate—the ingredients of baking soda—out of volcanic rocks. With no outflow, the lakes lose water only to evaporation, which concentrates the chemicals over time.

Catling and Toner noticed that along with the soda, phosphate levels, too, are often high in such lakes today. In ordinary lakes or the ocean, calcium ions readily bind phosphate, locking it away in solid minerals that become sediments. In soda lakes, the researchers suggested, carbonates bind the calcium ions before they can strip phosphate from the water. But it remained unclear why life thrives in some soda lakes today but struggles to do so in others, and what that might reveal about life's dawn.

To find out, Catling and colleagues have now measured the precise phosphorus inputs and sinks in a pair of small soda lakes in British Columbia. One, called Goodenough Lake, had moderately high levels of dissolved phosphate and abundant microbes and other life that were extracting phosphate from the water. The other lake, known as Last Chance, was so salty it kept microbes from harvesting nitrogen from the air, inhibiting their growth. That resulted in extremely elevated phosphate levels.

In a paper published online on 4 February in *Geochimica et Cosmochimica Acta*, Catling and his colleagues conclude that before life began, soda lakes could have accumulated enough phosphate to make life possible. "This type of lake would be archetypal on the early Earth," Catling says, because volcanic activity was so prevalent then.

Lakes as small as Last Chance and Goodenough, both little more than shallow ponds, could at best have offered early life a toehold before their phosphates would have been depleted. "This is a major barrier," says Craig Walton of the University of Cambridge. He and his colleagues recently analyzed much larger soda lakes, including Mono Lake in California, which is 21 kilometers long and up to 17 meters deep. Phosphate levels there are far higher than in nonsoda lakes, the researchers reported last week in *Science Advances*, although they don't rival the phosphate concentrations in the British Columbia ponds. But Mono and its peers offer a much more stable supply. "These large-scale lakes give you a bit of both," Walton says.

To him, the combination of volcanic activity and soda lakes is "pretty close to a geological solution" to the phosphorus problem. Pasek thinks hydrothermal pools probably played a role, too. "There is room for both," he says. But with any proposal about how life began billions of years ago, Preiner advises humility. "There's uncertainty here that we just have to live with." ■

SCIENTIFIC INTEGRITY

‘Patent mills’ offer intellectual property for sale

Companies register bizarre designs with U.K. office and sell them to scientists to boost CVs

By **Cathleen O’Grady**

Shady companies have long given unscrupulous scientists the opportunity to buy authorship of papers—a form of academic fraud. But according to a draft paper posted online last week and scheduled to appear in the *International Journal for Educational Integrity*, these outfits have now diversified into selling intellectual property (IP) rights, too.

Over the past 2 years, these firms have registered thousands of bizarre designs for medical equipment and other devices with the United Kingdom’s Intellectual Property Office (IPO)—and, for a fee, scientists can be listed as owners of the designs. The companies target researchers in countries including India and Pakistan, where universities reward researchers who patent inventions with career advancement and sometimes bonuses.

The finding is “bonkers” says Emily Hudson, an IP academic at the University of Oxford who was not involved with the research. The practice exploits ignorance about IP systems, she says: The U.K., like many countries, allows artists and others to protect their designs relatively cheaply and easily, without the arduous and expensive process of obtaining a formal patent. It is these design registrations, not patents, that companies are selling.

Northwestern University metascientist Reese Richardson and his colleagues made the discovery while monitoring social media channels used by paper mills to advertise fraudulent academic products for sale, including journal publications, student essays, and theses. About 2 years ago, the team started to notice ads for a new kind of product: so-called U.K. design patents, with “inventorship” slots being sold for 2000 to 30,000 Indian rupees ($23 to $398). The ads emphasize that a “patent filing” can give researchers a boost in the ranking systems used in India.

The researchers matched up more than 20 of these ads with design registrations filed with IPO. The two companies responsible for these registrations had filed almost 2000 more, the team found: mostly “childish” designs, Richardson says, with images often cribbed from repositories of 3D drawings, and titles invoking buzzwords such as “AI-powered” or “machine learning.”

The often absurd designs included everything from agricultural machinery to electrical equipment, but medical devices were the most common. One design, for instance, shows a shoe with what appears to be a camera and USB ports around the sole, titled “Smart shoe for visually impaired.” Another is titled “Designing an Artificial Intelligence Powered Skin Cancer Inspection Device with Design Thinking” and is a 3D drawing of a Glock pistol with the addition of a small screen and USB ports. “I was hooting and hollering when I saw that one,” Richardson says.

Two academics appearing 59 and 51 times, respectively, on the registrations, Reena Singh and B. K. Sarkar, together operate a company called Geh Research, which offers international “patent” filing, thesis writing, and paper publication services, among others. Singh and Sarkar did not respond to a request for comment

“Smart shoe for the visually impaired”

By further scouring the database of design registrations, the researchers identified an additional six suspicious companies. These firms were relatively new, with a limited web presence, and filed designs with flowery titles and high numbers of named owners. Together, these companies have registered more than 3000 designs in the past 2 years, representing 3.3% of all designs registered in the U.K. in that period.

The discovery “blew my mind when I heard about it,” says Sarah Fackrell, an IP law researcher at the Chicago-Kent College of Law who contributed legal expertise to the paper: “Getting IP rights in order to commit academic fraud or misconduct is new to me.”

Almost all the owners listed on the registrations found by the researchers were academics or universities in India.

Indian universities allocate points to employees for products such as journal papers and patents, and employees must reach a minimum number of points in order to pass annual reviews, says Achal Agarwal, founder of the research integrity organization India Research Watch. A ministry body that regulates and funds universities suggests researchers should get more points for international than local patents, although institutions differ in how closely they follow these recommendations, Agarwal says. But design registrations are not equivalent to patents, Fackrell notes, and the scheme uncovered in the new paper would not work if universities properly discriminated between the two.

The companies found by Richardson and his colleagues may be serving academics in India, but similar exploitation happens elsewhere, says Anna Abalkina, a paper mill researcher at the Free University of Berlin who was not involved in the research. Russian universities similarly incentivize patents, along with journal papers and other products, and companies advertise patent inventorship on social media—including the Russian equivalent of Craigslist, she says.

The exploitation is concerning for a few reasons, Fackrell says: Flooding the register with “garbage” could make it more difficult for good-faith applicants to check whether their design is new, and could raise questions about the legitimacy of the IP system.

But this doesn’t necessarily mean IPO should make it more onerous or expensive to register designs, Hudson says. That could hurt legitimate designers—the lack of oversight in the system “is a feature, not a bug,” Hudson adds.

In an email to *Science*, a spokesperson for IPO said designs, like other IP, can legitimately be bought and sold, and that “it would not be appropriate for the IPO to comment on arrangements in other jurisdictions relating to academic recognition.”

Indian institutions could help reduce the incentives for IP fraud by assessing researchers on the quality, not quantity, of their output, Agarwal says. The corruption is harming India’s reputation, he adds. “The only way this reputation can be improved is by calling it out … and India taking action.” ■

IMAGE: REGISTERED DESIGN 6281591/UK INTELLECTUAL PROPERTY OFFICE

FACING THE PAST

Researchers and an Indigenous Amazon nation team up to study charged ritual objects: shrunken heads

By **Kata Karáth**
in Guayaquil, Ecuador

Shuar leader Jefferson Lequi (right) and anthropologist María Patricia Ordoñez examine a shrunken head.

PHOTO: KATA KARÁTH

Jefferson Lequi delicately cups the remains of a human head in his gloved hands, examining every detail of the fist-size tsantsa, or shrunken head. The head's lips—once ceremonially sewn together—are slightly parted, the threads undone. The eyes, rimmed with long lashes, are sewn tightly shut beneath the furrowed brow. The once-lush dark hair is now sparse, allowing Lequi to see a sewn-up, straight cut in the back of the head. Behind him on a table, at the Guayaquil Municipal Museum, four other tsantsas are nestled in sheets of foam and bubble wrap, waiting to be studied.

Lequi, 32, is the administrator or community leader of Tsuer Entsa, a village of Indigenous Shuar people. Their ancestors in the Amazon rainforest created tsantsas until the first half of the 20th century, often from the heads of enemies killed in battle. But few of the heads remain with the Shuar. Exoticized and coveted by Western collectors, hundreds of tsantsas sit in museums and private homes worldwide. Lequi and his community want them back. "The heads are our Shuar heritage. They were taken away through trade, through illegality … without permission of the Shuars," Lequi says.

Tsuer Entsa is one of the few Shuar villages outside the Amazon and near the coast, located only about 120 kilometers from the museum. But Lequi wasn't aware the museum held five tsantsas until anthropologist María Patricia Ordoñez of the University of San Francisco de Quito (USFQ) told him. Since 2017, Ordoñez has partnered with Shuar organizations and museums in Ecuador and elsewhere. Her work combines Indigenous knowledge and Western scientific methods such as CT scans and DNA analysis to identify and authenticate tsantsas, distinguishing those created as part of Shuar rituals from those made for trade. The ultimate goal of the Tsantsa Project is to begin the long, slow work of bringing tsantsas home.

Although shrunken heads are known worldwide, few Western scientific studies have analyzed them. Most scholarly knowledge comes from secondary sources such as foreign anthropologists, settlers, and missionaries, but the Shuar think those accounts are incomplete. The Tsantsa Project is the first study to involve the Shuar in any capacity, as well as the largest comparative genetic study of tsantsas to date. Despite limited funding and much red tape, the team has so far analyzed 26 tsantsas and published on 14.

Returning tsantsas home to the Shuar is fraught with challenges. Because they are cultural objects and human remains more than 100 years old, most tsantsas legally belong to the government of Ecuador, rather than to the Shuar. In addition, many tsantsas were created from the remains of members of the Indigenous Achuar nation, who sometimes fought with the Shuar in the past, explains Laura Van Broekhoven, director of the Pitt Rivers Museum, which works with the Tsantsa Project and holds six tsantsas. The Achuar are not requesting the objects, but their potential claim makes the case for repatriation "a quite complicated one," she says.

The Shuar are adamant that the heads are theirs. David Tankamash, president of the Interprovincial Federation of Shuar Centers (FICSH), a leading Shuar organization representing some 500 communities, hopes the Tsantsa Project will help boost awareness that the heads belong with his people. "[Tsantsas] cannot remain in the hands of non-Shuar people or outside Ecuador," he says.

A central, sewn cut down the back helps authenticate a shrunken head, or tsantsa.

PHOTO: KATA KARÁTH

SHUAR TRADITIONS SUGGEST their ancestors created ritual tsantsas from the remains of humans, sloths, and monkeys for hundreds of years; Europeans noted the practice when they arrived in the 1500s. The Shuar were then seminomadic, hunting and gathering mainly along the Pastaza, Morona, Santiago, and Zamora rivers in the rainforest of today's Ecuador and Peru (see map, p. 922). For centuries, the Shuar have largely resisted colonization, first by the Inca, then by the Spanish. But their way of life became westernized around 1900. Today, most live in permanent settlements where they farm, make handicrafts, and work in forestry, conservation, and the oil and mining industries.

Lequi remembers his grandfather telling him stories of ancestors who created tsantsas. "Tsantsas were made as part of a ritual to give good energy [or power] to our leader, or during battles with other communities, such as the Achuar. The winner would take the head of the opposing leader," he says. The goal was not just to harness a fallen warrior's energy and leadership knowledge, but also to "give thanks to the god Arutam … as a tribute in gratitude to the Earth, the Sun, and the rain."

Ordoñez calls such tsantsas "ceremonial," because they fulfilled a ritual role. "The tsantsa is not a trophy, nor a sign of savage cruelty, but a means of ritually transferring the life of the dead into the warrior," the Catholic Salesian missionary Siro Pellizzaro wrote in a 1980 book, based on early written accounts and interviews with Shuar people. Because the Shuar language was at first unwritten, the Shuar themselves rely on such secondhand sources for some details about tsantsa creation.

The missionaries reported that a person called a *Tsánkram*, perhaps the victorious warrior or a shaman, carried out the shrinking ceremony. After the deceased person or animal was decapitated, the *Tsánkram* made an incision from the middle of the back of the head straight down to the neck. The skin, face, and hair were pulled entirely off the skull, which was discarded. The soft tissues were submerged in boiling water mixed with herbs until the skin shrunk to the desired size. Then the *Tsánkram* molded the tissue back into a hollow sack in the shape of a human head. To prevent the deceased's soul from escaping and causing harm, they sewed up the cut at the back, as well as the eyes and the mouth, likely with local palm fibers.

The whole ceremony could take days. Teenage boys practiced on the heads of sacred animals such as sloths as a form of initiation into adulthood, according to missionaries' and anthropologists' reports.

Change came to the Shuar culture starting in 1850, when white and mestizo settlers encroached on their lands, seeking quinine, rubber, wood, gold, and eventually oil. The Shuar exchanged pigs, deer, salt, and tsantsas for manufactured goods such as machetes, hammers, and rifles. But after Jesuit missionaries introduced cattle, white settlers no longer needed deer and pigs, and tsantsas became the most valuable trade item, satisfying Western cravings for "exotic" artifacts. A guns-for-heads trade arose, according to the late anthropologist Steven Rubenstein of the University of Liverpool, sending tsantsas to collectors around the world. "The Shuars were bribed so they would sell the tsantsas (to outsiders)" says Lequi, who thinks such trades were unfair given the power and technology imbalance of the time.

Science's photographs, taken with the permission of the Shuar nation, do not show the faces of the shrunken heads out of respect for the deceased.

To satisfy the demand, a new kind of tsantsa emerged, crafted specifically for the Western market. These were likely not made by the Shuar, or at least not for ceremonies. Ordoñez calls them "commercial" tsantsas and says the trade ignited warfare.

The practice of making tsantsa began to dwindle in the early 20th century, after missionaries began converting the Shuar and sending their children to Catholic boarding schools. Many gradually became alienated from their culture, as traditional songs, dances, and medicines fell into disuse, as did the creation of tsantsa. Today, Ordoñez and the Shuar people interviewed for this story say few of the 136,500 Shuar feel a strong connection to tsantsas; they are more eager to retrieve other elements of their culture, such as language. "Keeping the tsantsa is no longer something good," says Marcelly Lequi, Lequi's oldest aunt and a member of the Shuar delegation visiting the Guayaquil museum. By 1960, both Ecuador and Peru had outlawed the tsantsa ceremony.

Tsantsas occasionally still appear in auctions or online marketplaces, selling for anywhere from a few hundred dollars to about $31,000, and obvious fakes crop up in Ecuadorian markets. In October 2024, England's Swan auction house in Oxfordshire canceled the sale of human remains, including two tsantsas, after public outcry. Ordoñez says there are more than 100 tsantsas in the United States, and at least 295 in Europe, including about 120 in the United Kingdom, mostly in London. "They're lying in [storage] without [anyone] knowing much about their past or their future," Van Broekhoven adds. The Tsantsa Project hopes to explore both.

After CT scanning a shrunken head from the Guayaquil Municipal Museum, researchers could examine it in the computer for evidence of authentic Shuar ceremony, such as sewn-up eyes.

PHOTO: PLANIN 4D

AT THE MUSEUM here in Guayaquil, Ordoñez gently lifts another tsantsa to the light. This one fits Western ideas of an Amazonian shrunken head, with lush brown hair crowned with a headband with faded green feathers, and red and white feather earrings. But Ordoñez knows looks can be deceiving.

She thinks many tsantsas in museums and collections are likely fakes made for commerce. One goal of the Tsantsa Project is to identify the details of craftsmanship—the position of the cuts, the style of stitching—that signal authenticity. "The stitching [should be] characteristic of the [Shuar] nation. If it's not … it's not genuine," Tankamash says.

For years, Ordoñez had CT scanned ancient mummified human remains from the Andes, which in many cases lack a descendant community to speak for them. In 2017, she was asked to examine tsantsas in the Pumapungo Museum in Cuenca, Ecuador, near the Shuar homeland. She was drawn to the work in part because she could consult the Shuar on exactly how to handle their ancestors' ceremonial objects. She could "know exactly what [the Shuar] wanted to do and how they wanted it done, from the lips of the community."

With small grants provided by USFQ and sometimes from the researchers' own pockets, Ordoñez and her team have studied 26 tsantsas from three Ecuadorian museums, the Pitt Rivers Museum, and a private collection. The Guayaquil Municipal Museum, with its five tsantsas, is the project's newest partner.

No one knows exactly how the five tsantsas arrived at this museum. For years they were on display with little contextual information. Now, they are off exhibit until the Shuar and the museum's leadership agree on their fate. In November 2023, Shuar from Tsuer Entsa, with approval from FICSH, performed a tobacco ritual to obtain permission from their deities to study the tsantsas. Then, with Lequi and other Shuar present, Ordoñez and her team scanned the heads and took a 1-centimeter-square skin sample from the neck of each one for DNA analysis.

On the tsantsa with the feathers in its headband, the CT scan revealed a cut starting at the right temple and winding around the right side, rather than running down the back of the head in Shuar style. "This tsantsa is not original," Ordoñez says, noting that the headband was probably an attempt to cover up the unusual incision, which is not visible by simple examination.

Lequi agrees, adding that Ordoñez's CT scan also revealed that the tsantsa's eyes were not sewn shut from the inside, as the Shuar did. Museum officials were surprised to learn this tsantsa's origins were in doubt, and say they might use it in an exhibit as an example of a commercial shrunken head.

Lequi lifts another head into the bright overhead light. This one has graying blond hair in an uneven buzz cut and a mustache curling over lips whose threads have come undone. Lequi notes that Indigenous people in the Amazon typically have straight, dark hair. Yet Ordoñez's work has revealed that this blond shrunken head possesses the key traits of a ceremonial tsantsa: the correct incision at the back of the head and the sewn-up mouth and eyes.

The heads didn't yield enough DNA for whole genome sequencing. "Extracting DNA from a tsantsa is really a challenge because the (DNA) concentration is really low," says Verónica Baquero-Méndez, a master's student at USFQ who works on genetic analysis for the Tsantsa Project. "Boiling the skin for many hours … degraded the DNA."

She and her colleagues took extra precautions, including sterile tools and negative controls, to avoid contamination with mod-

ern DNA during analysis, she says. Then they analyzed whatever DNA they could, mostly mitochondrial DNA (mtDNA), an abundant form of DNA passed down from the mother.

The blond tsantsa had Indigenous Amazonian ancestry on the maternal side. Lequi says the head may date from the turn of the 20th century, when some Indigenous people mixed with European colonizers. The team also sequenced a nuclear gene that differs in men and women, the *amelogenin* gene, and so confirmed all five tsantsas in the Guayaquil museum were male. That fits historical reports saying tsantsas were made only from men. But similar analysis of a tsantsa with short, straight, gray hair, from the Pumapungo Museum, revealed it was female, says molecular biologist María de Lourdes Torres of USFQ, who is leading the genetics work.

Torres says some Shuar leaders were surprised to hear about a female tsantsa and about possible mixed heritage, and doubted the findings. But Lequi and others welcome it as proof that the ceremony was more complex than outside historians have described. The creation of a tsantsa "wasn't always because of a battle," Lequi says. He says sometimes, "The Shuars would offer [their bodies] as a tribute, as a sacrifice, to give thanks to the Earth for good harvests, or for the well-being of the community."

The DNA analysis has revealed other surprises. A tsantsa from the Pumapungo Museum had mtDNA variants typical of European populations, and two others had variants found in the Philippines, among Batak Negritos from Palawan. The researchers speculate that perhaps those people had maternal ancestors among enslaved Filipinos brought to South America by the Spanish.

Homelands of the tsantsas
The traditional territories of the Indigenous Shuar people, who once crafted shrunken heads, or tsantsas, overlap with the territories of their neighbors the Achuar in the Amazon rainforest. The homelands of the two nations, which are not precisely mapped, cross modern borders and extend into Peru. The Indigenous nations sometimes warred in the past, but now work together to protect the forest.

In part because international databases contain few samples from Amazonian Indigenous peoples, the tsantsa DNA can't link the heads to the Achuar, the Shuar, or other Indigenous nations or tribes. "To understand the origins of the tsantsas, we do need to have more data from the communities living now," Torres says. But many Amazonian Indigenous people are hesitant to provide DNA samples, she says, after decades of exploitation and some previous studies in which they weren't fully informed about how their genetic information would be used.

Neighboring Amazonian communities are probably too closely related for DNA to distinguish them, adds biologist Craig Byron of Mercer University. "These culture groups that are 20 miles away from each other [probably] came from the same [genetic group]," he says.

Despite the limitations, the team's work is sound science, Byron says. In 2019, he authenticated and eventually repatriated a ceremonial tsantsa in his university's collection to Ecuador. But he says Ordoñez's micro-CT scans allowed her to learn more about the stitching than his hospital-grade CT revealed.

After years of collaboration with the Shuar, Ordoñez has softened her approach to authenticating the tsantsas. The Shuar and Western scientific sources point to different features as crucial to authenticity, she says. "What defines it as authentic or inauthentic is the ritual it goes through, and I cannot speak of a ritual," she says.

If tsantsas are human, of Amazonian origin, have the mouth and the eyes sewn, and the incision located correctly, she considers the heads to have evidence of authenticity. But she leaves the final decisions to the closest Shuar community or the one most likely to be connected to the tsantsa. "What interests me now is what the community can get from [the tsantsas] and what they can do with this research."

AFTER A TSANTSA has been authenticated, what should happen to it? The original idea was to give it back, or at least get Indigenous input on any exhibition. But the question of who owns a tsantsa can be thorny: Is it the museum that acquired it, the community whose ancestors made it, or the community of the deceased person?

To the Shuar, the answer is clear: "They belong only to the Shuar nation because it's the only culture that practiced tsantsamaking," Tankamash says. He and Lequi say the Shuar federation is happy to make licensing arrangements with museums as long as FICSH remains owner, is consulted on exhibition, and gets financial benefit.

Ordoñez agrees. "For me, the people who claim it as theirs and who want to care for it are the Shuar, and so it belongs to them." The

GRAPHIC: M. HERSHER/*SCIENCE*

Shuar nation has yet to establish consensus on exactly where repatriated tsantsas would be stored or displayed and which communities would care for them, but Ordoñez hopes the Tsantsa Project can offer a platform for hashing out such details.

Although many tsantsas were probably made from the remains of Achuar people, Tankamash thinks involving the Achuar would only spark conflict. "We haven't touched this matter [with the Achuars]. It's very delicate."

Ordoñez has tried contacting the Achuar Nation of Ecuador (NAE) about the project, but was rebuffed. The Achuar did not make tsantsas themselves and are not interested in receiving those made by the Shuar, says Arutam Ichinki Tentets, a member of the Achuar nation in Ecuador; he is authorized by NAE President Wakiach Kuja to present the Achuar perspective on tsantsas. "According to all the Achuar I've talked to, I don't think there is an interest" in getting the tsantsas, Ichinki Tentets says. "We don't want to relive that [period of warfare], or claim anything. We don't want to think badly of [the Shuar]. They practiced that a long time ago."

Most of the fighting between Shuar and Achuar ceased after missionaries arrived, Ichinki Tentets says. Today the communities are often allies, defending their territories against environmental threats. "The goal is the same for all the nationalities of the Amazon: It's the protection of the forest, the flora, and the fauna. That is how we unite," he says.

"[The Shuar] could shrink their enemy's head within the framework of their customary right," which Western perspectives may not fully comprehend, adds Joaquin Moscoso of the Municipality of Guayaquil; he was director of the Guayaquil museum for most of the project's work there. If a tsantsa is genuine, he says, "its repatriation and territorialization should be in Shuar communities, where it acquires meaning."

Van Broekhoven, however, stresses that tsantsas are human remains as well as cultural objects, suggesting repatriation should include the wishes of a descendant community. She says the Achuar have a say, even if they have not claimed the tsantsas. "We can't just return and then potentially cause a lot of harm because the communities aren't in agreement," she says. The Pitt Rivers Museum has taken its tsantsas—and all other human remains—off display, and so far has not received a repatriation request.

Even if all parties agree tsantsas belong to the Shuar, few countries require international repatriation of human remains or cultural artifacts. "There are all these [bureaucratic] layers we have to cross," Ordoñez says.

A few museums are working on it. Tankamash has been negotiating with the Museum of Denver about returning tsantsas. In the 1990s, the Smithsonian Institution's National Museum of the American Indian returned tsantsas directly into the hands of what was then a Shuar-Achuar federation, and in 2017 the Vatican returned one tsantsa to a museum in Ecuador. And in 2021 Mercer University's tsantsa was repatriated to Ecuador's National Institute of Cultural Heritage.

The Pitt Rivers Museum in Oxford, England, has taken its once-famous shrunken heads, or tsantsas, off display.

PHOTO: GUY BELL/ALAMY

Even if they make it back to Ecuador, tsantsas seldom end up with the Shuar. All human remains from pre-Hispanic times and all ethnographic objects older than 100 years are considered by law to be national heritage, and are handled by the Ecuadoran government, Moscoso says. But he agrees tsantsas are unique. He says the government is working on its protocols, and that the Tsantsa Project and other efforts might one day spur repatriations directly to the Shuar nation.

For now, only the Ecuadorian government can legally return tsantsas to the Shuar. But the Guayaquil museum acknowledges that the heads belong culturally to the Shuar and is committed to working with them to create a co-curated exhibition. "It was very moving to have this community involvement, understanding that these goods belong to them. Eventually our exhibition must include their authorization," Moscoso says.

So far, the Shuar hold 11 tsantsas, guarded in a safe at the federation's headquarters in Sucúa. Tankamash's face lights up as he discusses the Shuar's big dream: to have their own museum based on their worldview, and to display tsantsas in context. Exhibitions about the Shuar culture tend to revolve solely around the shrunken heads. But Tankamash envisions a museum built like "a Shuar house, a *jéa*," an oval house of palm wood and a straw-covered roof, showcasing their culture.

The Shuar hope any new exhibit will help the world to see them as more than "headhunters." "There were stories, legends … written down, but someone else wrote it for us," Tankamash says. At the moment, he says, "we don't even speak our language well. We want to use this project to learn and train Shuar professionals so that we can … create a movie or a poem about our experience."

Back in Tsuer Entsa, Lequi fills in villagers about the tsantsas' DNA and CT results. For now, he says, the community is fine with leaving the five tsantsas in Guayaquil. Most Shuar have never seen an authentic ceremonial tsantsa, Lequi says. "Our community is practically disconnected from [our] history," he says. Ultimately, he hopes, a museum of their own will be "where the stories were explained, [where] the young people would go, learn, and remember." ■

Kata Karáth is a journalist in Quito, Ecuador.

INSIGHTS

PERSPECTIVES

ECOLOGY

Virtual reality rewrites rules of the swarm

Study of locusts in a virtual environment challenges models of collective behavior

By **Camille Buhl**[1] *and* **Stephen J. Simpson**[2,3]

Among the most spectacular phenomena in nature is the sight of millions of desert locust (*Schistocerca gregaria*) juveniles marching together, flowing like a river through the arid habitat of North Africa and consuming vegetation as they go before molting to become devastating swarms of winged adults. Understanding how and why locusts exhibit aligned collective motion is vital for predicting and managing outbreaks. However, present knowledge of the rules that govern the emergence of such complex, patterned behavior and decision-making is based on a handful of theoretical models that recapitulate only some aspects of the observed behavioral patterns. On page 995 of this issue, Sayin *et al.* (*1*) describe the integration of field, laboratory, and virtual reality studies to show that prevailing models for explaining collective motion in locusts, and perhaps other systems as well, require revision.

The desert locust is the most famous among a group of 20 or so species of grasshopper that become highly sociable in response to crowding (*2*). When reared alone, desert locusts tend to avoid one another and exhibit cryptic behavior, presumably to avoid attracting the attention of predators. Yet after only a few hours of crowding, they switch to being attracted to other locusts, forming jostling aggregations that then transition suddenly into marching bands. These groups behave as if they are of a single mind, yet there are no leader locusts or any hierarchy of control. Instead, collective behavior arises from interactions among individual locusts.

To investigate how such collective behavior arises, locust researchers turned to a self-propelled particle (SPP) model from statistical physics that had few underlying assumptions and elegantly predicted universal features of group behavior (*3*). This model, now two decades old, is based on moving particles that adjust their direction of movement to align with neighbors within a defined zone of interaction. The central prediction of the model is that as the density of particles (in this case locusts) in the group increases, a rapid transition occurs from disordered movement to highly aligned collective motion.

In previous tests to assess predictions of the SPP model, a laboratory-based marching arena was used to quantify the movement and interactions among different numbers of locusts (*4*). The results from these experiments supported predictions of the SPP model, as did field data from marching bands

PHOTO: DPA/PICTURE ALLIANCE/GETTY IMAGES

Cognitive rules, not explicit alignment or density changes, drive swarms of desert locusts.

of the Australian plague locust (*Chortoicetes terminifera*), which were derived by filming locust bands marching below a fixed camera (*5*, *6*).

Alternative models, however, have been proposed to explain locust collective behavior. These include mechanistic models involving insects responding to optic flow across the retina that is generated by moving neighbors (*7*, *8*). The escape-pursuit model (*9*) involves locusts chasing other locusts in front of them while avoiding contact with those beside and behind them, perhaps driven by a latent tendency to cannibalize one another (*10*, *11*). There were also two inconsistencies between the SPP model and observational data. Locusts in the field can march at low densities. This would require a term for inertia in the model, such that once locusts have started marching, they will tend to continue, even at lower densities than required to initiate marching in the first place. Another inconsistency was that the macroscopic features of band structure were not entirely as predicted by the model, requiring additional quantitative features of locust behavior to be added (e.g., attraction and repulsion forces, pausing, or hopping) (*5*).

Before the SPP model, or any other model, could be confirmed, a major technical challenge needed to be overcome. Studying locust groups in the laboratory or field cannot isolate the behavioral responses of individual locusts, which are intertwined in a constantly adjusting sensory interplay with the behavior of others. As a result, inferring individual behavioral responses has relied on complicated statistical analyses, the results of which need to be compared with the predictions of computational or mathematical models. Sayin *et al.* have solved this problem in a technical tour de force, using an immersive virtual environment for locusts. Locust nymphs were allowed to move freely on a high-speed motion-compensated sphere while immersed in a panoramic three-dimensional virtual projection of a scene programmed to include realistic simulations of other locusts. The authors found that the SPP model, and other models based on fixed interaction rules and zones of influence (*12*), did not accord with the behavior of locusts in the virtual reality system. Locusts did not follow fixed behavioral rules such as aligning with their moving neighbors within a zone of interaction or responding to wide-field optical flow. Instead, other locusts acted as targets toward which focal locusts were pulled. This is most consistent with a ring attractor model, in which a ring of recurrently connected neurons collectively encode movement direction, with the heading updated by dynamically changing external visual inputs and the internal dynamics of the circuit. For example, when a focal locust was placed in between two groups moving in a common direction, it didn't continue its movement in alignment with them, as predicted by all alignment-based models. Rather, it turned sharply and steered itself toward one group or the other. Additionally, a reanalysis of the data from the previous marching arena study (*4*) found no evidence of a density threshold for aligned collective movement.

A next step will be to see whether the new model of Sayin *et al.* can successfully predict the shape and trajectories of locust marching bands at larger spatial scales and in real-world visual environments. It will also be important to see what the model yields in terms of the distributions of neighbors within bands, which are known to reflect effective forces that act between individuals (*6*).

Sayin *et al.* conclude that it is time to move beyond the conception of locusts and other organisms as moving particles behaving according to fixed spatiotemporal rules and to consider organisms as probabilistic decision-makers responding dynamically to their sensory environment. Minimalist statistical physics models have been useful in bringing the field to a position where such a reframing is now possible, as a result of extraordinary advances in behavioral analysis, neuroscience, and virtual reality. As Sayin *et al.* have shown, in the search to understand the power of the collective, the threshold of entry to the cognitive realm of animals is within reach. ■

[1]School of Agriculture, Food, and Wine, The University of Adelaide, Adelaide, SA, Australia. [2]Charles Perkins Centre, The University of Sydney, Sydney, NSW, Australia. [3]School of Life and Environmental Sciences, The University of Sydney, Sydney, NSW, Australia. Email: stephen.simpson@sydney.edu.au; camille.buhl@adelaide.edu.au

REFERENCES AND NOTES

1. S. Sayin *et al.*, *Science* **387**, 995 (2025).
2. M. P. Pener, S. J. Simpson, *Adv. Insect Physiol.* **36**, 1 (2009).
3. T. Vicsek, A. Czirók, E. Ben-Jacob, I. Cohen, O. Shochet, *Phys. Rev. Lett.* **75**, 1226 (1995).
4. C. Buhl *et al.*, *Science* **312**, 1402 (2006).
5. C. Buhl, G. A. Sword, S. J. Simpson, *Interface Focus* **2**, 757 (2012).
6. J. Weinburd *et al.*, *Proc. R. Soc. London Ser. B* **291**, 20232121 (2024).
7. I. Bleichman, P. Yadav, A. Ayali, *Proc. Biol. Sci.* **290**, 20221862 (2023).
8. D. Castro, F. Ruffier, C. Eloy, *Phys. Rev. Res.* **6**, 023016 (2024).
9. P. Romanczuk, I. D. Couzin, L. Schimansky-Geier, *Phys. Rev. Lett.* **102**, 010602 (2009).
10. S. J. Simpson, G. A. Sword, P. D. Lorch, I. D. Couzin, *Proc. Natl. Acad. Sci. U.S.A.* **103**, 4152 (2006).
11. S. Bazazi *et al.*, *Curr. Biol.* **18**, 735 (2008).
12. I. D. Couzin, J. Krause, R. James, G. D. Ruxton, N. R. Franks, *J. Theor. Biol.* **218**, 1 (2002).

10.1126/science.adw0733

NANOMATERIALS

Tessellated with tiny dumbbells

Concave and convex surfaces direct nanocrystals to assemble into complex patterns

By **Brian A. Korgel**

Opal, a natural gemstone made of tiny silica particles dispersed in water, has a beautiful iridescence. The colloidal silica microspheres self-assemble over geological timescales into a close-packed, ordered crystal from which light diffracts to produce the gradual shift in colors (*1*). Synthetic techniques have not only reproduced opals in laboratories (*2*) but have yielded colloidal building blocks with chemical and structural complexity. Nanoparticles of metals, semiconductors, and magnets have been ordered into periodic patterns—so-called superlattice structures (*3*). Many seemingly exotic crystalline arrangements of spheres and polyhedra predicted computationally have been experimentally realized (*4*). However, these particles have lacked directionality. On page 978 of this issue, Wan *et al.* (*5*) report the self-assembly of dumbbell-shaped nanocrystals into dense lock-and-key structures, as well as low-density, chiral Kagome superlattices. This brings structural complexity to a level in which the surface curvatures of nanoparticles dictate the direction of assembly.

Superlattices have emergent physical and electronic properties that arise from their building blocks and their geometry. The Kagome structure—a non–close-packed six-membered star pattern—is particularly intriguing because of its chirality and frustrated packing geometry. This arrangement supports intimate interactions between neighboring nanoparticles with local close-packed order while preventing the overall system from ordering over long distances. Such assembly requires a specific organization of nanocrystals with a low density. It is not possible to arrange symmetric particles into such superlattices, including a Kagome

McKetta Department of Chemical Engineering, University of Texas, Austin, TX, USA. Email: korgel@che.utexas.edu

lattice, because they tend to pack densely into close-packed patterns throughout the entire structure.

Wan *et al*. synthesized dumbbell-shaped nanocrystals composed of multiple layers of different rare-earth elements (yttrium, ytterbium, erbium, gadolinium, and neodymium). These nanodumbbells were about 60 nm in length with a tunable head-to-waist ratio (d/D; d and D are diameters of the head and waist, respectively) that determined the nanocrystal's degree of curvature. The convex and concave surfaces of the nanodumbbells interacted with each other to assemble into various patterns. At a high degree of curvature (d/D of 0.4), the dumbbells were positioned side by side in parallel with the convex heads nestled into the concave waists of a neighbor (corner fitting). By contrast, at a low degree of curvature (d/D of 0.8), the cap of the head fitted into the waist perpendicularly (cap fitting), creating a herringbone pattern. The most interesting arrangement was observed when the head-to-waist ratio was 0.6. In this case, the nanodumbbells organized into a non–close-packed structure, which formed bi-chevron and Kagome lattices (see the figure).

It takes more than just uniformly dispersed nanocrystals to create a superlattice that extends over a large distance. Symmetric particles, such as spheres, do not have a preferred orientation during self-assembly. Thus, it only takes simple evaporation of solvent to reach a thermodynamically stable structure with a long-range order. By contrast, a mixture of different-sized nanocrystals or complex-shaped building blocks with preferred orientations can be kinetically stuck into disordered or metastable states (*6*, *7*). One way to overcome the trapped state is to chemically modify the colloidal solution of nanocrystals. Free ligands can be added to the solution to promote attraction between building blocks based on exclusion (depletion attraction). Thus, when two particles move closer together, small molecules are excluded from the region between them. This creates an osmotic pressure gradient and provides an extra driving force to attract the two particles. Such depletion interactions driven by additional ligands can promote self-assembly of specific superlattices from a dispersion of two different-sized nanoparticles (*8*), as well as by nanorods (*9*).

Wan *et al*. also observed that excess ligand (oleic acid) is essential to assemble nanodumbbells into superlattices with long-range order. Calculations showed that depletion attraction between two nanodumbbells depends on their orientations because of the coexistence of convex and concave surfaces. The most energetically favorable orientations arose when the convex caps nestled into the concave waists. The attractive interactions between nanodumbbells led to a strong preference in the bond angle between nanodumbbells, which dictated the assembly pattern.

Non–close-packed structures such as Kagome lattices tend to be unstable because of the free volume entropy (increase in a system's entropy from available empty spaces). Indeed, the Kagome structure of Wan *et al*. had a lower density than the disordered structures. Computational simulation confirmed that the Kagome superlattices are the least favored structure without an additional driving force, such as depletion attraction, between particles.

Although it is likely that oleic acid promoted depletion attraction between nanodumbbells, the role of free ligands, as well as other forces in the assembly process, should be further elucidated. A time-dependent molecular dynamics simulation that accounts for kinetics and interaction mechanisms other than depletion attraction, such as lateral capillary forces and van der Waals attractions, could provide some insight (*7*). Van der Waals forces between neighboring dumbbells could also promote the attraction between the convex and concave surfaces (*10*). Perhaps the primary role of excess ligands is to simply help circumvent kinetic trapping into disordered structures, while other mechanisms cause or contribute to the directional alignment of nanodumbbells in the Kagome superlattices. The question of whether the low-density Kagome structure is in a stable state also remains to be answered. These superlattices coexist with the high-density bi-chevron patterns. Thus, it is unclear which is the true equilibrium structure or if there is indeed coexistence between the sparse Kagome arrangement and dense bi-chevron pattern. The Kagome superlattice could be a frozen state in between disordered and bi-chevron phases.

The Kagome superlattices of Wan *et al*. are particularly interesting because of their chirality. Chiral structures offer the potential to generate a new class of nanomaterials in which light emission or magnetic fields are controlled precisely. The low density of the Kagome structure also offers additional functionality because small molecules can be included in the empty spaces, such as chiral centers of the superlattice. The ability to manipulate the surface curvature in the individual nanocrystal building blocks provides a powerful tool for controlling the self-assembly of superlattice structures. ■

Chiral superlattices made of nanodumbbells

Dumbbell-shaped nanocrystals have both convex and concave surfaces that can be adjusted for desired bond directionality. These particles assemble into complex patterns, such as chiral Kagome structures with emergent physical properties.

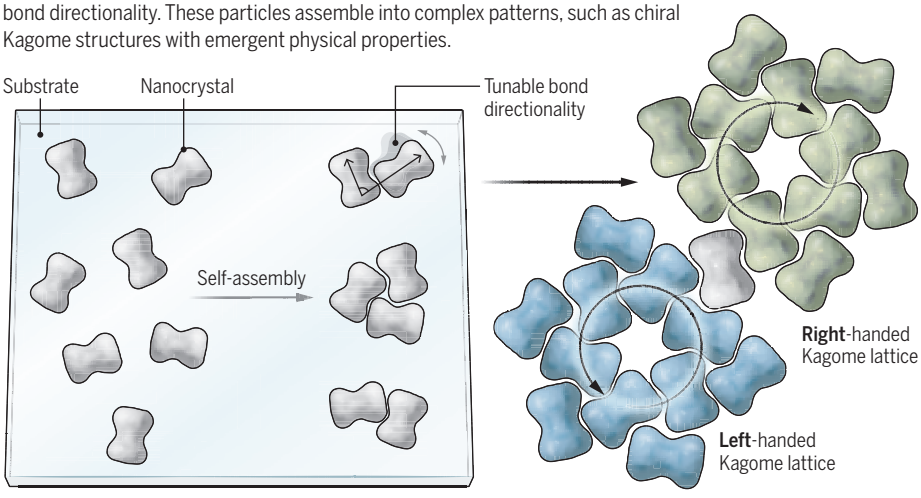

GRAPHIC: A. MASTIN/*SCIENCE*

REFERENCES AND NOTES

1. W. M. Gelbart, A. Ben-Shaul, *J. Phys. Chem.* **100**, 13169 (1996).
2. Y. Xia, B. Gates, Y. Yin, Y. Lu, *Adv. Mater.* **12**, 693 (2000).
3. M. A. Boles, M. Engel, D. V. Talapin, *Chem. Rev.* **116**, 11220 (2016).
4. J. Gong *et al*., *Nat. Commun.* **8**, 14038 (2017).
5. S. Wan *et al*., *Science* **387**, 978 (2025).
6. R. C. Doty, R. T. Bonnecaze, B. A. Korgel, *Phys. Rev. E Stat. Phys. Plasmas Fluids Relat. Interdiscip. Topics* **65**, 061503 (2002).
7. B. D. Rabideau, R. T. Bonnecaze, *Langmuir* **20**, 9408 (2004).
8. D. K. Smith, B. Goodfellow, D.-M. Smilgies, B. A. Korgel, *J. Am. Chem. Soc.* **131**, 3281 (2009).
9. D. Baranov *et al*., *Nano Lett.* **10**, 743 (2010).
10. S. Bhattacharjee, C.-H. Ko, M. Elimelech, *Langmuir* **14**, 3365 (1998).

ACKNOWLEDGMENTS

B.A.K. acknowledges support from the Robert A. Welch Foundation (F-1464).

10.1126/science.adw0351

PLANT SCIENCE

Outsmarted by fungi

A fungal pathogen fabricates phosphate starvation in plant cells to promote virulence

By **Caroline Gutjahr**

Global food security is under constant threat by fungal, bacterial, and viral plant pathogens. Although plants have evolved innate immune responses against pathogens, 10 to 23% of global crop yield is lost every year to fungal pathogens alone (*1*). Plant-interacting microorganisms, including pathogenic fungi, translocate effector proteins into plant cells. These effectors enhance pathogen virulence by directly interfering with the plant immune system or by manipulating other cellular functions. On page 955 of this issue, McCombe *et al.* (*2*) report that the pathogen *Magnaporthe oryzae* (which causes devastating rice blast) and two additional plant disease–causing fungi enhance their pathogenicity by manipulating the plant's monitoring of phosphate, a phosphorus-containing compound essential for plant growth. The mechanism tricks plants into entering a phosphate starvation response, which alters metabolism but also disrupts immune signaling and responses to infection. These findings represent a mechanism by which fungal pathogens can manipulate plant defense indirectly.

The success of pathogens is often improved when plants are starved of one or more nutrients, and it seems that the nutritional state of plants has a strong influence on their defense status (*3*). Phosphate starvation responses in plants are regulated by phosphate starvation response transcription factors (PHRs), which bind to regulatory regions of phosphate starvation response genes to promote their transcription. These genes encode proteins that are involved in mitigating phosphate starvation stress—for example, lipid modification proteins, which reduce the use of phosphate in lipids, and phosphate transporters and phosphatases, which increase phosphate uptake by the cell. When sufficient phosphate is available, plant cells accumulate inositol pyrophosphates (PP-InsPs) that bind to proteins containing the SPX domain. When bound to PP-InsPs, SPX proteins interact directly with PHRs to inhibit their action, thereby preventing phosphate starvation responses (*4*). Thus, the amount of PP-InsPs in the cell is an indicator of the plant's phosphate status and is directly translated into transcriptional outputs.

Plant phosphate status has emerged as an important regulator of plant-microbe interactions (*5*). Low phosphate concentrations are required to promote root colonization with the soil fungi that form a beneficial symbiotic relationship with ~80% of land plant species. This symbiosis, called arbuscular mycorrhiza, facilitates the delivery of mineral nutrients, especially phosphate, to the host plants. PHRs bind directly to the promoters of plant genes that are required to host these fungi inside root cells (*6*, *7*). Plant phosphate signaling also modulates the composition of bacterial communities colonizing the root and rhizosphere (soil surrounding the root). For example, inactivity or mutation of PHRs promotes the expression of bacterial flagellin-induced defense genes by the plant, which leads to the suppression of some bacterial taxa and thereby a shift in the composition of the community (*8*).

The study by McCombe *et al.* focuses on the pathogenic fungus *M. oryzae*. This fungus induces blast disease in major cereals, such as rice (*Oryza sativa*), barley (*Hordeum vulgare*), and wheat (*Triticum aestivum*). *M. oryzae* is considered the most destructive rice pathogen globally. It causes lesions in leaves, which reduces photosynthesis, and rotting and breaking of stems below the ear, which leads to severely reduced yield (*9*). The authors studied a specific effector that is released by *M. oryzae*. The effector was chosen because its amino sequence resembled that of a nucleoside-diphosphate linked to moiety X (Nudix) hydrolase. Nudix hydrolases are enzymes that are found across all domains of life. They hydrolyze a wide spectrum of organic pyrophosphates, including PP-InsPs.

McCombe *et al.* used RNA interference to inhibit the expression of the Nudix hydrolase effector gene (*MoNUDIX*) in *M. oryzae*.

Faking a lack of phosphate

In conditions of phosphate sufficiency, inositol pyrophosphates (PP-InsPs) are abundant in the plant cell. They bind SPX domain–containing proteins, enabling them to bind and inhibit phosphate starvation response transcription factors (PHRs). Therefore, PHR target genes are not expressed. Upon *Magnaporthe oryzae* infection, the biotrophic interfacial complex (BIC) of the fungus secretes nucleoside-diphosphate linked to moiety X (Nudix) hydrolase effectors into the plant cell. These effectors hydrolyze PP-InsPs. Without sufficient PP-InsPs, SPX proteins release PHRs from inhibition, enabling them to bind to target promoters and activate gene expression. Free SPX proteins are ubiquitinated (Ub) and degraded by the proteasome.

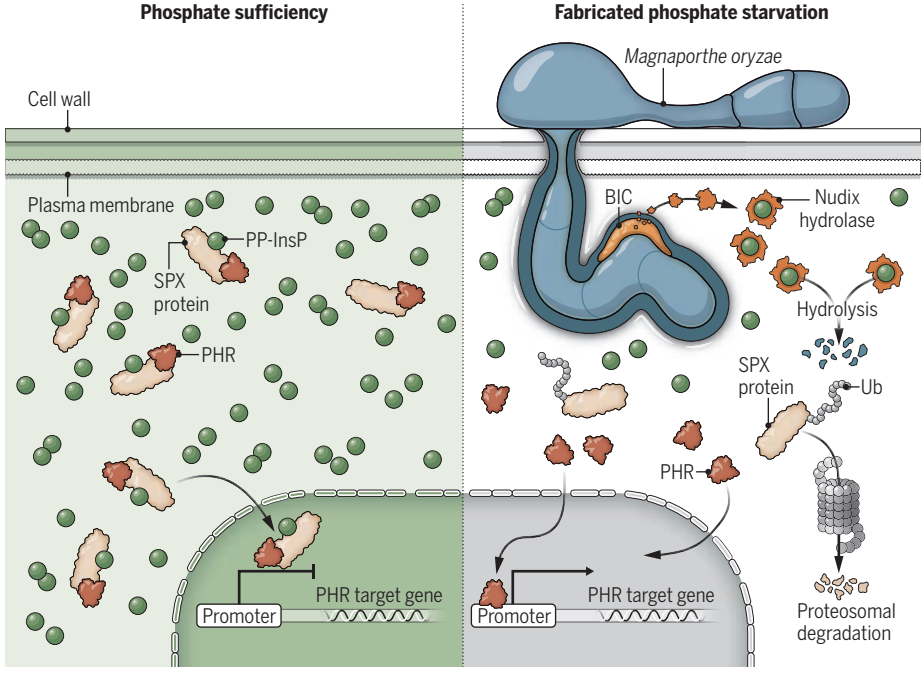

GRAPHIC: A. FISHER/*SCIENCE*

Max Planck Institute of Molecular Plant Physiology, Potsdam, Germany. Email: gutjahr@mpimp-golm.mpg.de

They also generated mutant lines of the fungus with CRISPR-Cas9–mediated deletion of *MoNUDIX*. Both interventions resulted in reduced virulence of *M. oryzae* in rice and barley. The authors also deleted the conserved Nudix hydrolase effector genes in the fungi *Colletotrichum higginsianum* and *Colletotrichum graminicola*, which cause anthracnose disease of *Arabidopsis thaliana* and maize (*Zea mays*), respectively. They found that the role of Nudix hydrolase effectors in promoting virulence was conserved across all three fungi.

McCombe *et al.* used crystallography to solve the structure of MoNUDIX. It was highly similar to that of human diphosphoinositol polyphosphate phosphohydrolase 1, a well-characterized Nudix hydrolase that hydrolyzes PP-InsPs. The authors showed that MoNUDIX and *C. higginsianum* NUDIX hydrolyze a specific PP-InsP in vitro. To understand whether MoNUDIX is translocated from the fungus into the plant cell, the authors transgenically expressed a version of MoNUDIX tagged with a red fluorescent protein in *M. oryzae*. They found that MoNUDIX is translocated from *M. oryzae* into barley and rice cells and that it localizes to the host cell cytoplasm as well as the biotrophic interfacial complex (BIC)—a site in the infecting hypha (branching filament that penetrates the host) that secretes effectors (*9*).

When McCombe *et al.* expressed MoNUDIX, PHRs, and SPX proteins in the leaves of the heterologous model system *Nicotiana benthamiana*, MoNUDIX disrupted the interaction between PHRs and SPX proteins and thus promoted the transcription of phosphate starvation genes. This did not occur when the authors used a mutant version of MoNUDIX that cannot bind PP-InsPs and is thereby unable to hydrolyze them, leaving them available for binding to SPX. Similarly, RNA sequencing of rice leaves infected with either wild-type *M. oryzae* or *M. oryzae* with a *MoNUDIX* deletion revealed that the group of genes with higher expression in the wild-type infected plants was enriched for phosphate starvation response genes. This indicates that *M. oryzae* promotes phosphate starvation responses in its natural host, rice, through the action of the Nudix hydrolase effector (see the figure).

Effectors with Nudix hydrolase domains have been described before in the flax rust fungus *Melampsora lini*, the oomycete *Phytophthora sojae*, and the bacterium *Ralstonia solanacearum* (*10*–*12*). However, other biochemical functions were ascribed to them. McCombe *et al.* now provide evidence that Nudix hydrolase effectors from pathogenic fungi can interfere with phosphate sensing by selectively hydrolyzing PP-InsPs.

How a manufactured state of cellular phosphate starvation promotes the success of *M. oryzae* remains an open question. On the basis of previous evidence from studies in *A. thaliana* (*8*), it is possible that the release of PHRs from inhibition by SPX proteins not only promotes phosphate starvation responses but also suppresses the expression of genes associated with defense against pathogens, for example, those encoding proteins that induce the death of infected cells to prevent pathogen spread. This hypothesis is supported by the observation of McCombe *et al.* that, compared with wild-type *M. oryzae*, infection of rice with *M. oryzae* lacking *MoNUDIX* results in a greater amount of reactive oxygen species in leaves, which is indicative of a stronger pathogen defense response. Alternatively, the reduction of PP-InsPs and resulting phosphate starvation response might lead to an increase in phosphate uptake and accumulation in plant cells. This extra phosphate could feed the fungus or modify plant cell metabolism in a way that favors the fungus.

Regardless of the underlying mechanisms, the study by McCombe *et al.* emphasizes the major role of plant phosphate signaling in regulating plant disease and highlights a route by which pathogens can exploit the cross-talk between nutrient signaling and immunity. More research into the connection between plant nutrient signaling and plant immunity might provide strategies to integrate fertilization with the management of plant disease in agriculture. ■

REFERENCES AND NOTES

1. M. C. Fisher *et al.*, *Nature* **484**, 186 (2012).
2. C. L. McCombe *et al.*, *Science* **387**, 955 (2025).
3. A. Dutta, P. M. Dracatos, G. A. Khan, *Plant J.* **120**, 1724 (2024).
4. S.-Y. Yang, W.-Y. Lin, Y.-M. Hsiao, T.-J. Chiou, *Plant Cell* **36**, 1504 (2024).
5. M. Paries, C. Gutjahr, *New Phytol.* **239**, 29 (2023).
6. D. Das *et al.*, *Nat. Commun.* **13**, 477 (2022).
7. J. Shi *et al.*, *New Phytol.* **236**, 2282 (2022).
8. G. Castrillo *et al.*, *Nature* **543**, 513 (2017).
9. E. Oliveira-Garcia, X. Yan, M. Oses-Ruiz, S. de Paula, N. J. Talbot, *New Phytol.* **241**, 1007 (2024).
10. C. L. McCombe *et al.*, *New Phytol.* **239**, 222 (2023).
11. S. Dong *et al.*, *PLOS Pathog.* **7**, e1002353 (2011).
12. Y. Sun *et al.*, *Mol. Plant Pathol.* **20**, 533 (2019).

ACKNOWLEDGMENTS

C.G. acknowledges support from the Trans Regio Collaborative Research Center 356 "Genetic Diversity Shaping Biotic Interactions of Plants" (491090170) of the German Research Council (DFG), the European Research Council (ERC) under the European Union's Horizon Europe research and innovation program (grant agreement no. 101089250, ERC-2022-CoG), and a core grant from the Max Planck Society.

10.1126/science.adw1568

HYDROGELS

Hot and cold hydrogel with still water

Carbon chains immobilize water molecules, making a hydrogel elastic across temperatures

By **Zhaohan Yu** *and* **Shaoting Lin**

The soft polymer network of a hydrogel is infiltrated with water molecules, a hydrated state that makes hydrogels useful in biomedical research and in a range of consumer products, such as contact lenses and wound dressing. In contrast to polymers that transform between different states when heated or cooled, a hydrogel generally does not undergo polymeric phase transition because of its hydration. However, a change in temperature can evaporate or freeze mobile water molecules within the polymer networks, which modifies the hydrogel's mechanical properties (*1*). This compromises elasticity of a hydrogel and makes it easily breakable. On page 967 of this issue, Zhang *et al.* (*2*) report a way to control water molecules in polymer networks and produce a temperature-tolerant hydrogel that maintains its elasticity across a wide range of temperatures from −115° to 143°C. This unlocks potential applications that were deemed impossible because of the operation conditions.

The primary challenge in making a hydrogel with temperature-tolerant elasticity lies in effectively immobilizing water molecules within polymer networks. One strategy to address this problem is to engineer functional groups on polymer networks (*3*). A group of atoms with distinct chemical properties can bind to water molecules that are in close vicinity while other water molecules flow freely within the network (*4*). An alternate method is incorporating hygroscopic salts—compounds that absorb moisture from the surrounding environment—into a hydrogel (*5*, *6*). This approach reduces the overall mobility of water molecules by promoting their interaction with ions present in the salts. However, hygroscopic salts cannot completely lock water

Department of Mechanical Engineering, Michigan State University, East Lansing, MI, USA. Email: linshaot@msu.edu

on the networks because they also move around within a hydrogel.

Zhang *et al.* used the sulfuric carbonization reaction to make a hydrogel temperature tolerant. In this reaction, sulfuric acid extracts water to produce a carbon-rich residue on a material. This method successfully immobilizes water molecules in polymer networks by forming sulfuric acid hydrates. However, the reaction breaks down polymers, which leads to fragmentation of polymers and thus degrades a hydrogel. To solve this problem, Zhang *et al.* created a hydrogel with two interpenetrating meshes of polymer chains in which one of them is a sacrificial network that primarily reacts with sulfuric acid to produce a carbon layer on the other polymers for protection and water immobilization (see the figure). The design of double-network hydrogels is known for enhanced toughness (*7*, *8*) but has not been implemented for temperature tolerance.

Two polymers with distinct properties are needed to achieve selective carbonization reaction. Alginate (a natural polysaccharide) forms a network through ionic interactions. By contrast, polyacrylamide (a synthetic polymer) is linked by covalent bonds. In the sulfuric carbonization reaction of Zhang *et al.*, sulfuric acid primarily reacted with the alginate network to produce short chains of carbon (carbon snakes) while preserving the structural integrity of cross-linked polyacrylamides. The carbonization reaction was confirmed by an observed exothermic peak at a temperature of around 143°C. The carbon snakes adhered to and encapsulated the main chains of the polyacrylamide networks and acted as a shield to protect the polymers from excessive reaction and degradation. The resulting hydrogel comprised a single network of polyacrylamide coated with sulfuric acid–bound carbons that immobilized adjacent water molecules. No phase transition was observed in either fragmented alginate chains or polyacrylamide networks across a wide range of temperatures. This confirmed the ability of carbon snakes to effectively lock water molecules within the hydrogel. Additionally, Zhang *et al.* did not observe an exothermic reaction associated with evaporation of water molecules, which is often present in conventional hydrogels at high temperatures (*9*). Consequently, the temperature-tolerant hydrogel maintained its elasticity between –100° and 140°C.

The selective carbonization strategy requires a sacrificial network, so it is intuitive to think that the method cannot be applied to a single-network hydrogel. To demonstrate the generality of the approach, Zhang *et al.* performed the reaction on a hydrogel made of one type of polymer. The synthetic polymer, poly(*N*-vinylpyrrolidone), forms

Temperature-tolerant hydrogel

A hydrogel that consists of two distinct networks of polymers can effectively immobilize water molecules without deteriorating its structural integrity. Locked moisture maintains the hydrogel's elasticity in a broad range of temperatures.

Alginate Polyacrylamide

Double-network hydrogel

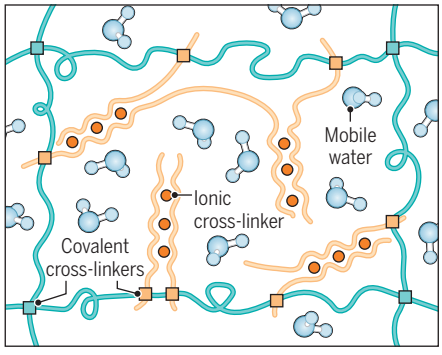

Alginates form a mesh through ionic interactions, whereas polyacrylamide chains are linked by covalent bonds. The two polymer networks are cross-linked covalently.

Water immobilization

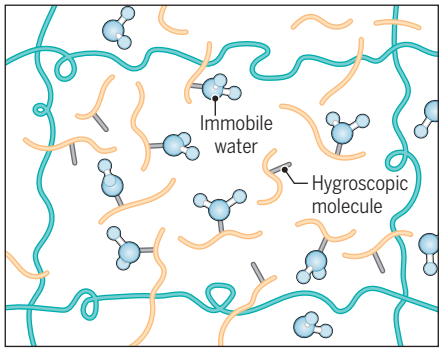

Alginates selectively react with hygroscopic molecules that immobilize water within the hydrogel. This causes fragmentation of the polymer network.

Selective carbonization

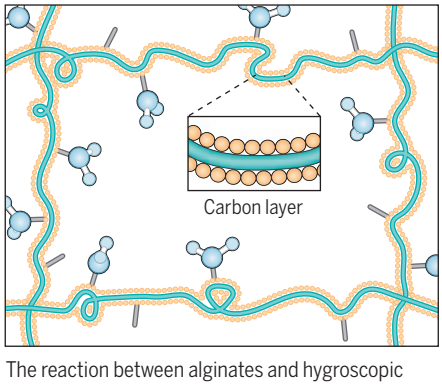

The reaction between alginates and hygroscopic molecules creates a protective carbon layer on the polyacrylamide network.

reactive side chains under acidic condition. Sulfuric acid primarily reacted with these short auxiliary chains to form carbon snakes that encapsulated the long chains that comprise the main network. The resulting hydrogel exhibited similar temperature-independent mechanical behavior between –112° and 135 °C.

Although the study of Zhang *et al.* confirms the broad applicability of the water immobilization strategy, additional analysis is needed to further elucidate the underlying mechanisms of temperature tolerance in hydrogels. For example, the differential scanning calorimetry used by Zhang *et al.* measures thermal transitions on the basis of the amount of heat absorbed or released by a sample, which shows absence of phase transitions within the hydrogels at extreme temperatures. Zhang *et al.* presented a plausible hypothesis of the immobilized water molecules suppressing phase transitions of polymers and water within the hydrogel. However, how water molecules that are far away from the polymer chains behave remain to be solved. Additional characterizations such as superresolution Raman microscopy (*10*) could potentially provide details of the underlying pictures.

The findings by Zhang *et al.* could have far-reaching implications. Research in developing high-performance hydrogels primarily focuses on exploiting the design of constituent polymer networks (*11*). Little attention has been given to water molecules within a hydrogel because they are generally considered to have negligible influence on mechanical properties. The strategy by Zhang *et al.* opens a new path for designing high-performance hydrogels by strategically engineering water molecules to immobilize them within the polymer networks. The ability to precisely manipulate water molecules in hydrogels could bring previously inaccessible advanced technologies, including but not limited to tissue preservatives and fire retardants. ■

REFERENCES AND NOTES

1. L. X. Hou *et al.*, *Adv. Mater.* **35**, 2300244 (2023).
2. X. Zhang *et al.*, *Science* **387**, 967 (2025).
3. D. Zhang *et al.*, *Adv. Mater.* **33**, 2104006 (2021).
4. Y. Jian *et al.*, *Mater. Horiz.* **8**, 351 (2021).
5. X. F. Zhang *et al.*, *Angew. Chem. Int. Ed.* **58**, 7366 (2019).
6. Y. Yan *et al.*, *Adv. Mater.* **35**, 2211673 (2023).
7. J. P. Gong, Y. Katsuyama, T. Kurokawa, Y. Osada, *Adv. Mater.* **15**, 1155 (2003).
8. J.-Y. Sun *et al.*, *Nature* **489**, 133 (2012).
9. Y. Tu *et al.*, *Proc. Natl. Acad. Sci. U.S.A.* **120**, e2312751120 (2023).
10. L. Shi, F. Hu, W. Min, *Nat. Commun.* **10**, 4764 (2019).
11. X. Zhao *et al.*, *Chem. Rev.* **121**, 4309 (2021).

ACKNOWLEDGMENTS

The authors acknowledge support from the US National Science Foundation (CMMI-2338747).

10.1126/science.adv8200

GRAPHIC: K. HOLOSKI/*SCIENCE*

POLICY FORUM

AGRICULTURE

Assessing market failures driving pesticide resistance

Some US farms' use of transgenic Bt corn raises questions

By **Zachary Brown**[1,2] *and* **Dominic Reisig**[2,3]

Greater use of a pesticide usually has two dynamic and countervailing effects on pest populations: (i) To the extent that susceptibility remains in the population, it reduces that population's growth (population suppression) or crop damage, and (ii) it selects for resistant genotypes, which can increase future crop damage (resistance selection). Because these effects occur simultaneously, it is challenging to disentangle them in field settings. Economists studying pesticide resistance have theorized that two potential market failures inherent to the problem can work in opposing directions; it is an empirical matter whether farms are over- or underusing a pesticide in any given context, compared to what would be optimal for their collective profits. On page 943 of this issue, Ye *et al*. (*1*) describe the use of transgenic *Bacillus thuringus* (Bt) corn to provide an important example of how to empirically assess the balance of these market failures in an applied, policy-relevant setting.

Pesticide resistance is a critical and growing challenge for agricultural sustainability, with social and economic drivers creating complex feedbacks with the problem's biological dynamics (*2*). Across crops and pests, resistance to available pesticide modes of actions (MOAs) is evolving faster than new MOAs are being discovered and deployed. Recent research has also identified broader public health risks than previously believed from escalating pesticide use (*3*).

One gap in the research literature on resistance, which Ye *et al*. seek to address, has been large-scale empirical economic assessments of Bt resistance. Transgenic Bt corn and cotton varieties, first commercially planted in the US in 1996, are engineered to express toxins naturally produced by Bt, which kill numerous economically damaging agricultural pests with high specificity. As part of commercial approval, the US Environmental Protection Agency (EPA) developed a regulatory framework in the 1990s to delay the evolution of pest resistance to Bt toxins, using its pesticide permitting authority under the Federal Insecticide, Fungicide, and Rodenticide Act (FIFRA). The EPA's action has proven farsighted: Bt varieties now dominate over 85% of US corn and cotton acreage (*4*), which has led to area-wide suppression of pests (*5*) and concomitant decreases in the use of riskier foliar (applied to leaves) and soil-applied insecticides on these crops (*6*). This has been counterbalanced by increases in the selection pressure on pests to evolve resistance to Bt toxins (*2*, *7*, *8*).

The crux of the EPA's Bt crop regulations takes the form of "refuge mandates," requirements for farmers to set aside a certain portion of their planted corn acreage for non-Bt hybrids, with the intention for this non-Bt acreage to serve as a refuge for Bt-susceptible pests—and their genes. The mandated non-Bt refuge varies by Bt toxin and region, ranging from 50% to as low as 5% of a farm's total corn acreage. The mandated spatial structure of refuge also varies by crop and region. In the Corn Belt, mixtures of Bt and non-Bt corn seed ("refuge in a bag") prior to planting satisfy these mandates. In most of the Cotton Belt, by contrast, the EPA requires spatially separate non-Bt corn refuge. These differences reflect differences in target pest species and their biology and have been developed in consultation with scientific advisory panels, industry, farmer interest groups, academia, and other stakeholders.

The EPA's Bt refuge regulations arguably remain the most comprehensive example globally of a governance system for managing and delaying pesticide resistance (*7*). Nevertheless, there are numerous resistance cases for several lepidopteran pests and *Diabrotica virgifera virgifera* [western corn rootworm (WCR)] (*8*). Key continuing challenges for the EPA's Bt policies include defining, monitoring, and identifying the evolution of resistance in complex agroecological systems with background fluctuations in overall pest pressure, especially for pests without high susceptibility to Bt, which are not completely controlled by Bt crops and are prone to quickly evolving resistance. WCR is a notable example.

The EPA acknowledges that extending the efficacy of Bt toxins is a public good. When current Bt toxins fail, there may be no new, improved Bt toxins ready for deployment. In these cases, farmers will likely return to using insecticides that pose more substantial risks to human health and the environment. Indeed, increased foliar spraying for *Helicoverpa zea* (corn earworm) has already been observed in the US Southeast owing to increased Bt resistance (*9*).

Despite the EPA's robust scientific advisory process for informing and adapting its regulations to changing circumstances and new research, it does not conduct or elicit equally comprehensive benefit-cost analysis (BCA) of its Bt regulations. This is striking for at least two reasons: First, the FIFRA from which the EPA derives its Bt regulatory authority states that the EPA's permitting decision for a pesticide must be based on whether it poses "unreasonable adverse effects on the environment" (*10*). The Act defines these to include "any unreasonable risk to man or the environment, taking into account the economic, social, and environmental costs and benefits of the use of any pesticide" (*10*). This statutory language obligates the EPA to include economic assessments of its pesticide-permitting decisions. Second, the size and scope of the EPA's Bt refuge mandates have been an ongoing point of contention between the EPA, farmers, industry, and concerned public advocacy groups, with some arguing that these mandates place undue burden on farmers and unnecessarily limit agricultural productivity, while others argue that overuse of Bt crops lessens the sustainability of our agricultural systems. Empirically grounded BCA could serve as a valuable foundation on which to build more constructive dialogue between conflicting stakeholders.

IDENTIFYING IMPACTS OF RESISTANCE

Ye *et al*. take an important step in improving empirical economic assessments of Bt resistance and pesticide resistance more generally. Their pest of interest is the WCR, which remains the most damaging and enigmatic insect pest in US corn fields. By assembling data from a large set of university field trials with hybrids containing Bt-targeting WCR (Bt-CR) traits and farmer survey data spanning the US Corn Belt, the authors apply a practical method for identifying and measuring the productivity impacts of rootworm

[1]Department of Agricultural and Resource Economics, North Carolina State University (NCSU), Raleigh, NC, USA. [2]Genetic Engineering and Society Center, NCSU, Raleigh, NC, USA. [3]Department of Entomology and Plant Pathology, NCSU, Plymouth, NC, USA. Email: zack_brown@ncsu.edu

resistance to Bt corn, controlling for simultaneous fluctuations in overall rootworm pressure (e.g., arising from weather conditions and other environmental factors).

Substantial Bt population-suppression effects have been documented in several economically relevant pests [e.g., (*5*)]. There are strong reasons to suspect that this effect also applies to WCR, and one innovation of Ye *et al.* lies in separately identifying the population-suppression and resistance-selection impacts of Bt-CR planting history. They do this using the corn field trial data, statistically testing the extent to which Bt history predicts recorded damage from WCR in both Bt and non-Bt (i.e., "refuge") plots.

Ye *et al.* find evidence that both effects are present and significant in WCR. WCR damage on non-Bt plots was lower if Bt had been planted on the same plot in the preceding year—clear evidence of a population-suppression effect. And WCR injury in Bt plots was higher if there was a history of Bt use on those plots—clear evidence of selection for resistance. The researchers find that only the preceding year's Bt planting history is significantly predictive of these effects, not the cumulative amount of Bt planted over several years. This appears at odds with biological theory and models of resistance evolution (and some previous empirical research), in which sustained selection pressure generates increasing resistance. The researchers caveat this finding by describing multiple environmental and economic dynamics that may impede measurement of the full, cumulative effects of resistance on observed corn root damage. This reveals one limitation of the study: its lack of pest sampling and bioassay data that could provide clearer signals of resistance, particularly in early stages when mitigation is likely to be most cost-effective (*11*).

Using estimated root-injury effects from suppression and selection, the researchers extrapolate impacts on corn yields using relationships established in previous research. In extrapolating these yield effects, the authors account for observed heterogeneity in background pest pressure between Eastern and Western Corn Belt states as measured by WCR damage on non-Bt corn plots with no prior Bt history. Field trials in Eastern states showed substantially lower WCR pressure, implying lower gains to farmers from Bt-CR traits.

BALANCING FARMER INCENTIVES

Farmers' Bt-CR planting decisions have effects on WCR pressure and resistance levels faced by neighboring farms. Without policies or institutions to account for these effects, individual farmers do not have any incentive to, either, even though doing so could improve farmers' collective profits. Economists refer to such mismatched economic incentives as "market failures." Yet it is not clear whether market failures in this case lead farmers to plant too much or too little Bt. If the potential for resistance selection is low, then Bt-CR planting would have a clearly positive effect on other farms in the area or region, by reducing overall pest pressure, similar to the area-wide effects of Bt crops seen with other pests (*5*). Alone, this effect would be expected to lead farmers to individually exert less control effort than would be collectively optimal for their profits, because they would ignore these benefits to other farms in their planting decisions. However, if Bt-CR traits posed a high potential for resistance but provided little population suppression, then individual farmers' use of these traits would have negative effects on other farms, by contributing to reduced Bt-CR efficacy. In reality, Ye *et al.* show that both population suppression and resistance selection from Bt-CR traits are present. So, it is an empirical question whether individual farmer incentives encourage over- or underplanting these traits.

Western rootworm beetles climb on a corn leaf in Illinois, July 2005.

PHOTO: GREG D. HESS/BLOOMBERG/GETTY IMAGES

Assessing the balance of these market failures, which are mediated by pest dispersal among farms (*12*), is challenging because it requires not only describing the observed economic outcomes, but also reckoning how farmers would behave under dynamically changing pest conditions and resistance levels, as well as in evaluating what would be collectively profit maximizing. This is necessarily an assumption-laden modeling exercise that goes beyond what even the most comprehensive datasets could reveal, but it is essential for normative economic assessments of resistance management outcomes and policies. Ye *et al.* use appropriate economic modeling techniques and make an admirable effort to examine the sensitivity of their results on the basis of different modeling assumptions, in particular the dispersal rates of WCR over different geographic scales, the science on which continues to improve (as Ye *et al.* discuss). Additionally, they consider the economic discount rate, which determines the present value of future profits, a factor with a long history of debate among economists and well-known to determine the conclusions of BCA.

Examining farm survey data, Ye *et al.* find that farmers in the Western Corn Belt planted 59% of their corn acreage with Bt-CR traits in 2014–2016—levels roughly in line with their own self-interest as well as the collective optimum. But this alignment did not arise because market failures were absent. Rather, the researchers' statistical analysis combined with their bioeconomic model imply that, in this region, the positive area-wide effects of WCR suppression from Bt-CR traits roughly balanced the negative effects of resistance.

By contrast, in the Eastern Corn Belt, Ye *et al.* estimate much lower collectively and privately profit-maximizing Bt-CR planting rates of between 12 and 20%, depending on WCR dispersion assumptions, even though farms in this region used Bt-CR traits at levels (averaging 50% of their total corn acreage) similar to those used in the Western Corn Belt over the same period. Ye *et al.*'s finding of lower optimal levels of Bt-CR in this region stem primarily from lower estimated WCR pressure based on the field trial. Lower pressure implies lower potential damage reductions and thus a lower potential value from Bt-CR traits in these areas. According to Ye *et al.*, by planting Bt-CR at rates over double what would have been privately profit maximizing (let alone collectively optimal), Eastern Corn Belt farms missed out on over $99 million per year for the period 2014–2016.

Ye *et al.* offer two possible explanations

for why Eastern Corn Belt farmers appear to be massively overplanting—and overpaying—for Bt-CR traits, each with different implications for policy. First, previous work cited by Ye *et al.* documents a more limited availability of non-Bt corn hybrids for sale than Bt hybrids. Thus, farmers may not be able to obtain a non-Bt hybrid suited to their needs. Other research also cited by Ye *et al.* shows that, particularly given the oligopolistic structure of the US corn seed industries, producers have an incentive to bundle their highest-value germplasm with transgenic traits (for which they charge an additional fee) and to limit the variety of hybrids without such traits. (Notably, Ye *et al.* do not include the diversity of hybrids in Bt-versus-non-Bt varieties within their bioeconomic model.) US corn and soy seed companies continue to face scrutiny and antitrust litigation for potentially unfair business practices stemming from their market power (e.g., the current FTC v Syngenta case). Ye *et al.*'s findings, together with previous research, suggest that such practices could include limiting the variety of non-Bt hybrids for sale, which can accelerate Bt resistance and ultimately cause additional harm to farmers.

Ye *et al.* also suggest that Bt-CR overplanting in the Eastern Corn Belt may result from farmers overestimating Bt-CR pest pressure. One should be skeptical of this argument: Typical corn farms in this region are competitive commercial enterprises with tens of thousands of dollars in operational cash receipts and expenditures. They have strong incentives to save on unnecessary production costs. Still, perfect competition and completely rational profit maximization are useful fictions in economic research. Ye *et al.* point to previous research revealing behavioral anomalies in US farms' chemical input decisions that apparently deviate from profit-maximizing behavior. A related potential explanation, not discussed by Ye *et al.*, lies in farmer risk aversion: Farmers may be willing to tolerate decreased expected profits from buying Bt-CR traits, to decrease their exposure to the risk of WCR infestation. Previous research has found farmer risk preferences influence pesticide demand in this way (*13*). Information- and risk-based explanations for Ye *et al.*'s findings implicate a clear, enhanced role for public agricultural extension to further its effective dissemination to farmers of findings from university field trials and entomological monitoring on the actual, localized risks of WCR (and other Bt-targeted pests).

IMPLICATIONS, LESSONS, GAPS

Ye *et al.* do not directly address the EPA's Bt refuge mandates, though their research has implications for these regulations. First, it suggests that existing Bt refuge mandates are insufficient for achieving collectively optimal levels of Bt planting, at least in the Eastern Corn Belt. Although planted refuge almost universally meets the EPA requirements in the Corn Belt using seed mixtures, the mandated non-Bt refuge level there is only 5% of a farmer's Bt acreage for prevailing Bt-CR "pyramids" (multiple Bt-CR traits in the same plant). Second, Ye *et al.*'s finding that economically efficient Bt-CR planting rates differ substantially between the Western and Eastern Corn Belt suggests that the EPA should consider setting refuge mandates separately for these subregions.

The EPA's most recent policy frameworks for WCR and lepidopteran pests make clear that refuge mandates alone are insufficient for its regulatory objectives (*14*, *15*). Recently, the EPA has proposed that in certain areas of the Cotton Belt, where corn refuge seed mixtures do not count toward refuge, farmers buying Bt corn seed must also purchase non-Bt corn seed at a 20% refuge proportion at the point of sale (*15*). For WCR, the EPA emphasizes integrated pest management (IPM). One IPM tactic for WCR that the EPA has sought to further incentivize is crop rotation (*14*). Economic evaluations of these expanded tactics will become more important as the agency tries to determine the most effective and efficient course forward, while transparently justifying its actions to a range of stakeholders. Ye *et al.* demonstrate an empirically grounded approach for such evaluations.

Another lesson from this research lies in data accessibility and transparency, the lack of which has imposed a barrier to more economic research on this topic. Crucial parts of Ye *et al.*'s economic analysis rely on farm seed purchase surveys from a private market research firm. Because they provide more detailed information on the sales and deployment of different genetically engineered (GE) traits across corn hybrids than any other existing data sources, including from the National Agricultural Statistics Service with the US Department of Agriculture (USDA), they have been in high demand among agricultural economists studying GE crops and pesticides. But they are proprietary and expensive, and multiple research projects funded by the USDA National Institute of Food and Agriculture have separately paid the costs for these same data products. Beyond the inefficiency of this arrangement, this poses considerable barriers to the scientific principles of transparency and reproducibility. More open, high-quality data on the deployment of Bt and other GE crop traits would improve the ability of the scientific community to build a richer evidence base on which to build regulatory programs. For comparison, it is noteworthy that another data product on pesticide sales—by the same market research firm—is used under contract to publicly report data on agricultural pesticide use for the National Water Quality Assessment within the National Oceanic and Atmospheric Administration. Those pesticide data have served as a critical evidence base for recent research examining the local public health effects of agricultural pesticides (*3*). In principle, a similar arrangement could be reached with the survey firm's Bt trait data, which could, for example, inform public understanding of corn hybrid availability and diversity in Bt and non-Bt products.

Finally, a continuing gap in applied research on the economics of resistance concerns the environmental and health risks of pesticides. Like other economic research on pesticide resistance, Ye *et al.*'s conclusions about whether Bt-CR traits are overused account only for farm profits. For the EPA to carry out economic evaluations of Bt resistance policies and regulations, it will need to also account for environmental and health effects, in order for such evaluations to directly address the agency's original rationale for regulating Bt crops using its FIFRA authority. Addressing the challenges faced by regulators and raised by Ye *et al.* will require balancing short-term farmer incentives with long-term agricultural and environmental sustainability, ensuring that Bt crops remain viable tools for pest management. ■

REFERENCES AND NOTES

1. Z. Ye *et al.*, *Science* **387**, eadn9388 (2025).
2. F. Gould, Z. S. Brown, J. Kuzma, *Science* **360**, 728 (2018).
3. E. G. Frank, *Science* **385**, eadg0344 (2024).
4. Economic Research Service, Adoption of Genetically Engineered Crops in the United States, July 2024; https://www.ers.usda.gov/data-products/adoption-of-genetically-engineered-crops-in-the-united-states/documentation.
5. W. D. Hutchison *et al.*, *Science* **330**, 222 (2010).
6. E. D. Perry *et al.*, *Sci. Adv.* **2**, e1600850 (2016).
7. Y. Carrière *et al.*, *Ambio* **49**, 1 (2020).
8. A. J. Gassmann, D. D. Reisig, *Annu. Rev. Entomol.* **68**, 31 (2023).
9. D. D. Reisig *et al.*, *J. Econ. Entomol.* **111**, 1824 (2018).
10. Federal Insecticide, Fungicide, and Rodenticide Act (FIFRA, 1996), 7 U.S.C. §136 *et seq.* (1996).
11. D. A. Andow *et al.*, *J. Econ. Entomol.* **109**, 1 (2016).
12. S. Ambec, M. Desquilbet, *Environ. Resour. Econ.* **51**, 79 (2012).
13. E. M. Liu, J. K. Huang, *J. Dev. Econ.* **103**, 202 (2013).
14. Environmental Protection Agency, Registration Terms for CRW IRM - Final Version (2016); https://www.regulations.gov (Docket ID EPA-HQ-OPP-2014-0805).
15. Environmental Protection Agency, EPA Update Regarding the Implementation Status of Ongoing Improvements to the Insect Resistance Management Framework for Plant-Incorporated Protectants (PIPs) (2025); https://www.regulations.gov (Docket ID EPA-HQ-OPP-2019-0682-0055).

ACKNOWLEDGMENTS

The authors acknowledge support from the US National Institute of Food and Agriculture, through Hatch Projects NC-BROWN and NC-02543.

10.1126/science.adv4313

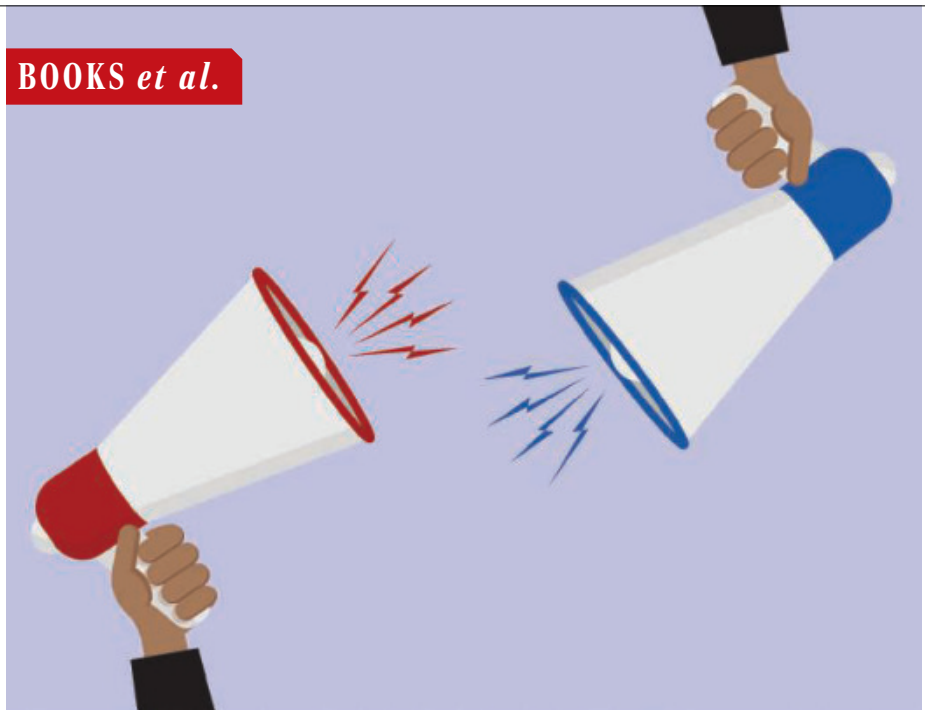

Moral disagreements are often rooted in different ideas about what needs protecting, argues Gray.

ILLUSTRATION: TOMMY/ISTOCK PHOTO

PSYCHOLOGY

Turning down the outrage

A moral psychologist offers a framework for bridging divides

By **Sean M. Laurent**

Navigating conflict is difficult in the best of circumstances. It becomes even harder when our disagreements are deeply rooted in opposing moral convictions about the directions in which our collective lives are moving. When these tensions are embedded in contexts involving existential threats such as a changing climate that brings devastating storms or low wages and high prices for everything from grocery staples to health care and housing, fighting naturally erupts over the best way to fix a broken system. Political polarization seems inevitable.

In his compelling book, *Outraged: Why We Fight About Morality and Politics and How to Find Common Ground*, moral psychologist Kurt Gray uses stories and science to help readers understand why people are so angry at each other about almost everything. The reason, in his view? They feel threatened. They are afraid of what the future holds for them and for those they love. They feel as though the things that might ease their daily struggles are being ignored or even mocked by "the other side."

Outraged: Why We Fight About Morality and Politics and How to Find Common Ground
Kurt Gray
Pantheon, 2025. 368 pp.

Gray does not take sides. Instead, using a conversational tone and real-world examples, he deftly lays out a case for why people on any side of an issue often feel that they are victims and that those with opposing views are villains. Woven into his narrative is Gray's own research on morality and political division as well as other relevant research by scholars such as Elliot Turiel, Richard Shweder, and Jonathan Haidt. Importantly, he also lays out a path forward to better understanding those with whom we disagree.

Outraged tackles, in three sections, what Gray describes as three myths. The first myth is that humans evolved as predators rather than prey. Using evidence from anthropology and primatology, he argues that we need to look further into our past than the relatively recent history of humans as apex predators to a time when our species' major concern was staying out of the stomachs of the many animals that wanted to eat us. His conclusion—that humans evolved as prey and that our primary evolutionary motivation is to defend rather than attack—sets the stage for why he believes we are constantly vigilant for threats and frequently feel like victims, even as the world has grown considerably safer.

The second myth Gray seeks to dispute is that harmless wrongs exist. Here, he outlines much of his research program and makes his second major point: that all moral understanding is implicitly rooted in variable perceptions of harm.

Naturally, if avoiding threats is our primary concern, we fall prey to the idea that people are either hunters or the hunted, but not both—a phenomenon Gray calls "moral typecasting." According to this framework, we and those on "our side" are innocent victims, pursued by attackers who want to destroy us and the things we value. However, neither of these things are usually true.

Because we are all programmed to be sensitive to threats of harm, everyone's morality operates in the same way, Gray maintains. Thus, our moral disagreements generally involve conflicting ideas about who and what is vulnerable and needs protection. His team's research challenges the idea that distinct "types" of morality exist, because seemingly "harmless wrongs," such as eating the wrong kind of food too soon after a father's funeral or disobeying an authority figure, can nonetheless be perceived as harmful by those who moralize such behaviors.

To close the book, Gray makes a case against a third and final myth: that fact-based arguments can bridge moral divides. Facts might make us seem rational, he concedes, but it is our stories of vulnerability that help heal divisions, and sharing them can open the door to finding common ground.

Although scientific findings are again used here, I found myself emotionally moved by the description of a facilitated conversation between Todd Underwood, a staunch gun-rights advocate, and Carolyn Tuft, a woman who was injured and whose child was killed in a mass shooting incident. The pair's ability to acknowledge each other's humanity and suffering suggests hope for us all and offers a template for anyone to initiate overcoming differences by connecting, sharing, and, most importantly, listening. ■

The reviewer is at the Department of Psychology, The Pennsylvania State University, University Park, PA, USA. Email: slaurent@psu.edu

10.1126/science.adu7406

PUBLIC HEALTH

The air as ecosystem

We ignore the organisms that swirl around us at our peril

Air-Borne: The Hidden History of the Life We Breathe
Carl Zimmer
Dutton, 2025. 496 pp.

By **Nathan H. Lents**

One could be forgiven for not knowing much about the life that floats in the air around us. As journalist Carl Zimmer explains in *Air-Borne: The Hidden History of the Life We Breathe*, few of us do. His meticulously researched tome is at once a popular science book, a historical monograph, a public policy lesson, and a comprehensive primer on the subdiscipline of science known as "aerobiology," practitioners of which study this very topic.

Zimmer dramatically describes how aerobiology burst onto the public stage during the 19th-century debates surrounding the theory of spontaneous generation—the idea that life could arise from nonliving matter. Louis Pasteur's veal bouillon and swan-necked flasks will be well known to most scientists, but Zimmer also recounts Pasteur's lesser-known journey to the top of a glacier to see whether life teemed in the air there, too. (Spoiler alert: It does.) Colorful and informative historical anecdotes about the work of many other pioneers of microbiology, such as Robert Koch, Joseph Lister, and John Snow, appear here as well.

Unsurprisingly, much of the research on airborne life is, and always has been, focused on how pathogens spread. What is surprising is how often—and how badly—we have gotten things wrong.

As contagionists, miasmatists, and sanitarians staked out their various public health positions throughout history, pandemics and plagues raged. The quarantine, first conceived of as a 30-day restriction meant to prevent entry of the Black Death into Dubrovnik, Croatia, in 1377, was a spectacular success. Yet five centuries later, yellow fever quarantines were being referred to by anticontagionists as "willful murder"—a refrain with a familiar echo.

Zimmer's tour through global scourges includes discussions of historical outbreaks of tuberculosis, pertussis, measles, and chicken pox, among others. The fact that physicians seeking to treat these outbreaks used the same approaches to characterize pathogens of widely different natures—viruses, aerobic and anaerobic bacteria, and fungi—without appreciating the risk of cross-contamination within their facilities, ensured that the results were often conflicting, contradictory, and confusing.

How aerosolized pathogens spread is less well understood than many assume.

As Zimmer carefully explains, most contagions are spread through direct contact with infected persons or contaminated fluids, objects, or surfaces. Others hitch a ride on the respiratory droplets that form during speaking, sneezing, or coughing. But these droplets can perniciously spin off smaller aerosols, known as droplet nuclei, which are just a few microns in diameter and can waft long distances and be carried in updrafts. Influenza, severe acute respiratory syndrome (SARS), and the common cold can be spread by all three modes of transmission, but, shockingly, we still do not know the relative contribution of each mode. Given how many people die from respiratory infections each year, our continued ignorance on this topic is nothing short of a scientific scandal.

The public policy scandals are far worse. Neither SARS, nor MERS (Middle East respiratory syndrome), nor Ebola, nor the H1N1 or H5N1 influenza strains could compete with anthrax and smallpox for attention from policy-makers at the dawn of the 21st century. With palpable frustration, Zimmer describes an ambitious 2005 speech in which George W. Bush announced a generous budget for pandemic preparedness that failed to include substantial funding for research into how respiratory infections spread. Officials assumed that we knew.

Zimmer's reporting is at its most penetrating when he reaches Wuhan in December 2019. Here, he maintains, officials at the Chinese Ministry of Health, the US Centers for Disease Control and Prevention, and the World Health Organization put their ignorance of respiratory transmission on full display. Zimmer describes the early efforts of a group of 36 aerobiology experts to warn the world that SARS coronavirus 2 was an airborne pathogen, spread not just through fluids and droplets but also by quiet breathing. While the public focused on handwashing and disinfecting surfaces rather than donning masks and respirators, the outbreak became a pandemic.

The final three chapters of *Air-Borne* constitute the most comprehensive scientific history of COVID-19 that I have read. Informed by personal interviews with many top officials, physicians, and scientists, Zimmer's reporting is equal parts riveting and infuriating. Although the rapid development of incredibly safe and effective COVID-19 vaccines remains a scientific triumph, Zimmer hauntingly concludes that on most other scores—especially public resistance to vaccination, quarantines, and masks—we are worse off now than we were 5 years ago. ■

The reviewer is at the Department of Sciences, John Jay College of Criminal Justice, City University of New York, New York, NY, USA. Email: nlents@jjay.cuny.edu

10.1126/science.adt1510

PHOTO: DMYTRO ZINKEVYCH/ALAMY STOCK PHOTO

Exceptions to environmental and animal welfare requirements for farmers have undermined the EU's legislative framework for conservation and biodiversity protection.

PHOTO: NURPHOTO VIA GETTY IMAGES

Edited by **Jennifer Sills**

Stop regression of EU conservation laws

Over the past three decades, the European Union (EU) has established a strong legislative framework to protect the environment and biodiversity. However, recent political decisions have created legal uncertainties and internal conflicts among EU regulations, with negative effects on nature conservation. To ensure that political decisions do not impede progress toward conservation objectives, the EU and its Member States must integrate the principle of non-regression into conservation laws.

EU climate and energy policies (Regulations 2022/0160 and 2022/2577) (*1*, *2*) have streamlined infrastructure project development at the expense of the environment. For example, environmental impact assessments and controls by authorities have been simplified or even removed (*3*, *4*). In some cases, public participation in environmental impact assessment processes has also been eliminated, in violation of the Aarhus Convention (*5*), which requires that the public have a voice in decision-making on environmental issues.

EU agricultural policies have also eliminated some guarantees of environmental protection (*6*). Regulation 2024/1468 of the EU Common Agricultural Policy (*7*) reduced some of the conditionality requirements for farmers in relation to animal welfare and the environment (*8*). For example, nonproductive areas are no longer required in arable lands, crop rotation is now optional, farmers have more flexibility in claiming exceptions to conditionality requirements, and small farmers are exempted from checks and penalties associated with such requirements. Furthermore, proposed biodiversity protections, such as regulations related to the sustainable use of pesticides, were withdrawn in 2024 (*9*), and the European Commission decreased the budget for promoting sustainable agriculture and animal welfare in 2025 (*10*).

These policy amendments, which reflect political and economic priorities, collide with the EU's biodiversity strategy for 2030, which aims to strengthen the EU legal framework for nature recovery and to increase compliance with EU environmental legislation. They also undermine the Treaty on the Functioning of the European Union (Article 191), a commitment to protect and improve the environment (*11*).

According to the 2012 Rio+20 Summit non-regression principle, countries are prohibited from weakening their domestic environmental protection (*12*). The EU and Member States should integrate the principle of non-regression into conservation laws and adhere to Article 11 of the Treaty on the Functioning of the European Union, which states that all policies must include environmental protection requirements (*11*). Only by ensuring that European policies remain aligned with conservation laws can the EU continue to be an international reference for conservation goals.

Carlos Javier Durá-Alemañ[1,2] and José Vicente López-Bao[3]
[1]Institute of Advanced Social Studies, Spanish National Research Council, Córdoba, Spain. [2]International Center for Environmental Law Studies, Soria, Spain. [3]Biodiversity Research Institute, Spanish National Research Council, Mieres, Spain.
*Corresponding author.
Email: jv.lopez.bao@csic.es

REFERENCES AND NOTES

1. European Commission, "Council Regulation (EU) 2022/2577 of 22 December 2022 laying down a framework to accelerate the deployment of renewable energy" (2022); https://eur-lex.europa.eu/eli/reg/2022/2577.
2. European Commission, "Proposal for a Directive of the European Parliament and of the Council amending Directive (EU) 2018/2001 on the promotion of the use of energy from renewable sources, Directive 2010/31/EU on the energy performance of buildings

and Directive 2012/27/EU on energy efficiency" (2022); https://eur-lex.europa.eu/legal-content/EN/TXT/?uri=celex%3A52022PC0222.
3. C. J. Durá-Alemañ *et al.*, *Conserv. Lett.* **16**, e12958 (2023).
4. L. Bolonio *et al.*, *Environ. Impact Assess. Rev.* **105**, 107432 (2024).
5. European Commission, The Aarhus Convention and the EU; https://environment.ec.europa.eu/law-and-governance/aarhus_en#overview.
6. A. Navarro, J. V. López-Bao, *Science* **384**, 169 (2024).
7. European Commission, "Regulation (EU) 2024/1468 of the European Parliament and of the Council of 14 May 2024 amending Regulations (EU) 2021/2115 and (EU) 2021/2116 as regards good agricultural and environmental condition standards, schemes for climate, environment and animal welfare, amendment of the CAP Strategic Plans, review of the CAP Strategic Plans and exemptions from controls and penalties" (2024); https://eur-lex.europa.eu/legal-content/EN/TXT/PDF/?uri=OJ:L_202401468.
8. European Commission, Conditionality; https://agriculture.ec.europa.eu/common-agricultural-policy/income-support/conditionality_en.
9. T. Rabesandratana, "Europe's backpedaling on green legislation has scientists concerned," *ScienceInsider*, 9 February 2024; https://www.science.org/content/article/europe-s-backpedaling-green-legislation-has-scientists-concerned.
10. European Commission, "Commission allocates €132

OUTSIDE THE TOWER

Assessing soil health with underpants

We watched as the two young boys stuck their shovels in the ground and painstakingly dug up the remains of the underpants. Most of the organic cotton fabric had decomposed in the 2 months that the underpants had been buried. "The worms, insects, and bacteria ate most of our underpants!" they exclaimed. "We have good soil!"

The boys' experience was one of about 1000 moments across Switzerland in which citizen scientists revealed information about the biological activity of soil in their gardens, fields, and lawns. They did so as participants in our citizen science project (*1*), which we organized to raise awareness and collect data about the state of Swiss soils. At first, we considered using cotton squares or socks, but we wondered whether nonscientists would be interested enough to participate. Then we had an idea: Cotton underpants with elastic "skeletons" would be both intriguing and practical! Our suspicions proved correct. Once the project was announced, farmers and hobby gardeners all over the country leaped at the chance to fill the 1000 spots.

Call for submissions
Outside the Tower is an occasional feature highlighting scientists' advocacy experiences. Submit your advocacy story at http://cts.sciencemag.org.

We provided 1000 identical pairs of underpants for burial, and the participants recorded their management practices and collected nearly 900 soil samples. Although we encouraged them to investigate their soils, we also analyzed all soil samples and assessed underpants degradation from each location in our lab. We then correlated soil samples and management data with underpants degradation, finding that cotton underpants serve as easily accessible soil-health indicators. As a result of media coverage, the project extended beyond Swiss borders, with reports from more than 25 countries spanning almost every continent.

This project helped us collect a unique dataset and gave us the opportunity to advocate for soil conservation in Switzerland and beyond. We provided the citizen scientists with personalized feedback, including soil analysis results, interpretation tools, and tips for sustainable soil management. Hopefully, the sensory experience of recovering a decomposed pair of underwear from their own land has inspired the participants to see soil as a living system and a vital resource and empowered them to serve as conscientious soil stewards.

S. Franz Bender[1,2]* and Marcel G. A. van der Heijden[1,2]*
[1]Research Division Agroecology and Environment, Agroscope, Zürich, Switzerland. [2]Department of Plant and Microbial Biology, University of Zürich, Zürich, Switzerland.
*Corresponding author. Email: franz.bender@agroscope.admin.ch; marcel.vanderheijden@botinst.uzh.ch

REFERENCES AND NOTES

1. Beweisstück Unterhose; www.beweisstueck-unterhose.ch.

10.1126/science.adw0030

Citizen scientists buried and retrieved underpants to assess soil health. Here, underpants showing a range of decomposition hang from a clothesline.

PHOTO: AGROSCOPE, GABRIELA BRAENDLE

million to promote sustainable and high-quality agri-food products in the EU and worldwide," press release (12 December 2024); https://ec.europa.eu/commission/presscorner/detail/en/ip_24_6421.
11. European Commission, "Consolidated version of the Treaty on the Functioning of the European Union" (2012); https://eur-lex.europa.eu/LexUriServ/LexUriServ.do?uri=CELEX:12012E/TXT:en:PDF.
12. M. Prieur, in *A Global Pact for the Environment - Legal Foundations*, Y. Aguila, J. E. Viñuales, Eds. (C-EENRG, 2019), pp. 142–148.

COMPETING INTERESTS

J.V.L.-B. is a member of the Canid Specialist Group of the International Union for Conservation of Nature and Natural Resources (IUCN) Species Survival Commission and a member of the scientific committee advising the Spanish Ministry for the Ecological Transition and the Demographic Challenge, both unpaid advisory roles.

10.1126/science.adu1943

Protect US racial affinity groups

On its first day, the Trump administration released several executive orders terminating diversity, equity, and inclusion (DEI) programs, calling them "illegal," "immoral," and "discriminatory" (*1*, *2*). DEI programs include racial affinity groups, which counter the systemic barriers to inclusion and advancement that Black, Indigenous, and People of Color (BIPOC) face in science, technology, engineering, and mathematics (STEM) disciplines (*3*, *4*). These organizations provide a welcoming space for underrepresented scientists to give and receive culturally aware mentorship (*5*). Given that diverse teams produce more innovative science (*6*), racial affinity groups benefit not only BIPOC scientists but also their employers and the public. Racial affinity groups do not violate US antisegregation or antidiscrimination laws; they enable equitable access to resources that support academic advancement for all. To protect scientists and scientific output, US stakeholders must work to protect affinity groups from government interference.

Racial affinity groups—which include academic societies, social media groups, nonprofits, employee resource groups, and institutional and departmental organizations—strengthen the STEM community. They increase retention of BIPOC scientists through professional development and mentoring (*7*). These scientists then contribute to the scientific enterprise by bringing new perspectives through their academic work, expanding science networks, and mentoring the next generation of STEM trainees (*8*). Racial affinity groups are critical communities of support and compassion for BIPOC scientists, many of whom are the only member of their racial or ethnic community in their workplace.

Although most employed US adults support DEI efforts in the workplace (*9*), the recent federal directives are only the latest in a series of attacks on DEI. More than half of all states have introduced legislation limiting DEI activities, and members of Congress have mocked DEI programs (*10*). These actions, in addition to the removal of race-related affirmative action policies in colleges (*11*), foreshadowed the current onslaught of anti-DEI actions.

The current political climate is tremendously hostile for BIPOC scientists. Affinity groups provide solace and a loving community, but the burden of resistance cannot fall on the most marginalized (*12*). Those with privilege must step up on personal, collective, and institutional levels. Institutions—including private and public universities, professional societies, state governments, nonprofits, and private foundations—must financially support racial affinity groups and challenge disinformation about their role in STEM. These institutions must resist by taking legal action against civil liberty violations that result from anti-DEI directives. Last, rather than advise BIPOC scientists to stay quiet, institutions and those in positions of authority should provide affinity groups and their members with protection and job security. As political parties in the US and beyond seek to recodify white supremacist philosophies (*10*), STEM leadership must take urgent action to protect and support all members of our diverse scientific community.

V. Bala Chaudhary[1], Sora Kim[2], Mónica Medina[3], Diane S. Srivastava[4], Nikki Traylor-Knowles[5], Marlene Brito-Millan[6], Alejandra Camargo-Cely[7], Snehanjana Chatterjee[8], Nancy Chen[9], Yolanda H. Chen[10], Kiyoko M. Gotanda[11], Samniqueka J. Halsey[12], Chandra N. Jack[13], Rosa M. McGuire[14], Cassandra M. L. Miller[15], Alex C. Moore[16,17], Suegene Noh[18], Theresa W. Ong[1], Ariane L. Peralta[19], Amanda Puitiza[20], Lucia N. Ramirez[21], Adriana L. Romero-Olivares[22], M. Fabiola Pulido-Barriga[23], Karina A. Sanchez[24], Christine Y. Sit[25], Chenyang Su[1], Juleyska Vazquez-Cardona[26], Yaamini R. Venkataraman[27], Chhaya M. Werner[28], Lily Khadempour[29]*

[1]Environmental Studies Department, Dartmouth College, Hanover, NH, USA. [2]Department of Life and Environmental Sciences, University of California, Merced, Merced, CA USA. [3]Department of Biology, The Pennsylvania State University, University Park, PA, USA. [4]Department of Zoology and Biodiversity Research Centre, University of British Columbia, Vancouver, BC, Canada. [5]Marine Biology and Ecology, Rosenstiel School of Marine, Atmospheric, and Earth Science, University of Miami, Miami, FL, USA. [6]School of Environmental Sustainability, Loyola University Chicago, Chicago, IL, USA. [7]Department of Biology, Boston University, Boston, MA, USA. [8]Department of Biological Sciences, Texas Tech University, Lubbock, TX, USA. [9]Department of Biology, University of Rochester, Rochester, NY, USA. [10]Department of Agriculture, Landscape, and Environment, University of Vermont, Burlington, VT, USA. [11]Department of Biological Sciences, Brock University, St. Catharines, ON, Canada. [12]School of Natural Resources, University of Missouri, Columbia, MO, USA. [13]Biology Department, Clark University, Worcester, MA, USA. [14]Department of Biology, Stanford University, Stanford, CA, USA. [15]Department of Biology University of New Mexico, Albuquerque, NM, USA. [16]Department of Forest Resources, University of Minnesota, St. Paul, MN, USA. [17]Department of Botany, University of British Columbia, Vancouver, BC, Canada. [18]Biology Department, Colby College, Waterville, ME, USA. [19]Department of Biology, East Carolina University, Greenville, NC, USA. [20]Department of Animal and Rangeland Sciences, Oregon State University, Corvallis, OR, USA. [21]Department of Biological Sciences, North Carolina State University, Raleigh, NC, USA. [22]Department of Biology, New Mexico State University, Las Cruces, NM, USA. [23]Department of Ecology and Evolutionary Biology, University of California Irvine, Irvine, CA, USA. [24]Department of Natural Resources and the Environment, University of New Hampshire, Durham, NH, USA. [25]School for Environment and Sustainability, University of Michigan, Ann Arbor, MI, USA. [26]Psychology Department, University of Lethbridge, Lethbridge, AB, Canada. [27]Biology Department, Woods Hole Oceanographic Institution, Woods Hole, MA, USA. [28]Department of Environmental Science, Policy and Sustainability, Southern Oregon University, Ashland, OR, USA. [29]Department of Earth and Environmental Sciences, Rutgers University Newark, Newark, NJ, USA.
*Corresponding author. Email: lily.khadempour@rutgers.edu

REFERENCES AND NOTES

1. R. Moore, "Trump's executive orders rolling back DEI and accessibility efforts, explained," ACLU, 2025; https://www.aclu.org/news/racial-justice/trumps-executive-orders-rolling-back-dei-and-accessibility-efforts-explained.
2. D. Trump, "Ending radical and wasteful government DEI programs and preferencing," The White House, 2025; https://www.whitehouse.gov/presidential-actions/2025/01/ending-radical-and-wasteful-government-dei-programs-and-preferencing.
3. Committee on Advancing Antiracism, Diversity, Equity, and Inclusion in STEM Organizations, Board on Behavioral, Cognitive, and Sensory Sciences, Division of Behavioral and Social Sciences and Education, National Academies of Sciences, Engineering, and Medicine, *Advancing Antiracism, Diversity, Equity, and Inclusion in STEMM Organizations: Beyond Broadening Participation* (National Academies Press, 2023).
4. M. J. Hopkins, B. N. Moore, J. L. Jeffery, A. S. Young, *eLife* **13**, e94422 (2024).
5. A. M. Byars-Winston *et al.*, *J. Clin. Transl. Sci.* **2**, 86 (2018).
6. "How diversity improves science and technology," American Association for the Advancement of Science (AAAS); https://www.aaas.org/news/how-diversity-improves-science-and-technology.
7. R. S. Markle *et al.*, *Front. Ed.* **7**, 10.3389/feduc.2022.674669 (2022).
8. V. B. Chaudhary, A. A. Berhe, *PLOS Comp. Biol.* **16**, e1008210 (2020).
9. R. Minkin, "Diversity, Equity and Inclusion in the Workplace," Pew Research Center, 2023; https://www.pewresearch.org/social-trends/2023/05/17/diversity-equity-and-inclusion-in-the-workplace.
10. S. Harper *et al.*, "Truths about DEI on college campuses: Evidence-based expert responses to politicized misinformation" (USC Race and Equity Center, 2024).
11. N. Totenberg, "Supreme Court guts affirmative action, effectively ending race-conscious admissions," *NPR* (2023); https://www.npr.org/2023/06/29/1181138066/affirmative-action-supreme-court-decision.
12. C. R. Domingo *et al.*, *J. Divers. High. Ed.* **15**, 365 (2022).

COMPETING INTERESTS:

N.T.-K. is the executive director and founder of the nonprofit Black Women in Ecology, Evolution, and Marine Science.

10.1126/science.adq4733

AAAS Announces 2025 Award Winners

Recipients include distinguished researchers, educators, and science communicators

AAAS has announced the 2025 winners of eight awards that recognize scientists, engineers, innovators, and public servants for their contributions to science and society. These recipients' achievements include spurring undergraduate students to pursue further study in the sciences, communicating the serious health risks faced by migrant laborers, and standing in solidarity with Iranian protestors at great personal and professional risk. The winners, who were honored at the 2025 AAAS Annual Meeting, are:

AAAS Philip Hauge Abelson Prize: Mary Woolley

AAAS Mani L. Bhaumik Award for Public Engagement with Science: Brian Greene

AAAS Early Career Award for Public Engagement with Science: Barrak Alahmad

AAAS David and Betty Hamburg Award for Science Diplomacy: Daniel Whittle, Valerie Miller, and Eduardo Boné Morón

AAAS Award for Scientific Freedom and Responsibility: Encieh Erfani

AAAS Lifetime Mentor Award: Juan F. Arratia

AAAS Mentor Award: LaShan Simpson Hendrix

AAAS Newcomb Cleveland Prize: "Nitrogen-fixing organelle in a marine alga"

AAAS Philip Hauge Abelson Prize

Mary Woolley, the president and CEO of Research!America, is the recipient of the 2025 AAAS Philip Hauge Abelson Prize, which honors an individual who has made significant contributions to the advancement of science in the United States through their research, policy work, or public service.

Research!America is an alliance of member organizations in the medical, health, and scientific fields that are committed to making medical and health research a higher national priority. Under Woolley's 35 years of leadership, the group has grown into a unified and respected voice representing hundreds of member organizations, and their reports, resources, and education initiatives have earned the attention and respect of policy-makers, researchers, media, and community leaders.

AAAS Mani L. Bhaumik Award for Public Engagement with Science

Brian Greene, professor and director of Columbia University's Center for Theoretical Physics, is the recipient of the AAAS Mani L. Bhaumik Award for Public Engagement with Science, which recognizes scientists and engineers who demonstrate excellence in their public engagement with science. Since 2019, it has been endowed by quantum physicist Mani L. Bhaumik.

Greene is well known in the scientific world for his groundbreaking co-discovery of mirror symmetry and spatial topology change, two key breakthroughs of superstring theory. His 1999 book, *The Elegant Universe*, which brought string theory to broad audiences, was a finalist for the Pulitzer Prize and was adapted into a 2003 PBS documentary of the same name. His books, which also include *The Fabric of the Cosmos: Space, Time and the Texture of Reality*, have sold a total of more than 2 million copies worldwide and have spent a combined 65 weeks on the *New York Times* bestseller list.

AAAS Early Career Award for Public Engagement with Science

Barrak Alahmad, a research fellow at the Harvard T.H. Chan School of Public Health, is the recipient of the 2025 AAAS Early Career Award for Public Engagement with Science. The award recognizes early-career scientists and engineers—those who are within 7 years of completing their terminal degree—who demonstrate excellence in their activities that engage the public with science.

After earning his medical degree and practicing as a doctor in his native Kuwait, Alahmad noticed the negative health impacts of Kuwait's hot climate on the country's population of migrant workers. Alahmad pursued research that found that otherwise young and healthy individuals–who had minimal access to health care–were particularly vulnerable to dust storms and extreme temperatures. His multifaceted public engagement work around these impacts has communicated his findings to those affected and to the public with the goal of building consensus on the issue and changing policy to improve outcomes for affected individuals.

AAAS David and Betty Hamburg Award for Science Diplomacy

Daniel Whittle, Valerie Miller, and Eduardo Boné Morón from the Environmental Defense Fund are the recipients of the AAAS David and Betty Hamburg Award for Science Diplomacy. The award recognizes an individual or a small group working together in the scientific, engineering, or foreign affairs communities making an outstanding contribution to furthering science diplomacy.

The work of Whittle, Miller, and Boné Morón has yielded opportunities for connection and dialogue between Cuban and US scientists and officials, including many opportunities for officials to interact informally years before the US and Cuba normalized diplomatic relations. Their work has also produced joint scientific research, including dozens of peer-reviewed articles, and seen significant conservation of marine and coastal ecosystems and sustainable fisheries, with the Cuban government implementing the region's most ambitious network of marine protected areas, conserving about 25 percent of coastal waters.

AAAS Award for Scientific Freedom and Responsibility

Encieh Erfani is the recipient of the AAAS Award for Scientific Freedom and Responsibility, which honors individuals or organizations whose exemplary actions—sometimes taken at significant personal cost—have served to foster and protect those ideals.

Erfani was an assistant professor of physics whose research focused on cosmology in her native Iran, but following the death of activist Mahsa Amini and ensuing peaceful "Woman, Life, Freedom" protests, she resigned her faculty position at her Iranian institution in solidarity with protestors. Erfani, who was abroad in Mexico as a visiting researcher at the time, is now in exile as a result. After her resignation, she has continued her advocacy by cofounding

the International Community of Iranian Academics and compiling a report containing the latest statistics on students killed, detained, and imprisoned in Iran.

AAAS Lifetime Mentor Award

Juan F. Arratia, former director and principal investigator of the Model Institutions for Excellence project for the National Science Foundation at Universidad Metropolitana in Puerto Rico, is the recipient of the AAAS Lifetime Mentor Award. The award honors an individual with more than 25 years of experience who has mentored significant numbers of underrepresented students.

To achieve the goals of recruiting and increasing the number of Hispanic students in STEM fields and increasing STEM major retention, the multifaceted Model Institutions for Excellence initiative at UMET has offered scholarship funding, research opportunities, support for students intending to pursue graduate school, an annual research symposium, and a precollege program. During Arratia's tenure, the number of Hispanic students enrolled as STEM majors at UMET nearly doubled.

AAAS Mentor Award

LaShan Simpson Hendrix, associate professor in the Department of Biomedical Engineering at the University of Cincinnati, is the recipient of the AAAS Mentor Award. The award honors an individual who has mentored significant numbers of underrepresented students.

Hendrix earns the award for guiding many of her students to become biomedical scientists and engineers. Students who offered letters of recommendation for her award praised Hendrix's warmth as a mentor. They noted how she has encouraged her mentees to apply for prestigious positions and has demystified the path to graduate school and research, teaching many of her mentees research skills they still use daily. She has kept in contact with her mentees beyond graduation—according to her mentees, Hendrix is truly a lifelong mentor.

AAAS Newcomb Cleveland Prize

A team of researchers has won the AAAS Newcomb Cleveland Prize for their work that has identified a new organelle within single-celled algae that converts nitrogen gas into ammonia. The AAAS Newcomb Cleveland Prize, supported by The Fodor Family Trust, is awarded annually to the author or authors of an outstanding paper published in the Research Articles or Reports sections of *Science*.

"Nitrogen-fixing organelle in a marine alga" was published in *Science* on 12 April 2024 by researchers representing the University of California Santa Cruz, Diamond Light Source, UC San Francisco, Lawrence Berkeley National Laboratory, National Taiwan Ocean University, and Kochi University.

The conversion of nitrogen gas into ammonia helps the algae survive in the nutrient-poor ocean. The cellular structure is derived from another microbe that the algae have incorporated. The researchers' discovery fundamentally expands our understanding of cell biology by providing insight into the evolution of organelles, a process that was pivotal in the evolution of complex life and has likely only occurred a handful of times in biology.

RESEARCH

IN *SCIENCE* JOURNALS

Edited by **Michael Funk**

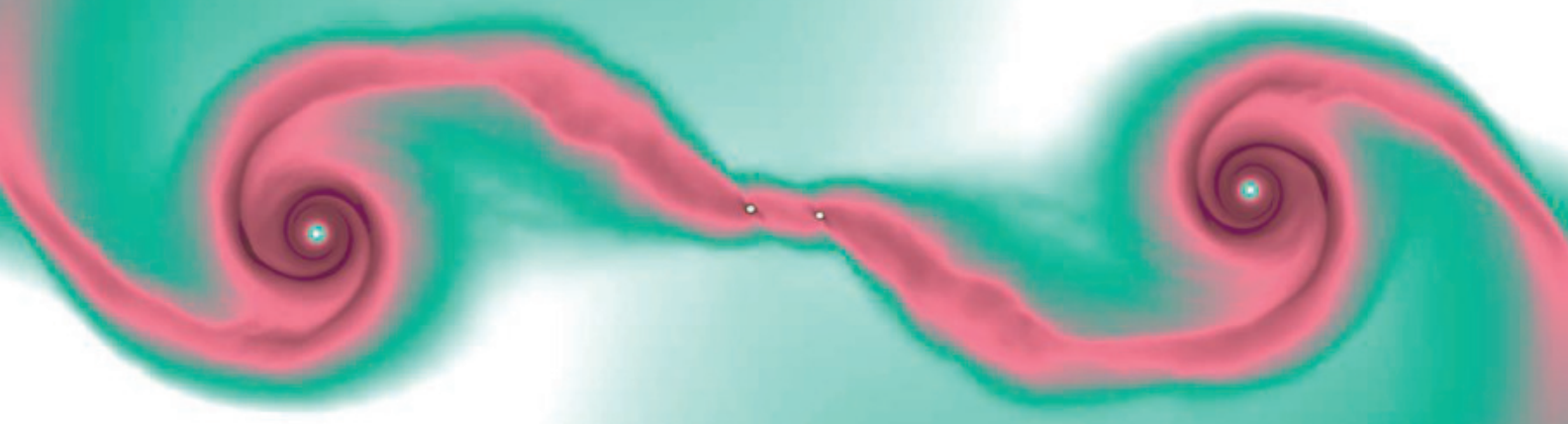

ASTROPHYSICS

Forming planetary mass objects

The origin of free-floating planetary mass objects (PMOs) that are not gravitationally bound to a single star or brown dwarf remains enigmatic. A new proposal is that they form through the breakdown of structures of gas flowing between two protoplanetary disks due to tidal forces. Fu *et al.* showed that producing PMOs in this way would be highly efficient in some start clusters and less so in others, resulting in variations in the observed number of PMOs established in different settings. If correct, this hypothesis implies that free-floating PMOs form in a manner distinctive from planets or brown dwarfs. —Kip Hodges *Sci. Adv.* (2025) 10.1126/sciadv.adu6058

Simulations reveal that free-floating planetary mass objects can be formed during encounters between two young circumstellar disks.

MOLLUSK GENETICS

The complicated molluscan family tree

Genome sequencing has allowed for a much greater understanding of how species relate to one another than did earlier morphology-based approaches. A particularly difficult phylum to study using genomic data has been mollusks, which encompass species ranging from squid to sea snails, in part due to their high levels of heterozygosity and repetitiveness. Chen *et al*. sequenced 13 new complete genomes from across the phylum to assemble a new phylogeny for *Mollusca*. They resolved several highly debated nodes and provide additional genomes for future study of this highly diverse and genomically complex phylum. —Corinne Simonti

Science p. 1001, 10.1126/science.ads0215

ORGANIC AEROSOLS

Brown absorption

Atmospheric aerosols affect climate by either scattering or absorbing solar radiation. Li *et al*. found that brown nitrogen, the nitrogenous component of organic aerosols, dominates their solar absorption globally. The authors used a model to quantify the atmospheric distribution of brown nitrogen, calculated how chemical aging affects its optical properties, and quantified its radiative impacts. These results will help to improve attribution of the climate effects of organic aerosols. —Jesse Smith

Science p. 989, 10.1126/science.adr4473

ELECTRON MICROSCOPY

Denoising reveals nanoparticle dynamics

Continuous transitions of the surfaces of metal nanoparticles in a gas environment have been revealed with transmission electron microscopy. Crozier *et al*. used unsupervised deep denoising to overcome the poor signal-to-noise ratios inherent in imaging with both high spatial and millisecond time resolution. Stress fields that penetrated below the surface of platinum nanoparticles supported on cerium oxide destabilized the nanoparticles and led to a series of transitions between ordered and disordered configurations. —Phil Szuromi

Science p. 949, 10.1126/science.ads2688

CHEMICAL PHYSICS

Methane interference

Interference effects are easily seen when light passes through closely spaced slits or bounces off an etched grating. Quantum

IMAGE: FU *ET AL.*

mechanics dictates that an analogous type of behavior pertains to molecules, not just to light, but molecular interference tends to be harder to discern. Reilly *et al*. observed that when methane molecules scatter off a gold surface, an interference effect clearly manifests: Certain final rotational states are entirely suppressed depending on their reflection symmetry relationship to the incoming states. —Jake S. Yeston

Science p. 962, 10.1126/science.adu1023

AUTOIMMUNITY

Sequencing at the scene of the crime

Epstein bar virus (EBV) infection predisposes individuals to multiple sclerosis. Adaptive immune responses to EBV occur in deep cervical lymph nodes, yet the immune landscape in patients with multiple sclerosis is not well understood. Sarkkinen *et al*. profiled immune cells in such patients using fine needle aspirations. Using multiple sequencing methods, the authors identified an expansion of double-negative memory B cells enriched for a transcriptional profile that resembled a lytic EBV infection. Furthermore, fewer germinal center B cells and T follicular helper cells were detected in patients with multiple sclerosis, and germinal center clonality was reduced. —Hannah Isles

Sci. Immunol. (2025) 10.1126/sciimmunol.adl3604

ACTINIDE CHEMISTRY

Berkelium sandwich

Elucidating the structure of ferrocene, an iron ion sandwiched between two carbon rings, was foundational to the theory and practice of organometallic chemistry. In the ensuing decades, numerous analogous metal sandwich compounds have been prepared and applied. Russo *et al*. now extend the motif to berkelium, a radioactive element heavier than uranium. Their experiments required rapid synthesis and characterization on a submilligram scale to compensate for the ongoing decay. Spectroscopic and theoretical analysis supported covalent interactions between the cyclic ligands and f orbitals of the metal. —Jake S. Yeston

Science p. 974, 10.1126/science.adr3346

COLLECTIVE MOTION

Not like particles, in fact

Nearly 20 years ago, a study of collective motion in locusts published in *Science* concluded that animals moving collectively do so in a way similar to particles. This conclusion has set the tone for much thinking about such movement in nature. Sayin *et al.*, including authors of the original study, combined field and laboratory studies and found that locusts, and likely also other animals moving collectively, do not follow a "self-propelled" particle model (see the Perspective by Buhl and Simpson). Rather, they found that sensory and cognitive mechanisms mediate the interactions. —Sacha Vignieri

Science p. 995, 10.1126/science.adq7832; see also p. 924, 10.1126/science.adw0733

NEUROSCIENCE

Ago2 couples neurons and blood vessels

The blood–brain barrier is made up of multicellular contacts referred to as the neurovascular unit (NVU), which mediate the exchange of fluid and nutrients in the brain. Sona *et al*. found that tight control of the abundance of the phosphatase PTEN in excitatory neurons is critical to the postnatal development of the NVU in mice. Mice lacking the mRNA regulator Ago2 in glutamatergic neurons had decreased NVU development and defective blood–brain barrier integrity. These effects were mediated through the loss of Ago2-dependent suppression of *Pten*, leading to decreases in the signaling that supports neuronal survival and migration. Thus, Ago2 in excitatory neurons supports brain development through the formation of the blood–brain barrier. —Leslie K. Ferrarelli

Sci. Signal. (2025) 10.1126/scisignal.adl6745

IN OTHER JOURNALS

Edited by **Corinne Simonti** *and* **Jesse Smith**

The genetic impacts of population declines in giant kelp (*Macrocystis pyrifera*) have implications for conservation efforts.

CONSERVATION

Kelp forest management

Kelp forests are integral to aquatic ecosystems, but species such as giant kelp and bull kelp have experienced population bottlenecks in recent decades. Bemmels *et al.* sequenced more than 600 bull kelp and giant kelp individuals to better understand how genetic variation has been shaped by these population declines. They found that populations of these kelp species were highly structured, with some gene flow between adjacent populations. Although there were not as many predicted deleterious variants as they expected, their loss was likely due to genetic drift rather than purging. Overall, this genetic characterization offers insight into the effectiveness of management strategies such as outcrossing between small populations. —Corinne Simonti

Curr. Biol. (2025) 10.1016/j.cub.2024.12.025

ANGIOGENESIS

ADP spurs new blood vessel formation

Vascular endothelial growth factor (VEGF) promotes the survival of cells that line blood vessels, which are known as endothelial cells (ECs). VEGF also contributes to the formation of new blood vessels (angiogenesis) in cancers, which

Compound climate extremes are transforming the characteristics of some West Greenland lakes.

PHOTO: J. SAROS *ET AL.*

ARCTIC LAKES

Blue and brown states

Warmer temperatures and abundant rainfall have changed the color of lakes in West Greenland from "blue" to "brown." West Greenland normally is cold and dry, but in 2023 and 2024, a string of atmospheric rivers inundated the region, subjecting it to record heat and rainfall. Saros *et al.* found that this combination drove an unprecedented state change in lakes there from "blue" to "brown," altering their physical, chemical, and biological features. These changes flipped the lakes from being carbon sinks to carbon sources. Compound events such as these have great potential to suddenly upend ecosystems of all types in a warming world. —Jesse Smith

Proc. Natl. Acad. Sci. U.S.A. (2025)
10.1073/pnas.2413855122

provide nutrients to help tumors survive. Drugs inhibiting VEGF can improve patient survival, but tumors frequently relapse. Biswas *et al.* searched for small molecules that could modulate EC growth independently of VEGF and identified adenosine diphosphate (ADP). Biochemical analysis and single-cell transcriptomics revealed that ADP mediated effects through the platelet receptor P2Y1. Furthermore, ADP administration enhanced angiogenesis in a laser-induced mouse model of choroidal neovascularization. The ADP-P2Y1 axis may provide insights into mechanisms aiding escape from anti-VEGF therapy. —Priscilla N. Kelly

Proc. Natl. Acad. Sci. U.S.A. (2025)
10.1073/pnas.2418752122

POLLUTION

Leaden legacy of Roman plumbing

What did the Romans ever do for us? They invented "mod cons" such as central heating, hot baths, and cookware, all of which required readily malleable lead. Analysis of Arctic ice cores and aerosol modeling by McConnell *et al.* have added to existing evidence that Roman industrial activities resulted in widespread lead pollution. Lead is toxic at any level, especially for children, and exposure is linked to negative outcomes such as cognitive and immune defects. The authors speculate that the effects of lead pollution, especially emanating from the Rio Tinto mineral area in Spain, may have exacerbated the impact of the Antonine plague that devastated the Roman Empire from 165 to 180 CE. —Caroline Ash

Proc. Natl. Acad. Sci. U.S.A. (2025)
10.1073/pnas.2419630121

NEUROSCIENCE

Spatiotemporal dynamics in the fly brain

Neuropeptides and neurotransmitters work in concert to modulate neuronal activity, ultimately determining behavior. In *Drosophila*, the neuromodulator short neuropeptide F (sNPF) and the neurotransmitter acetylcholine (ACh) have been shown to be important for learning and memory. To investigate their spatiotemporal dynamics, Xia and Li developed a high-performance sensor for detecting sNPF in vivo in *Drosophila*. By expressing the new sensor together with an ACh sensor, the authors elucidated the dynamics of sNPF and ACh and the molecular mechanism mediating their release. The new tool provided valuable insights into the mechanisms mediating the spatiotemporal differences between neurotransmitter and neuromodulator release. —Mattia Maroso

Nat. Commun. (2025)
10.1038/s41467-025-56129-w

PHYSICS

Thinning bismuth

Elemental bismuth exhibits exotic properties such as superconductivity and nontrivial topological states. Past investigations have largely focused on bulk bismuth. Yu *et al.* used a recently developed variant of the mechanical exfoliation technique to make thin bismuth devices. The researchers performed systematic transport measurements in a large range of magnetic fields and temperatures. They found a nearly temperature-independent anomalous Hall resistance, consistent with an intrinsic origin associated with a nonzero Berry curvature. —Jelena Stajic

Phys. Rev. Lett. (2025)
10.1103/PhysRevLett.134.066603

POLITICAL SCIENCE

Differing perceptions of Latinos as "Americans"

To understand intergroup relations and their political implications, we must consider how people define groups. Using a conjoint survey experiment, Ocampo-Roland varied written and visual characteristics of hypothetical people to assess what factors influence white and Black Americans to consider members of the heterogeneous Latino population to be American. Across respondents, Latinos born in the US were considered less American if they had undocumented parents. Black Americans' responses, which were more open to undocumented immigrants, aligned with an economics-focused view. White Americans' views suggested more focus on cultural identity. —Brad Wible

Am. Polit. Sci. Rev. (2025)
10.1017/S000305542400131X

REVIEW SUMMARY

CATALYSIS

Hydrogenation of CO_2 for sustainable fuel and chemical production

Jingyun Ye, Nikolaos Dimitratos, Liane M. Rossi, Nils Thonemann, Andrew M. Beale, Robert Wojcieszak*

BACKGROUND: Carbon dioxide (CO_2) has become synonymous with climate change. Acting like a blanket in the atmosphere, it traps heat, causing a rise in global temperatures. This warming disrupts weather patterns, melts glaciers, and raises sea levels, posing a substantial threat to the planet. The primary culprit? The burning of fossil fuels such as coal, oil, and natural gas, which releases massive quantities of CO_2 into the air. But what if CO_2 was not just waste? Innovative technologies are emerging that aim to transform CO_2 into a valuable resource. These technologies focus on utilizing captured CO_2 as a feedstock for producing cleaner fuels and chemicals. One promising approach involves creating "green methanol." By combining captured CO_2 with hydrogen, methanol, a versatile fuel and chemical building block, can be synthesized. Methanol's story stretches back thousands of years, when the ancient Egyptians used it for embalming. A breakthrough in methanol synthesis arrived in the 1920s with the development of a zinc chromite catalyst. This paved the way for the introduction of Cu/Zn/Al_2O3 (CZA), a game-changing catalyst, in the 1940s, which became the industry standard. However, CZA catalysts have a drawback—they favor the reverse water-gas shift (RWGS) reaction over direct CO_2 conversion to methanol. This reduces the efficiency of CO_2 utilization in the process. In addition, a large contributor to catalyst deactivation is sintering, where the catalyst particles clump together, reducing their active surface area and hindering performance. Interestingly, a link between high activity and faster deactivation exist—catalysts with the highest initial activity (often containing the most copper) also deactivate most rapidly. The CZA life span ranges from 2 to 8 years, with a gradual decline in activity.

ADVANCES: Scientists are hunting for the most effective catalysts to convert CO_2 into useful fuels (methanol, or CH_3OH). Recently, indium oxide–based catalysts (In_2O_3) have garnered considerable interest. In research articles published between 2020 and 2024, most of the studied catalysts (85 out of 96) achieved selectivity to methanol above 50%. Most methanol catalysts work best at lower temperatures (below 300°C) and higher pressures (above 3 MPa), whereas most hydrocarbon catalysts perform better at higher temperatures (above 300°C) and lower pressures (below 3 MPa). A positive development is that reported methanol yields are still increasing. The present champion is a Cu/ZnO/MnO/KIT-6 catalyst, which operates at a moderate temperature (180°C) and efficiently converts CO_2 while producing a high yield of methanol. However, the fight against climate change goes beyond optimizing methanol production—it is about creating a sustainable future for all. CO_2 hydrogenation seems promising for reducing greenhouse gas emissions compared with traditional production methods, especially when powered by renewable energy sources such as wind power. However, it is not a simple picture. Trade-offs exist between different environmental impacts. For example, the source of the CO_2 and the specific conversion technology used can markedly affect the overall environmental footprint. CO_2 hydrogenation offers a clean-fuel solution (e-fuels) for hard-to-electrify sectors such as aviation and shipping. However, sustainability requires efficient water management and heat integration. Moreover, when considering the environmental impacts of the hydrogenation technologies, the major benefit in the "independence" of crude-oil carbon sources is its potential to substantially reduce greenhouse gas emissions.

OUTLOOK: Present catalysts such as CZA have limitations, including short life spans and reliance on critical elements. Research efforts should focus on designing new catalysts that promote direct CO_2 conversion to methanol while minimizing the RWGS reaction. Strategies to mitigate sintering and extend catalyst life span are crucial. This might involve exploring different catalyst supports or incorporating stabilizing elements into the catalyst structure. Understanding the relationship between activity, copper content, and deactivation is essential for developing catalysts that offer a balance between high initial performance and long-term stability. Alternatives such as Pd-In catalysts are presently being researched, but costs are a concern. Despite remaining challenges, advancements in catalyst design and characterization techniques are paving the way for a cleaner future fueled by CO_2 hydrogenation. Although CO_2 hydrogenation is attractive as a means of utilizing a readily available carbon source, its climate mitigation potential is less clear-cut. Net negativity can only be achieved when CO_2 comes from direct air capture, and considering all background emissions, net negativity might be difficult to achieve. However, for sectors that are hard to make sustainable, such as aviation, use of CO_2 might be an optimal option. ■

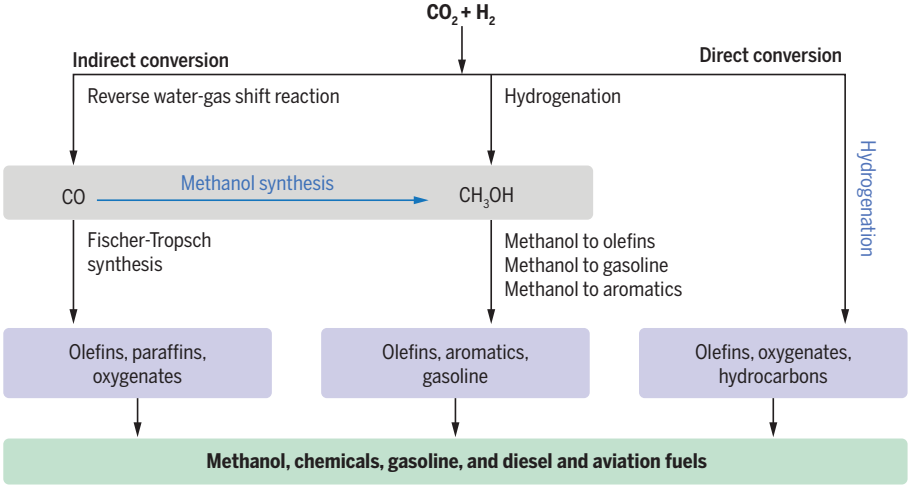

Reaction pathways in CO_2 thermal conversion. Several routes for CO_2 hydrogenation are possible depending on the nature of the catalyst. Methanol can be produced directly from CO_2 using, for example, CZA and indirectly, by passing through the RWGS reaction favored by the presence of non-noble metals such as Ni and Fe or metal carbides.

The list of author affiliations is available in the full article online.
*Corresponding author. Email: robert.wojcieszak@cnrs.fr
Cite this article as J. Ye *et al.*, *Science* **387**, eadn9388 (2025).
DOI: 10.1126/science.adn9388

READ THE FULL ARTICLE AT
https://doi.org/10.1126/science.adn9388

RESEARCH ARTICLE SUMMARY

METABOLISM

Liver ALKBH5 regulates glucose and lipid homeostasis independently through GCGR and mTORC1 signaling

Kaixin Ding†, Zhipeng Zhang†, Zhengbin Han†, Lei Shi, Xinzhi Li, Yutong Liu, Zhenzhi Li, Chongchong Zhao, Yifeng Cui, Liying Zhou, Bolin Xu, Wenjing Zhou, Yikui Zhao, Zhiqiang Wang, He Huang, Liwei Xie, Xiao-wei Chen, Zheng Chen*

INTRODUCTION: The liver plays central roles in glucose and lipid homeostasis, which are essential for metabolic health. Disruptions in the liver's regulatory pathways lead to various metabolic disorders such as hyperglycemia, hyperlipidemia, and metabolic dysfunction–associated fatty liver disease (MAFLD), often associated with obesity and type 2 diabetes mellitus (T2DM). However, the molecular mechanisms underlying coordinated regulation of hepatic glucose and lipid homeostasis remain largely unknown.

RATIONALE: RNA-binding proteins (RBPs) are a diverse group of proteins that interact with both double- and single-stranded RNA in cells, playing crucial roles in various RNA processing activities, including RNA capping, polyadenylation, modification, splicing, stabilization, localization, and translation. Some RBPs are vital for sustaining life processes. Growing evidence indicates that certain RBPs regulate glucose or lipid homeostasis in response to metabolic signals and stimuli, and their dysregulation contributes to the development of metabolic diseases. However, it remains unclear whether RBPs integratively regulate glucose and lipid homeostasis. We hypothesized that specific metabolism-related RBPs may coordinately regulate hepatic glucose and lipid homeostasis.

RESULTS: Alkylation repair homolog protein 5 (ALKBH5) has been identified as a metabolism-related RBP through comprehensive quantitative proteomic and phosphoproteomic analyses. ALKBH5 is up-regulated in the liver during obesity. It undergoes phosphorylation at Ser^{362} by protein kinase A, which results in its translocation from the nucleus to the cytosol. Mice with hepatocyte-specific *Alkbh5* knockout (HKO) or the S362A point mutation exhibit lower blood glucose levels and are protected against high-fat diet (HFD)–induced hyperglycemia and glucose intolerance by inhibiting glucagon receptor (GCGR) signaling. Hepatocyte-specific deletion of *Alkbh5* also mitigates HFD-induced MAFLD and hyperlipidemia by suppressing epidermal growth factor receptor (EGFR)–phosphatidylinositol 3-kinase (PI3K)–AKT–mammalian target of rapamycin complex 1 (mTORC1) signaling. Restoration of GCGR expression in *Alkbh5*-HKO livers negates the improvements in glucose homeostasis, but does not affect lipid-related phenotypes. Similarly, restoring EGFR expression in *Alkbh5*-HKO livers counteracts the suppression of EGFR-PI3K-AKT-mTORC1 signaling, leading to increased liver triglycerides (TAG), serum TAG, total cholesterol (TC) levels, and serum ALT activity, without affecting glucose-related phenotypes. Mechanistically, ALKBH5 regulates GCGR signaling through its demethylase activity while also enhancing EGFR-PI3K-AKT-mTORC1 signaling independently of this activity by directly interacting with the intronic enhancer of *Egfr* to increase its expression. Two specific loops of ALKBH5, Gln^{145}-Gly^{152} and Cys^{231}-Glu^{242}, are critical for this interaction, promoting EGFR-PI3K-mTORC1–driven MAFLD and hyperlipidemia by up-regulating *Egfr* transcription. However, these loops are not required for glucose homeostasis in *Alkbh5*-HKO mice. Therapeutically, targeted knockdown of hepatic *Alkbh5* using either GalNAc-siAlkbh5 or AAV-shAlkbh5 reverses T2DM and MAFLD in the db/db diabetic mouse model, highlighting its therapeutic potential.

CONCLUSION: This study demonstrates that ALKBH5 is up-regulated during obesity and regulates glucose and lipid homeostasis through distinct pathways. Hepatocyte-specific deletion of *Alkbh5* improves glucose tolerance and mitigates MAFLD in obesity by inhibiting GCGR–cyclic adenosine monophosphate (cAMP) and EGFR-PI3K-AKT-mTORC1 signaling. Although the demethylase activity of ALKBH5 is essential for glucose homeostasis, its interaction with the *Egfr* enhancer enhances lipogenesis independently of its demethylase activity. Targeted knockdown of *Alkbh5* reverses T2DM and MAFLD in diabetic mice, underscoring its therapeutic potential. ■

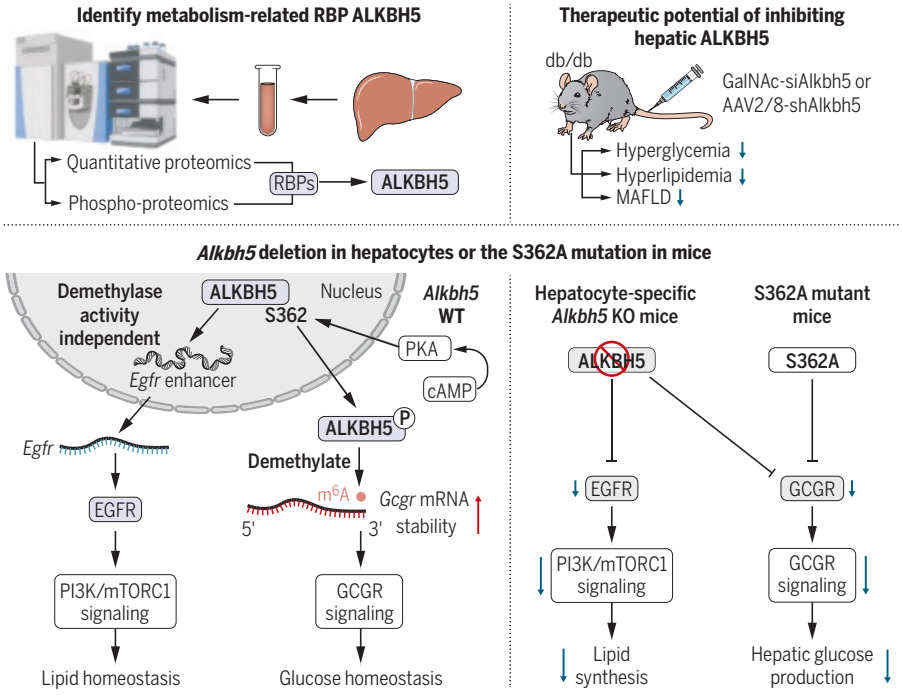

Hepatic ALKBH5 regulates glucose and lipid homeostasis. ALKBH5 regulates glucose homeostasis through GCGR signaling in a process dependent on its demethylase activity and Ser^{362} phosphorylation. By contrast, it modulates lipid homeostasis through EGFR-mTORC1 signaling independently of its demethylase activity using its two structural loops. Hepatocyte-specific deletion of *Alkbh5* improves glucose tolerance and alleviates MAFLD in obesity by independently inhibiting GCGR and EGFR-mTORC1 signaling through distinct mechanisms. [Figure created with BioRender.com]

The list of author affiliations is available in the full article online.
*Corresponding author. Email: chenzheng@hit.edu.cn
†These authors contributed equally to this work.
Cite this article as K. Ding *et al.*, *Science* 387, eadp4120 (2025). DOI: 10.1126/science.adp4120

READ THE FULL ARTICLE AT
https://doi.org/10.1126/science.adp4120

RESEARCH ARTICLE SUMMARY

MULTIPLE SCLEROSIS

4D marmoset brain map reveals MRI and molecular signatures for onset of multiple sclerosis–like lesions

Jing-Ping Lin*, Alexis Brake, Maxime Donadieu, Amanda Lee, Ginger Smith, Kevin Hu, Govind Nair, Riki Kawaguchi, Pascal Sati, Daniel H. Geschwind, Steven Jacobson, Dorothy P. Schafer, Daniel S. Reich*

INTRODUCTION: Multiple sclerosis (MS) is a complex disease characterized by focal inflammation, myelin loss in the central nervous system, and eventual neurodegeneration. The precise cause of MS remains unclear, but the disease involves an inappropriate immune response and subsequent failure to repair myelin. Although MS therapies have been effective in controlling peripheral inflammation, understanding the cellular dynamics of lesion progression during early phases is crucial for developing treatments that promote timely remyelination and repair.

RATIONALE: Current understanding of MS pathology is largely derived from postmortem human tissue studies or rare brain biopsies, which capture disease at a single, often late, time point. To address this limitation, we used a clinically relevant model, the common marmoset (*Callithrix jacchus*) with experimental autoimmune encephalomyelitis (EAE), to study MS-like lesions. This model closely mimics MS lesion development and evolution, offering insights that are transferable to the clinical setting. Although structural magnetic resonance imaging (MRI) is noninvasive and effective for monitoring lesion changes, it lacks the specificity required to reveal the cellular and molecular diversity within lesions. Therefore, we integrated longitudinal MRI, histopathology, spatial transcriptomics, and single-nucleus RNA profiling to examine the signaling profiles involved in lesion development and resolution.

RESULTS: We identified five microenvironment (ME) groups—related to neural function, immune and glial responses, tissue destruction and repair, and regulatory networks at brain borders—that emerged during lesion evolution. Before visible demyelination, astrocytic and ependymal secretory signals marked perivascular and periventricular regions, which later became demyelination hotspots. We identified an MRI biomarker, the ratio of proton density–weighted signal to T_1 relaxation time, which was sensitive to the hypercellularity phase preceding myelin destruction. At lesion onset, we observed a global shift in cellular connectivity, particularly in extracellular matrix–mediated signaling. Early responses involved the proliferation and diversification of microglia and oligodendrocyte precursor cells (OPC). As lesions developed, EAE-associated glia were replaced by monocyte derivatives at the lesion center, with persistent lymphocytes seen in aged lesions. Concurrently with demyelination, reparative signaling modules appeared at the lesion edge as early as 10 days after lesion establishment. We also noted an overrepresentation of genes involved in the senescence-associated secretory phenotype (SASP) at the brain borders and the formation of concentric glial barriers at the lesion edge, prompting perturbation analysis to contextualize EAE-associated changes and identify potential therapeutics to protect tissue and enhance repair.

CONCLUSION: We identified a SERPINE1$^+$ astrocytic subtype, acting as a secretory hub at the perivascular and periventricular zones, which underlies the onset of lesions in both marmoset EAE and MS. Our work offers a spatiotemporally resolved molecular map as a resource to benefit MS research and to guide identification of candidates for therapeutic intervention. ■

The list of author affiliations is available in the full article online.
*Corresponding author. Email: jing-ping.lin@nih.gov (J.-P.L.); daniel.reich@nih.gov (D.S.R.)
Cite this article as J.-P. Lin *et al.*, *Science* **387**, eadp6325 (2025). DOI: 10.1126/science.adp6325

READ THE FULL ARTICLE AT
https://doi.org/10.1126/science.adp6325

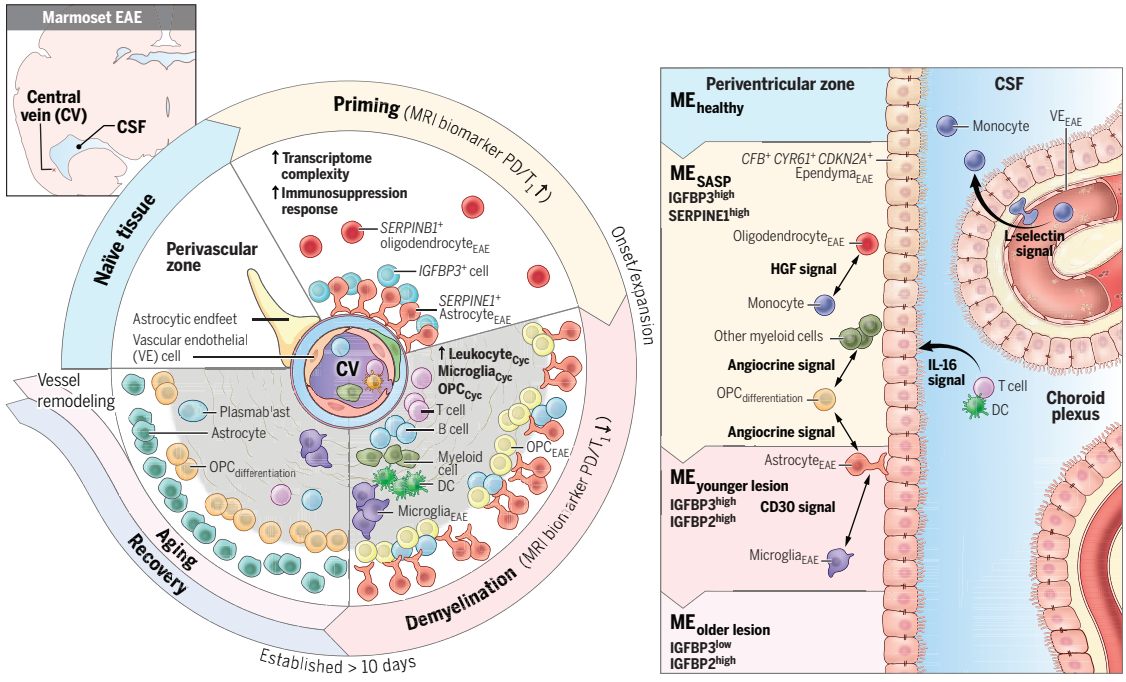

Dynamics of cells and microenvironments in perivascular and periventricular zones. MS-like lesions form and expand near central veins and ventricles, enriched with SASP markers. Molecular and MRI biomarkers spatiotemporally define lesion stages. As lesions evolve, EAE-related (astrocyte$_{EAE}$, oligodendrocyte$_{EAE}$, OPC$_{EAE}$, microglia$_{EAE}$, ependyma$_{EAE}$, and VE$_{EAE}$), proliferative (leukocyte$_{Cyc}$, microglia$_{Cyc}$, and OPC$_{Cyc}$), and myelin-repairing (OPC$_{differentiation}$) cells dominate specific lesion zones, with SERPINE1$^+$ astrocyte$_{EAE}$ acting as a signaling hub at lesion edges during microenvironment transitions. Cyc, cycling; CSF, cerebrospinal fluid; DC, dendritic cell.

RESEARCH ARTICLE SUMMARY

PHYLOGENETICS

CASTER: Direct species tree inference from whole-genome alignments

Chao Zhang, Rasmus Nielsen, Siavash Mirarab*

INTRODUCTION: With the rapid availability of new genomes, phylogenetics has gained an opportunity to infer not only more accurate species-level relationships (species trees) but also the heterogeneity of evolution across the genome (gene trees). However, available methods are lacking. The dominant approach, concatenating all genomic loci, fails to account for discordance across the genome, leading to statistical bias. An alternative widely used approach infers gene trees from individual loci and then combines them. However, this two-step approach struggles with defining loci that are both short enough to avoid recombination and long enough to prevent high error rates per tree. Bayesian methods that coinfer gene trees and species trees exist but are not scalable. Another promising approach has been inferring the tree from all sites while accounting for discordance, but these site-based methods have shown limited scalability and accuracy. As a result of these limitations, genome-wide analyses are forced to sample loci instead of using the entire genome as input.

RATIONALE: We developed a site-based method called Coalescence-Aware Alignment-Based Species Tree Estimator (CASTER) to enable truly genome-wide phylogenomic analyses. CASTER is based on the idea that each site in the alignment can "vote" for or against each tree topology for four species (a quartet), with the tree receiving the maximum total vote across sites and quartets winning. CASTER has four key features: (i) It provides theoretical statistical guarantees under the multispecies coalescent model of incomplete lineage sorting, coupled with several sequence evolution models, without requiring costly likelihood calculations. (ii) It is extremely scalable (linear in the number of sites and roughly quadratic in the number of species), allowing for the analysis of entire mammalian genomes (1.8 billion sites) across 241 species in 30 hours using 512 GB of memory. (iii) It eliminates the need for arbitrary locus delineation. (iv) It produces a score for each genomic position that, when summarized across windows, reveals changes in evolutionary histories across the genome. CASTER can handle simpler nucleotide models by using patterns of sites (CASTER-site) or more complex models by using pairs of sites (CASTER-pair).

RESULTS: Comparing CASTER to several alternative methods representing the current best approaches, we demonstrated through simulations that CASTER outperforms these methods in terms of scalability and is the most accurate under most conditions tested. Our simulations included a range of realistic biological processes, including recombination, which is often missing from previous studies, and incomplete lineage sorting. CASTER-site and CASTER-pair handled 2 billion and 500 million sites, respectively, given only 64 cores, 256 GB of memory, and up to two days of running time. CASTER scores correlate well with the amount of gene tree discordance, and its estimates of statistical uncertainty are accurate. On mammalian and avian genome-wide datasets, we demonstrate that CASTER can analyze the entirety of the data, generate accurate trees, and produce scores that reveal heterogeneities across the genome. Deviations in CASTER scores from our expectations indicated errors in input alignments, instances of rapid radiation among species, and cases where evolution appears reticulate.

CONCLUSION: CASTER enables phylogenetic analyses that include all the sites in a genome, modeling the heterogeneity of rates and topologies across the genome. It requires no demarcation of loci and provides interpretable outputs that help biologists understand not only the species relationships but also the mosaic of evolutionary histories across the genome. ■

The list of author affiliations is available in the full article online.
*Corresponding author. Email: smirarab@ucsd.edu
Cite this article as C. Zhang *et al.*, *Science* **387**, eadk9688 (2025). DOI: 10.1126/science.adk9688

READ THE FULL ARTICLE AT
https://doi.org/10.1126/science.adk9688

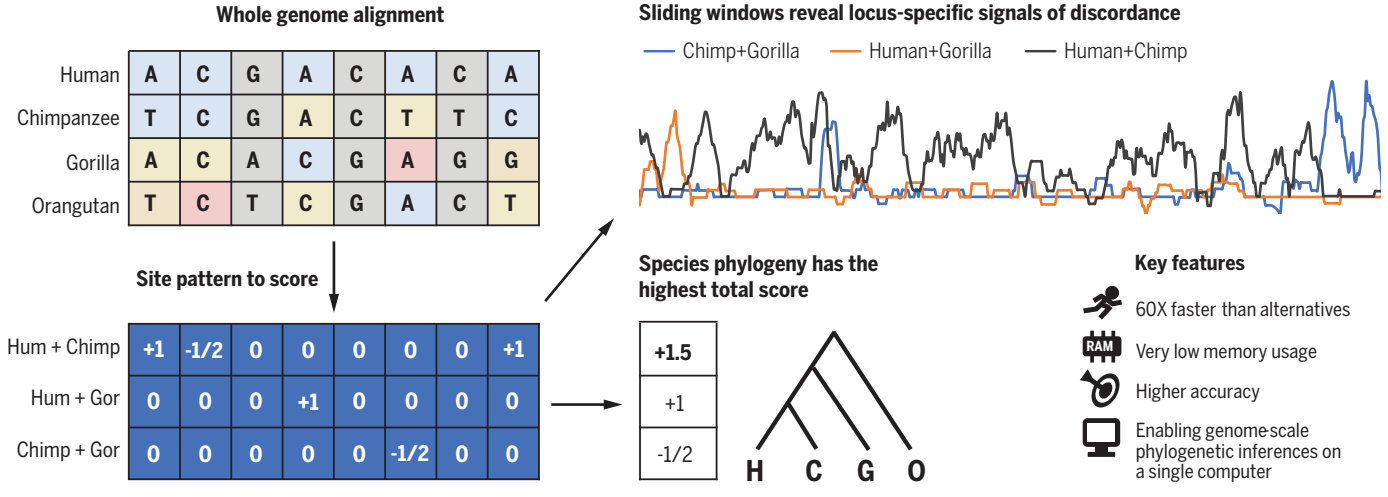

Overview of CASTER. CASTER assigns a score to each site in the input alignment for any tree topology on any selection of four species (quartet). The tree topology with the highest score across the entire input and all quartets is chosen. Sliding windows of CASTER scores across sites can reveal locus-specific signals of discordance. CASTER is scalable and accurate.

RESEARCH ARTICLE SUMMARY

GLACIAL CYCLES

Distinct roles for precession, obliquity, and eccentricity in Pleistocene 100-kyr glacial cycles

Stephen Barker*, Lorraine E. Lisiecki, Gregor Knorr, Sophie Nuber, Polychronis C. Tzedakis

INTRODUCTION: Milankovitch theory suggests that the waxing and waning of enormous continental ice sheets across the Northern Hemisphere results from slight changes in axial tilt and the geometry of Earth's orbit around the Sun, which influence the seasonal and geographical distribution of incoming sunlight. Changes in the tilt of Earth's rotational axis with respect to the orbital plane (obliquity) cause variations in seasonality, with a period of ~41 thousand years (kyr), and strongly affect the total (integrated) summer energy received at high latitudes. Precession of the rotational axis (and of the orbit itself) causes variations in the timing of the solstice with respect to the Earth-Sun distance, with a period of ~21 kyr. Precession has most influence over peak summer intensity across mid- to high latitudes. The shape of Earth's orbit (eccentricity) also varies from more to less circular, with a period of ~100 kyr (and ~400 kyr). Eccentricity has most influence on the amplitude of precession.

RATIONALE: Milankovitch developed his theory in the early 20th century, but it remained unproven until Hays, Imbrie, and Shackleton presented the first robust geological evidence to support it in 1976. Identification of the characteristic periods of precession and obliquity within a range of paleoclimate records confirmed that both parameters must play some part in the pacing of Pleistocene glacial cycles, but their precise roles remained obscure. Moreover, observation of a strong ~100-kyr periodicity was difficult to reconcile with the very weak direct influence of eccentricity. Since then, there have been many attempts to differentiate between the relative importance of precession versus obliquity, especially in the process of glacial termination (deglaciation). The biggest obstacle facing such an exercise is the difficulty in producing absolute ages for paleorecords with sufficient precision to differentiate between the direct influence of either parameter. We took an alternative approach that circumvents the need for such precision; we looked at the morphology of deglaciation-inception and compared that with orbital phasing.

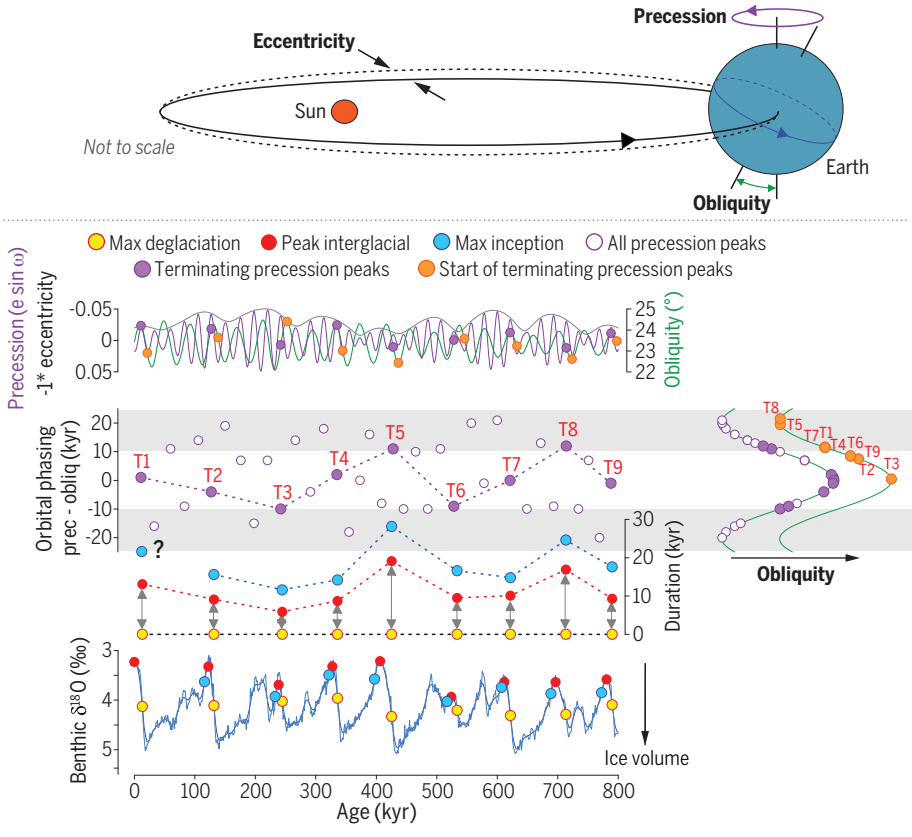

Morphology of glacial cycles reflects Earth's orbital geometry. Variations in interglacial duration are dominated by the deglacial phase (double-headed gray arrows), which is a function of the phasing between precession and obliquity. Glacial termination begins with the first precession peak to start while obliquity is rising, after a minimum in eccentricity. Glacial inception then follows with the next decrease in obliquity. ‰, per mil; T1, Termination 1.

RESULTS: We found a strong correlation between deglacial duration and the phasing of precession versus obliquity during termination, with the onset of deglaciation most likely driven by peak summer intensification (i.e., precession) in combination with rising obliquity, whereas obliquity alone is responsible for glacial inception. Our results can be explained by variations in the average latitude of northern ice sheets, with inception occurring at high latitudes under the influence of obliquity, and deglaciation reflecting the dual effects of precession and obliquity across fully extended glacial ice sheets. A protracted deglaciation occurs when the responsible change in precession starts early with respect to the phase of obliquity, effectively delaying the northward retreat of ice sheets toward their interglacial state. Finally, we found that the precession peaks leading to termination (which always coincide with increasing obliquity) follow directly after minima in eccentricity. This is consistent with suggestions that decreasing eccentricity can enable the growth of large ice sheets by reducing the amplitude of precession.

CONCLUSION: Our results suggest that ~100-kyr glacial cycles of the mid- to late Pleistocene are largely deterministic, allowing us to predict the occurrence and duration of all deglacial and interglacial periods over the past 900 kyr on the basis of orbital phasing alone. This permits us to make first-order estimates about the natural future of Earth's climate in the hypothetical absence of CO_2 forcing resulting from human activities. ■

The list of author affiliations is available in the full article online.
*Corresponding author. Email: barkers3@cf.ac.uk
Cite this article as S. Barker *et al.*, *Science* **387**, eadp3491 (2025). DOI: 10.1126/science.adp3491

READ THE FULL ARTICLE AT
https://doi.org/10.1126/science.adp3491

RESEARCH ARTICLE SUMMARY

PLANT PATHOLOGY

A widespread plant defense compound disarms bacterial type III injectisome assembly

Pei Miao†, Haijun Wang†, Wei Wang†, Zhengdong Wang, Han Ke, Hangyuan Cheng, Jinjing Ni, Jingnan Liang, Yu-Feng Yao, Jizong Wang, Jian-Min Zhou*, Xiaoguang Lei*

INTRODUCTION: Plants employ immune receptors to perceive pathogen-associated molecular patterns (PAMPs) to trigger immune signaling. How plants impede pathogen progression following successful signal transduction, however, has remained largely elusive. Plants produce diverse secondary metabolites, called phytoalexins, in response to pathogen infections. Various phytoalexins show strong lineage specificity and are believed to act upon microbes by growth inhibition or toxicity. Whether any phytoalexins protect plants by targeting specialized virulence machinery of pathogens has not been well studied. For instance, numerous gram-negative bacterial pathogens employ the type III secretion system (T3SS), a multiprotein injectisome, to deliver virulence proteins into animal and plant host cells for pathogenesis. Immune-activated plants are known to possess activity that inhibits the bacterial T3SS, although the nature of this activity and underlying mechanism remain unknown. This immune-induced anti-T3SS activity serves as a model to investigate potential antivirulence phytoalexins in plants.

RATIONALE: We hypothesized that immune-activated plants accumulate metabolite(s) that inhibit bacterial T3SS. Such knowledge will not only add a new dimension to our understanding of the plant immune system but also shed light on the future development of biopesticides. We set out to identify plant metabolite(s) that could inhibit bacterial T3SS in vitro, determine the biological importance of such metabolite(s), and elucidate the mechanism underlying T3SS inhibition.

RESULTS: We found that crude extracts of *Arabidopsis* leaves inhibit *Pseudomonas syringae* effectors secretion through T3SS. Activity-guided purification identified erucamide as a broad-spectrum inhibitor against T3SS secretion of diverse bacterial pathogens of plants and animals. We found that erucamide is a lineage-nonspecific phytoalexin of both dicot and monocot plant species, induced by PAMPs and suppressed by virulent *P. syringae* DC3000. At physiological concentrations equivalent to those determined in immune-activated *Arabidopsis* plants, exogenously applied erucamide strongly protected plants against DC3000. Pathway analysis indicated that 3-ketoacyl-CoA synthases (KCSs) are required for erucamide synthesis and fatty acid amide hydroxylase (FAAH) could degrade erucamide in *Arabidopsis*. *Arabidopsis kcs* mutants and *FAAH*-OE lines were significantly impaired in the immune-induced accumulation of erucamide, and these plants were severely compromised in antibacterial immunity normally induced by PAMPs. Exogenous application of erucamide to these plants restored their antibacterial immunity. Conversely, *faah* mutants accumulated more erucamide and exhibited significantly enhanced antibacterial immunity. Profiling of *P. syringae* proteins identified HrcC, an outer membrane ring structure protein that is essential for injectisome assembly, as a target of erucamide. AlphaFold prediction, molecular docking, molecular dynamics simulation, and site-directed mutagenesis identified an erucamide-binding pocket composed of five amino acid residues highly conserved in the HrcC of diverse bacterial species. We additionally identified a mutation in HrcC that abolished erucamide binding and rendered the bacterium insensitive to erucamide, regarding T3SS secretion and virulence on plants with varying levels of erucamide accumulation. Furthermore, structure-activity analyses of erucamide analogues showed that the amide group, position of the double bond, and alkyl chain length play crucial roles in the T3SS-inhibitory activity. Unlike erucamide, analogues that do not inhibit T3SS neither bind HrcC nor protect plants from virulent bacteria.

CONCLUSION: We identify erucamide as an ancient, broad-spectrum, antivirulence phytoalexin that selectively disarms the T3SS injectisome of diverse bacterial pathogens. Our results suggest that erucamide binds a pocket composed of invariant residues essential for injectisome function. The elucidation of enzymes involved in the biosynthesis and degradation of erucamide may help engineer crop plants with increased immunity against various bacterial pathogens. The information about the structure-activity relationship of erucamide analogues may shed light on the future development of eco-friendly antibacterial pesticides. Our work additionally uncovers a contest between erucamide accumulation in *Arabidopsis* and effector secretion by *P. syringae*. Although successful induction of erucamide can prevent bacterial T3SS secretion, the rapid secretion of bacterial effectors can dampen erucamide accumulation in plants. The speed of these two processes may be crucial for the disease resistance/susceptibility outcomes of plant-bacterial interactions. ■

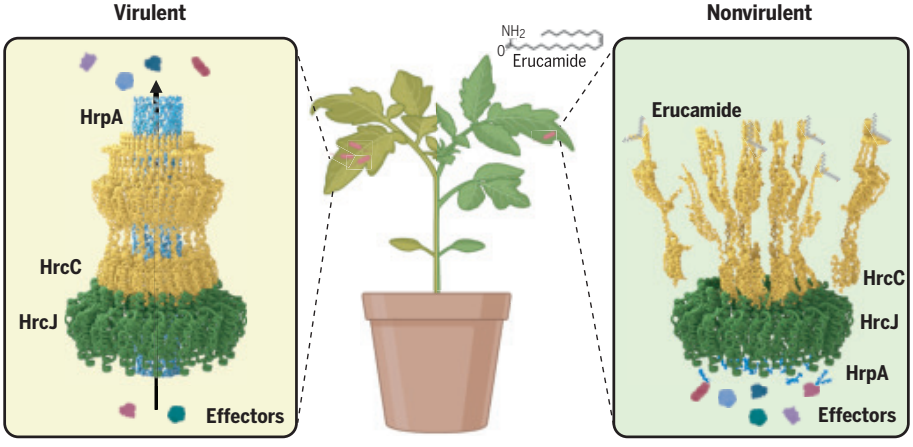

Working model of erucamide-mediated defense. Erucamide directly binds HrcC, a ring-structure protein shared by numerous bacteria, to disrupt the assembly of the T3SS injectisome, thereby inhibiting the virulence of pathogenic bacteria. [Image created using BioRender]

The list of author affiliations is available in the full article online.
*Corresponding author. Email: xglei@pku.edu.cn (X.L.); jmzhou@genetics.ac.cn (J.-M.Z)
†These authors contributed equally to the work.
Cite this article as P. Miao *et al.*, *Science* **387**, eads0377 (2025). DOI: 10.1126/science.ads0377

READ THE FULL ARTICLE AT
https://doi.org/10.1126/science.ads0377

RESEARCH ARTICLES

ELECTRON MICROSCOPY

Visualizing nanoparticle surface dynamics and instabilities enabled by deep denoising

Peter A. Crozier[1]*, Matan Leibovich[2], Piyush Haluai[1], Mai Tan[1], Andrew M. Thomas[3], Joshua Vincent[1], Sreyas Mohan[4], Adria Marcos Morales[4], Shreyas A. Kulkarni[4], David S. Matteson[5], Yifan Wang[1], Carlos Fernandez-Granda[2,4]*

Materials functionalities may be associated with atomic-level structural dynamics occurring on the millisecond timescale. However, the capability of electron microscopy to image structures with high spatial resolution and millisecond temporal resolution is often limited by poor signal-to-noise ratios. With an unsupervised deep denoising framework, we observed metal nanoparticle surfaces (platinum nanoparticles on cerium oxide) in a gas environment with time resolutions down to 10 milliseconds at a moderate electron dose. On this timescale, many nanoparticle surfaces continuously transition between ordered and disordered configurations. Stress fields can penetrate below the surface, leading to defect formation and destabilization, thus making the nanoparticle fluxional. Combining this unsupervised denoiser with in situ electron microscopy greatly improves spatiotemporal characterization, opening a new window for the exploration of atomic-level structural dynamics in materials.

Nanoparticle surface structural dynamics, sometimes referred to as fluxionality, may play an important role in regulating functionalities such as diffusion, reactivity, and catalysis, but the atomic-level processes are not well understood (*1*). The importance of atomic-level structural dynamics is well established for protein functionality but has been less discussed in materials (*2*). Recent works have shown that surface fluxionality may be directly correlated with catalytic functionality (*3*, *4*). For example, fluxional effects at the atomic level were found to be correlated with CO oxidation activity in a Pt on a CeO_2 catalyst, but the spatiotemporal details were obscured by poor signal-to-noise ratios (SNRs) (*3*). Atom dynamics consist of different types of motions ranging from very fast vibrations to slower migrations. If we could locally characterize atom migration (which depends on temperature) on millisecond timescales, this would deepen our understanding of functionalities. For example, in heterogeneous catalysis, reaction rates per active site are typically in the range of 1 to 100/s and may be associated with the formation of short-lived metastable surface structures that exist on the tens of milliseconds timescale. However, atomic resolution characterization of nanoparticle surface dynamics is challenging because it requires both high spatial and temporal resolution. Ultrafast transmission electron microscopy (TEM) can achieve picosecond temporal resolution but is limited to nanometer spatial resolution (*5*–*7*). Fortunately, the high readout rates of new electron detectors could allow conventional TEM to visualize atomic structures on a millisecond timescale. Unfortunately, the need to reduce electron beam damage to the sample makes it necessary to limit the electron dose rates, yielding millisecond images that are dominated by noise, which obscures the structural details. Here, we show that a newly developed unsupervised denoising framework based on deep learning enables observations of metal nanoparticle surfaces in a gas environment with time resolutions down to 10 ms at a moderate electron dose. On this timescale, we find that many nanoparticle surfaces continuously transition between ordered and disordered configurations. The associated stress fields can penetrate below the surface, which leads to defect formation and destabilization and makes the entire nanoparticle fluxional.

The concept of fluxionality, in which a system rapidly moves through different isomers, was first discussed for organometallic molecules in the 1950s, as summarized by Cotton (*8*). In the early days of nanoscience, there was interest in fluxional behavior of nanoparticles due in part to observations performed on the newly developed atomic-resolution electron microscopes (*9*). However, older, less-sensitive electron detector technology limited temporal resolutions to ~100 ms and required large electron dose rates (>10^4 e Å^2 s^{-1}). The desire to understand structure and functionality in catalytic nanoparticles has driven the continued development of gas and liquid cell TEM (*10*–*13*). However, to limit beam damage, the timescale for much of the reported atomic structural dynamics is often minutes (*14*, *15*). Recently, time resolutions on the order of 10 ms have been reported, but they used high electron dose rates (≥10^4 e$^-$ Å^{-2} s^{-1}) (*16*, *17*). Here, we used the power of machine learning to reduce the electron dose rate by at least an order of magnitude (~10^3 e$^-$ Å^{-2} s^{-1}) while achieving temporal resolutions of ~10 ms and spatial resolutions of 1 Å. This enabled us to explore the challenging issue of surface dynamics in metal particles.

To address the image noise challenge, we propose a denoising framework based on artificial intelligence (AI), which enables the recovery of atomic-resolution information from noisy images. AI models based on neural networks have achieved impressive results for natural images but often require training datasets with ground-truth clean images (*18*, *19*). Simulating such datasets is challenging; in fact, it is often impossible when the goal of denoising is scientific discovery. We propose a fully unsupervised framework to train and evaluate AI-powered denoising models using exclusively real noisy data (*20*). The framework enabled recovery of atomic-resolution information from TEM data, improving the SNR by a factor of almost 40 at a spatial resolution of 1 Å and time resolution near 10 ms. This enhanced time resolution revealed that supposedly stable, low-energy nanoparticle surfaces can display highly active atom dynamics, triggering instabilities that result in rapid structural fluctuations. The spatiotemporal capability enabled by the proposed AI framework substantially enhances our ability to explore surface dynamics and the evolution of metastable states in nanoparticles at the atomic level, offering insights into their evolving structures.

Data collection and noise processing

For this investigation, we explored the structural dynamics of Pt particles supported on CeO_2 in a CO environment at room temperature. CO interacts strongly with Pt surfaces, with a binding energy of ~1.5 eV and a migration energy of ~0.02 eV (*21*, *22*). The CO surface coverage exceeds 50% even at the modest pressures of 10^{-4} to 10^{-2} Torr used in the current experiment (*23*). To investigate the dynamics, we recorded movies from a Pt/CeO_2 sample with an electron dose rate of 2000 e$^-$ Å^{-2} s^{-1} and a readout rate of 75 frames/s (see movies S1 and S4 in the supplementary materials, section 8), corresponding to a single frame exposure time of 13 ms (individual frames had an electron dose of 26 e$^-$ Å^{-2} s^{-1} and the dose per pixel was 0.2 e$^-$). Each movie was composed of ~1000 to 2000 frames (3500 × 3500 pixels in size) with an SNR (measured in the vacuum) of ~0.45,

[1]Materials Science and Engineering, School for Engineering of Matter, Transport & Energy, Arizona State University, Tempe, AZ, USA. [2]Courant Institute of Mathematical Sciences, New York University, New York, NY, USA. [3]Department of Statistics & Actuarial Science, University of Iowa, Iowa City, IA, USA. [4]Center for Data Science, New York University, New York, NY, USA. [5]Department of Statistics & Data Science, Cornell University, Ithaca, NY, USA.
*Corresponding author. Email: crozier@asu.edu (P.A.C.); cfgranda@cims.nyu.edu (C.F.-G.)

which obscured much of the surface structure in the raw data and made it impossible to observe the underlying dynamics (see the supplementary materials, section 2, for more details).

To process the low-SNR data, we leverage a deep-learning model trained and evaluated exclusively on the same real noisy data. The model is based on recently developed unsupervised deep video denoiser (UDVD), (*20*, *24*) trained to estimate each noisy pixel value using the surrounding spatiotemporal neighborhood but without considering the noisy pixel itself (Fig. 1A). This blind-spot structure, which was enforced through a specialized architectural design, was critical because it prevented the model from learning to trivially map the input to the output directly. Instead, the denoiser learned to estimate the underlying clean image structure without overfitting the noise. Effective denoising occurs provided (i) each pixel in the clean image is correlated with if the surrounding pixels, which is the case if the spatial sampling is sufficiently high with respect to the features of interest (e.g., lattice fringes), and (ii) the noise is spatially and temporally uncorrelated (see the supplementary materials, section 41; see part 4 for an analysis of the spatiotemporal correlation in the noise). UDVD combined several convolutional neural networks with a UNet architecture to process multiple frames at the same time, which enabled it to exploit temporal patterns and multiscale structure (see the supplementary materials, section 1 for additional details). The results achieved by the denoiser are shown in Fig. 1, B and C. After denoising, the atomic structure of the nanoparticles, including the surface, was clearly resolved, showcasing the advantage of unsupervised denoising for scientific discovery.

To evaluate the performance of UDVD, we applied a recently developed unsupervised evaluation metric: the unsupervised peak SNR (uPSNR) (*20*). This metric is computed by using held-out adjacent noisy frames combined with a correction term (Fig. 1, D and E) that yields an unbiased, consistent estimate of the true PSNR, under the assumption that the noise is independent across frames (this is approximately true, as shown in the supplementary materials, section 1). An additional qualitative evaluation of the denoised output

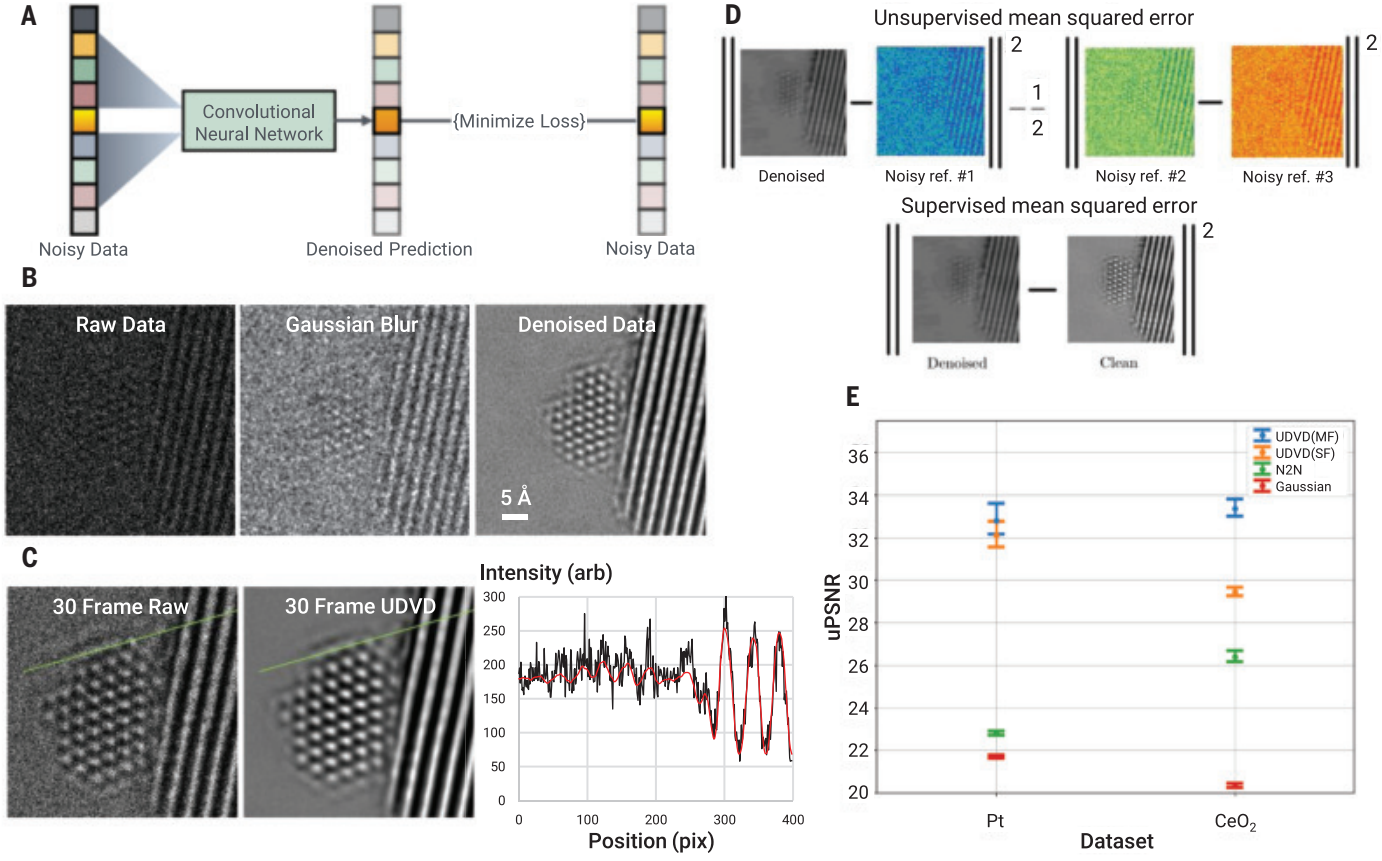

Fig. 1. Unsupervised deep denoising methodology. (**A**) The proposed UDVD learns to remove noise from noisy datasets without access to ground-truth clean images. A deep convolutional neural network is trained to estimate each noisy pixel from its spatiotemporal surrounding but without using the noisy pixel itself. Because the noisy component of the pixel is unpredictable, the network learns to estimate the underlying clean signal. (**B**) Example of denoising results showing the structure of the Pt nanoparticle in a CO atmosphere at room temperature. Left, raw data (13-ms exposure time). Right, same frame after UDVD denoising. Middle, raw frame after Gaussian blur filter for noise reduction. (**C**) Comparison of summed data and denoised data of the 30-frame sum. The surface structures look very similar. Intensity linescans along green lines in images is graphed on the right showing similar intensity variations for the denoised (red trace) and raw (black trace line) data. (see the supplementary materials, section 2). (**D**) To perform quantitative evaluation of unsupervised denoisers, we propose a metric called unsupervised mean squared error (uMSE), which is computed exclusively from noisy data. The uMSE was obtained by comparing the denoised image with an adjacent noisy frame and adding a correction term computed from two additional noisy frames (top row). If the signal content across the noisy frames is consistent and the noise is independent, the uMSE is an unbiased consistent estimator of the supervised MSE between the denoised image and the underlying clean signal (bottom row). (**E**) Comparison of the performance of a single-frame and multiframe version of UDVD against a traditional baseline based on Gaussian filtering (Gaussian) and an alternative unsupervised method known as Neighbor2Neighbor (*1*). The metric was the uPSNR, which equals the logarithm of the uMSE. UDVD achieved a statistically significant superior performance for two datasets containing CeO_2 and Pt nanoparticles. Section 1 of the supplementary materials provides additional details about the models and datasets.

was performed by comparing a temporal average of the raw and denoised data. Figure 1C shows that there is reasonable agreement between the two temporal averages. Further details on training and evaluation of the denoiser output from generating nanoparticle surface structure are provided in the supplementary materials, sections 1 and 2. Based on the vacuum region, the SNR in the UDVD output was ~16.5, which was improved by a factor of ~36 compared with the raw data. To achieve a similar improvement through counting statistics alone would require an increase in beam current or acquisition time by a factor of 1300. Increasing the beam current by such a large factor would destroy the material, whereas increasing the acquisition time by this factor would destroy the time resolution. This result demonstrates the power of the proposed denoising framework (for a more detailed discussion on the role of exposure time for detecting short-lived surface structures, see the supplementary materials, section 7).

Denoised imaging results

The denoiser revealed new dynamics on nanoparticle surfaces. A typical evolution of a 1.2-nm Pt nanoparticle surface supported on a (100) face of a CeO_2 during exposure to 10^{-4} Torr of CO at room temperature is shown in Fig. 2, A to F. The first image at t = 0 s shows the particle in a (110) zone axis with crystallographic terminations corresponding to (111) surfaces. The particle underwent rotation, and its evolved shape led to the formation of a (100) facet. The presence of (111) and (100) crystallographic facets corresponds to the low-energy Winterbottom shape for Pt nanoparticles (*25*). The electron beam will always influence observations in the electron microscope. In this case, section 3 of the supplementary materials addresses this issue and compares energy transfers from the electron beam and thermal processes for Pt surface migration. The calculations show that thermally activated Pt jumps are 10^6 times more likely than electron beam activated jumps, suggesting that the structural fluctuations are predominantly the result of thermal processes.

The high spatiotemporal resolution images revealed diffuse contrast that appeared to "float" above the crystallographic terminations. This component constantly changed in time and space, and a layered chimney structure (labeled in Fig. 2D) is a pronounced example in which despite the nanoparticle being in a zone axis orientation with clearly resolved atomic columns, the chimney structure did not show atomic column contrast (see movies S2 and S3 in the supplementary materials, section 8). This external surface layer was not an artifact of denoising and could also be seen (after suitable averaging) in the raw data (see the supplementary materials, section 4).

Even low-energy (111) facets often had diffuse layers present a substantial fraction of the time. An example from a different particle in which the diffuse surface layer transformed to an ordered bulk terminated-like (111) Pt surface is shown in Fig. 2, G and H. This transformation implied that the diffuse layer, which we call an adlayer, was primarily associated with Pt atoms, but the atoms were neither stationary nor in bulk terminated lattice sites. The electron scattering from CO is much smaller than that from Pt, so the contribution to the diffuse layer signal from CO is not apparent. Consideration of the image contrast suggests (see the supplementary materials, section 7) that similar numbers of atoms are present in rows C and D in Fig. 2, G and H). As shown by Fig. 2 and the associated images in the supplementary materials, section 4, and movies S2, S3, S5, S6, and S7 in the supplementary materials, section 8, the surface is constantly transforming between ordered crystallographic terminations and disordered adlayers on the nanoparticles studied here. Occasionally, the adlayer is associated with the nucleation or dissolution of a crystalline layer on the nanoparticle, whereas other times, an existing crystalline layer transforms to an adlayer and then back to a crystalline layer, as seen in Figs. 2 and 3.

Adlayers composed of diffusing atoms have been reported during thin film growth and the particle sintering that occurs through Ostwald ripening, but we are not aware that this phenomenon has been directly observed on nanoparticles. In Ostwald ripening of supported metal particles, adatoms diffuse on the metal surface, detach from the particles, and migrate across the support to join other larger particles (*26*). In the present case, the strong interaction with CO disrupted metal-metal surface bonds, which increased the likelihood that Pt atoms detached from lattice sites and migrated. Moreover, most nanoparticles would not have the correct number of atoms to form complete (111) and (100) layers to make the perfect Winterbottom shapes. This incomplete layer filling would increase the concentration of low-coordination Pt atoms at step edges and corners sites, which would make adatom detachment more facile. Once the atoms detached from crystal lattice sites, they would likely be highly mobile. For example, the migration energy of Pt on Pt(111) surface is ~0.3 eV, which could result in millions of jumps per second at room temperature (*27*) (see the supplementary materials, section 3).

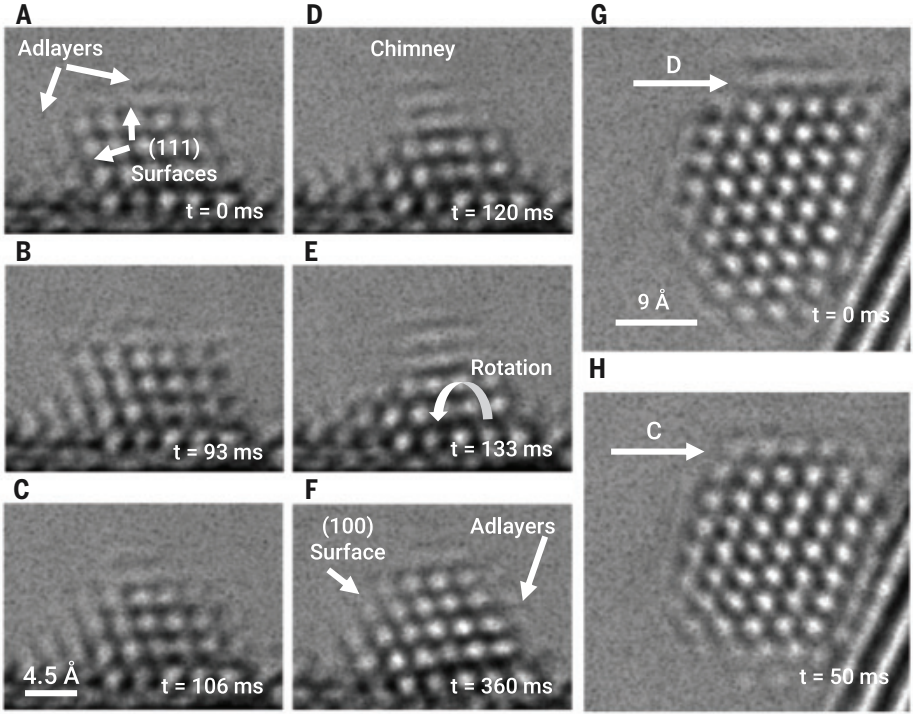

Fig. 2. Surface dynamics in Pt particles. (**A** to **F**) Variation in the surface of a 1.2-nm Pt particle in a CO atmosphere during a time period of 360 ms. The diffuse contrast at the surface of the nanoparticle are the dynamic adlayers of moving atoms. Rapid surface diffusion caused particle shape evolution, such as the formation of metastable chimney structures and (100) facets. (**G** and **H**) Two-nanometer particle showing a disordered fluxional adlayer (D) transforming into a (111) crystallographic termination (C).

Strain effects and fluxionality

The surface instabilities generate dynamic strain fields that penetrate below the surface and may trigger disruptions of subsurface

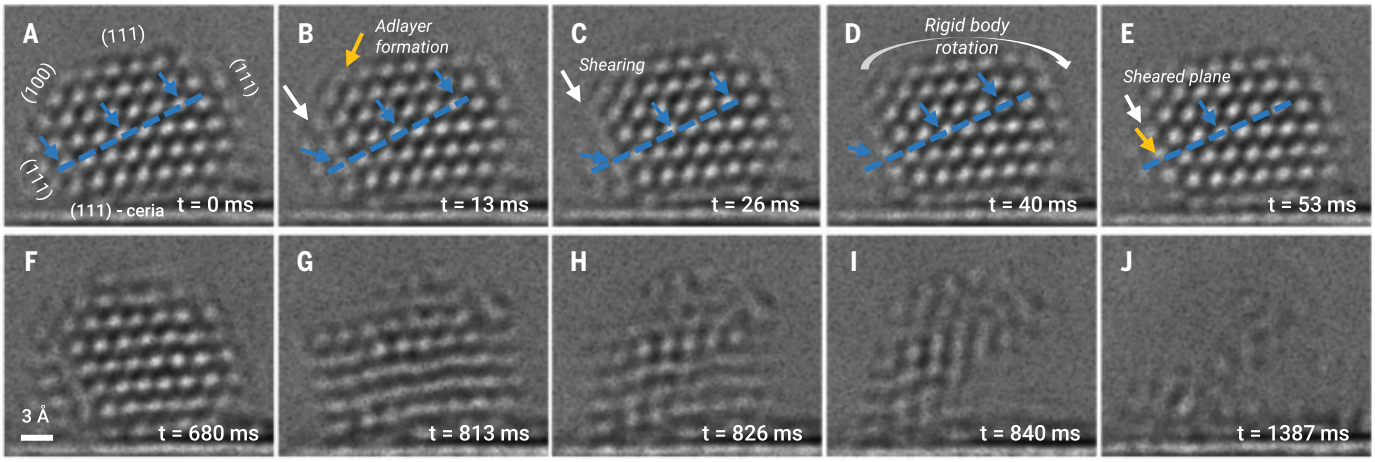

Fig. 3. Dynamics at subsurface sites and nanoparticle fluxionality. (**A** to **E**) Sequence of images of Pt nanoparticle showing the formation of a subsurface stacking fault. (A) Presheared state of the nanoparticle. Blue dotted line is perpendicular to a set of (111) planes, with the bulk showing usual ABCA stacking and blue arrows showing the location of the A layers. (B) The (111) plane (marked by white arrow) and (100) plane (marked by yellow arrow) showing streaking contrast demonstrating the onset of plane instability. (C) The (111) and (100) dynamic adlayer formation indicating that pronounced atomic motion occurred at rates beyond the frame exposure time of 13 ms. Rigid body rotation was also observed of the entire nanoparticle. (D and E) The (111) plane stabilizes in its new shifted position forming a stacking fault showing ABCB stacking (yellow arrow). The adlayers transformed back to crystallographic terminations. (**F** to **J**) Surface interface instabilities drove structural dynamics and the phase contrast images became highly fluxional. The entire particle was destabilized, which resulted in rapid changes in crystal orientation and structure.

layers. Figure 3 (and movie S5 in the supplementary materials, section 8) captures the occurrence of a crystallographic shearing event taking place on a plane just below the surface leading to the formation of a stacking fault. In this case, a (111) Pt plane slid laterally, causing the ideal face-centered cubic stacking sequence (Fig. 3A) to transform into a hexagonal close-packed surface domain (Fig. 3E and the supplementary materials, section 5). At the same time, the particle underwent a rigid body rotation of ~10° clockwise, which made the (111) Pt plane parallel to the (111) surface of the CeO_2.

The temporal evolution shows that the system passed through a transition state lasting ~13 ms (Fig. 3C), during which time the entire (111) plane showed streaked contrast characteristic of structural disorder or motion. Simultaneously, the adjacent surface layers on the left and upper left side of the particle showed adlayer contrast. This observation demonstrated that instabilities associated with surface adlayers could destabilize the crystal structure below the surface.

The adlayers renucleated into ordered crystallographic terminations as the stacking fault was created (Fig. 3, D and E) and the structure stabilized. The stabilization associated with stacking fault formation was short lived, and the particle underwent a reverse shear 600 ms later. The surface and subsurface layers then became very dynamic, which led to the entire particle becoming fluxional, manifesting as rapid changes in atomic structure, particle shape, and orientation (Fig. 3, F to J; movie S5 in the supplementary materials, section 8; and discussion in the supplementary materials, section 4). The structure present in Fig. 3J was not easy to determine. The raw data (see movie S4 raw) showed very low contrast with a sparse, rapidly changing phase contrast speckle indicative of rapid changes occurring. The denoiser picked out the stronger features of the speckle pattern, but these did not correspond to atomic columns. The particle may also have been changing more rapidly than the frame time. Each frame would then have been a superposition of images of the particle with different structures and orientations, and, for phase contrast imaging, this would wash out the contrast in the recorded frame. This entire particle fluxionality was more frequently observed in the smaller particles <1.5 nm (see movie S7 in the supplementary materials, section 8). We may hypothesize that adlayer-initiated disruptions below the surface were more likely when the surface-to-volume ratio was higher and the contact area with the oxide support was smaller, making small particles less stable.

Quantifying fluxionality

To explore this hypothesis in greater depth, we have developed an approach to quantify the order and/or disorder in images based on topological data analysis, specifically by means of summaries of persistent homology (*28*). A brief description of the approach is given in the supplementary materials, section 6. Persistent homology tracked the change in the degree of connectivity between dark (or light) pixels in a single image during intensity thresholding, and in a more ordered image, this connectivity was more persistent with thresholding. Specifically, the so-called accumulated lifetime persistent survival (ALPS) statistic acts as a measure of structural order in the image. This summary is normalized for particle size in such a way that gives a value near unity in the vacuum (corresponding to no order or contrast). An advantage of this approach is that it makes no assumptions about the form of the image (that is, the presence of atomic columns or fringes, etc.), so it can be applied to images from particles in any orientation. Applying this approach to a sequence of images from the same particle provided a quantitative measure of the order evolution with time and allowed comparison of the degrees of order between nanoparticles.

The ALPS statistic, plotted as a function of time in Fig. 4A for the particle shown in Fig. 3, had values ranging from ≥1.3, which correspond to ordered structures, to values ≤1.1, which correspond to low degrees of order. The rapid small ALPS fluctuations of ~0.1 unit were not noise but were associated with constantly changing surface structures. The plot in Fig. 4A provides a quantitative, high-level view of particle stability and explicitly shows the time that the system spends in metastable ordered states versus highly disordered states.

Particle-size effects

We applied ALPS statistics to quantitatively compare the structural dynamics in nanoparticles of different size in 23 movies (~25,000 frames) from particles in the size range 0.7

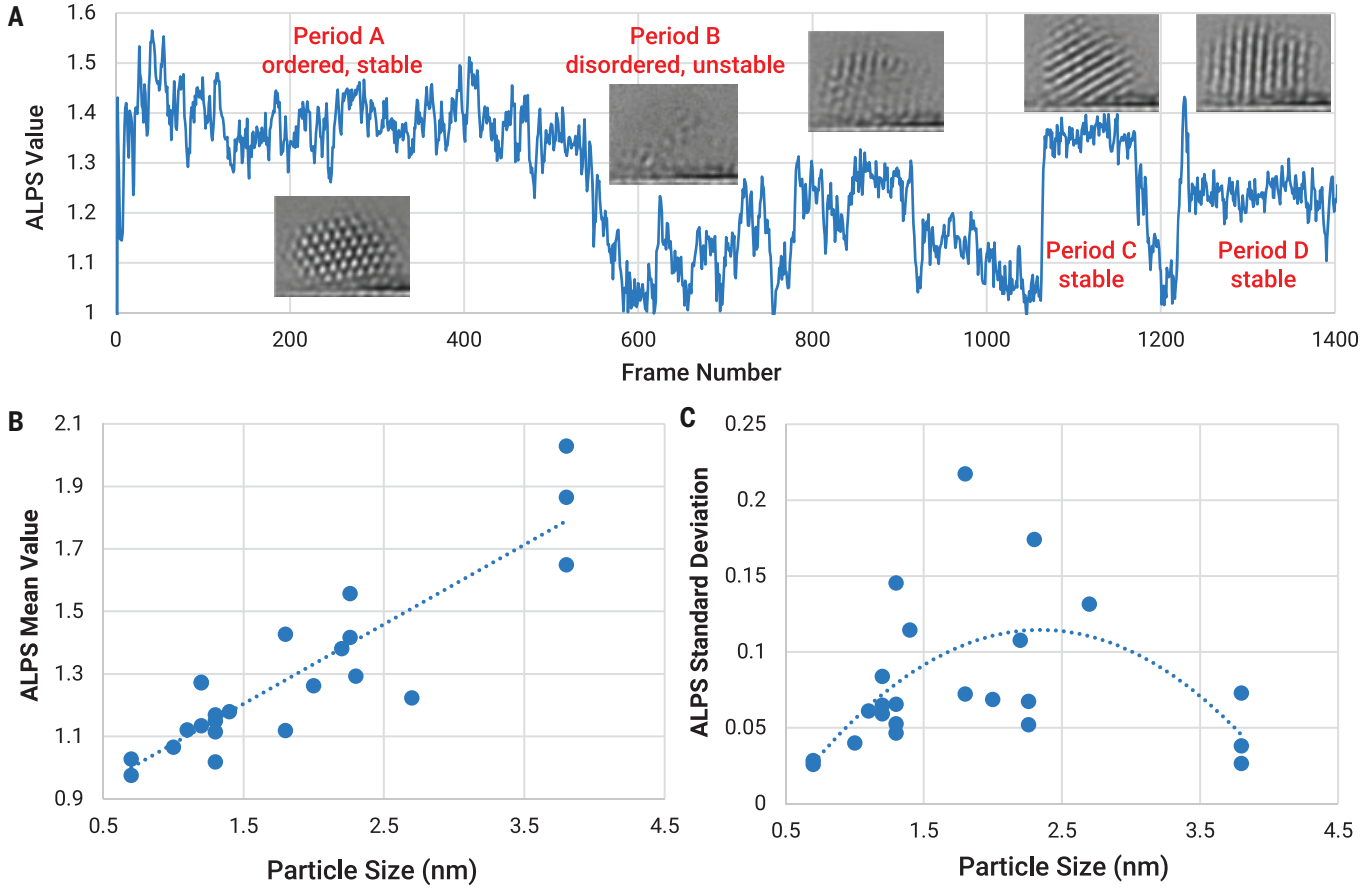

Fig. 4. Quantifying global structural dynamics in Pt nanoparticles. (**A**) The order parameter (ALPS) versus frame number (frame time = 1/75 s ~13 ms) for the same particle showing the transition from ordered to disorders configuration (inserts are typical images for each of the four stable time periods A to D). (**B** and **C**) The mean order parameter and SD as a function of particle size for different nanoparticle measured with 13-ms time resolution over periods of 8 to 15 s.

to 4 nm (for details, see the supplementary materials, section 6, and movies S6 and S7 in section 8). To simplify and facilitate the comparison between particles, the mean and standard deviation (SD) of each ALPS plot were determined and plotted as a function of particle size in Fig. 4, B and C. The mean value of the ALPS statistic showed an approximately linear dependence with particle size (and surface-to-volume ratio), quantitatively confirming the hypothesis that instability is inversely proportional to size.

The SD showed a poorly defined maximum in the size range 1.5 to 3 nm, which suggested that there were three categories of structural dynamics for the Pt particles. The first category had the largest ALPS value (>1.5) and relatively small SDs, corresponding to larger particles that remain well ordered throughout the period of observation. Although their surfaces were dynamic, their ALPS statistic was dominated by the bulk because of their small surface-to-volume ratio, and these particles remained relatively stable.

The second category had the smallest ALPS values (<1.2) and small SDs. These were particles 1.5 nm or smaller and had high degrees of disorder. Their low SDs showed that they were rarely in highly ordered states. From inspection of the denoised movies, the high degree of disorder was associated with high degrees of fluxionality. Because the particles have a high surface-to-volume ratio, fluxional surface adlayers drove fluxionality for the entire particle.

The third category showed a wide range of SDs and a wide range of ALPS values. They were predominantly intermediate-sized particles between 1.5 and 3 nm, which manifested very diverse behaviors and could either be extremely fluxional or relatively stable. The particle dynamics depended on the degree of stability of their surfaces and on the stability of the interface with the support.

The particle shown in Figs. 3 and 4 belonged to this third category and exhibited different degrees of order at different time periods. For period A in Fig. 4A, the particle shows a well-defined orientation with the support. Activation of the reverse shear (Fig. 3F) marked a period of more pronounced structural instability (period B), which manifested through large surface and interface changes.

The availability of the denoised atomic-resolution image for each ALPS point allowed the structural origin for the stability or instability transformation to be explored. For example, the degree of instability was oscillatory throughout period B, and inspection of the images shows that this was associated with a set of Pt (111) fringes (making an angle of 77° with the support) that repeatedly appeared and disappeared. The particle continuously attempted to establish a stable interfacial structure with the CeO_2 support but failed to achieve a stable configuration. The Pt particle surface was extremely fluxional throughout this process.

The particle then entered a more ordered period C, characterized by Pt (111) fringes that made an angle of ~30° with respect to the support. Another shearing operation (at frame 1141) caused the particle to enter a brief period of instability before entering period D, an ordered stable period characterized by Pt(111) fringes making and angle of ~87° with respect to the support. The transitions from metastable to unstable configurations represented a rich and complex space, but the topological analysis allowed this complexity to be quantified

in time and the denoised images permitted the associated evolutionary structural pathways to be elucidated.

Discussion

Consideration of thermodynamic and kinetic factors can provide a framework from which to interpret the fluxional observations. Before exposure to CO, most of the Pt particles exhibited the thermodynamically favored Winterbottom shape consisting of (111) and (100) facets (see the supplementary materials, section 2). The structural dynamics initiated almost immediately after exposure to CO with the particles evolving away from the Winterbottom shape. The behavior was stochastic and particles in the 1.5- to 4-nm range did temporarily revisit the equilibrium shape for various periods of time. The smaller ones were too fluxional to make any strong statement about a favored shape. The disruptive and dynamic role of the chemisorbed CO on the stability of the Pt surface facets and equilibrium shape should not be underestimated. The large chemisorption energy (~1.5 eV) was associated with significant electron transfer between the metal and the molecule and disrupted the local Pt–Pt bonding, which led to enhanced Pt migration accelerating the kinetics. However, the concept of a global equilibrium shape in such an environment for small particles may be questionable. The equilibrium shape is dominated by surface energies, and the CO will cause dynamics changes in surface energies because it was diffusing on the surface and also adsorbed and desorbed with time at certain sites. For example, the local surface energy of a Pt (111) facet with 50% CO coverage will change if the coverage spontaneously changes to 40% or 60%. Consequently, the thermodynamic driving force was constantly changing on the atomic scale, and there was no well-defined Winterbottom shape.

Thermal fluctuations constantly perturbed the system, locally driving surface migration, but there was no global equilibrium shape for the system on the timescale of our observation. Any conclusion that the observed transition structures, such as stacking faults and chimney structures, are high-energy configurations may be incomplete because we are not able to directly observe the associated CO surface overlayer. The complex surface dynamics that were observed at the atomic level can be understood from a kinetic perspective by considering the Arrhenius relations governing the migration rate r ($r = A \exp(-E_a/kT)$, where k is Boltzmann's constant). Any process in or on a material with an activation energy $E_a \leq 0.7$ eV will occur many times per second at room temperature (the attempt frequency, A, can be approximated as the phonon frequency ~10^{12} Hz). Prior TEM observations of static nanoparticle surfaces at room temperature may have appeared stationary, because the image recording averaged over the atomic-level dynamics. Going to higher temporal resolution revealed that atomic-level dynamics were constantly taking place. The surface will only become truly static at absolute zero. Although the observations reported here are in CO, it seems likely that many nanoparticle surfaces may show fluxionality under a wide range of different conditions.

In conclusion, with the help of a newly developed unsupervised AI denoising algorithm and in situ electron microscopy, we made atomic-resolution observations of nanoparticle surfaces with time resolutions down to 10 ms and under a moderate electron dose. The structural dynamics of Pt nanoparticles in a CO atmosphere were observed and characterized as a function of particle size. The nanoparticle surfaces continuously transitioned between relatively stable crystallographic terminations and more active adlayers composed of rapidly diffusing Pt atoms. The atoms of the adlayer temporarily "floated" on top of the conventional crystallographic terminations and sometimes nucleated, adding a crystallographic monolayer to the surface or diffusing away. This process was continuous with the crystallographic terminations repeatedly stabilizing and destabilizing on timescales of <100 ms at room temperature. The surface structural dynamics and stress fields penetrated below the surface and led to defect formation such as stacking faults. Many of the particles, especially the smaller ones, were observed to go through extended periods of extreme structural instability. Through the application of topological data analysis, we were able to quantify and differentiate periods when the particle was in a well-ordered metastable state from the more fluxional disordered configurations. The high spatiotemporal information from the denoiser allowed the short-lived atomic-resolution elementary structural steps associated with nanoparticle transitions to be identified. The combination of AI-powered unsupervised denoising and in situ electron microscopy provides a new approach with which to investigate the field of atomic structural dynamics and stability. This will provide a new perspective for fundamental materials research by allowing functionalities to be correlated, not only to static atomic structure, but also to local structural dynamics.

REFERENCES AND NOTES

1. Y. Zhou, C. Jin, Y. Li, W. Shen, *Nano Today* **20**, 101–120 (2018).
2. D. E. Shaw *et al*., *Science* **330**, 341–346 (2010).
3. J. L. Vincent, P. A. Crozier, *Nat. Commun.* **12**, 5789 (2021).
4. S. B. Vendelbo *et al*., *Nat. Mater.* **13**, 884–890 (2014).
5. J. S. Kim *et al*., *Science* **321**, 1472–1475 (2008).
6. T. LaGrange *et al*., *Micron* **43**, 1108–1120 (2012).
7. Y. Zhang, D. J. Flannigan, *Nano Lett.* **19**, 8216–8224 (2019).
8. F. A. Cotton, *J. Organomet. Chem.* **100**, 29–41 (1975).
9. L. D. Marks, *Rep. Prog. Phys.* **57**, 603–649 (1994).
10. H.-Y. Chao *et al*., *Chem. Rev.* **123**, 8347–8394 (2023).
11. M.-J. Xiao, H. Sun, Y. Meng, F. Zhu, *Catal. Sci. Technol.* (2024).
12. F. F. Tao, P. A. Crozier, *Chem. Rev.* **116**, 3487–3539 (2016).
13. J. R. Jinschek *et al*., *MRS Bull.* **49**, 174–183 (2024).
14. A. Nassereddine *et al*., *ChemCatChem* **15**, e202300434 (2023).
15. A. De Wael *et al*., *Phys. Rev. Lett.* **124**, 106105 (2020).
16. H. Frey, A. Beck, X. Huang, J. A. van Bokhoven, M. G. Willinger, *Science* **376**, 982–987 (2022).
17. E. L. Lawrence, B. D. A. Levin, B. K. Miller, P. A. Crozier, *Microsc. Microanal.* **26**, 86–94 (2020).
18. K. Zhang, W. Zuo, Y. Chen, D. Meng, L. Zhang, *IEEE Trans. Image Process.* **26**, 3142–3155 (2017).
19. S. Mohan *et al*., *IEEE Trans. Comput. Imaging* **8**, 585–597 (2022).
20. A. Marcos-Morales *et al*., Evaluating unsupervised denoising requires unsupervised metrics. arXiv:2210.05553 [cs.CV] (2022).
21. M. A. van Spronsen, J. W. M. Frenken, I. M. N. Groot, *Chem. Soc. Rev.* **46**, 4347–4374 (2017).
22. A. von Oertzen, H. H. Rotermund, S. Nettesheim, *Surf. Sci.* **311**, 322–330 (1994).
23. S. R. Longwitz *et al*., *J. Phys. Chem. B* **108**, 14497–14502 (2004).
24. D. Y. Sheth *et al*., Unsupervised deep video denoising. arXiv:2011.15045 [eess.IV] (2020).
25. Z. R. Mansley, L. D. Marks, *J. Phys. Chem. C Nanomater. Interfaces* **124**, 28038–28043 (2020).
26. S. B. Simonsen *et al*., *J. Am. Chem. Soc.* **132**, 7968–7975 (2010).
27. N. Panagiotides, N. I. Papanicolaou, *Int. J. Quantum Chem.* **110**, 202–209 (2010).
28. A. M. Thomas, P. A. Crozier, Y. Xu, D. S. Matteson, *Technometrics* **65**, 590–603 (2023).
29. Code for: P. A. Crozier *et al*., Zenodo (2025); https://doi.org/10.5281/zenodo.14630448.
30. Data for: P. A. Crozier *et al*., Zenodo (2025); https://doi.org/10.5281/zenodo.14618961.

ACKNOWLEDGMENTS

We thank ASU Research Computing and NYU HPC for providing high-performance computing resources and the electron microscopes in the Eyring Materials Center at Arizona State University. **Funding:** This work was supported by the National Science Foundation (grants OAC-1940263 and 2104105 to P.A.C. and P.H., grant CBET 1604971 to J.V., grant DMR 1840841 to M.T., grant CHE 2109202 to Y.W., grant OAC-1940097 to M.L., grant OAC-2103936 to C.F.-G., and grants OAC-1940124 and DMS-2114143 to D.S.M. and A.M.T.). **Author contributions:** P.A.C. and C.F.-G. conceived and directed the project. J.V., M.T., and P.H. acquired the TEM data. M.L., S.M., A.M.M., and S.A.K. wrote and tested the denoising codes. Y.F., M.T., and P.H. performed additional tests of the denoising codes and denoised and analyzed all the experimental data. D.S.M. and A.M.T. wrote and tested the persistent homology codes. M.T. and A.M.T. applied the persistent homology codes to the Pt nanoparticles and analyzed the results. **Competing interests:** The authors declare no competing interests. **Data and materials availability:** The denoising code (*29*) and the raw data and denoised data for Figs. 2, 3, and 4 (*30*) are available on Zenodo. All data needed to evaluate the conclusions in the this study are present in the main text or the supplementary materials.

SUPPLEMENTARY MATERIALS

science.org/doi/10.1126/science.ads2688
Materials and Methods
Figs. S1 to S7
References (*31*–*58*)
Movies S1 to S7

Submitted 7 August 2024; accepted 14 January 2025
10.1126/science.ads2688

PLANT PATHOLOGY

Plant pathogenic fungi hijack phosphate signaling with conserved enzymatic effectors

Carl L. McCombe[1]†, Alex Wegner[2]†, Louisa Wirtz[2], Chenie S. Zamora[3], Florencia Casanova[2], Shouvik Aditya[1], Julian R. Greenwood[1], Samuel de Paula[3], Eleanor England[1], Sascha Shang[1], Daniel J. Ericsson[4], Ely Oliveira-Garcia[3]*, Simon J. Williams[1]*, Ulrich Schaffrath[2]*

Inorganic phosphate (Pi) is essential for life, and plant cells monitor Pi availability by sensing inositol pyrophosphate (PP-InsP) levels. In this work, we describe the hijacking of plant phosphate sensing by a conserved family of Nudix hydrolase effectors from pathogenic *Magnaporthe* and *Colletotrichum* fungi. Structural and enzymatic analyses of the Nudix effector family demonstrate that they selectively hydrolyze PP-InsP. Gene deletion experiments of Nudix effectors in *Magnaporthe oryzae*, *Colletotrichum higginsianum*, and *Colletotrichum graminicola* indicate that PP-InsP hydrolysis substantially enhances disease symptoms in diverse pathosystems. Further, we show that this conserved effector family induces phosphate starvation signaling in plants. Our study elucidates a molecular mechanism, used by multiple phytopathogenic fungi, that manipulates the highly conserved plant phosphate sensing pathway to exacerbate disease.

Plant-microbe interactions range from beneficial to parasitic. Balancing the recruitment and support of mutualists while maintaining the ability to defend against pathogens is a major driver of plant evolution (*1*). Approximately 71% of vascular plant species recruit arbuscular mycorrhizal fungi (AMF) to access more inorganic phosphate (Pi) and other mineral nutrients from the environment (*2*). In contrast to AMF, pathogenic fungi steal nutrients and constrain plant growth. Fungal diseases of widely grown calorie crops threaten global food security by reducing yield (*3*). For example, *Magnaporthe oryzae* causes blast disease in major cereal crops, including rice, wheat, and barley (*4*), resulting in annual food losses that could sustain hundreds of millions of people (*5*).

Beneficial and detrimental plant-microbe interactions can be influenced by plant phosphate status (*6*). In eukaryotic cells, inositol pyrophosphates (PP-InsPs) signal Pi availability by binding to SPX protein domains (*7*). When Pi in plant cells is abundant, PP-InsP–bound SPX-domain proteins inhibit phosphate starvation response transcription factors (PHRs), thereby suppressing the expression of starvation-induced genes (*8*–*11*). PHRs are conserved throughout land plants and green algae (*12*), and the regulation of plant-AMF symbiosis in both monocots and dicots is dependent on the PP-InsP–SPX–PHR signaling pathway (*13*–*16*). In addition to controlling PHR activity, PP-InsPs are implicated in regulating phosphate transporters (*7*), ubiquitin ligases (*17*), and hormone receptors (*18*–*21*), effectively integrating Pi availability into various cellular processes.

Plant pathogens may use secreted proteins, called effectors, to target plant phosphate signaling to promote disease (*6*). Overexpression of the bacterial effector SAP11 in *Arabidopsis thaliana* up-regulates multiple *At*PHR1 target genes and increases cellular phosphate levels (*22*). Another bacterial effector, XopH from *Xanthomonas campestris* pv. *vesicatoria*, decreases plant PP-InsP levels through dephosphorylation of inositol hexakisphosphate ($InsP_6$) and interferes with hormone signaling (*23*); however, whether this disrupts Pi sensing remains unclear. In this study, we demonstrate that a conserved family of Nudix (nucleoside-diphosphate linked to moiety X) hydrolase effectors secreted by pathogenic fungi hydrolyze PP-InsPs. This function successfully mimics phosphate depletion and activates the plant PHR signaling pathway. We generated Nudix effector deletion strains of *M. oryzae*, *Colletotrichum higginsianum*, and *Colletotrichum graminicola* and demonstrate that PP-InsP hydrolase activity is essential for the full virulence of multiple pathogenic fungi.

A conserved Nudix hydrolase effector family promotes blast and anthracnose disease

Nudix hydrolase effectors are used by fungal, oomycete, and bacterial plant pathogens; however, their role in virulence, preferred substrates, and putative functions vary (*24*–*29*). Pathogenic *Magnaporthe* and *Colletotrichum* fungi have effectors with predicted Nudix hydrolase activity, and little is known about their role in disease (fig. S1 and data S1) (*30*). There are three predicted Nudix effector genes in *M. oryzae* (data S1) (*31*); two of these, named *MoNUDIX*, are identical in sequence and are among the most up-regulated genes during rice infection (*32*). To examine the role of Nudix effectors in blast disease, we first used RNA interference (RNAi) to simultaneously lower the expression of both identical *MoNUDIX* genes (fig. S2, A and B). Silencing of *MoNUDIX* reduced blast disease symptoms compared with wild-type (WT) *M. oryzae* in whole–rice plant spray inoculation assays (fig. S2, C and D). Silencing *MoNUDIX* also enhanced reactive oxygen species (ROS) accumulation, slowed disease progression, and increased cell wall autofluorescence (fig. S2, E to J). Collectively, the results indicate that *MoNUDIX* is important for *M. oryzae* virulence and host immune suppression.

We generated *MoNUDIX* deletion and complementation mutants in *M. oryzae* using CRISPR-Cas9 genome editing (fig. S3). The deletion of both identical *MoNUDIX* gene copies (*M. oryzae*$^{\Delta\Delta MoNUDIX}$) resulted in a reduction in rice blast lesion size (Fig. 1A). To assess whether the contribution of MoNUDIX to blast virulence was specific to rice infection, we also performed infection assays with barley and again observed significantly reduced lesion size with *M. oryzae*$^{\Delta\Delta MoNUDIX}$ (Fig. 1B). Although MoNUDIX appears to play a more important role when infecting certain rice and barley cultivars, overall, the results consistently indicate that MoNUDIX significantly promotes blast disease (Fig. 1A and fig. S4, A and B). Microscopy analysis also demonstrated a clear reduction in the growth of *M. oryzae*$^{\Delta\Delta MoNUDIX}$ running hyphae during infection (fig. S4C). The two identical *MoNUDIX* genes likely function redundantly because single-deletion mutants exhibit only slight reductions in disease symptoms when compared with WT *M. oryzae* (fig. S5, A and B). *M. oryzae*$^{\Delta\Delta MoNUDIX}$ displays normal vegetative growth, abiotic stress tolerance, conidia germination, appressorium formation, and infection after leaf wounding, which bypasses the requirement for an appressorium-mediated penetration (fig. S5, C to F). Collectively, our data indicate that MoNUDIX is specifically relevant for appressorium-mediated plant infection, which is consistent with the previously reported timing of Nudix effector gene induction during the biotrophic growth stage of *M. oryzae*, *Colletotrichum lentis*, and *C. higginsianum* (*30*, *32*, *33*).

Nudix hydrolases typically hydrolyze pyrophosphate bonds in molecules with a nucleoside diphosphate. The Nudix motif, $GX_5EX_7REUXEEXGU$—where U represents a hydrophobic amino acid and X is any amino acid (*34*)—is essential for substrate hydrolysis by Nudix hydrolases. To investigate the role of Nudix hydrolase activity in promoting blast disease, we introduced either WT *MoNUDIX* or a mutated *MoNUDIX* with the second glutamate in the motif mutated to glutamine (*MoNUDIX*^{E79Q})

[1]Research School of Biology, The Australian National University, Canberra, ACT, Australia. [2]Department of Molecular Plant Physiology, RWTH Aachen University, Aachen, Germany. [3]Department of Plant Pathology and Crop Physiology, Louisiana State University Agricultural Center, Baton Rouge, LA, USA. [4]ANSTO, Australian Synchrotron, Crystallography Beamline Group, Melbourne, VIC, Australia.
*Corresponding author. Email: schaffrath@bio3.rwth-aachen.de (U.S.); simon.williams@anu.edu.au (S.J.W.); eoliveiragarcia@agcenter.lsu.edu (E.O.-G.)
†These authors contributed equally to this work.

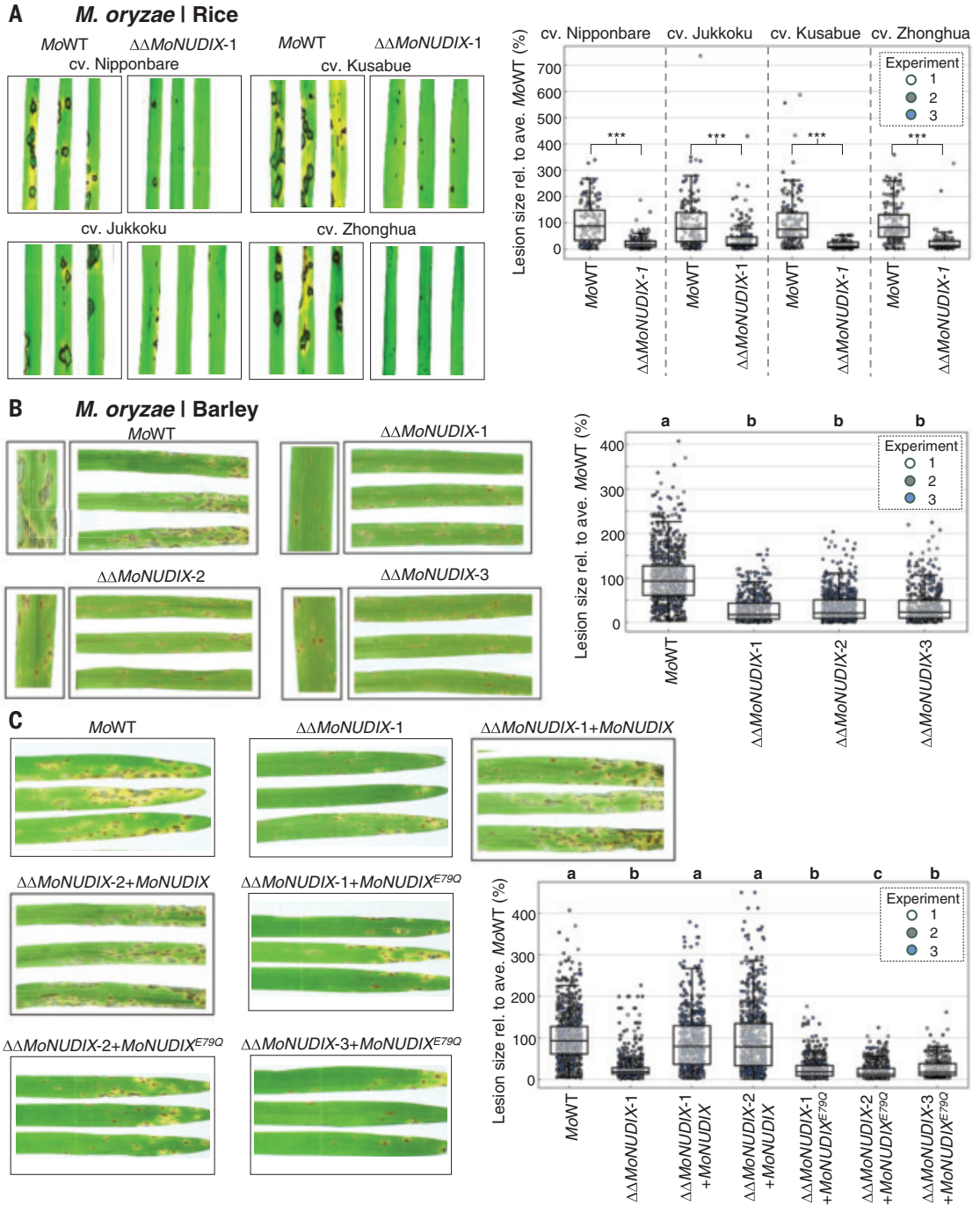

Fig. 1. MoNUDIX is important for *M. oryzae* virulence on rice and barley. (**A**) Rice cultivars inoculated with *M. oryzae* isolate Guy11 (*Mo*WT) and *MoNUDIX* double gene deletion mutant Δ*MoNUDIX*-1. Leaves were photographed 6 days postinoculation (dpi). Approximately 50 lesions were measured across five rice leaves per treatment in three independent experiments, and significant differences are indicated (Mann-Whitney *U* test, ***$P < 0.001$). (**B**) Barley (cv. Ingrid) inoculated with *Mo*WT, Δ*MoNUDIX*-1, Δ*MoNUDIX*-2, and Δ*MoNUDIX*-3. Leaves were photographed 7 dpi. Approximately 150 lesions were measured across 10 barley leaves per treatment per experiment, and letters indicate significant differences between treatments (Kruskal-Wallis *H* test, Dunn's post hoc test, $P < 0.01$). (**C**) Barley (cv. Ingrid) inoculated with *Mo*WT, Δ*MoNUDIX*-1, and *MoNUDIX* double gene deletion mutants expressing either WT *MoNUDIX* (Δ*MoNUDIX*-1+*MoNUDIX* and Δ*MoNUDIX*-2+*MoNUDIX*) or *MoNUDIX* with a mutation in the Nudix motif (Δ*MoNUDIX*-1+*MoNUDIX*^{E79Q}, Δ*MoNUDIX*-2+*MoNUDIX*^{E79Q}, Δ*MoNUDIX*-3+*MoNUDIX*^{E79Q}). Leaves were photographed 7 dpi. Approximately 150 lesions were measured across 10 barley leaves per treatment per experiment, and letters indicate significant differences between treatments (Kruskal-Wallis *H* test, Dunn's post hoc test, $P < 0.01$).

into *M. oryzae*$^{\Delta\Delta MoNUDIX}$. Although the expression of WT *MoNUDIX* successfully rescues the virulence of *M. oryzae*$^{\Delta\Delta MoNUDIX}$, the expression *MoNUDIX*^{E79Q} does not (Fig. 1C). We also tested various other Nudix motif mutant proteins, and all failed to rescue *M. oryzae*$^{\Delta\Delta MoNUDIX}$ virulence (fig. S5G). These data demonstrate that the Nudix motif and therefore hydrolytic activity is essential for the promotion of blast disease by MoNUDIX.

To determine whether related Nudix effectors have functions in other diseases, we generated *C. higginsianum* and *C. graminicola* Nudix effector deletion mutants. *C. higginsianum* has four putative Nudix effectors (fig. S1 and data S1; this includes a duplicate gene copy of *ChNUDIX*). *ChNUDIX* and *ChNUDIX2* are highly expressed during infection and are located on a mini chromosome that is essential for pathogen virulence (*33*, *35*). The deletion of both identical *ChNUDIX* gene copies (*C. higginsianum*$^{\Delta\Delta ChNUDIX}$) reduced disease symptoms when infecting *A. thaliana* (Fig. 2A and fig. S6). *C. graminicola* has only a single putative Nudix effector, *CgNUDIX* (fig. S1 and data S1), and deletion of *CgNUDIX* (*C. graminicola*$^{\Delta CgNUDIX}$) significantly reduced disease symptoms when infecting maize without affecting vegetative growth or conidia germination (Fig. 2B and fig. S7, A to G). We observed that the loss of *CgNUDIX* reduced

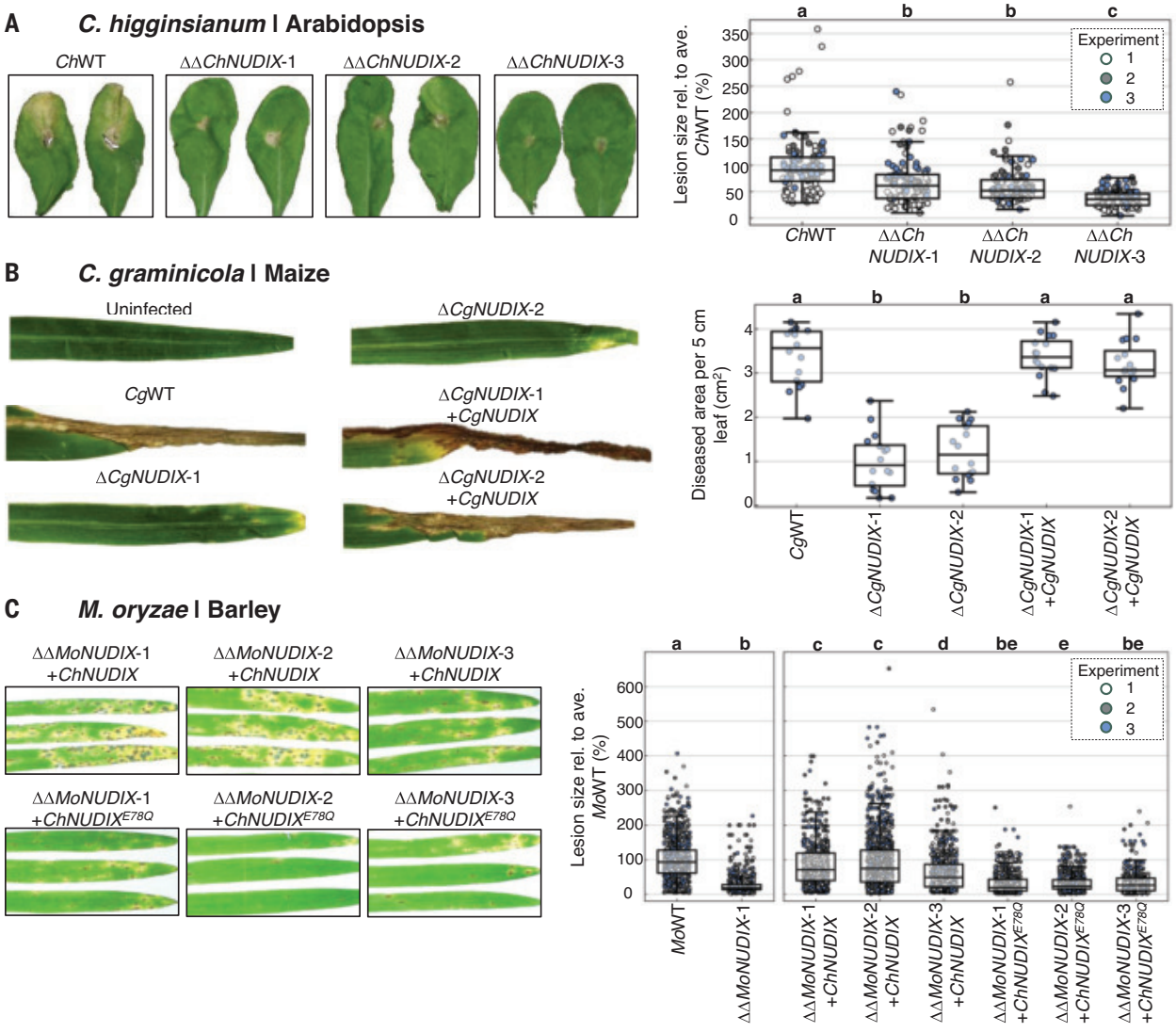

Fig. 2. Nudix effectors in *Colletotrichum* have important and shared functions with MoNUDIX during infection. (**A**) *A. thaliana* leaves inoculated with *C. higginsianum* isolate IMI349063 (*Ch*WT) and three independent *ChNUDIX* double gene deletion mutants (ΔΔ*ChNUDIX*-1, ΔΔ*ChNUDIX*-2, and ΔΔ*ChNUDIX*-3). Leaves were photographed 5 dpi. Approximately 40 lesions were measured per treatment per experiment, and letters indicate significant differences between treatments (Kruskal-Wallis *H* test, Dunn's post hoc test, $P < 0.01$). (**B**) *Zea mays* (cv. B73) inoculated with *C. graminicola* strain M2 (*Cg*WT), two independent *CgNUDIX* gene deletion mutants (Δ*CgNUDIX*-1 and Δ*CgNUDIX*-2), and the mutants complemented with an ectopic copy of *CgNUDIX* (Δ*CgNUDIX*-1 +*CgNUDIX* and Δ*CgNUDIX*-2+*CgNUDIX*). Leaves ($n = 16$) were photographed 6 dpi and the diseased area quantified, and letters indicate significant differences between treatments [one-way analysis of variance (ANOVA), Tukey's honestly significant difference (HSD), $P < 0.01$]. (**C**) Barley (cv. Ingrid) inoculated with *Mo*WT, ΔΔ*MoNUDIX*-1, and *MoNUDIX* double gene deletion mutants expressing either WT *ChNUDIX* (ΔΔ*MoNUDIX*-1+*ChNUDIX*, ΔΔ*MoNUDIX*-2+*ChNUDIX*, and ΔΔ*MoNUDIX*-3 +*ChNUDIX*) or *ChNUDIX* with a mutation in the Nudix motif (ΔΔ*MoNUDIX*-1 +*ChNUDIX*^{E78Q}, ΔΔ*MoNUDIX*-2+*ChNUDIX*^{E78Q}, and ΔΔ*MoNUDIX*-3+*ChNUDIX*^{E78Q}). Leaves were photographed 7 dpi. Approximately 150 lesions measured across 10 barley leaves per treatment per experiment, and letters indicate significant differences between treatments (Kruskal-Wallis *H* test, Dunn's post hoc test, $P < 0.01$). The inoculation experiments were completed alongside those presented in Fig. 1C, and the control treatment results (MoWT and ΔΔMoNUDIX-1) are included in both figures. For representative leaf images of MoWT and ΔΔMoNUDIX-1, see Fig. 1C.

fungal growth in maize cells and slowed the infection process (fig. S7, H and J). Our results demonstrate that Nudix effectors increase virulence of multiple pathogens with diverse host plants. Furthermore, WT ChNUDIX, but not a Nudix motif mutant, restored virulence in *M. oryzae*$^{\Delta\Delta MoNUDIX}$ (Fig. 2C), demonstrating that Nudix effectors from *Colletotrichum* and *Magnaporthe* species have conserved virulence functions that are dependent on hydrolytic activity.

Magnaporthe and *Colletotrichum* Nudix effectors are PP-InsP hydrolases

To characterize the enzymatic activity and substrate specificity of the Nudix effectors, we purified MoNUDIX (fig. S8A) and determined its crystal structure at a resolution of 1.57 Å (data S2). Structural similarity searches revealed that *Homo sapiens* diphosphoinositol polyphosphate phosphohydrolase 1 (HsDIPP1) is similar to MoNUDIX in both overall structure and surface charge properties (Fig. 3A). HsDIPP1, a well-characterized Nudix hydrolase, hydrolyzes diadenosine polyphosphates (Ap_nAs) (*36*), the protective 5′ mRNA cap (*37*), and PP-InsPs (*38*). Substrate screening with purified MoNUDIX

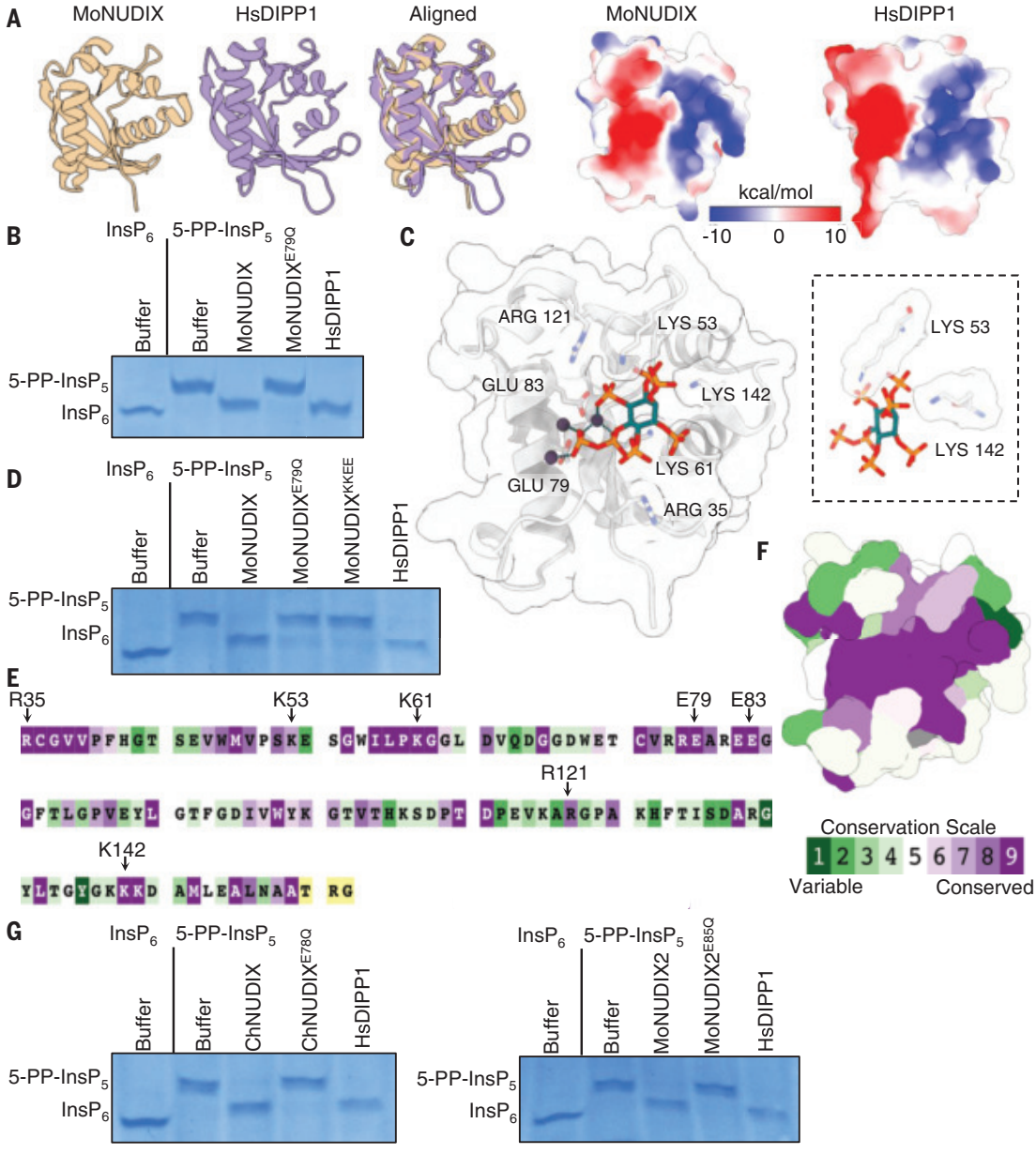

Fig. 3. *Magnaporthe* and *Colletotrichum* Nudix effectors are diphosphoinositol polyphosphate phosphohydrolases. (**A**) MoNUDIX and *H. sapiens* DIPP1 [Protein Data Bank (PDB) ID: 6WO7] (*39*) crystal structures superimposed to demonstrate their structural similarity despite low levels of sequence identity (25%). (Right) Both MoNUDIX and HsDIPP1 demonstrate similar surface charge properties at the putative active site. (**B**) Purified MoNUDIX, MoNUDIX^{E79Q}, and HsDIPP1 were incubated with 5-PP-InsP$_5$. Buffer alone was incubated with both InsP$_6$ and 5-PP-InsP$_5$. The reaction products were separated using a polyacrylamide gel and stained with toluidine blue. (**C**) MoNUDIX with Mg^{2+} and 5-PP-InsP$_5$ docked into the crystal structure via alignment with HsDIPP1 (PDB: 6WO7). The amino acids potentially important for Mg^{2+} and 5-PP-InsP$_5$ binding are labeled. In the box (right) are the two lysine amino acids selected for mutagenesis. (**D**) PP-InsP hydrolysis assays demonstrate the importance of lysine 53 and 142. (**E**) The sequence of MoNUDIX used to determine the crystal structure, with coloring indicating amino acid conservation across homologous effectors. The amino acids labeled in (C) are indicated with arrows. Single-letter abbreviations for the amino acid residues are as follows: A, Ala; C, Cys; D, Asp; E, Glu; F, Phe; G, Gly; H, His; I, Ile; K, Lys; L, Leu; M, Met; N, Asn; P, Pro; Q, Gln; R, Arg; S, Ser; T, Thr; V, Val; W, Trp; and Y, Tyr. (**F**) MoNUDIX with the protein surface colored according to amino acid conservation across homologous effectors, demonstrating high conservation of the putative substrate binding site. (**G**) PP-InsP hydrolysis assays with MoNUDIX homologs ChNUDIX and MoNUDIX2 demonstrates Nudix motif–dependent hydrolysis of 5-PP-InsP$_5$.

protein demonstrated Nudix motif–dependent hydrolysis of 5-PP-InsP$_5$ (Fig. 3B), whereas no activity was detected with Ap$_n$As, mRNA caps, or other common substrates of Nudix hydrolases (fig. S8, B and C). Our results demonstrate that MoNUDIX is a selective PP-InsP hydrolase in vitro. To understand the mode of PP-InsP binding to MoNUDIX, we modeled 5-PP-InsP$_5$ into the MoNUDIX crystal structure through alignment with substrate-bound HsDIPP1 (*39*) (Fig. 3C). We identified basic amino acids likely required for PP-InsP binding (Fig. 3C); to confirm their involvement, two lysines were mutated to glutamate (MoNUDIX^{KKEE}). The MoNUDIX^{KKEE} protein demonstrated an ~70-fold reduction in InsP$_6$ binding affinity as measured by microscale thermophoresis (fig. S8D) and was unable to hydrolyze 5-PP-InsP$_5$ (Fig. 3D). The predicted PP-InsP binding site, including the basic amino acids, are conserved throughout the *Magnaporthe* and *Colletotrichum* Nudix effector family (Fig. 3, E and F), which suggests conservation of substrate selectivity and enzymatic activity. We show that purified ChNUDIX and a second predicted *M. oryzae* Nudix effector (MoNUDIX2) both hydrolyze 5-PP-InsP$_5$, and this activity is dependent on a Nudix motif glutamate (Fig. 3G). By contrast, Nudix effectors from other plant pathogens lack the conserved PP-InsP binding residues, and we found that the *Melampsora lini* Nudix effector AvrM14 does not hydrolyze 5-PP-InsP5 (fig. S8E). All proteins used throughout this study were purified to homogeneity before in vitro characterization (figs. S8A and S9) (*29*). Overall, structural analysis and enzymatic assays

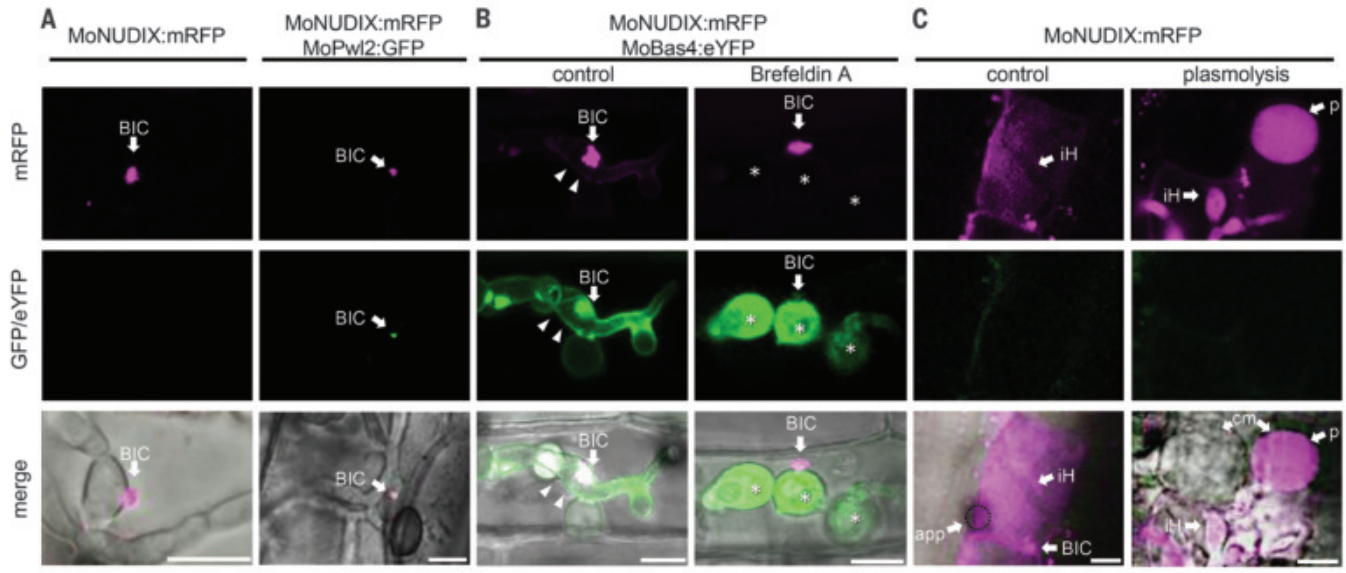

Fig. 4. MoNUDIX localizes to the BIC and is secreted into host cells during infection. Confocal laser scanning microscopy images of barley and rice leaves infected with *M. oryzae* expressing fluorescent protein–tagged effectors. (**A**) (Left) Barley leaves inoculated with *M. oryzae* expressing MoNUDIX:mRFP. At 48 hours postinoculation (hpi), punctual accumulation of the mRFP fusion protein in the fungal hyphae was observed in the first infected cell, consistent with BIC localization. (Right) The cytoplasmic effector *Mo*Pwl2 (*41*) was coexpressed as a green fluorescent protein (GFP)–fusion protein demonstrating colocalization of MoNUDIX:mRFP (magenta) and MoPwl2:GFP (green). (**B**) Rice leaves were inoculated with *M. oryzae* expressing MoNUDIX:mRFP and MoBas4:eYFP. MoBas4:eYFP (green) shows apoplastic localization outlining the invasive hypha (arrowheads). In the presence of BFA, MoBas4:eYFP (green) is retained in the fungal endoplasmic reticulum (ER) (asterisks), but MoNUDIX:mRFP (magenta) remains BIC localized (arrow), imaged with the same transformant at 3 hours after exposure to BFA. (**C**) Secretion of MoNUDIX into the rice cell. Rice leaves inoculated with *M. oryzae* expressing MoNUDIX:mRFP and analyzed 48 hpi. For concentration of the intracellular mRFP signal, we used plasmolysis with 0.5 M KNO_3 before imaging. eYFP, enhanced yellow fluorescent protein; iH, invasive hyphae; p, rice protoplast after plasmolysis; i, infected cell; cm, cell membrane of protoplast. Scale bars, 10 μm.

reveal that the *Magnaporthe* and *Colletotrichum* Nudix effectors are PP-InsP hydrolases.

MoNUDIX localizes to the host cell cytoplasm during plant infection

Fungal effectors can function within the host plant cell or in the apoplastic space between the fungal cell wall and plant plasma membrane. PP-InsPs are intracellular signaling molecules (*40*). We therefore hypothesized that the Nudix effector family would function within the host plant cell during infection. We sought to identify the localization of MoNUDIX during plant infection using live-cell imaging techniques. First, we transformed *M. oryzae* with monomeric red fluorescent protein (mRFP)–tagged MoNUDIX controlled by the native promoter and determined that the effector colocalizes with the known cytoplasmic effector *Mo*Pwl2 in the biotrophic interfacial complex (BIC) (Fig. 4A). Using the native promoter required for BIC localization, constitutive expression of MoNUDIX resulted in mislocalization throughout the fungal hyphae and did not alter infection phenotypes (fig. S10). The BIC is the site of cytoplasmic effector translocation from the fungus into the host cell (*41*, *42*), therefore our data suggest that MoNUDIX is translocated into the cytoplasm. Treatment with brefeldin A (BFA), a potent inhibitor of Golgi trafficking (*43*), prevents the secretion of apoplastic but not cytoplasmic *M. oryzae* effectors (*42*). The BIC localization of MoNUDIX was not influenced by BFA treatment, which further indicates that MoNUDIX functions as a cytoplasmic effector (Fig. 4B). For concentration of intracellular fluorescence and verification of MoNUDIX localization inside the host cell, we used a gentle plasmolysis procedure. The MoNUDIX:mRFP signal is clearly observed in the host plant cell protoplasts after plasmolysis (Fig. 4C). Expression of *M. oryzae* mRFP-tagged ChNUDIX and MoNUDIX Nudix motif mutant proteins demonstrated that they also localize to the BIC (fig. S11). Overall, our results demonstrate that MoNUDIX transits to the host cell during plant infection, where it likely hydrolyses plant PP-InsPs to promote disease.

The Nudix effector family activates plant phosphate starvation responses

A reduction in intracellular PP-InsP concentration, which occurs when phosphate is limited, prevents SPX-domain proteins from binding to and inhibiting PHRs, which leads to the expression of phosphate starvation–induced genes (fig. S12A) (*8*). To determine whether the Nudix effectors hydrolyse PP-InsPs in plant cells, we assessed changes in PHR function. First, we used a split GAL4 in planta protein interaction system in *Nicotiana benthamiana* (*44*), to determine whether the effectors prevent *At*SPX1 from binding to *At*PHR1. In this assay, interactions between *At*SPX1 and *At*PHR1 will bring together a GAL4 DNA binding domain fused to *At*SPX1 and a VP16 transcriptional activation domain fused to *At*PHR1 to activate the expression of a luciferase reporter gene. To first observe a positive interaction between *At*PHR1 and *At*SPX1, we needed to coexpress the kinase domain of VIH2, an enzyme that produces PP-InsPs in plants (Fig. 5A) (*45*). Using the VIH2 coexpression system, we found that both ChNUDIX and MoNUDIX reduced luciferase expression when compared with Nudix motif mutants (MoNUDIX^{E79Q} and ChNUDIX^{E78Q}) (Fig. 5A), which suggests that their hydrolase activity disrupts *At*SPX1 binding to *At*PHR1. To determine whether the Nudix effectors induce PHR transcriptional activity, we designed a PHR-responsive promoter reporter gene. The RUBY reporter gene (*46*) was controlled by a synthetic promoter with multiple P1BS (PHR1-binding sequence) elements (fig. S12B). We screened six Nudix effector family members along with their corresponding Nudix motif mutants. All six Nudix effectors significantly

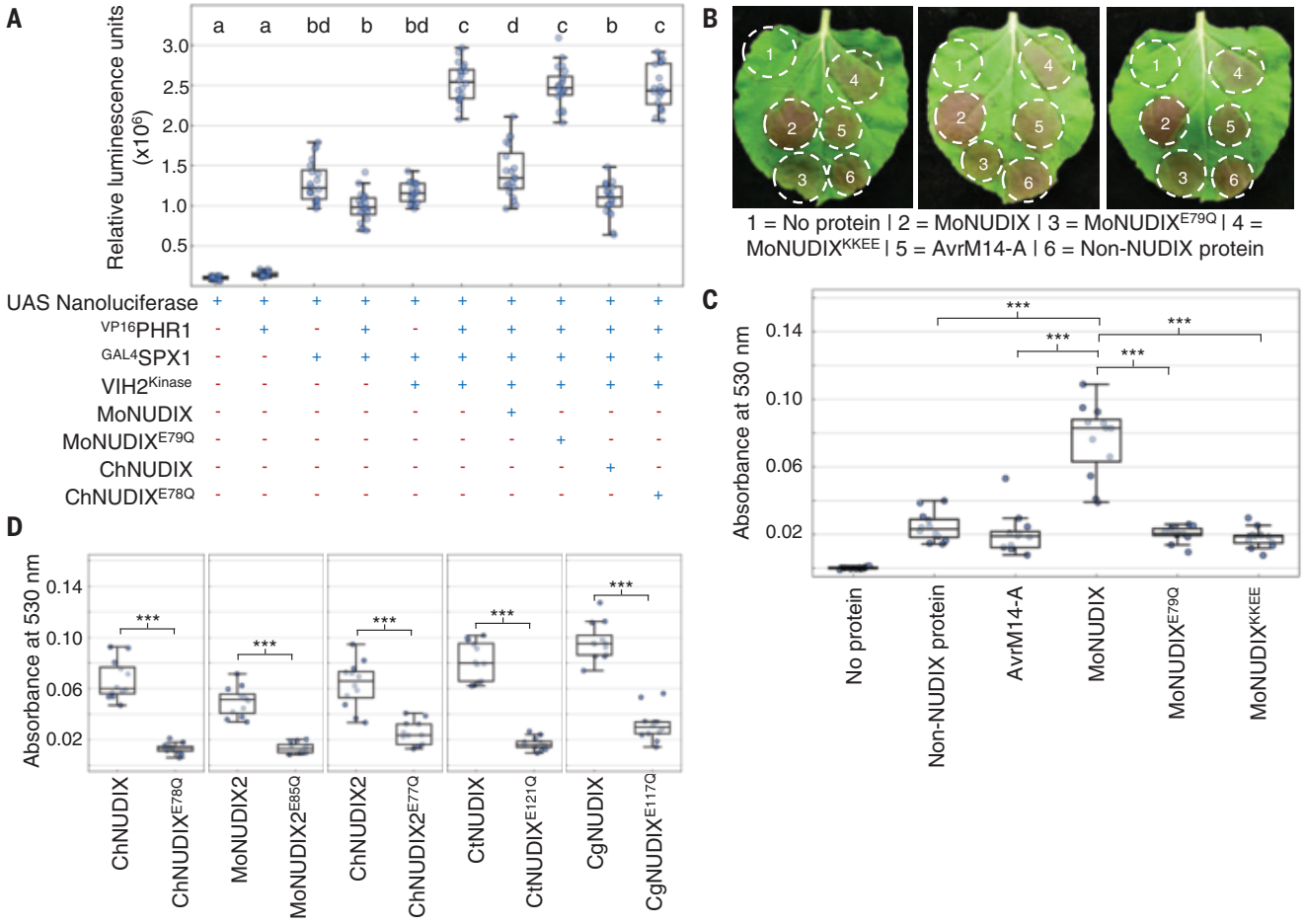

Fig. 5. The Nudix effector family activates plant phosphate starvation responses. (**A**) Split GAL4-VP16 assays to investigate interactions between *At*SPX1 and *At*PHR1 proteins were completed in *N. benthamiana*. Leaves were agroinfiltrated with genes, as indicated in the figure. At 5 days postinfiltration, nanoluciferase activity was measured (n = 20). Letters indicate significant differences between treatments (one-way ANOVA, Tukey's HSD, $P < 0.001$). (**B**) Visible RUBY production in leaves cotransformed with P1BS:RUBY and Nudix effectors or controls. (**C** and **D**) The absorbance of extracts from leaves cotransformed with P1BS:RUBY and Nudix effectors or controls (n = 12); asterisks indicate significant differences between treatments (one-way ANOVA, Tukey's HSD, ***$P < 0.001$).

increase the expression of the RUBY reporter when compared with the corresponding Nudix motif mutant proteins and the negative controls (Fig. 5, B to D). Additionally, MoNUDIX^{KKEE} results in reduced RUBY expression when compared with WT MoNUDIX, consistent with the reduced $InsP_6$ binding affinity and the lack of 5-PP-$InsP_5$ hydrolysis observed in vitro (Fig. 5, B and C). We also observe similar results when swapping the synthetic P1BS promoter with the 1-kb promoter region from a native *N. benthamiana* phosphate starvation–induced gene (fig. S12, C to E). To confirm that the increased release and activation of PHR results in the expression of phosphate starvation–induced genes, we measured the transcript abundance of *Nb*SPX1 and *Nb*PECP1, both of which have multiple P1BS elements in their promoters (fig. S12C) and are homologs of established *A. thaliana* phosphate starvation–induced genes (*47*). MoNUDIX and ChNUDIX significantly increased the abundance of *Nb*SPX1 and *Nb*PECP1 mRNA, when compared with MoNUDIX^{E79Q}, ChNUDIX^{E78Q}, and a no effector protein control (fig. S12F). For all proteins, accumulation in *N. benthamiana* leaf tissue was detected using immunoblotting (fig. S12G).

To observe host transcriptome changes induced by the Nudix effectors during infection, we completed RNA sequencing (RNA-seq) on uninfected rice and rice at 72 hours postinoculation with WT *M. oryzae* or *M. oryzae*$^{\Delta\Delta MoNUDIX}$. Overall, infection with both WT *M. oryzae* and *M. oryzae*$^{\Delta\Delta MoNUDIX}$ resulted in similar gene expression changes in rice (fig. S13, A and B). We completed gene ontology enrichment analysis on genes up-regulated when comparing WT *M. oryzae* with *M. oryzae*$^{\Delta\Delta MoNUDIX}$. We observed the overrepresentation of genes involved in typical responses to infection, including hydrogen peroxide catabolism and ethylene signaling, as well as genes involved in the regulation of phosphate starvation responses (fig. S13C). Some gene expression differences may stem from differences in disease symptoms between treatments (Fig. 1A). To distinguish between transcriptome changes caused by MoNUDIX and those resulting from differences in infection severity, we filtered out transcripts up-regulated when comparing both infection datasets with the uninfected control (fig. S13D). After controlling for general responses to infection, cellular response to phosphate starvation emerged as the only significantly enriched up-regulated biological process in the comparison of WT *M. oryzae* with *M. oryzae*$^{\Delta\Delta MoNUDIX}$, which indicates that MoNUDIX is responsible for inducing phosphate starvation signaling during rice infection (fig. S13E).

To investigate the potential activation of PHRs by MoNUDIX during rice infection, we examined the expression of genes previously identified as directly regulated by *Os*PHR2 (*15*) and responsive to phosphate supply in rice shoots (*48*). There is a significant increase in

the expression of ~50% of the *Os*PHR2 target genes when comparing WT *M. oryzae* with *M. oryzae*$^{\Delta\Delta MoNUDIX}$ (fig. S13F), which indicates that MoNUDIX increases PHR-regulated gene expression during rice infection. We also observed that multiple *Os*PHR2 target genes had significantly reduced expression levels in either infection dataset when compared with the uninfected control (fig. S13F), which suggests additional MoNUDIX-independent regulation of some PHR target genes during plant infection. Because MoNUDIX is a PP-InsP hydrolase, we assessed the expression of the six rice SPX single-domain proteins (*Os*SPX1 to *Os*SPX6), which act as PP-InsP receptors. We found that *Os*SPX1, *Os*SPX2, *Os*SPX5, and *Os*SPX6 were all up-regulated in the presence of MoNUDIX, whereas *Os*SPX3 was expressed at very low levels in our samples, and *Os*SPX4 gene expression levels remained constant across treatments (fig. S13G). *Os*SPX4 is the only *Os*SPX gene not up-regulated during phosphate starvation (*49*). Overall, the RNA-seq results indicate that the presence of MoNUDIX during infection induces phosphate starvation signaling in rice. To further investigate MoNUDIX-induced phosphate starvation throughout the infection process, we used quantitative polymerase chain reaction (qPCR) to determine the expression of SPX1 and induced by phosphate starvation 2 (IPS2) in two different rice cultivars infected with either WT *M. oryzae* or *M. oryzae*$^{\Delta\Delta MoNUDIX}$ at four time points. Both genes were up-regulated in WT infection when compared with *M. oryzae*$^{\Delta\Delta MoNUDIX}$, and the increase in expression peaked at 72 hours postinfection (fig. S13H), which corresponds with the timing of MoNUDIX expression (*33*). Collectively, our data demonstrate that the enzymatic activity of the Nudix effectors disrupts SPX-PHR binding, activates PHRs, and increases phosphate starvation–responsive gene expression in *N. benthamiana* and rice, all consistent with PP-InsP hydrolysis in plants.

Discussion and conclusions

On the basis of our data, we propose the following model describing the function of MoNUDIX (fig. S14A). First, the effector is translocated into host plant cells. Once inside, it functions as PP-InsP hydrolase enzyme, effectively uncoupling PP-InsP levels from intracellular phosphate availability. This induces a plethora of physiological changes typically associated with phosphate starvation that ultimately promote disease.

Phosphate is an essential but often limiting nutrient for plant growth, and plants have evolved sophisticated mechanisms to regulate phosphate homeostasis. Our results show that pathogenic fungi can disrupt plant phosphate sensing using Nudix hydrolase effectors. We present evidence that the Nudix effectors from *Magnaporthe* and *Colletotrichum* spp. hydrolyze PP-InsPs in host plants, though the exact downstream mechanism by which this enhances disease symptoms remains unclear. Several possibilities exist, including increased transcription of immune-suppressing genes regulated by PHR transcription factors (*50*, *51*), altered jasmonate perception owing to the PP-InsP cofactor requirement of the COI1 jasmonate receptor (*18*, *19*, *45*), and that elevated intracellular phosphate levels from starvation responses could benefit fungal nutrition. In support of the Nudix effectors suppressing immunity to promote disease, we observed that the activity of MoNUDIX and ChNUDIX suppresses ROS production in *N. benthamiana* after immune elicitation (fig. S14B), and the silencing of MoNUDIX during rice infection leads to increased ROS accumulation (fig. S2, E and F). Ultimately, disentangling the various potential mechanisms through which PP-InsP hydrolysis promotes disease will be difficult, and it is likely that multiple pathways regulated by PP-InsPs influence disease symptoms. Despite this, our results demonstrate that the PP-InsP–regulated mechanism or mechanisms that the Nudix effectors are exploiting to exacerbate disease are conserved across diverse plant linages.

Nudix hydrolases from *A. thaliana* were reported to hydrolyze PP-InsPs in vitro and in plants (*52*). Ectopic expression of the *A. thaliana* proteins in *N. benthamiana* resulted in the increased expression of a phosphate starvation reporter gene, similar to our findings with the Nudix effectors. This suggests that fungal Nudix effectors might have evolved to mimic endogenous plant Nudix hydrolases to promote disease.

The critical role of PP-InsPs in plant-microbe interactions is not limited to pathogens with Nudix effectors. Plant-AMF symbiosis is regulated by the PHR family of transcription factors (*13*–*16*), which in turn are regulated by PP-InsP levels. Likewise, the *A. thaliana* root microbiome and root colonization by the mutualistic fungus *Colletotrichum tofieldiae* are both influenced by plant phosphate signaling through *At*PHR1 (*53*, *54*). Furthermore, *A. thaliana* mutants defective in PP-InsP synthesis exhibit enhanced susceptibility to necrotrophic fungi (*45*). Given the critical role of phosphate sensing in plant-microbe interactions, we anticipate that future studies will identify more microbial effectors that target PP-InsP signaling to enhance plant colonization.

REFERENCES AND NOTES

1. P.-M. Delaux, S. Schornack, *Science* **371**, eaba6605 (2021).
2. M. C. Brundrett, L. Tedersoo, *New Phytol.* **220**, 1108–1115 (2018).
3. E. Stukenbrock, S. Gurr, *Nature* **617**, 31–34 (2023).
4. N. J. Talbot, *Annu. Rev. Microbiol.* **57**, 177–202 (2003).
5. M. C. Fisher *et al*., *Nature* **484**, 186–194 (2012).
6. M. Paries, C. Gutjahr, *New Phytol.* **239**, 29–46 (2023).
7. R. Wild *et al*., *Science* **352**, 986–990 (2016).
8. M. K. Ried *et al*., *Nat. Commun.* **12**, 384 (2021).
9. Z. Guan *et al*., *Nat. Commun.* **13**, 1581 (2022).
10. J. Dong *et al*., *Mol. Plant* **12**, 1463–1473 (2019).
11. J. Zhu *et al*., *eLife* **8**, e43582 (2019).
12. V. Rubio *et al*., *Genes Dev.* **15**, 2122–2133 (2001).
13. P. Wang *et al*., *Plant Cell* **33**, 3470–3486 (2021).
14. D. Liao *et al*., *Plant Cell* **34**, 4045–4065 (2022).
15. D. Das *et al*., *Nat. Commun.* **13**, 477 (2022).
16. J. Shi *et al*., *Cell* **184**, 5527–5540.e18 (2021).
17. S.-H. Park, J. S. Jeong, C.-H. Huang, B. S. Park, N.-H. Chua, *New Phytol.* **237**, 1215–1228 (2023).
18. L. B. Sheard *et al*., *Nature* **468**, 400–405 (2010).
19. D. Laha *et al*., *Plant Physiol.* **171**, 2364–2370 (2016).
20. X. Tan *et al*., *Nature* **446**, 640–645 (2007).
21. N. P. Laha *et al*., *Plant Physiol.* **190**, 2722–2738 (2022).
22. Y. T. Lu *et al*., *Plant Physiol.* **164**, 1456–1469 (2014).
23. D. Blüher *et al*., *Nat. Commun.* **8**, 2159 (2017).
24. S. Dong, Y. Wang, *PLOS Pathog.* **12**, e1005704 (2016).
25. Y. Sun *et al*., *Mol. Plant Pathol.* **20**, 533–546 (2019).
26. S. Dong *et al*., *PLOS Pathog.* **7**, e1002353 (2011).
27. G. Kong *et al*., *PLOS Pathog.* **11**, e1005139 (2015).
28. D. Yu *et al*., *Cell* **185**, 2370–2386.e18 (2022).
29. C. L. McCombe *et al*., *New Phytol.* **239**, 222–239 (2023).
30. V. Bhadauria, S. Banniza, A. Vandenberg, G. Selvaraj, Y. Wei, *Eukaryot. Cell* **12**, 2–11 (2013).
31. R. A. Dean *et al*., *Nature* **434**, 980–986 (2005).
32. X. Yan *et al*., *Plant Cell* **35**, 1360–1385 (2023).
33. R. J. O'Connell *et al*., *Nat. Genet.* **44**, 1060–1065 (2012).
34. A. G. McLennan, *Cell. Mol. Life Sci.* **63**, 123–143 (2006).
35. P. L. Plaumann, J. Schmidpeter, M. Dahl, L. Taher, C. Koch, *Front. Microbiol.* **9**, 1005 (2018).
36. S. T. Safrany *et al*., *J. Biol. Chem.* **274**, 21735–21740 (1999).
37. E. Grudzien-Nogalska, X. Jiao, M.-G. Song, R. P. Hart, M. Kiledjian, *RNA* **22**, 773–781 (2016).
38. S. T. Safrany *et al*., *EMBO J.* **17**, 6599–6607 (1998).
39. G. Zong *et al*., *FASEB J.* **35**, e21275 (2021).
40. S. B. Shears, H. Wang, *Molecules* **25**, 4515 (2020).
41. C. H. Khang *et al*., *Plant Cell* **22**, 1388–1403 (2010).
42. M. C. Giraldo *et al*., *Nat. Commun.* **4**, 1996 (2013).
43. P. Chardin, F. McCormick, *Cell* **97**, 153–155 (1999).
44. J. Chen *et al*., *Plant J.* **114**, 1209–1226 (2023).
45. D. Laha *et al*., *Plant Cell* **27**, 1082–1097 (2015).
46. Y. He, T. Zhang, H. Sun, H. Zhan, Y. Zhao, *Hortic. Res.* **7**, 152 (2020).
47. R. Morcuende *et al*., *Plant Cell Environ.* **30**, 85–112 (2007).
48. D. Secco *et al*., *Plant Cell* **25**, 4285–4304 (2013).
49. D. Secco *et al*., *New Phytol.* **193**, 842–851 (2012).
50. G. Castrillo *et al*., *Nature* **543**, 513–518 (2017).
51. J. Tang *et al*., *EMBO J.* **41**, e109102 (2022).
52. R. Schneider *et al*., *bioRxiv* 2024.10.18.619122 [Preprint] (2024).
53. O. M. Finkel *et al*., *PLOS Biol.* **17**, e3000534 (2019).
54. K. Hiruma *et al*., *Cell* **165**, 464–474 (2016).

ACKNOWLEDGMENTS

We thank the Plant Services Team at the Australian National University for providing *N. benthamiana* seedlings and all the Williams laboratory members and P. Solomon for helpful discussion. The authors acknowledge the use of the ANU crystallization facility. The authors also acknowledge the use of the Australian Synchrotron MX facility and thank the staff for their support. This research was undertaken in part using the MX2 beamline at the Australian Synchrotron, part of ANSTO, and made use of the Australian Cancer Research Foundation (ACRF) detector. Figures S12A and S14A were created with BioRender.com. **Funding:** This study was supported by an Australian Institute of Nuclear Science and Engineering Ltd. Postgraduate Research Award (C.L.M.); an Australian Government Research Training Programme Stipend (C.L.M.); ANU Future Scheme 35665 (S.J.W.); ARC Future Fellowship FT200100135 (S.J.W.); CAPES scholarships for Doctoral Students FC001 (S.d.P.); Louisiana Board of Regents grant no. LEQSF (2022-24)-RD-A-01 (E.O.-G. and C.S.Z.); Louisiana State University AgCenter Hatch project no. LAB94477 (E.O.-G.); RWTH Aachen University scholarships for doctoral students (A.W., F.C., and L.W.); and the Deutsche Forschungsgemeinschaft (DFG, German Research Foundation) 410278620 (U.S. and A.W.). **Author contributions:** Conceptualization: C.L.M., A.W., S.J.W., U.S.; Formal analysis: C.L.M., A.W., C.S.Z., F.C., S.A., D.J.E., E.O.-G., S.J.W.; Funding acquisition: E.O.-G., S.J.W., U.S.; Investigation: C.L.M., A.W., L.W., C.S.Z., F.C., S.A., J.R.G., S.d.P., E.E., S.S., E.O.-G.; Methodology: C.L.M., A.W., S.A., J.R.G., E.O.-G., S.J.W., U.S.; Project administration: C.L.M., A.W., S.J.W., U.S.; Supervision: C.L.M., A.W., E.O.-G., S.J.W., U.S.; Visualization: C.L.M., A.W., C.S.Z., F.C., S.A., E.O.-G.; Writing – original draft: C.L.M., A.W., E.O.-G.; Writing – review & editing: C.L.M., A.W., F.C., S.A., J.R.G., L.W., S.S., E.E., D.J.E., E.O.-G., S.J.W., U.S. **Competing interests:** The authors declare that they have no

competing interests. **Data and materials availability:** Where possible, all materials generated in this study will be made available upon request to the corresponding authors. The data that support the MoNUDIX protein structure described in this study are openly available under accession 8SXS at the PDB. The raw RNA-seq data are available from the National Center for Biotechnology Information under accession no. PRJNA1181513. All other data are available in the main text or the supplementary materials. **License information:** Copyright © 2025 the authors, some rights reserved; exclusive licensee American Association for the Advancement of Science. No claim to original US government works. https://www.science.org/about/science-licenses-journal-article-reuse

SUPPLEMENTARY MATERIALS

science.org/doi/10.1126/science.adl5764
Materials and Methods
Figs. S1 to S14
References (*55*–*98*)
MDAR Reproducibility Checklist
Data S1 to S16

Submitted 19 November 2023; resubmitted 7 November 2024
Accepted 10 January 2025
10.1126/science.adl5764

CHEMICAL PHYSICS

Quantum interference observed in state-resolved molecule-surface scattering

Christopher S. Reilly[1]*, Daniel J. Auerbach[2], Liang Zhang[3], Hua Guo[3], Rainer D. Beck[1]

Although the dynamics of collisions between a molecule and a solid surface are ultimately quantum mechanical, decohering effects owing to the large number of interacting degrees of freedom typically obscure the wavelike nature of these events. However, a partial decoupling of internal molecular motion from external degrees of freedom can reveal striking interference effects despite significant momentum exchange between the molecule and the bath of surface vibrations. We report state-prepared and state-resolved measurements of methane scattering from a room-temperature gold surface that demonstrate total destructive interference between molecular states related by a reflection symmetry operation. High-contrast interference effects prevail for all processes investigated, including vibrationally excited and vibrationally inelastic collisions. The results demonstrate the distinctly quantum mechanical effect of discrete symmetries in molecular collision dynamics.

The wave nature of matter, as described by the laws of quantum mechanics, is most directly manifested by interference phenomena. The first interference effects demonstrating the wave nature of atoms and molecules were observed by Immanuel Estermann and Otto Stern in 1930, just a few years after the advent of quantum mechanics, in the form of diffraction peaks in angular distributions measured for beams of helium (He) and molecular hydrogen (H_2) scattering from the surface of a lithium fluoride crystal (*1*). Diffraction of larger molecules, such as methane (CH_4), from crystalline surfaces is, however, much more difficult to observe owing to the dominating background of incoherent scattering events associated with collisional generation of surface phonons (quanta of surface vibrations) (*2*). Phonon generation is much stronger for these systems because of not only the better mass matching between the molecule and the heavy surface atoms but also the stronger van der Waals–mediated acceleration of impinging molecules (*3*, *4*). Coherent diffraction effects associated with elastic scattering therefore in general exert only a minor influence on measured angular distributions for larger molecules.

Despite the decohering influence of phonon-mediated momentum transfer, strong interference phenomena in surface collisions may nonetheless persist if the surface vibrations fail to couple to some subset of the molecule's internal degrees of freedom. In this event, quantum interference may manifest itself not in the angular distribution of the scattered molecules but rather in the distribution of population among the molecule's different rovibrational states. Notably, the interference effect that we investigated in this work applies only to molecules with some nontrivial low-energy internal structure (see supplementary text) so that the greater internal complexity of a polyatomic molecule, such as CH_4, relative to closed-shell atoms and diatomic molecules, such as He and H_2, serves in this context not to mask but rather to reveal quantum behavior.

A close analogy exists between the rovibrational state interference effect that we report in this work for methane scattering from a gold

[1]Institute of Chemical Sciences and Engineering (ISIC), École Polytechnique Fédérale de Lausanne (EPFL), Lausanne, Switzerland. [2]Max Planck Institute for Multidisciplinary Sciences, Göttingen, Germany. [3]Department of Chemistry and Chemical Biology, Center for Computational Chemistry, University of New Mexico, Albuquerque, NM, USA.
*Corresponding author. Email: christopher.reilly@epfl.ch

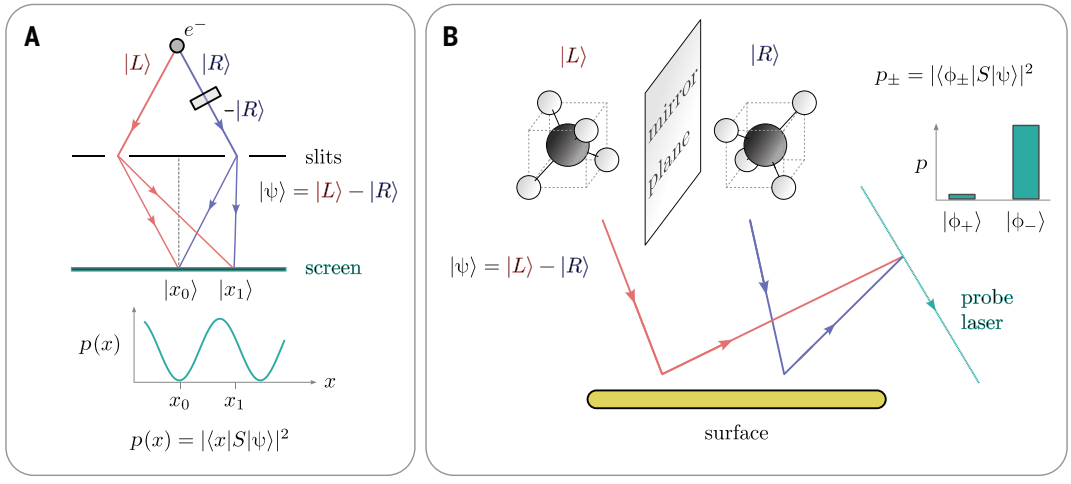

Fig. 1. Analogy between double-slit interference and methane-surface collisions. (**A**) In an electron (e^-) double-slit experiment, interference occurs between states $|L\rangle$ and $|R\rangle$, related to one another by a reflection about the system symmetry axis (dashed line), producing an oscillating intensity pattern $p(x)$ created by electrons striking a fluorescent screen. If a 180° phase shifter (gray rectangle) is placed between the source and one of the slits, destructive interference occurs at the point x_0 lying on the symmetry axis. (**B**) In a scattering event between a methane molecule and a solid surface, the probability p_+ for a transition to a reflection-symmetric state $|\phi_+\rangle$ from an antisymmetric state $|\psi\rangle$ is zero if the molecule-surface interaction is symmetric with respect to reflection, resulting in zero absorption of laser light tuned resonant with $|\phi_+\rangle$. In both scenarios, S represents the operator transforming the initial state $|\psi\rangle$ to its postscattering state $S|\psi\rangle$.

(Au) surface and the phenomenon of two-slit interference, the quintessential hallmark of wavelike behavior (*5*). It is worthwhile to clearly establish in what way the two effects are analogous. Figure 1A illustrates the classic electron double-slit experiment, which, for the purposes of the analogy, is modified to include a phase-shifting element (*6*, *7*) (gray rectangle). In this experiment, the left and right slits serve to respectively select the momentum states $|L\rangle$ and $|R\rangle$, and the state $|R\rangle$ is subjected to a 180° phase shift, $|R\rangle \rightarrow -|R\rangle$, resulting in the preparation of a quantum state $|\psi\rangle = |L\rangle - |R\rangle$ at the slit exits. A fluorescent screen placed after the slits serves as a detector, where a well-known sinusoidal interference pattern is observed (*8*).

In particular, destructive interference occurs at the point x_0 exactly between the two slits, resulting in a minimum in the measured screen intensity. The reason for this can be understood by considering the reflection symmetry (dashed line) of the system. The intensity at a point x on the screen is proportional to the probability $p(x)$ for an electron to be found at this location, which, according to the laws of quantum mechanics, is equal to the squared modulus of the complex amplitude $\langle x|S|\psi\rangle$, where $|x\rangle$ corresponds to a state localized at x, S is the operator transforming an initial state $|\psi\rangle$ to the state $S|\psi\rangle$ obtained after scattering from the two slits to the screen, and $\langle x|S|\psi\rangle$ is the overlap between the states $|x\rangle$ and $S|\psi\rangle$. For the initial state $|\psi\rangle$ considered in this example, this amplitude is a coherent difference $\langle x|S|L\rangle - \langle x|S|R\rangle$ of the amplitudes associated with the two slits. Upon a reflection Σ of the system about its symmetry axis, the states $|L\rangle$ and $|R\rangle$ are interchanged so that $\Sigma|L\rangle = |R\rangle$ and $\Sigma|R\rangle = |L\rangle$, whereas the state $|x_0\rangle$ is equal to its reflection $\Sigma|x_0\rangle$ because the point x_0 lies on the symmetry axis. In addition, by virtue of the system symmetry, we can also say that, for any initial state $|\psi'\rangle$, a reflection $\Sigma S|\psi'\rangle$ of the scattered wave $S|\psi'\rangle$ must be equal to the scattered wave $S\Sigma|\psi'\rangle$ produced by the reflected copy $\Sigma|\psi'\rangle$ of the initial state (i.e., Σ and S commute). From these considerations, it follows that the amplitudes $\langle x_0|S|L\rangle$ and $\langle x_0|S|R\rangle$ are equal, as:

$$\langle x_0|S|R\rangle = \langle x_0|S\Sigma|L\rangle = \langle x_0|\Sigma S|L\rangle = \langle x_0|S|L\rangle \quad (1)$$

This explains the destructive interference observed at the point x_0 because:

$$P(x_0) = |\langle x_0|S|\psi\rangle|^2 = |\langle x_0|S|L\rangle - \langle x_0|S|R\rangle|^2 = |\langle x_0|S|L\rangle - \langle x_0|S|L\rangle|^2 = 0 \quad (2)$$

One can more generally conclude that any initial state composed of a negative superposition $|L\rangle - |R\rangle$ of two states $|L\rangle$ and $|R\rangle$ related by reflection Σ will, after evolving through a Σ-symmetric system, necessarily experience destructive interference when projecting onto final states that are themselves Σ symmetric.

As stated earlier, a completely analogous interference effect occurs between the rovibrational states of a methane molecule during a collision with a gold surface. A conceptual illustration of the scattering experiment is shown in Fig. 1B. A methane molecule in its rovibrational ground state $|\psi\rangle$ exists in a negative superposition $|L\rangle - |R\rangle$ of quantum states $|L\rangle$ and $|R\rangle$ related to one another by a mirror reflection (see supplementary text). A collision with the surface will induce transitions from the ground rovibrational state $|\psi\rangle$ into excited rovibrational states $|\phi\rangle$, with the probability $p(|\phi\rangle)$ for a given transition $|\psi\rangle \rightarrow |\phi\rangle$ equal to the squared modulus of the amplitude $\langle\phi|S|\psi\rangle$, where S is the operator acting to transform an initial state to its postcollision state. As in the case of double-slit interference, the amplitude of a transition will be the coherent difference of the amplitudes associated with the states $|L\rangle$ and $|R\rangle$. However, unlike the double-slit case in which these amplitudes are determined simply by the path length of their associated trajectories, the amplitudes associated with different rovibrational transitions are, in general, very difficult to determine owing to the large number of participating degrees of freedom and the complexity of the associated potential energy surface (*9*).

Despite this, strong selection rules forbidding certain transitions may nonetheless prevail if the system possesses a reflection symmetry, permitting one to relate the transition amplitudes $\langle\phi|S|L\rangle$ and $\langle\phi|S|R\rangle$. In this event, one again recovers Eq. 2, which forbids scattering-induced transitions from a state $|\psi\rangle$ that is antisymmetric with respect to reflection (or of "odd" reflection parity $\sigma = -1$), to states $|\phi_+\rangle$ that are symmetric with respect to reflection (of "even" reflection parity $\sigma = +1$). No analogous symmetry restrictions on the other hand exist for transitions $|\psi\rangle \rightarrow |\phi_-\rangle$ between two states of odd σ so that such processes can, in general, occur.

The rovibrational states of methane are grouped into energy levels that are classified by pairs of quantum numbers (J, P) consisting of a quantum number J quantifying the squared angular momentum $J(J+1)$ (in units of $\hbar^2$) and an inversion parity P (not to be confused with reflection parity σ) equal to +1 or −1, depending on whether the states in the level are respectively even or odd under an inversion $\mathbf{x} \rightarrow -\mathbf{x}$ of the coordinates of the nuclei composing the molecule. Within each energy level, there are $2J+1$ states $|J, M_J, P\rangle$ corresponding to the different possible projections $M_J = -J, \ldots, J$ of the angular momentum vector onto an axis perpendicular to the surface (the "surface normal"). The reflection parity σ of the states $|J, M_J, P\rangle$ with $M_J = 0$ with respect to any symmetry plane containing the surface normal is determined by the product:

$$P(-1)^J \equiv \sigma_{PJ} \quad (3)$$

The ground rovibrational state $|J = 1,\ M_J = 0,\ P = -1\rangle$, for example, has an odd reflection parity, justifying our earlier assertion that this state can be represented by an antisymmetric superposition $|L\rangle - |R\rangle$ of mirror-image states. Incidentally, the symmetric superposition $|L\rangle + |R\rangle$ produces a hypothetical state $|J = 1, M_J = 0,\ P = +1\rangle$ that is essentially degenerate with the ground state but whose existence is forbidden by the requirement of antisymmetry under permutation of methane's four identical hydrogen nuclei (*10*).

In contrast with the states with quantum number $M_J = 0$, those with $M_J \neq 0$ have no definite reflection symmetry, in the same way that, in the two-slit experiment, a final state $|x_1\rangle$ corresponding to a point x_1 not located on the symmetry axis can be written as a combination $\frac{1}{2}[(|x_1\rangle + |-x_1\rangle) + (|x_1\rangle - |-x_1\rangle)]$ of states of even and odd reflection parity. Therefore, energy levels with $J > 0$ containing states with $M_J \neq 0$ are necessarily of mixed reflection parity, whereas those with $J = 0$ containing just a single state $|J = 0, M_J = 0, P\rangle$ are of a pure reflection parity $\sigma = \sigma_{P0} = P$.

Because the different states $|J, M_J, P\rangle$ occurring in an energy level (J, P) are degenerate, our spectroscopic detection technique cannot distinguish them and instead returns a signal proportional to the incoherent sum $\sum_{M_J=-J}^{+J} p(|J, M_J, P\rangle)$ of the state transition probabilities over an energy level. Therefore, even with preparation of an initial state of pure reflection parity, the existence of only a single reflection symmetry plane will not, in general, yield signatures of interference in final levels with $J > 0$, as every such level will necessarily contain states with $M_J > 0$ of mixed reflection parity that can be coupled by scattering to the initial state. If, however, we suppose that the scattering system is symmetric with respect to every plane containing the surface normal, then the implied continuous rotational symmetry gives rise to a well-known $\Delta M_J = 0$ scattering selection rule corresponding classically to conservation of the projection of angular momentum about the symmetry axis. Scattering from an initial level (J_i, P_i) with $J_i = 0$ to a final level (J_f, P_f) will therefore only populate the $M_J = 0$ state of the final level, which is of pure reflection parity $\sigma_{P_f J_f}$. If this reflection parity is not equal to that of the initial state, then the corresponding transition probability should be zero.

Collecting the levels (J_f, P_f) of equal P_f, one therefore expects, in light of Eq. 3, an alternation between strongly populated levels to very weakly populated levels as one goes from a level of "allowed" $\sigma_{P_f J_f} = P_i$ reflection parity to

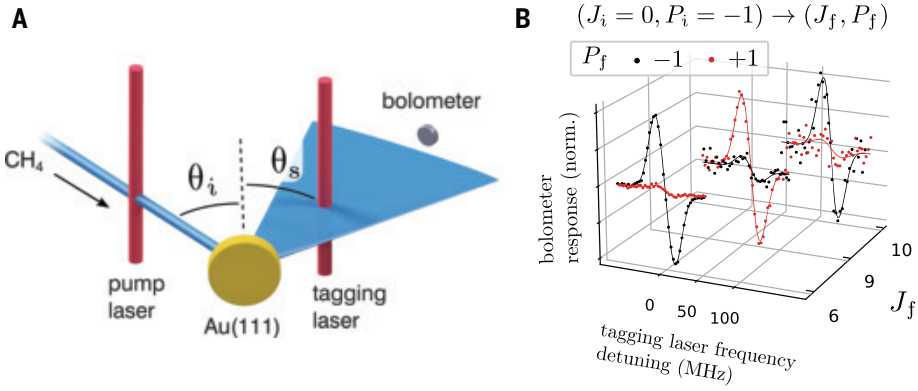

Fig. 2. Experimental diagram and v = 0 scattering results. (**A**) Schematic diagram of experiment. A molecular beam of CH_4 scatters from a Au(111) surface held at room temperature (300 K). A pump laser is used for rovibrational state preparation before scattering, and a tagging laser combined with a bolometer detector permit rovibrational state–resolved population measurements of the scattered molecules. The incident angle θ_i and scattering angle θ_s, defined with respect to the surface normal (dashed line), are independently variable. (**B**) FM tagging laser absorption lines probing CH_4 energy levels v = 0(J_f, P_f) populated by vibrationally elastic transitions from the ground rovibrational level v = 0 (J_i = 0, P_i = −1) induced by collisions with a Au(111) surface at an incident angle θ_i = 35° and kinetic energy E_t = 210 meV. The scattering angle θ_s at which measurements were made is J_f dependent (table S1). Each pair of traces of equal J_f are uniformly rescaled so that the taller traces of each pair all have the same height. Measurements are represented by points, and the curves, included as guides, are derivative-normal fits.

an adjacent level of necessarily "forbidden" reflection parity $\sigma_{P_f J_f \pm 1}$, mimicking the probability oscillations of the double-slit interference pattern $p(x)$. We herein use the term rovibrational state interference (RSI) to refer to the suppression of certain scattering channels owing to the quantum interference effect just described. In this work, we report the observation of high-contrast RSI signatures in our quantum state–prepared and quantum state–resolved experiments of methane scattering from a gold surface, revealing an infinite-fold reflection symmetry in the molecule-surface interaction never before observed in molecule-surface scattering.

Quantum state preparation and detection

Figure 2A presents a schematic diagram of our experimental technique, which uses a continuous molecular beam of rovibrationally cold methane that, before scattering from a clean and well-ordered (111) facet of a monocrystalline gold sample, is excited by a continuous-wave infrared (CW-IR) laser (the pump laser) tuned resonant to a transition between two rovibrational levels of methane. A second CW-IR laser (the tagging laser) tuned to another rovibrational transition transfers energy to scattered molecules occupying the lower level $\Lambda_f = (J_f, P_f)$ of the transition, and this absorbed energy is detected by a cryogenic bolometer, which captures the scattered molecules. We could independently vary the incident angles θ_i and the scattering angles θ_s and found that, for a given θ_i, the relative θ_s-resolved transition probabilities were insensitive to θ_s (fig. S2). For the measurements reported in the section "Methane scattering experiments", the angles θ_s were selected for large observed or expected molecular flux (tables S1 to S6). The initial kinetic energy E_i of the molecules is controllable, and the energies used range from 100 to 240 meV. In comparison, upon approaching the Au(111) surface, a methane molecule gains an additional estimated 150 meV of kinetic energy (*4*) owing to attractive van der Waals interactions mentioned earlier.

To study scattering originating from an energy level $\Lambda_i = (J_i, P_i)$, where the molecules are vibrationally excited, the pump laser was tuned to drive a transition, taking molecules from a highly populated level in the ground vibrational state manifold (v = 0) to the vibrationally excited level Λ_i, whereas the frequency of the tagging laser was modulated at a frequency f_t so that the response of the bolometer at f_t provided a relative measure of the $\Lambda_i \rightarrow \Lambda_f$ scattering probability. To measure relative scattering probabilities $\Lambda_i \rightarrow \Lambda_f$ when Λ_i and Λ_f are in the v = 0 manifold, a heterodyne technique was used, where the pump laser was tuned to transfer population out of the level Λ_i and the laser intensity was modulated at a frequency $f_p > f_t$. The intensity modulation served to generate in the bolometer response a beat note of frequency $f_p - f_t$, the amplitude of which was independent of contributions to the scattered population in Λ_f originating from any other levels $\Lambda_i' \neq \Lambda_i$ populated in the incident molecular beam. For further details, refer to the materials and methods and previous work (*11*).

Methane scattering experiments

Figure 2B presents CH_4/Au(111) scattering measurements for molecules originating in the ground state rovibrational level Λ_i, which, as we noted earlier, contains just a single state $v = 0|J = 0, M_J = 0, P = -1\rangle$. Plotted is the recorded bolometer response as the wavelength of the frequency-modulated (FM) tagging laser is scanned across a rovibrational transition with lower level $\Lambda_f = (J_f, P_f)$, producing a characteristic FM absorption line shape. We note that, for all the experiments presented in this work, we only probed final levels Λ_f belonging to the same nuclear spin species (*12*) as the initial level Λ_i, since collisional interconversion between the different species is, before consideration of any RSI effects, already expected to be very weak on account of the absence of strong magnetic interactions between the molecule and the nonmagnetic gold surface.

The values J_f = 6, 9, and 10 were found to be the only ones for which levels of both inversion parities $P_f = \pm 1$ exist and for which at least one of these levels was significantly populated in the scattered flux. For each of these values, there is, for a given J_f, one parity channel clearly dominating over the other. Moreover, the suppressed parity level for each J_f is the one whose suppression is predicted on the basis of RSI, as the associated M_J = 0 state reflection parity $\sigma = \sigma_{P_f J_f} = +1$ of these levels is opposite to that of the initial state.

We are unable to explain such striking disparities in the measured transition probabilities, as high as 20:1 for J_f = 6, without consideration of interference effects. The wave function ϕ_- of a state in a weakly populated level (J_f, P_f) can always be expressed as a superposition $\phi_- = \phi_l - \phi_r$ of wave functions ϕ_l and ϕ_r that only couple together through very weak centrifugal effects (*13*, *14*) and can be added together to form a wave function $\phi_+ = \phi_l + \phi_r$ of a state in the strongly populated level of equal J_f but opposite inversion parity. The relative phase in the superposition $\phi_+ = \phi_l \pm \phi_r$ has therefore, on one hand, a negligible influence on the molecule's energy and angular momentum but, on the other hand, a decisive influence on the transition probability in scattering. See fig. S1 for a concrete example of these wave functions for the M_J = 0 states of the (J = 6, $P = \pm 1$) levels.

RSI effects are also seen for surface collisions of molecules in vibrationally excited states. Figure 3, A and B, presents rovibrational state transition probabilities for vibrationally elastic scattering of molecules in the antisymmetric stretching mode fundamental (ν_3). Similar to v = 0, the ν_3 manifold has a distinct J = 0 level of odd inversion parity. However, in contrast to v = 0, for which the J = 0 level belongs to the *meta*-CH_4 nuclear spin species, the J = 0 level of the ν_3 manifold belongs to the *ortho*-CH_4 species, which has a rovibrational state structure roughly three times denser than the meta

species (*12*). When this fact is combined with the three-fold degeneracy of the ν_3 vibrational mode, the result is that, for moderate values of J, there exist several *ortho*-CH_4 ν_3 levels for each inversion parity P, which explains why there are, for example, five populations plotted for each P_f for $J_f = 6$.

For scattering originating from the $J_i = 0$ level (Fig. 3A), the results were remarkable. For each final level inversion parity P_f, the transition probabilities exhibited a pronounced alternation between strong and weak with an incrementing of the rotational quantum number J_f. The alternation was also seen to be staggered for the two different inversion parities $P_f = \pm 1$ and phased so that it was again the levels with positive $\sigma_{J_f P_f}$ that are suppressed, in conformance with the expectation that these channels will be RSI-suppressed in scattering originating from the ($J_i = 0$, $P_i = -1$) initial level of purely odd reflection parity. We note in passing that the RSI-forbidden ($J_f = 5$, $P_f = -1$) transition probabilities were found to be no stronger on average than those measured for the neighboring channels $J_f = 4$ and 6, their more prominent appearance on the plot owing rather to the normalization convention used (see caption of Fig. 3) and the anomalously low population measured in the RSI-allowed $J_f = 5$ channels.

The transition probability distributions completely change when the molecules were instead prepared in the rotationally excited $J_i = 2$ level (Fig. 3B). In this case, there was no discernible correlation in the transition probabilities with the final-level product $\sigma_{J_f P_f}$. The absence of RSI effects here is explained by the significant population of states $M_J \neq 0$ in the initial level, which will, as explained in the introduction, possess RSI-allowed scattering channels to any final level ($J_f > 0$, P_f).

Although the RSI effects demonstrated thus far concern scattering from levels with $J_i = 0$, we note that, by an identical logic, an analogous effect should exist for scattering into levels with $J_f = 0$. Figure 3C presents absorption traces probing $\nu_3 \rightarrow \nu_3$ scattering into the ($J_f = 0$, $P_f = -1$) level from two levels, $J_i = 1$ and $J_i = 2$, also of odd inversion parity. For the initial level $J_i = 1$, which has a positive $\sigma_{P_i J_i}$, no measurable population was detected in the negative $\sigma_{P_f J_f}$ final level, whereas this same level was significantly populated when the $J_i = 2$ level of positive $\sigma_{J_f P_f}$ was prepared.

RSI effects were also found to strongly influence transition probabilities in vibrationally inelastic collisions, taking molecules from the ν_3 ($J_i = 0$, $P_i = -1$) level to levels in the symmetric stretch mode fundamental (ν_1). Despite the nondegeneracy of the ν_1 vibrational mode, *ortho*-CH_4 levels of both inversion parity occurred for all states $J_f \geq 3$, with 18 total levels contained in the range $3 \leq J_f \leq 8$. Scattering results for these levels are summarized in Fig. 3D in the form of "parity ratios" obtained by dividing the average of the RSI-allowed $P_f = -(-1)^{J_f}$ transition probabilities by that of the RSI-forbidden levels $P_f = (-1)^{J_f}$. These ratios, approaching 10:1 at low J_f, show that RSI effects, though not quite as pronounced as those observed for $\nu_3 \rightarrow \nu_3$ scattering, nonetheless exert a dominating influence on the transition probabilities even for these more exotic scattering processes. We note that, for the three lowest plotted parity ratios ($J_f = 6$, 7, and 8), the RSI-forbidden channels are all below or just at the detection threshold so that reported parity ratios represent lower limits determined by the noise floor of our tagging measurements.

$\nu_3 \rightarrow \nu_1$ transitions in collisions with Au(111) were already known from recent work by our group to be rare (*15*), almost five times less likely than for collisions with Ni(111) under identical conditions (*16*). This fact we tentatively attributed to the limited catalytic activity of the chemically inert Au(111) surface toward methane activation (*15*, *17*). In these previous studies, only the ν_3 ($J_f = 1$, $P_f = +1$) *meta*-CH_4 level was prepared, precluding observation of RSI phenomena. The new observation of RSI signatures in these vibrationally inelastic processes sheds light on their mechanism. Their relative rarity might, for example, suggest that these events occur only at steps and other defects sparsely populated on the surface. Surface defects are, however, sites where a continuous reflection symmetry would be expected to be broken so that scattering into RSI-forbidden channels will be, in general, permitted. That scattering into these channels is still highly suppressed suggests that $\nu_3 \rightarrow \nu_1$ processes at Au(111) are not restricted to surface defect sites.

In addition to the RSI channel suppression effects so far reported, the existence of a continuous reflection symmetry should also give rise to a strong collisional alignment of molecular rotation in rotationally inelastic collisions. In particular, the associated $\Delta M_J = 0$ scattering selection rule implies that, on excitation from a rotationless $J_i = 0$ level to a rotationally excited $J_f > 0$ level, only the $M_J = 0$ state of the excited level will be populated, where the quantization axis about which the projection M_J is measured corresponds to the surface normal (dashed lines, Fig. 4A). The rotational properties of molecules scattering into a particular rovibrational level are, in other words, completely determined by the direction of the surface normal.

Rotational alignment of molecules in a given rovibrational level is evidenced by a polarization dependence in the line strength of a transition in which the level is a participant (see materials and methods). Our experimental geometry permits rotation of the surface and rotation of the tagging laser polarization about parallel axes (illustrated by angles θ_i and θ_t, respectively, in Fig. 4A). Figure 4B presents three traces that demonstrate the effect of rotations of the surface on the bolometer response $R(\theta_t)$

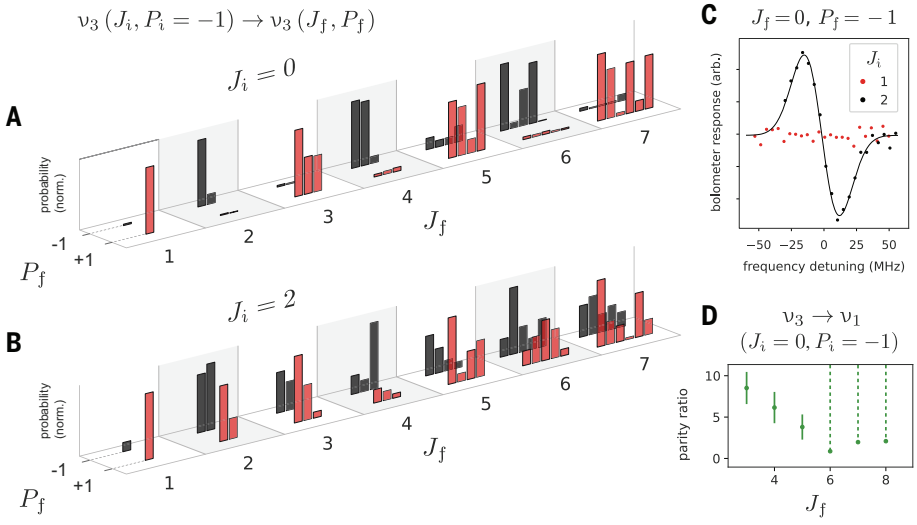

Fig. 3. CH_4/Au(111) scattering for $P_i = -1$ molecules in ν_3 vibrationally excited state. For all measurements, the incident angle $\theta_i = 35°$. (**A** and **B**) Vibrationally elastic $\nu_3 \rightarrow \nu_3$ transition probability distributions for levels $J_f > 0$. Bar heights for transitions of equal J_i and J_f are uniformly scaled to give a fixed height for the most probable transition, and transitions of equal J_f and P_f are ordered from left to right by energy. Estimated transition probabilities and corresponding uncertainties are compiled in table S7. Norm., normalized. (**C**) FM absorption lines for $\nu_3 \rightarrow \nu_3$ transitions for $J_f = 0$ and $J_i > 0$. A derivative-normal fit is applied as a guide. Arb., arbitrary. (**D**) Parity ratios for $\nu_3 \rightarrow \nu_1$ vibrationally inelastic scattering. For $J_f = 3$, 4, and 5, the vertical bars indicate 1σ uncertainty, whereas for $J_f = 6$, 7, and 8, the markers represent lower bounds. For $\nu_3 \rightarrow \nu_3$ transitions, levels $J_f < 4$ and $J_f \geq 4$ were respectively measured with an incident kinetic energy E_t of 100 and 210 meV. For $\nu_3 \rightarrow \nu_1$ transitions, $E_t = 100$ and 240 meV for $J_f < 6$ and $J_f \geq 6$, respectively. For selected scattering angles θ_s, see tables S2 to S5.

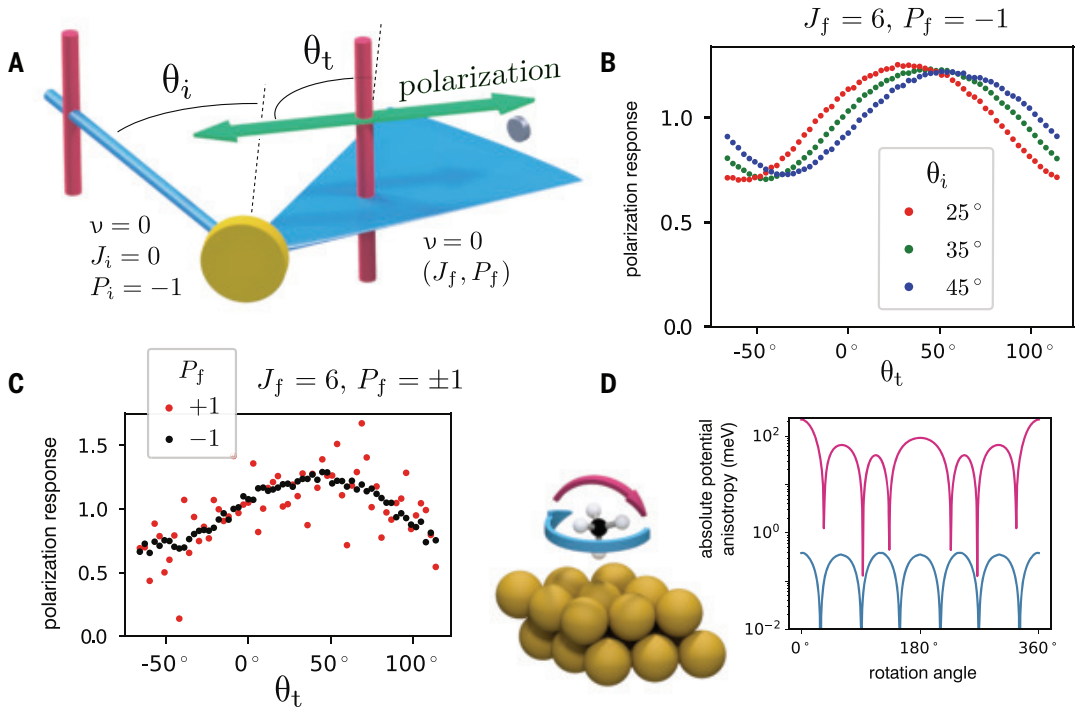

Fig. 4. CH_4/Au(111) rotational alignment measurements and potential energy curves. (**A**) Schematic of $v = 0$ collisional alignment measurements. See Fig. 2A for a description of unlabeled elements. (**B**) Tagging laser polarization scans for various incident angles θ_i. Measured scattering angle θ_s depends on incident angle θ_i (see table S6). (**C**) Comparison of polarization scans for RSI-allowed $P_f = -1$ and RSI-forbidden $P_f = +1$ channels and $\theta_i = 35°$ and $\theta_s = 36.4°$. Polarization response is defined to have a fixed mean of unity. For all measurements, $E_t = 210$ meV. (**D**) Cuts of the CH_4/Au(111) potential energy surface for rotations about the molecule center-of-mass at the $E_t = 100$ meV classical turnaround point. The three-dimensional model of molecule and surface atoms indicates for both traces the molecular orientation at rotation angle of 0°, and the color-coded arrows indicate the corresponding rotation axes. See the materials and methods for details on the construction of the potential energy surface.

to the polarization of the tagging laser tuned to probe scattering from the $v = 0$ *meta*-CH_4 scattering from $J_i = 0$ into the RSI-allowed $J_f = 6$ level. If the surface normal serves as a continuous symmetry axis, then a rotation $\theta_i \rightarrow \theta_i + \Delta\theta_i$ should result in a perfect translation $R(\theta_t) \rightarrow R(\theta_t - \Delta\theta_i)$ of the polarization response curve, which is precisely what the measurements reflect.

Notably, despite limited signal to noise, measurements in the RSI-forbidden $J_f = 6$ channel reveal a clear signature of strong rotational alignment that is indistinguishable in form from that of the RSI-allowed channel (Fig. 4C). RSI-forbidden transitions from a $J_i = 0$ level can occur either (i) through $\Delta M_J \neq 0$ collisions resulting from a breaking of the continuous rotation symmetry or (ii) through $\Delta\sigma \neq 0$ collisions resulting from a breaking of reflection symmetry (or both). The similarity of the polarization response curves for the two $J_f = 6$ channels suggests that the RSI-forbidden transitions reported here occurred through mechanism (ii).

Discussion

Several general conclusions follow from our results. We first discuss the implications of the strict M_J quantum number conservation required for RSI channel suppression. The large parity ratios we observed for scattering from $J_i = 0$ levels, greater than 80:1 for the $J_f = 2$ $v_3 \rightarrow v_3$ channels, indicate a M_J state purity in the RSI-allowed levels heretofore unobserved in molecule-surface scattering. Whereas previous scattering studies of diatomic molecules from an Ag(111) surface (*18*, *19*) have reported a strong propensity for collisional population of states of low $|M_J|$ relative to J_f, the polarization-based techniques used, combined with the relatively large J_f values involved, do not permit distinction of population in quantum states of neighboring M_J. The RSI phenomenon, in this sense, offers specifically "quantum" insight into the rotational scattering dynamics.

The high degree of M_J conservation we observed in turn implies a high degree of flatness of the Au(111) surface with respect to the methane molecule's rotational motion. This flatness manifests not only in our measurements but also in electronic structure calculations, which show the potential anisotropy for molecular rotations about the surface normal to be far weaker than that about axes parallel to the surface (Fig. 4D). We emphasize that this degree of flatness is certainly not the rule in methane-surface scattering. RSI parity ratios extracted from similar measurements reported for CH_4 scattering from Ni(111) (*11*), another close-packed metal surface, are never greater than 3:1, and oxidation of this surface is moreover found to completely eliminate any preference for σ_{PJ}-conserving channels.

Another equally significant implication of the reported results concerns the molecule's translational degrees of freedom (i.e., molecular center-of-mass motion). As mentioned, quantum signatures in the form of diffraction peaks for larger molecules such as CH_4 are typically obscured by exchange of momentum between the molecule and the surface, particularly at noncryogenic surface temperatures (*2*, *20*–*24*). The presence of very-high contrast interference effects in the rovibrational state transition probabilities reported in this work for a room-temperature surface implies that molecular rotation in the plane parallel to the surface must be strongly decoupled from the decohering influence of the bath of surface vibrations. This is further attested to by the lack of any signification variation observed in the measured RSI parity ratios across the phonon-broadened range of scattering angles θ_s over which significant scattering occurs (fig. S2).

Lastly, we note that these results serve as a particularly cogent illustration of the role of symmetry in quantum mechanics. To explain the striking regularities in the scattering measurements reported here, we consider the existence of a continuous family of reflection symmetries in the molecule-surface interaction. These symmetries are all discrete in that their action results always in a finite change in the molecular coordinates. In a classical context, discrete symmetries are confined to a limited role (*25*) owing to the inapplicability of Noether's theorem (*26*), which concerns only infinitesimal symmetry operations. The quantum mechanical principle of superposition elevates the role of reflections and other discrete symmetries (*27*). The high-contrast interference phenomena that we report in this work are a product of precisely this interplay between symmetry and superposition and demonstrate that, even for complex room-temperature molecular scattering systems, quantum mechanical effects can dominate. These findings therefore not only contribute to our fundamental understanding of molecule-surface

interactions but might also find application in quantum information science.

REFERENCES AND NOTES

1. I. Estermann, O. Stern, *Eur. Phys. J. A* **61**, 95–125 (1930).
2. A. Al Taleb, G. Anemone, L. Zhou, H. Guo, D. Farías, *J. Phys. Chem. Lett.* **10**, 1574–1580 (2019).
3. J. R. Manson, in *Handbook of Surface Science*, vol. 3 of Dynamics, E. Hasselbrink, B. I. Lundqvist, Eds. (North-Holland, 2008), pp. 53–93.
4. S. M. Wetterer, D. J. Lavrich, T. Cummings, S. L. Bernasek, G. Scoles, *J. Phys. Chem. B* **102**, 9266–9275 (1998).
5. "Quantum Behavior" in *The Feynman Lectures on Physics*, vol. 3 (Basic Books, 2011), chap. 1.
6. V. L. Lyuboshitz, Ya. A. Smorodinksii, *Sov. Phys. JETP* **48**, 19–22 (1978).
7. N. Osakabe *et al*., *Phys. Rev. A Gen. Phys.* **34**, 815–822 (1986).
8. R. Bach, D. Pope, S.-H. Liou, H. Batelaan, *New J. Phys.* **15**, 033018 (2013).
9. L. Zhang, B. Jiang, *Phys. Rev. Lett.* **123**, 106001 (2019).
10. M. Quack, in *Handbook of High-Resolution Spectroscopy* (John Wiley & Sons, Ltd., 2011), pp. 659–722.
11. C. S. Reilly, P. Floß, B.-J. Chen, D. J. Auerbach, R. D. Beck, *J. Chem. Phys.* **158**, 214202 (2023).
12. E. B. Wilson Jr., *J. Chem. Phys.* **3**, 276–285 (1935).
13. K. T. Hecht, *J. Mol. Spectrosc.* **5**, 355–389 (1961).
14. K. T. Hecht, *J. Mol. Spectrosc.* **5**, 390–404 (1961).
15. P. Floß, C. S. Reilly, D. J. Auerbach, R. D. Beck, *Front Chem.* **11**, 1238711 (2023).
16. J. Werdecker, M. E. van Reijzen, B.-J. Chen, R. D. Beck, *Phys. Rev. Lett.* **120**, 053402 (2018).
17. J. Werdecker *et al*., *Phys. Rev. Res.* **2**, 043251 (2020).
18. A. C. Luntz, A. W. Kleyn, D. J. Auerbach, *Phys. Rev. B Condens. Matter* **25**, 4273–4275 (1982).
19. G. O. Sitz, A. C. Kummel, R. N. Zare, *J. Chem. Phys.* **89**, 2558–2571 (1988).
20. T. Andersson *et al*., *J. Chem. Phys.* **113**, 9262–9267 (2000).
21. T. Kondo, T. Sasaki, S. Yamamoto, *J. Chem. Phys.* **116**, 7673–7684 (2002).
22. T. Kondo, D. Mori, R. Okada, M. Sasaki, S. Yamamoto, *J. Chem. Phys.* **123**, 114712 (2005).
23. T. Kondo, A. Al Taleb, G. Anemone, D. Farías, *J. Chem. Phys.* **149**, 084703 (2018).
24. A. Al Taleb, D. Farías, *Phys. Chem. Chem. Phys.* **19**, 21267–21271 (2017).
25. E. P. Wigner, *Proc. Am. Philos. Soc.* **93**, 521–526 (1949).
26. E. Noether, *Mathematisch-Physikalische Klasse* **1918**, 235–257 (1918).
27. P. R. de Olano, *Philos. Sci.* **84**, 1275–1288 (2017).
28. C. Reilly, D. J. Auerbach, L. Zhang, H. Guo, R. D. Beck, Quantum interference observed in state-resolved molecule-surface scattering, Dryad (2025); https://doi.org/10.5061/dryad.g4f4qrg0j.

ACKNOWLEDGMENTS

We acknowledge J. Hutson, A. van der Avoird, and M. Quack for enlightening discussions about the role of symmetry in molecular scattering. **Funding:** Funding for this work was provided by SNFS 200497 to R.D.B. and US NSF (CHE-2306975) to H.G. **Author contributions:** Conceptualization: R.D.B., D.J.A., C.S.R.; Methodology: R.D.B., D.J.A., C.S.R., L.Z., H.G.; Funding acquisition: H.G., R.D.B.; Project administration: H.G., R.D.B.; Supervision: H.G., R.D.B.; Writing: C.S.R., D.J.A., R.D.B., H.G. **Competing interests:** The authors declare that they have no competing interests. **Data and materials availability:** The data underlying the results presented in this work, including those presented in the supplementary materials, have been made publicly available on Dryad (*28*).

SUPPLEMENTARY MATERIALS

science.org/doi/10.1126/science.adu1023
Materials and Methods
Supplementary Text
Figs. S1 and S2
Tables S1 to S7
References (*29*–*53*)

Submitted 23 October 2024; accepted 15 January 2025
10.1126/science.adu1023

HYDROGELS

Hydro-locking in hydrogel for extreme temperature tolerance

Xiaochen Zhang[1]†, Dong Li[1]†, Xuxu Yang[2,3,4,5]†*, Lei Wang[1], Guo Li[1], Tuck-Whye Wong[2], Tiefeng Li[2,3,5]*, Wei Yang[2], Zisheng Luo[1,4]*

Hydrogels consist of cross-linked polymers that are highly swollen with water. Water evaporation or freezing during temperature changes may lead to stiff and brittle hydrogels. We introduce a strategy called "hydro-locking," which involves immobilizing the water molecules within the polymer network of the hydrogel. This is accomplished by establishing robust connections between water molecules and the polymer by using sulfuric acid. A sacrificial network is introduced to shield the prime polymer network from collapsing. Under the hydro-locking mode, an alginate-polyacrylamide double-network hydrogel remains soft and stretchable within a temperature range that spans from −115° to 143°C. The strategy works with a range of hydrogels and solutions and may enable the preservation and observation of materials or even living organisms at extreme temperatures.

Hydrogels, composed of water-filled cross-linked polymer networks, have been studied and used in tissue engineering (*1*, *2*), flexible electronics (*3*, *4*), and soft robotics (*5*, *6*). Enhancements in polymer networks have rendered hydrogels highly stretchable and tough (*7*–*9*). However, unlike elastomers with intrinsic entropic elasticity, hydrogels rely on the presence of mobile water molecules for their flexibility (*10*). Consequently, such dependency causes hydrogels to become stiff and brittle when subjected to water loss through evaporation or freezing during temperature change.

Locking water molecules within the polymer network of a hydrogel and maintaining its mobility are crucial for preserving the mechanical properties of the hydrogel across a broad temperature range (*10*). Current approaches involve substituting water with other liquids, increasing the phase transition temperature of the hydrogels. These solvents include ionic liquids (*11*) and aqueous solutions of inorganic salts (*12*, *13*), nonvolatile organic compounds such as trehalose (*14*), zwitterionic osmolytes (*15*), and combinations thereof (*16*, *17*). Ionic liquid gels exhibit a wide temperature range; however, they tend to absorb moisture from the air, leading to performance degradation over time (*18*, *19*). Aqueous solutions can incorporate additional components to raise the energy barrier for water transformation from a disordered to an ordered ice structure (*20*), reducing the freezing temperature of the solvent, typically between −20° and −80°C. The freezing temperature of the substituted solvent thus determines the lower temperature boundary of the hydrogel. Because water boils at 100°C at ambient pressure, the upper temperature threshold of hydrogels in these aqueous systems typically remains below 80°C (*16*, *21*). In hydrogels of substituted solvents, the water molecules are still mobile, leaving risks for their transition into ice or departure from the hydrogel, rendering the polymer network fragile.

[1]College of Biosystems Engineering and Food Science, Key Laboratory of Ago-Products Postharvest Handling of Ministry of Agriculture and Rural Affairs, Zhejiang University, Hangzhou, China. [2]Center for X-Mechanics, Department of Engineering Mechanics, Zhejiang University, Hangzhou, China. [3]State Key Laboratory of Fluid Power and Mechatronic Systems, Hangzhou, China. [4]Innovation Center for Postharvest Agro-Products Technology, Zhejiang University, Hangzhou, China. 5Institute of Fundamental and Transdisciplinary Research, Zhejiang University, Hangzhou, China.
***Corresponding author. Email: xxyang@zju.edu.cn (X.Y.); litiefeng@zju.edu.cn (T.L.); luozisheng@zju.edu.cn (Z.L.)**
†These authors contributed equally to this work.

Design and preparation for hydro-locking

In this study, we achieved the stabilization of hydrogels at temperatures that surpass the typical liquid-phase temperature range of aqueous solutions through complete "hydro-locking," in which a majority of the water molecules are securely immobilized within the polymer network of the hydrogel, preventing their departure or transformation into ice. Sulfuric acid (H_2SO_4) demonstrates robust binding capabilities to water (*22*), as well as to polymers through ionic interactions and hydrogen bonds (Fig. 1A) (*23*). A single H_2SO_4 molecule can form multiple hydrates, with the binding energy surpassing 60 kcal mol^{-1} for hexahydrate (*22*). At elevated concentrations, H_2SO_4 can dehydrate hydrogen and hydroxy groups within polymer networks (*24*). During this dehydration process, acidification and sulfating reactions occur, and H_2SO_4 binds to polymers by displacing protonable groups, such as hydroxy groups, on the polymer chains (*25*).

We used an alginate-polyacrylamide double-network hydrogel (DN-gel) as the model material and treated it with H_2SO_4 to demonstrate the hydro-locking strategy (Fig. 1A). The DN-gel was initially immersed in H_2SO_4 solutions of varying concentration to create sulfuric hydrogel (S-gel). During immersion, H_2SO_4

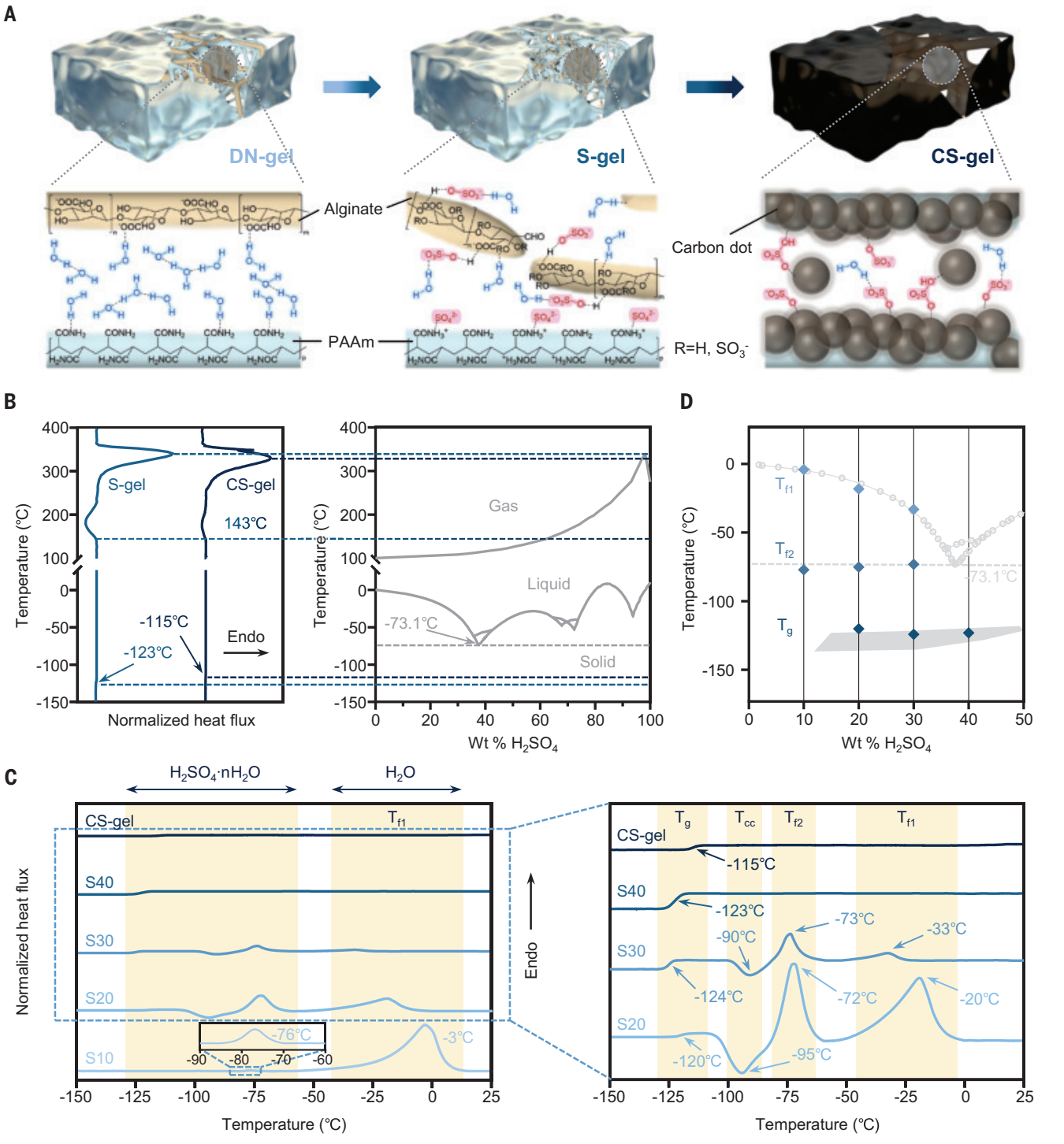

Fig. 1. Hydro-locking strategy and the phase transition temperature of S-gels. (**A**) A double-network hydrogel has a large proportion of free water among their polymer networks. H_2SO_4 molecules lock all water molecules on the polymer networks of hydrogels. (**B**) DSC measurements of S-gel and CS-gel demonstrate that no phase transition occurs between −115° and 143°C. The temperature range exceeds that of the liquid state of the binary H_2SO_4-H_2O system. (**C**) DSC measurements of various hydrogels from −150° to 25°C. The temperature regions of the glass transition (T_g), cold crystallization (T_{cc}), and freezing (T_{f1} and T_{f2}) are highlighted. The disappearance of these peaks signifies a reduction in free water molecules. (**D**) Comparison of thermodynamic events with phase diagram of the H_2SO_4-H_2O system from −175° to 25°C. Diamonds indicate the T_g and T_f emphasized in (C). The phase change progresses of the binary H_2SO_4-H_2O system are indicated in gray. Circles inidcate ice transition (*26*). The dashed line indicates the lowest freezing temperature of the binary H_2SO_4-H_2O system as a eutectic melting of ice and H_2SO_4 hydrates (*27*). The shaded area indicates the range of T_g for the binary H_2SO_4-H_2O system (*37*).

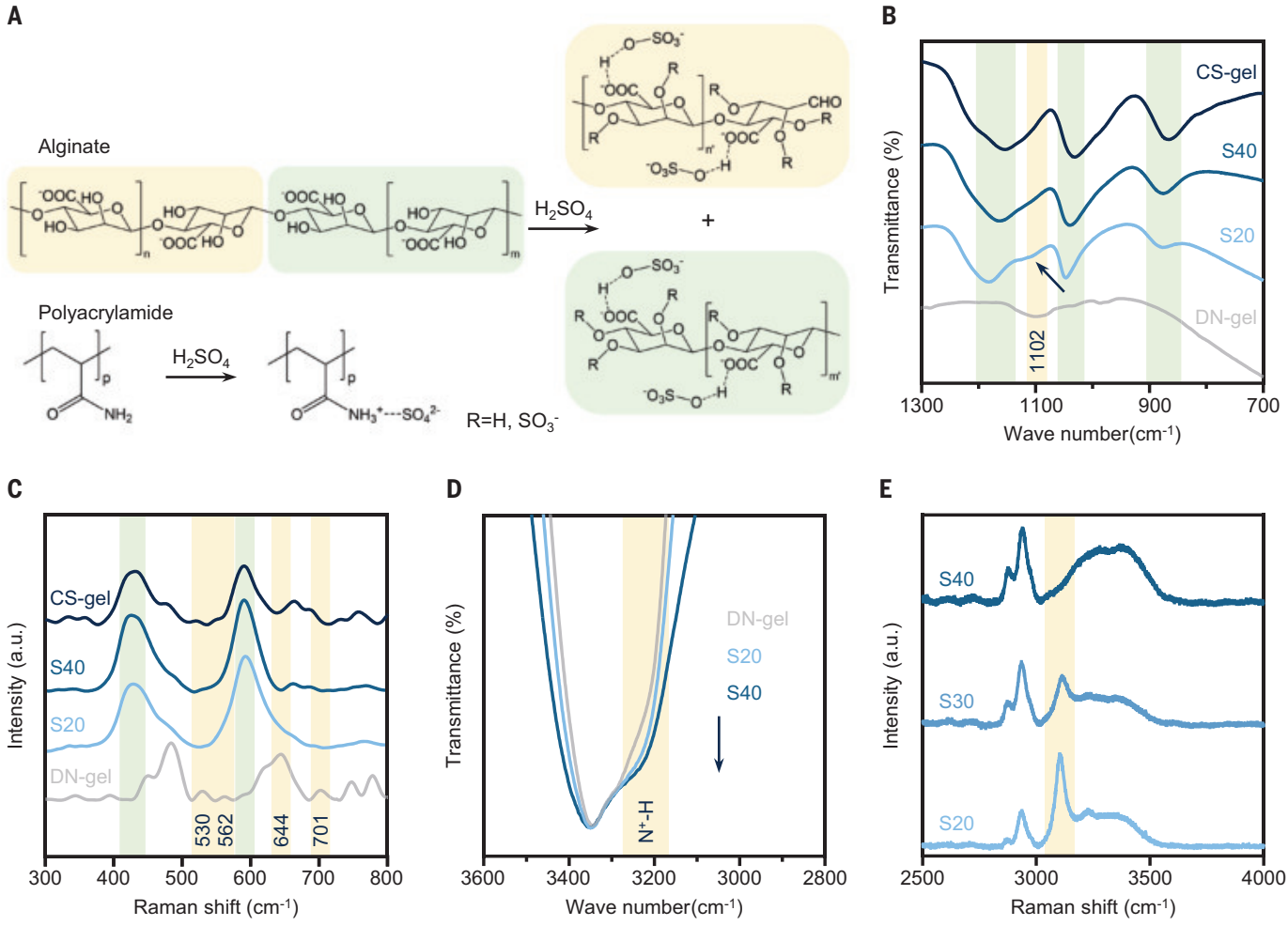

Fig. 2. Reactions and interactions in S-gels. (**A**) Chemical structures of alginate and polyacrylamide and structure alterations of them after treated with H_2SO_4. (**B**) FTIR spectra of DN-gel, S20, S40, and CS-gel in the range of 700 to 1300 cm^{-1}. The shoulder peak in S20 assigned to C–O stretching is indicated with an arrow, and the peaks related to H_2SO_4 are indicated in green. (**C**) Raman spectra of S20, S30, S40, and CS-gels from 300 to 800 cm^{-1}. The peaks related to HSO_4^- and/or SO_4^{2-} ions are indicated in green. (**D**) FTIR spectra of DN-gel, S20, and S40 in the range of 2800 to 3600 cm^{-1}. In (B) to (D), the changes in the peak intensity highlighted in yellow characterize [(A), top] the hydrolysis of alginate and [(A), bottom] the acidification of polyacrylamide. They exhibit a concentration-dependent manner, indicating stronger reactions and acidification upon increased acidity. (**E**) Raman spectra of S20, S30, and S40 gels at −130°C from 2500 to 4000 cm^{-1}. The highlighted area indicates the peak for $-NH_2$ symmetric stretching. The disappearance of this peak indicates that $-NH_2$ groups are being grafted by H_2SO_4 hydrates.

reacts with the polymer chains, particularly alginate, leading to hydrolysis of glycosidic linkages and sulfation of hydroxy groups. Meanwhile, the H_2SO_4 molecules are connected on the surface of the polymer chains, spatially extending the area where the polymer could lock water molecules and accomplishing it by forming H_2SO_4 hydrates. The reactions generate fragments and branched structures of glycosyl polymer chains (Fig. 2A). Subsequently, we carbonized the S-gel in a 60°C oven for more than 48 hours, resulting in a fully carbonized sulfuric hydrogel (CS-gel). In the CS-gel, alginate chains degraded further, forming carbon dots that attach to and cover the main polyacrylamide chains, preventing it from overreaction with H_2SO_4 and collapse (Fig. 3).

Characterization and validation of hydro-locking

Hydro-locking induces a delay in the phase transition of all components within the hydrogel. Differential scanning calorimetry (DSC) results revealed a singular glass transition event for both S-gel and CS-gel, occurring at glass transition temperatures (T_g) of −123° and −115°C, respectively (Fig. 1B). This phase transition temperature is 42°C lower than the lowest freezing temperature (T_f) recorded for the H_2SO_4-H_2O binary system (*26*). The H_2SO_4 solution exhibited a tendency to avoid nucleation at low temperatures (*27*), aligning with the characteristic of hydrogel to inhibit nucleation (*28*), which contributes to the low phase-transition temperature. Hydro-locking also eliminates the evaporation of water from the hydrogel. DSC results showed an exothermic peak, with an onset temperature at 143°C, instead of an endothermic peak. A wide endothermic peak followed at >300°C that corresponded to the evaporation of the H_2SO_4-H_2O binary solution (Fig. 1B). These results demonstrated that the hydrogel did not exhibit a phase transition across a temperature range from −115° to 143°C.

We validated the success and impact of hydro-locking with a comparative analysis of a

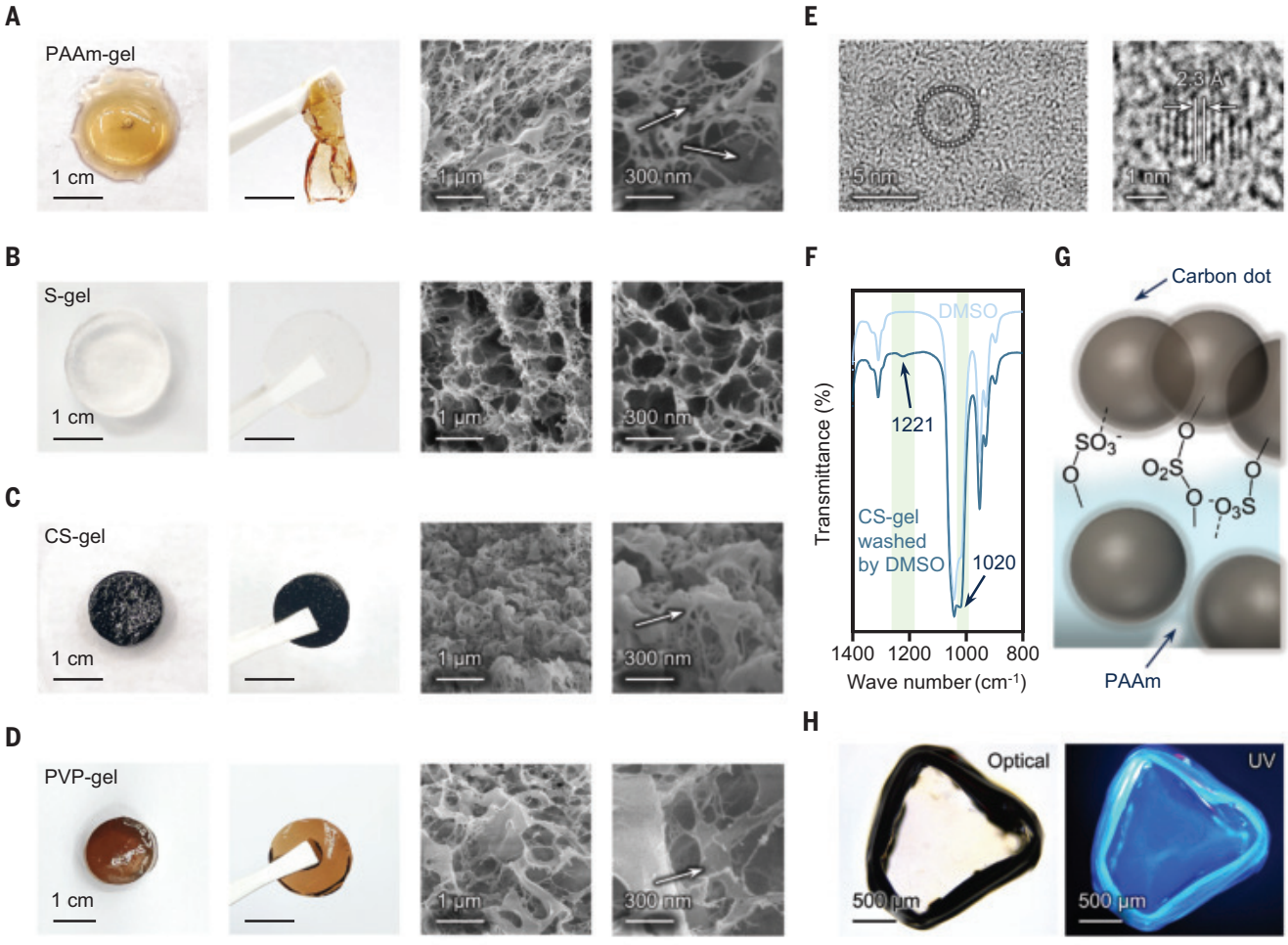

Fig. 3. Structure properties of S-gels and in situ carbon dots. (**A** to **D**) Optical and scanning electron microscope (SEM) images illustrating the microscope morphology of polymers in (A) PAAm-gel after treating with H_2SO_4 and heating in an oven at 60°C, (B) S-gel, (C) CS-gel, and (D) PVP hydrogel after treating with H_2SO_4 and heating in an oven at 60°C (PVP-gel). The arrows indicate the discontinuous filaments in PAAm-gel and protective carbon layer in CS-gel and PVP-gel. (**E**) Transmission electron microscopy images of carbon dots extracted from the CS-gel. (**F**) FTIR spectra of CS-gel washed by DMSO and DMSO from 800 to 1400 cm^{-1}. The peaks at 1020 cm^{-1} and 1221 cm^{-1} indicate the organo sulfate groups, which (**G**) connect carbon dots to the PAAm chains. (**H**) Optical and UV images of CS-gel washed with DMSO. The images were obtained with an inverted fluorescence microscope (Leica DMi8, Leica Biosystems, Germany) equipped with an excitation light source of 340 to 380 nm.

series of S-gels on their phase-transition behaviors (Fig. 1C). At lower H_2SO_4 concentrations, as seen in the S10 gel (the number indicates the H_2SO_4 concentration), we observed two peaks, at −3°C (T_{f1}) and −76°C (T_{f2}). As the H_2SO_4 concentration increased, as seen in the S20 and S30 gels, two endothermic peaks appeared above −50°C (T_{f1}) and around −73°C (T_{f2}), along with an exothermic peak connected to T_{f2} representing the cold crystallization process (T_{cc}) and a T_g at around −120°C. T_{f1} is associated with the ice crystallization, which diminishes with increasing H_2SO_4 concentration (Fig. 1D). The area of this peak, with higher H_2SO_4 concentration, decreases to 2.15% of S10 at S30 gel, indicating reduced overall water mobility (details and molar ratio analysis based on the enthalpy changes acquired from the DSC diagrams and the heat of fusion for H_2O and H_2SO_4 hydrates are provided in the supplementary text, with results in table S1). T_{f2} matches the phase-transition temperature of H_2SO_4 hydrates (*27*, *29*). The area of this peak initially increases around 24-fold with the rise in H_2SO_4 concentration from S10 to S20 and then decreases to about 27% of its value at S20 as the concentration further increases from S20 to S30. The emergence of T_g signifies the creation of a new phase, which we posit as being the H_2SO_4 hydrates grafted onto the polymer network. At sufficiently high H_2SO_4 concentrations, as in the S40 gel, the peaks of T_{f1}, T_{f2}, and T_{cc} disappeared, and only the T_g remains. In this case, an adequate amount of H_2SO_4 molecules serve as anchors, connecting both the water molecules and the polymer chains. Therefore, a vast majority of water molecules are locked by H_2SO_4 as H_2SO_4 hydrates and grafted onto the polymer network of the hydrogel.

Fourier transform infrared (FTIR) and Raman spectroscopy helped to identify the reactions and acidification during the forge of hydro-locking (Fig. 2, B to D). In the FTIR spectra, the intensity of the peak at around 1102 cm^{-1} for C–O stretching in CH–OH reduces evidently in S-gels, indicating the hydrolysis of alginate. The process can also be characterized by the reduction of the peaks in Raman spectra at 644 and 701 cm^{-1} for symmetrical stretching of ring deformation and glycosidic linkage, along with the peaks at 530 and 562 cm^{-1} for the deformation vibration of

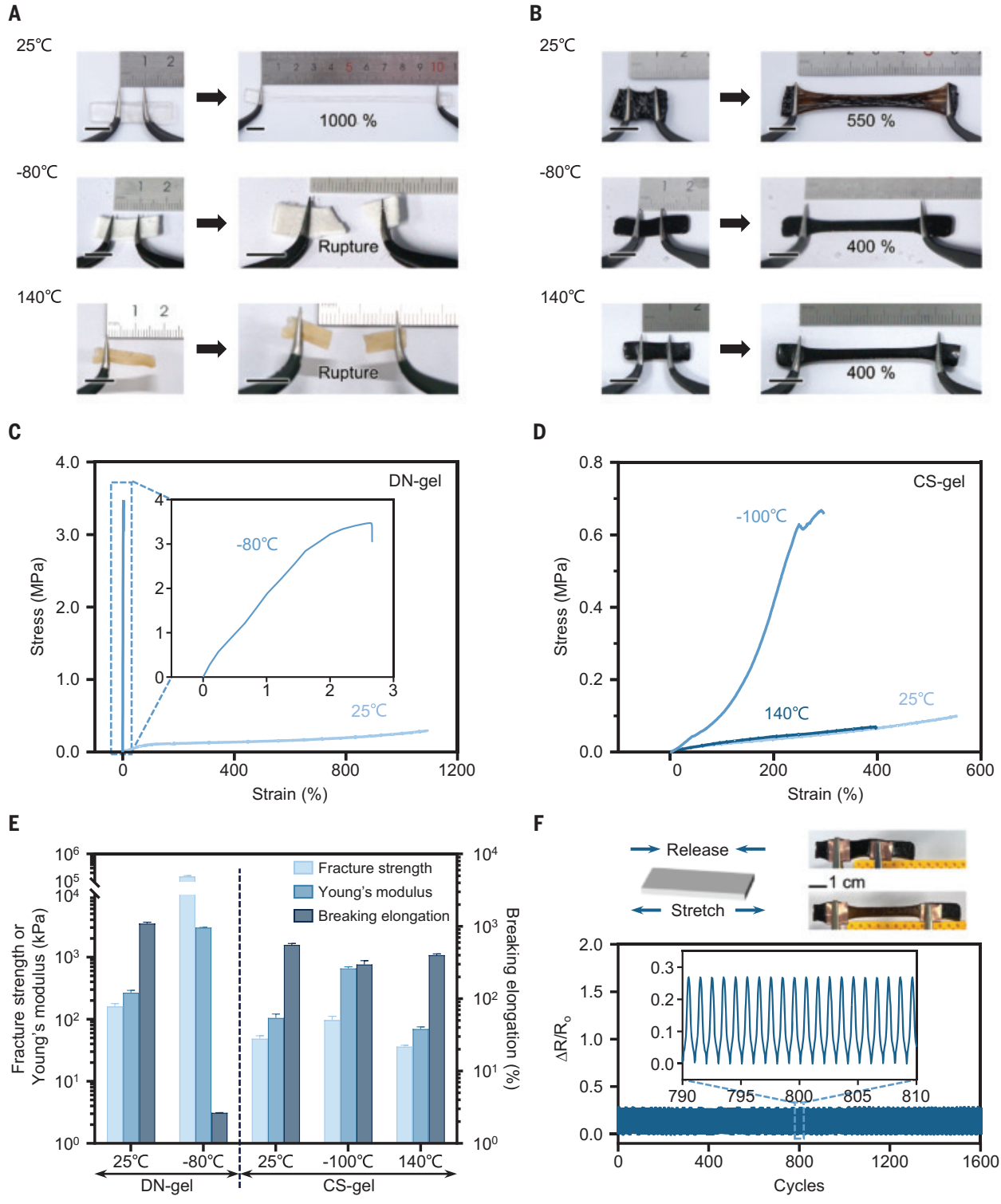

Fig. 4. Mechanical properties of CS-gel at extreme temperatures. (**A** and **B**) Optical images of (A) DN-gel and (B) CS-gel when stretched at 25°, −80°, and 140°C. (**C** and **D**) Tensile stress-strain curves of (C) DN-gel at 25° and −80°, and (D) CS-gel at 25°, −100°, and 140°C. (**E**) A comparison of fracture energy, Young's modulus, and breaking elongation of DN-gel at 25° and −80°, and CS-gel at 25°, −100°, and 140°C (n = 3 independent measurements). (**F**) Relative resistance ratio of the CS-gel when subjected to repeated stretch.

C–C–C and C–O–C. The hydrolysis of alginate not only binds sulfate groups onto the polymer networks and extends the area of locking water molecules spatially but also facilitates the sacrifice of alginate during the protective carbon layer formation at the later carbonization process. The H_2SO_4 molecules are also connected to the polymer chains through ionic interactions based on acidification. Such a process produces

acidified groups such as amide cation, resulting in a shoulder peak in the FTIR spectra near 3200 cm^{-1} assigned to the stretching vibration of N^+–H.

The hydro-locking was further validated by detecting the binding status of water on the polymer chains at various temperatures. In the Raman spectra, a peak between 3100 and 3200 cm^{-1} represents –NH_2 symmetric stretching in the acrylamide monomer. This group is typically obscured by water or other solvent molecules through hydrogen bonding, rendering it undetectable (*30*). Only upon the full detachment of solvent molecules from polymer networks by freezing does –NH_2 become exposed, allowing the peak to manifest (fig. S1A). The presence of this peak serves as an indicator of the binding state of polymer with the solvent molecule, which is typically water and, in this case, also H_2SO_4 hydrates. Raman spectroscopy of the S-gels was conducted at various temperatures (Fig. 2E and fig. S1). In the presence of ample free water, as in S20, –NH_2 covered by free water was exposed at –50°C when the water freezes. By increasing the H_2SO_4 concentration, water molecules were captured by H_2SO_4, forming H_2SO_4 hydrates. Hence, the peak of –NH_2 symmetric stretching remained indistinct at –50°C but appeared at –100°C and lower temperatures. In S40, the peak of NH_2 symmetric stretching did not emerge at any tested temperature. This is attributed to the strong connections forged between –NH_2 groups and H_2SO_4 hydrates. The covering of H_2SO_4 hydrate persisted even at a temperature of –130°C, which is below the T_g of S40, when the entire system vitrifies.

At elevated temperatures, the CS-gel undergoes a phase transition at around 140°C, which diverges from conventional hydrogels that typically desiccate at the water boiling point of 100°C.

Thermogravimetric analysis (TGA) and DSC analysis were performed to investigate the difference (figs. S2 and S3). Heating from 30°C, the H_2SO_4 exhibits varying water absorption capacities, and the H_2SO_4 solution is gradually concentrated as the H_2SO_4 hydrates lose bound water. Each temperature corresponds to a different water content in the hydrogel once the hydrogel achieves equilibrium, thus locking in different amounts of water. The boiling point of the H_2SO_4 solution increases with the solution concentrating and reaches higher than that of water, so the concentrating process continues above 100°C. At around 140°C, we observed an exothermic peak in the DSC curve of CS-gel, representing a degradation process rather than evaporation. We synthesized a series of CS-gels with varying contents of acrylamide and alginate, treated them with different concentrations of H_2SO_4 solutions, and carbonized them at temperatures ranging from 60° to 140°C. The reactions between H_2SO_4 and polymer components were consistent, resulting in almost identical onset temperatures of the degradation process at around 140°C and peak temperatures at around 180°C. The reaction degrades the polymer components and generates products such as CO_2, which cause an additional decrease in mass.

Further investigations into the performance of CS-gels at temperatures exceeding 140°C reveals that at around 200°C, at which the exothermic peak has been passed, the reaction gradually slows down because the polymer network has collapsed. The decreasing rate of mass loss in the TGA results also slows down at around 200°C. The disrupted polymer networks fail to graft the H_2SO_4 hydrate, causing it to leak, forming cavities inside the hydrogels, and the hydrogel dries into a sponge-like structure (fig. S4). The H_2SO_4 solution that leaks from the hydrogel gradually evaporates and becomes more concentrated as the temperature rises. The concentrating continues beyond 300°C, the highest boiling point of the H_2SO_4-water binary solution (*31*), generating a strong endothermic peak at around 300°C (Fig. 1B and fig. S3).

Protective carbon dot layer in CS-gel

We used a DN-gel as the model hydrogel to prevent network collapse during the reaction with H_2SO_4 (Fig. 3 and fig. S5). In a single-network hydrogel of polyacrylamide, treating and reacting with H_2SO_4 at 60°C leads to chain cleavage, network fragmentation into discontinuous filaments, and degradation into a viscous liquid (Fig. 3A). However, in a DN-gel, the alginate network sacrificially reacts with H_2SO_4, creating a carbon shield around the acrylamide network (Fig. 3C). This sacrificial process occurs during the heat treatment, changing the hydrogel from transparent to black as carbon attaches to the remaining networks, preventing further degradation and leaving a higher proportion of the amino group from the polyacrylamide (fig. S6). The generation of carbon is proportional to the content of alginate (fig. S7) and affects the mechanical properties of the DN hydrogel. After treatment, a DN gel with 1.5 wt % alginate and 21 wt % polyacrylamide exhibits a modulus of 48.6 kPa and a stretchability of 5.34-fold (fig. S8 and table S2).

We used dimethyl sulphoxide (DMSO) to remove the free H_2SO_4 in the CS-gel and compared it with DMSO in the FTIR spectra (Fig. 3F and fig. S9). Although the peaks at 1160 and 876 cm^{-1} representing free H_2SO_4 are absent, in the FTIR spectra of the DMSO-washed CS-gel we observed peaks at 1020 cm^{-1} contributing to the S–O–C group of sulfate ester and at 1221 cm^{-1} contributing to the –SO_3^- group of organo metal sulfate. The FTIR spectra revealed that the surface of the remaining acrylamide network is covered by smooth carbon based on the organo sulfate groups. We observed the generated carbon to be in the form of carbon dots (*32*), with diameters ranging from 1.98 to 4.06 nm in a weighted arithmetic mean measured with a Zetasizer (fig. S10). We observed the in-plane lattice spacing of the (100) facet of graphite, and the distinguishable lattice fringes (2.3 Å) of carbon dots was highlighted (Fig. 3E). These carbon dots protect the polymer networks (Fig. 3G) and exhibit fluorescence (Fig. 3H and fig. S11).

Generality for hydro-locking strategy

The hydro-locking strategy can be achieved with solutions other than H_2SO_4 and is applicable to various hydrogels. DMSO is a widely used biocompatible solvent in life science and can form strong hydrogen bonds with water and the hydrophilic groups on polymer networks (*33*). We treated the DN-gel with DMSO solutions (figs. S5E and S12A) and found that the hydrogel exhibited an extended functional temperature range with increasing DMSO concentration. We detected a broad functional temperature range expending to –125°C at a DN-gel treated with a 60 wt % DMSO solution. We also used the 60 wt % DMSO solution to treat the CS-gel. Such a treatment not only prevents the potential damage that may be caused by the H_2SO_4 on the surface of the CS-gel but also maintains the wide functional temperature range of the CS-gel (fig. S13).

We also demonstrated the strategy using a poly(*N*-vinylpyrrolidone) (PVP) hydrogel (Fig. 3D and figs. S5 and S12). A single network hydrogel typically collapses during the treatment of H_2SO_4 (Fig. 3A). However, PVP hydrolyzes in an acidic medium, leading to the breaking of an amide bond (*34*). The reactive side chain of PVP hydrolysis in the presence of H_2SO_4 (fig. S14) will further be carbonized during treatment below 60°C in an oven (Fig. 3D). The carbons cover the main chains of the polymer to prevent them from collapsing under continuous high temperature. Consequently, the PVP hydrogel has an extended functional temperature range from –112° to 135°C. (fig. S12B). The DMSO-treated PVP hydrogel showed similar results with a functional temperature range expanded to –122°C (fig. S12A).

Stretchability of CS-gel at extreme temperature

Hydro-locking in hydrogels maintains their softness and high stretchability under extremely low and high temperatures. We conducted tensile tests using a dynamic thermomechanical analyzer (DMA) (Fig. 4). We also tested a DN-gel for comparison, representing the mechanical properties of most tough hydrogels. At room temperature, the DN-gel exhibited excellent stretchability and toughness. However, after reaching equilibrium at low temperature (–80°C, held for 5 min in the DMA chamber), the DN-gel froze when the water within the

polymer networks froze, becoming brittle. A similar phenomenon was observed at 140°C (the gels were preequilibrated in an oven for 24 hours at the required temperature, held for 5 min in the DMA chamber), where most water evaporated from the network, making the DN-gel crispy and distorted, rendering the sample barely stretchable (Fig. 4, A and C). We observed that the treatment with H_2SO_4 reduced the performance of the DN-gel, with the stretchability decreased to 50% (Fig. 4, D and E) and the toughness decreased to 30%. We attribute this performance degradation to the degradation of alginate and the decrease in the ionic cross-linker of the alginate network when the SO_4^{2-} combines with the cross-linker Ca^{2+}. The modulus and toughness of the hydrogel degrade when the cross-linker density and the energy dissipator decrease (*7*). However, their properties are better preserved in the CS-gel at extreme temperatures (Fig. 4D and fig. S15). A CS-gel undergoes an increase in modulus and a decrease in stretch limit but remains soft. The modulus of the CS-gel increased 1.1-fold from room temperature to −80°C and 1.8-fold from −80° to −100°C, owing to the exponential growth in the viscosity of H_2SO_4 hydrate with decreasing temperature (*35*). For better presentation, we preserved a CS-gel in a −80°C chamber for more than 24 hours, and it resisted stretching and twisting (Fig. 4B, fig. S16, and movie S1). At elevated temperatures as high as 140°C, the CS-gel retained its shape and stretchability (Fig. 4, B and D). The stress-strain curve of a CS-gel at 140°C is parallel to and slightly higher than that at 25°C (fig. S17). The modulus did not differ much from that at 25°C. When the influence of temperature was eliminated, the modulus increased significantly, indicating that the CS-gel softens at 140°C compared with 25°C (fig. S17 and supplementary text)

We also tested the stretchability of CS-gel at 140°C under an oil bath, which provides a stabler and more homogeneous thermal environment, and the test validated its thermal stability (fig. S18 and movie S2). The results demonstrate the softness of the CS-gel within the temperature range from −100° to 140°C. Our results were compared with recent works on hydrogel materials that tolerate wide temperature ranges, derived from nonvolatile organic solutions (NO), inorganic salts (IS), heterogeneous network organohydrogels (OH), ionic liquids (IL), or zwitterionic osmolytes (ZO) (fig. S19 and table S3).

Functionality and application

After washing the CS-gels, we captured a fluorescence image by exposing the hydrogel under ultraviolet (UV) light at 340 to 380 nm, showing a bright blue emission light with a peak emission wavelength at 461 nm (figs. S11 and S20). The color of the emission light also corresponds to the diameter of the carbon dots (fig. S10). The washing process lowers the concentration of carbon dots to prevent quenching. Without the washing process, the gel was black, and the concentration of carbon dots was too high to generate a clear image (Fig. 3H and fig. S11A). Because the carbon dots originate from the reaction of alginate and H_2SO_4, the fluorescence intensity can be controlled by altering the alginate content (figs. S11, C to E, and S20C and movie S3).

The CS-gel can serve as a resistive strain-pressure sensor across an extended temperature range. During fabrication, conductive components, including sulfate ions and carbon dots, were introduced to the CS-gels. Consequently, the CS-gel exhibited a conductivity of about 1.27 S m^{-1} (fig. S21A). Maintaining stretchability over an extended temperature range, the CS-gel preserves its conductivity. Measurements from −80° to 140°C show that the CS-gel retains 22.17% of the conductivity at −20°C and 0.07% at −80°C. At elevated temperatures, conductivity increases, reaching 3.26 S m^{-1} at 140°C. The temperature-dependent behavior of conductivity correlates with the characteristics of a semiconductor, in which electron mobility increases with temperature (*36*). We applied mechanical loadings to the hydrogels within an electric circuit. Relative resistance alteration (ΔR), with ΔR representing the difference between the real-time resistance R and the initial resistance R_0, was measured. Stretching and pressing increased ΔR, which diminished if the load was released (Fig. 4F and fig. S21B). $\Delta R/R_0$ curves also displayed a clear step-like trend during step-by-step stretching-releasing cycles (fig. S21C). In cyclic loading at an extended temperature range, $\Delta R/R_0$ changed smoothly and evenly (movies S4 and S5).

Summary

We demonstrated a strategy of hydro-locking in hydrogel by connecting the majority of water molecules to the hydrogel network. The hydrogel, with complete hydro-locking, exhibits strong stability in extreme temperatures and maintains its softness and stretchability in the range of −115°C to 143°C. This hydro-locking strategy is proved applicable to various hydrogels with appropriate connecting agents.

REFERENCES AND NOTES

1. K. H. Vining, D. J. Mooney, *Nat. Rev. Mol. Cell Biol.* **18**, 728–742 (2017).
2. M. A. English *et al*., *Science* **365**, 780–785 (2019).
3. T. Zhou *et al*., *Nat. Mater.* **22**, 895–902 (2023).
4. Y. Zhang *et al*., *Chem. Rev.* **123**, 11722–11773 (2023).
5. G. Li *et al*., *Nature* **591**, 66–71 (2021).
6. T. Li *et al*., *Sci. Adv.* **3**, e1602045 (2017).
7. J.-Y. Sun *et al*., *Nature* **489**, 133–136 (2012).
8. J. Gong, Y. Katsuyama, T. Kurokawa, Y. Osada, *Adv. Mater.* **15**, 1155–1158 (2003).
9. M. Hua *et al*., *Nature* **590**, 594–599 (2021).
10. L. X. Hou *et al*., *Adv. Mater.* **35**, e2300244 (2023).
11. Y. Ren *et al*., *Sci. Adv.* **5**, eaax0648 (2019).
12. Y. Lu *et al*., *InfoMat* **5**, e12409 (2023).
13. X.-F. Zhang *et al*., *Angew. Chem. Int. Ed.* **58**, 7366–7370 (2019).
14. Z. Han *et al*., *Sci. Adv.* **8**, eabl5066 (2022).
15. X. Sui *et al*., *Adv. Funct. Mater.* **30**, 1907986 (2020).
16. X. Dong *et al*., *Mater. Today* **72**, 25–35 (2024).
17. Z. Wang *et al*., *Research* **2020**, 1426078 (2020).
18. D. Zhao *et al*., *J. Mater. Chem. C Mater. Opt. Electron. Devices* **10**, 2732–2741 (2022).
19. H. Dong, A. A. Askalany, C. Olkis, J. Zhao, G. Santori, *Energy* **189**, 116186 (2019).
20. Q. Zhang *et al*., *Nat. Commun.* **11**, 4463 (2020).
21. H. Gao *et al*., *Nat. Commun.* **8**, 15911 (2017).
22. B. Temelso *et al*., *J. Phys. Chem. A* **116**, 2209–2224 (2012).
23. S. Zhou, C.-S. Li, X.-H. Fan, Z. Shen, *Polymer* **143**, 316–323 (2018).
24. C. Wang *et al*., *Bioresour. Technol.* **355**, 127251 (2022).
25. K. Yao, Q. Meng, V. Bulone, Q. Zhou, *Adv. Mater.* **29**, 1701323 (2017).
26. C. M. Gable, H. F. Betz, S. H. Maron, *J. Am. Chem. Soc.* **72**, 1445–1448 (1950).
27. K. D. Beyer, A. R. Hansen, M. Poston, *J. Phys. Chem. A* **107**, 2025–2032 (2003).
28. S. Li *et al*., *Research* **6**, 0190 (2023).
29. X. P. Morelle *et al*., *Adv. Mater.* **30**, e1801541 (2018).
30. M. K. Gupta, R. Bansil, *J. Polym. Sci., Polym. Phys. Ed.* **19**, 353–360 (1981).
31. D. Schwartz, R. Gadiou, J.-F. Brilhac, G. Prado, G. Martinez, *Ind. Eng. Chem. Res.* **39**, 2183–2189 (2000).
32. H. Choi *et al*., *Nat. Photonics* **7**, 732–738 (2013).
33. D. Lv *et al*., *J. Phys. Chem. A* **126**, 6882–6889 (2022).
34. M. T. Taghizadeh, S. Nasirianfar, *J. Polym. Sci. Technol.* **5**, 13–24 (2020).
35. L. R. Williams, F. S. Long, *J. Phys. Chem.* **99**, 3748–3751 (1995).
36. V. Coropceanu *et al*., *Chem. Rev.* **107**, 926–952 (2007).
37. T. Koop, *Z. Phys. Chem.* **218**, 1231–1258 (2004).

ACKNOWLEDGMENTS

The authors thank Z. Han. for advice in demonstration and Zhejiang University for assistance with SEM measurements. **Funding:** This work was supported by the National Natural Science Foundation of China, T2125009 (T.L.); the National Key R&D Program of China, 2023YFD2201300 (Z.L.); the National Natural Science Foundation of China, 12102388 (X.Y.); the National Natural Science Foundation of China, 92048302 (T.L.); the National Natural Science Foundation of China, 12321002 (X.Y.); the National Natural Science Foundation of China, 1247020271 (X.Y.); the National Key R&D Program of China, 2017YFA0701100 (T.L.); the Fundamental Research Funds for the Central Universities, 226-2022-00141 (T.L.); the Key Research and Development Project of Zhejiang Province, 2022C01022 (T.L.); the "Pioneer" R&D Program of Zhejiang, 2023C03007 (T.L.); and the Laoshan Laboratory, LSKJ202205300 (T.L.). **Author contributions:** Conceptualization: X.Z., D.L., X.Y., T.-W.W. Methodology: X.Z., D.L., X.Y., L.W., T.-W.W. Validation: X.Z., D.L., X.Y. Formal analysis: X.Z., D.L., X.Y. Investigation: X.Z., L.W. Resources: X.Y., Z.L., T.L. Data curation: X.Z. Writing – original draft: X.Z., D.L., X.Y., L.W. Writing – review & editing: X.Z., D.L., X.Y., T.-W.W., T.L., W.Y., Z.L. Visualization: X.Z., D.L., G.L. Supervision: X.Y., T.L., W.Y., Z.L. Project administration: X.Y., T.L., Z.L. Funding acquisition: X.Y., T.L., Z.L. **Competing interests:** Z.L., X.Z., X.Y., and D.L. are inventors on China National Intellectual Property Administration provisional patent application (202410167970.4) submitted by Zhejiang University that covers a preparation method of the conductive hydrogel tolerating extreme temperature. All other authors declare no competing interests. **Data and materials availability:** All data are available in the main text or the supplementary materials.

SUPPLEMENTARY MATERIALS

science.org/doi/10.1126/science.adq2711
Materials and Methods
Supplementary Text
Figs. S1 to S26
Tables S1 to S3
References (*38*–*59*)
Movies S1 to S5

Submitted 8 May 2024; resubmitted 28 August 2024
Accepted 3 January 2025
10.1126/science.adq2711

ACTINIDE CHEMISTRY

Berkelium–carbon bonding in a tetravalent berkelocene

Dominic R. Russo[1,2]†, Alyssa N. Gaiser[1]†, Amy N. Price[1,2]†, Dumitru-Claudiu Sergentu[3,4]†, Jennifer N. Wacker[1], Nicholas Katzer[1,2], Appie A. Peterson[1], Jacob A. Branson[1,2], Xiaojuan Yu[5], Sheridon N. Kelly[1,2], Erik T. Ouellette[1,2], John Arnold[1,2], Jeffrey R. Long[1,2,6,7], Wayne W. Lukens Jr.[1], Simon J. Teat[8], Rebecca J. Abergel[1,2,9]*, Polly L. Arnold[1,2]*, Jochen Autschbach[5]*, Stefan G. Minasian[1]*

Interest in actinide–carbon bonds has persisted since actinide organometallics were first investigated for applications in isotope separation during the Manhattan Project. Transplutonium organometallics are rarely isolated and structurally characterized, likely owing to limited isotope inventories, a scarcity of suitable laboratory infrastructure, and intrinsic difficulties with the anaerobic conditions required. Herein, we report the discovery of an organometallic "berkelocene" complex prepared from 0.3 milligrams of berkelium-249. Single-crystal x-ray diffraction shows a tetravalent berkelium ion between two substituted cyclooctatetraene ligands, resulting in the formation of berkelium–carbon bonds. The coordination in berkelocene resembles that of uranocene, and calculations show that the berkelium 5f orbitals engage in covalent overlap with the δ-symmetry orbitals of the cyclooctatetraenide ligand π system. Charge transfer from the ligands is diminished relative to uranocene and other actinocenes, which maximizes contributions from the stable, half-filled $5f^7$ configuration of tetravalent berkelium.

Modern organometallic chemistry can be traced to the elucidation of a "sandwich" structure for ferrocene, $Fe(Cp)_2$ (Cp = C_5H_5), in the early 1950s by Wilkinson, Fischer, and colleagues (*1*, *2*). These reports nearly coincided with the discovery of two actinide elements, berkelium (Bk) and californium (Cf), which were reported by Seaborg and colleagues in 1950 (*3*, *4*). Despite this, for many years the fields of organometallic and actinide chemistry followed essentially separate trajectories. In contrast to $Fe(Cp)_2$, the first Cp complexes of actinides were highly reactive and air-sensitive (*5*), and actinide alkyl and carbonyl complexes—which are ubiquitous for d-block metals—were far too unstable to isolate (*6*). Interest in organoactinide chemistry was reignited with the synthesis and structural characterization of uranocene, $U(COT)_2$ (COT = C_8H_8), in the late 1960s by Streitwieser, Raymond and colleagues (*7*, *8*). $U(COT)_2$ had remarkable thermodynamic stability compared with actinide Cp complexes, which was attributed to the COT ligands being a better match for the U 5f orbitals in terms of size, energy, and symmetry (*9*). By 1976, all the actinocenes of the form $An(COT)_2$ (An = actinide), from Th through Pu (*10*–*12*), as well as the lanthanide analog with Ce, cerocene (*13*), were characterized. Save for some early microscale studies (*14*, *15*), the organometallic chemistry of transplutonium elements remained undeveloped until recently. The isolation and characterization of the trivalent Am and Cf complexes with Cp ligands, $Am(Cp^{tet})_3$ and $[Cf(Cp^{tet})_3Cl_2K(OEt_2)]_n$ (Cp^{tet} = C_5Me_4H), reported by Gaunt and colleagues in 2019 and 2021, respectively, constituted the first structural verifications of An–C bonds for elements beyond Pu (*16*, *17*). Ultraviolet–visible–near-infrared (UV-vis-NIR) spectroscopy and electronic structure calculations suggest that the bonding in these trivalent transplutonium organometallics is largely ionic in nature.

Several characteristics of $An(COT)_2$ complexes make them ideal subjects for spectroscopic and theoretical investigations of actinide covalency. Their high symmetry enables mixing of the 5f and 6d orbitals with the ligand frontier orbitals to form molecular orbitals of local σ, π, δ, and ϕ symmetry (*18*–*23*). The presence of an inversion center also restricts 5f- and 6d-orbital hybridization, which can complicate analyses of bonding. Further, the greater metal charge found in tetravalent actinocenes stabilizes the An 5f and 6d orbitals relative to trivalent actinide complexes, thereby reducing the difference in energy with ligand orbitals and enhancing covalent mixing (*21*). The discovery of a transplutonium COT actinocene would enable spectroscopic and theoretical studies across the actinide series and show how models of covalent bonding derived from the chemistry of early actinides can be applied to the transplutonium elements (*24*–*26*). However, the tetravalent oxidation state is difficult to stabilize for transplutonium elements and is particularly rare in molecular complexes that can be isolated and characterized by single-crystal x-ray diffraction (*27*). In targeting a transplutonium actinocene for synthesis, we noted that the tetravalent oxidation state is more accessible for Bk compared with the neighboring elements because of the stability of the associated half-filled $5f^7$ electronic configuration (*28*, *29*). In this study, we describe our efforts to develop the organometallic chemistry of tetravalent Bk, leading to the discovery of tetravalent Bk actinocene, or "berkelocene."

Synthesis

Developing high-valent Bk organometallic chemistry required overcoming several scientific and technical challenges because of the scarcity and high radioactivity of its most readily available isotope, ^{249}Bk [$t_{1/2}$ = 330(4) days]. Recent progress in molecular transuranium synthetic chemistry has provided the tools necessary to explore the synthetic chemistry of Bk (*25*, *26*). Synthetic protocols were developed that are compatible with the air and moisture sensitivity typical of organometallics and reproducible even at ultrasmall scales, while ensuring responsible stewardship of the precious and hazardous isotope. For example, the entire experimental process, from the first synthetic step through to isolation and characterization of the final product, was designed to be achievable within a ~48-hour time frame. Short-duration experiments were

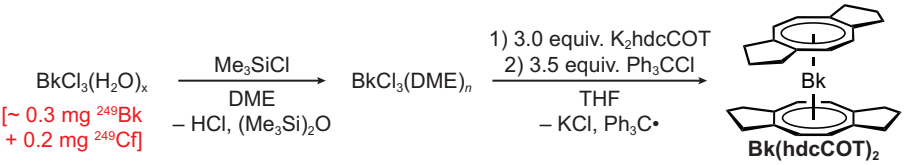

Fig. 1. Synthesis of a tetravalent Bk metallocene, $Bk(hdcCOT)_2$. The shorthand Ph_3C• refers to the radical by-product from reduction of Ph_3CCl, which couples to form Gomberg's dimer. Excess amounts of Me_3SiCl, $K_2hdcCOT$, and Ph_3CCl are used to ensure complete conversion to the $Bk(hdcCOT)_2$ product even in the presence of impurities due to the nature of small-scale synthesis (see SM, materials and methods).

[1]Chemical Sciences Division, Lawrence Berkeley National Laboratory, Berkeley, CA, USA. [2]Department of Chemistry, University of California, Berkeley, Berkeley, CA, USA. [3]Faculty of Chemistry, Alexandru Ioan Cuza University of Iași, Iași, Romania. [4]RA-03 (RECENT AIR) Laboratory, Alexandru Ioan Cuza University of Iași, Iași, Romania. [5]Department of Chemistry, University at Buffalo, Buffalo, NY, USA. [6]Department of Chemical and Biomolecular Engineering, University of California, Berkeley, Berkeley, CA, USA. [7]Department of Materials Science and Engineering, University of California, Berkeley, Berkeley, CA, USA. [8]Advanced Light Source, Lawrence Berkeley National Laboratory, Berkeley, CA, USA. [9]Department of Nuclear Engineering, University of California, Berkeley, Berkeley, CA, USA.
*Corresponding author. Email: rjabergel@lbl.gov (R.J.A.); pla@lbl.gov (P.L.A.); jochena@buffalo.edu (J.Au.); sgminasian@lbl.gov (S.G.M.)
†These authors contributed equally to this work.

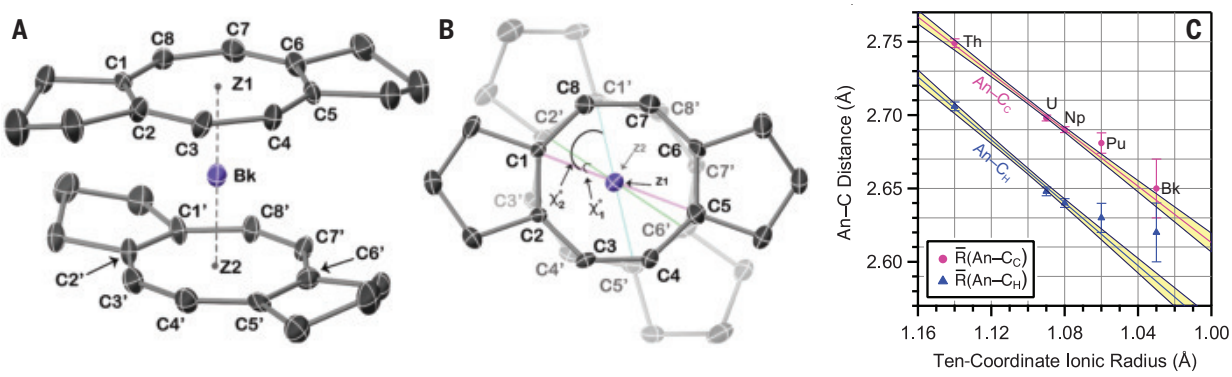

Fig. 2. X-ray crystallography. (**A**) Thermal ellipsoid (50%) plot of Bk(hdcCOT)$_2$, viewed from the side and (**B**) down the centroid–Bk–centroid axis. (**C**) Plot of the mean An–C distances (Å) in An(hdcCOT)$_2$ complexes (An = Th, U, Np, Pu, and Bk) as a function of the 10-coordinate ionic radius of the metal cations. Refer to the SM for details on the calculation of 10-coordinate ionic radii. Error bars are based on the standard deviation in the mean of chemically equivalent distances.

necessary to avoid potential product decomposition and crystal disintegration due to radiolysis and in-growth of ^{249}Cf, the primary daughter of ^{249}Bk. Additionally, the synthesis had to be resilient to ^{249}Cf impurities present in the starting material (~0.2 mg or ~0.8 μmol of Cf^{3+}), while also accommodating excess reagents left over from preceding synthetic steps. Crucially, no solvents or reagents could be used that would impede future Bk reprocessing or prevent proper disposal.

Synthetic protocols were designed for 0.5 mg (2 μmol of total metal content) scale reactions with all details of the procedure optimized in advance using Ce as a nonradioactive and abundant lanthanide surrogate to demonstrate reproducibility. Chemical oxidation (*28*) and electrolytic experiments have shown that the Bk^{4+}/Bk^{3+} reduction potential and its sensitivity to the surrounding ligand environment are comparable with those of Ce^{4+}/Ce^{3+} (*30*–*32*). In addition to unsubstituted COT, small-scale cerocene syntheses were tested using four substituted COT ligands with different solubilizing and electron-donating characteristics. The hdcCOT ligand (hdcCOT = hexahydrocyclopenta[8]annulene) consistently provided the Ce(hdcCOT)$_2$ complex when using ~0.5 mg of Ce, and hence hdcCOT was selected for subsequent Bk experiments [see supplementary materials (SM)] (*33*, *34*). Tetravalent cerocenes are best synthesized by oxidation of a trivalent cerium complex (*35*, *36*), so a variety of organic oxidants were also tested. Ultimately, chlorotriphenylmethane (Ph_3CCl) was selected as an oxidant owing to waste management constraints (see above). All other reaction conditions, including stirring times, solution concentrations, and the relative ratios of each reactant were optimized in advance during these small-scale preparations of Ce(hdcCOT)$_2$ (see SM).

The anhydrous precursor $BkCl_3(DME)_n$ (DME = 1,2-dimethoxyethane) was prepared as an off-white solid by treating a pale-green sample of hydrated $BkCl_3$ with Me_3SiCl in DME (Fig. 1) (*24*, *26*). After evaporation, the solid residue was suspended in tetrahydrofuran (THF) and 3 equiv of K_2hdcCOT were added to form a yellow-orange solution. No color change was observed after ~16 hours of stirring. Addition of a THF solution containing 3.5 equiv of Ph_3CCl resulted in an immediate color change to indigo. After work-up, evaporation of a *n*-pentane solution yielded indigo crystals that were analyzed by single crystal x-ray diffraction, confirming the formation of Bk(hdcCOT)$_2$.

Crystallography

The complex crystallizes in the space group $P\bar{1}$ with the Bk atom positioned on an inversion center and a hdcCOT$_{cent(1)}$–Bk(1)–hdcCOT$_{cent(2)}$ angle of 178.3(5)° (Fig. 2, A and B). The two hdcCOT rings are rotated about the Bk-centroid axis to form a pseudo-D_2 symmetric structure, with all four carbocyclic cyclopentane rings adopting a boat-like, all *endo* conformation (bending toward the Bk atom). The average torsion angle between the observed pseudo-D_2 conformation and a C_{2h} (eclipsed) conformation is 55(2)° (χ_2; Fig. 2B). By contrast, Ce(hdcCOT)$_2$ (see SM) crystallizes in the space group $P2_1/c$, exhibiting rigorous D_{2h} point symmetry, with the two carbocyclic cyclopentane rings adopting a chair-like, *exo-endo* conformation at low temperature. Notably, uranocene adopts a range of structural conformations depending on the nature of COT ligand substituents (*37*–*39*). For Bk(hdcCOT)$_2$, the potential energy associated with the staggered-to-eclipsed transformation for the *endo* system is computed to be nearly invariant between 0° to 30° (see below).

The C–C bond distances in Bk(hdcCOT)$_2$ are between 1.40(2) and 1.42(3) Å, which is typical of C–C distances in both substituted and unsubstituted COT ligands (*33*, *40*–*42*). The Bk–C distances range between 2.60(3) to 2.66(4), and the average Bk–hdcCOT$_{cent}$ distance is 1.88(2) Å. With additional structural data for other An(hdcCOT)$_2$ complexes (*43*), the crystal structure of Bk(hdcCOT)$_2$ provides a new opportunity to compare changes in ligand coordination across a large segment of the actinide series. Comparisons of bond distance require a precise definition of the metal's coordination number (*CN*), partially because ionic radii are dependent on *CN* (*44*). Although there are 16 carbon atoms coordinated to the metal centers in An(hdcCOT)$_2$ complexes, *CN* is defined here as equal to the formal number of electron pairs that are available for donation to the An metal from both hdcCOT ligands. Using nomenclature from the ionic model of electron counting, the cyclooctatetraene dianion is classified as an L_3X_2, five–electron pair donor ligand (three double bonds and two anionic carbon atoms) (*45*). Thus, a total of 10 electron pairs are involved in bonding for An(hdcCOT)$_2$ complexes, and therefore the An ions have a *CN* of 10.

Because the ionic radii for An ions with *CN* of 10 were not tabulated for all An, the ionic radii for *CN* of 10 were determined from the ionic radii for *CN* of 8, according to methodology described by Raymond and Eigenbrot (see SM) (*46*). Figure 2C compares changes in the An–C distances to the 10-coordinate ionic radii. The central C_8 ring of the hdcCOT ligand has two types of C atoms: those bonded to the carbocyclic rings (C_C) and those bonded to H atoms (C_H). Figure 2C shows that M–C_C distances are typically ~0.02 Å longer than M–C_H distances, which is attributed to differences in the steric environment. Linear fits provide good coefficients of determination (R^2) of 0.956 and 0.992 for the An–C_C and An–C_H data, respectively. Shorter An–C_C and An–C_H distances are observed for metals with smaller ionic radii. The strong linear correlation suggests that the bond metrics may be well rationalized, solely on the basis of changes in the metal ionic radii (*46*); however, differences in crystallographic disorder, local symmetry, space group, and crystal packing effects cannot be fully ruled out.

UV-vis-NIR absorption spectroscopy

Absorption spectra of Ce(hdcCOT)$_2$ and Bk(hdcCOT)$_2$ are provided in Fig. 3A. Intense

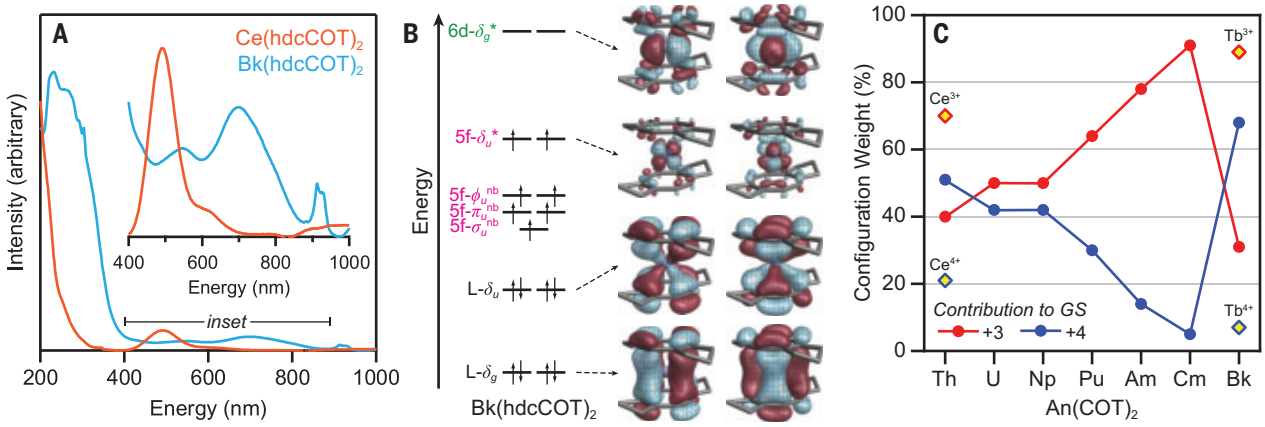

Fig. 3. Spectroscopic and theoretical analysis. (**A**) Experimental UV-vis-NIR absorption spectra of Bk(hdcCOT)$_2$ in *n*-pentane (blue) obtained from the mother liquor solution compared with a spectrum of Ce(hdcCOT)$_2$ in *n*-pentane (orange). The inset shows an expansion of the LMCT region. Experimental determination of extinction coefficients was precluded by the low sample concentration and by the presence of soluble redox byproducts (e.g., Gomberg's dimer and neutral hdcCOT). Absorption features >400 nm are partially attributed to Ph_3C• and Gomberg's dimer by-products formed during the oxidation with Ph_3CCl, which were not removed before the measurement (*57*). Sharp features at 913 and 927 nm are characteristic of f-f transitions, which could be associated with the Bk^{4+}($5f^7$) ion in Bk(hdcCOT)$_2$ or with small amounts of Bk^{3+} ($5f^8$) or Cf^{3+} ($5f^9$) impurities. (**B**) Qualitative valence molecular orbital diagram showing the most important metal–ligand bonding interactions and ordering of the nonbonding 5f orbitals from a CAS calculation targeting the ground state. (**C**) Contributions from An^{4+} and An^{3+} configurations to the ground state (GS) CAS wave functions of D_{8h}-An(COT)$_2$ (An = Th to Bk), expressed in an orbital basis with localized δ_u species. Data for Ce(COT)$_2$ and Tb(COT)$_2$ (*55, 56*) are provided for comparison.

features are observed in the visible region at 545 and 700 nm for Bk(hdcCOT)$_2$ and at 500 and 600 nm for Ce(hdcCOT)$_2$, which are commensurate with the purple-indigo colors observed for both compounds. As described in previous studies of Ce(COT)$_2$ (*35*, *47*), these bands are assigned to ligand-to-metal charge transfer (LMCT) transitions. Because the $4f^7$ configuration of Gd^{3+} is analogous to the $5f^7$ configuration of Bk^{4+}, we prepared [K(crypt)][Gd(hdcCOT)$_2$] as a reference for Bk(hdcCOT)$_2$ (see SM, materials and methods). The UV-vis spectrum of [K(crypt)][Gd(hdcCOT)$_2$] is essentially featureless in this energy regime with its first absorption band appearing at 345 nm. In this regard, the UV-vis spectrum [K(crypt)][Gd(hdcCOT)$_2$] closely resembles that of the ligand salt, K_2hdcCOT (fig. S10), which suggests that most transitions in this spectral region are ligand-based and not reflective of metal–ligand bonding. The slight increase in energy for the LMCT bands may reflect the higher energy of the Ce 4f orbitals relative to the Bk 5f orbitals, on the basis of fourth ionization potentials (*48*, *49*). Compared with other known Bk^{4+} compounds, the lower energy of the LMCT bands for Bk(hdcCOT)$_2$ relative to Bk[3,4,3-LI(1,2-HOPO)] (400 nm) (*50*) and Bk$(IO_3)_4$ (450 nm) (*26*) is attributed to the higher energy of the ligand-based C 2p versus O 2p atomic orbitals. Taken together with theory (see below), these observations and assignments are consistent with a Bk^{4+} organometallic complex.

Electronic structure calculations

Density functional theory (DFT) calculations (*51*) for isolated Bk(hdcCOT)$_2$ predict a global minimum structure with D_{2d} symmetry and a completely *endo* conformation of the carbocylic cyclopentanes. At higher energy, within 19 kJ mol^{-1}, are the *endo-exo* and *exo-exo* conformers (fig. S23). These structures have Bk–hdcCOT$_{cent}$ and average Bk–C$_{hdcCOT}$ distances of 1.88 and 2.61 to 2.65 Å, which are in excellent agreement with the experimental data (see above). The potential energy profile associated with the rotation between the calculated D_{2d} conformer and the experimentally observed D_{2h} geometry for the endo hdcCOT system is nearly flat between 0° and 30° (fig. S24), suggesting that the observed geometry of Bk(hdcCOT)$_2$ in the crystal could easily be due to crystal packing.

Relativistic complete active space (CAS) self-consistent field wave function calculations of all possible ligand-field spin states of the $5f^7$ configuration for the Bk^{4+} ion, followed by multireference treatment of the dynamic electron correlation and treatment of spin-orbit coupling (SOC), were performed for Bk(hdcCOT)$_2$ and the experimentally unknown Bk(COT)$_2$. The resulting energy-level scheme (fig. S25) shows an $^8S_{7/2}$ ground state, along with ligand-field-split Kramers components of $^6D_{7/2}$ ion parentage around 1.69 eV (corresponding to a photon wavelength of 733 nm). This energy, although somewhat overestimated, matches that of the sharp f-f transitions in the absorption spectrum at 913 and 927 nm (1.36 and 1.34 eV). Time-dependent DFT calculations of LMCT states (table S17) yield the most intense excitation around 500 nm [2.48 eV, Perdew–Burke–Ernzerhof (PBE) functional] and 450 nm (2.76 eV, PBE0), and assign it to a dipole-allowed, *z*-polarized L-δ_g → f-δ_u* transition. The calculations therefore support the assignment of the experimental absorption feature at 545 nm (2.27 eV) when considering that previous calculations for M(COT)$_2$ also deviated from experimental UV-vis-NIR absorption energies by up to ~0.5 eV (*20*). LMCT states calculated near the observed band at 700 nm are assigned to L-δ_u → f-δ_u* transitions, with small oscillator strengths because of the parity selection rule; the increased intensity observed experimentally for these transitions may arise from vibronic coupling, which was not accounted for in the calculations.

The CAS calculations were also used to evaluate the ground state configuration, chemical bonding, and the formal oxidation state for both D_{2d}-Bk(hdcCOT)$_2$ and the unsubstituted D_{8h}-Bk(COT)$_2$. When expressed in the basis of metal-ligand hybridized natural orbitals, the ground state for D_{2d}-Bk(hdcCOT)$_2$ and D_{8h}-Bk(COT)$_2$ is dominated by the (L-δ_g)^4(L-δ_u)^{4}f^{7}d^0 configuration. The wave function is essentially single-configurational (96% weight) when only the ground spin-octet state is targeted in the calculation. The ground state wave function was used in all subsequent analyses. However, it gradually becomes multiconfigurational when excited states are included in the state averaging. The (L-δ_g)^4(L-δ_u)^{4}f^{7}d^0 configuration has 87% weight in the ground state with a state average of 1 octet and 14 sextets, and 64% with a state average of 14 octet and 14 sextet states. Similarly to what previous spectroscopic and theoretical studies of bonding in early actinide sandwich complexes have found (*52*), metal–ligand covalency in D_{2d}-Bk(hdcCOT)$_2$ occurs primarily in the doubly degenerate L-δ_u and

L-δ_g orbitals (Fig. 3B), which have considerable metal weights (22% 5f and 26% 6d, respectively).

To evaluate the oxidation state, the ground state wave function can alternatively be expressed by using ligand- and metal-localized linear combinations of the bonding-antibonding δ_u/δ_u^* pairs, in which case the covalent ligand-to-5f donation appears primarily through admixture of charge-transfer configurations. Localization of the δ_u combinations on the metal and ligands, respectively, was achieved by "rotation" (in orbital space) between the bonding-antibonding pairs (22° angle). This results in 70% weight of the $5f^7$ (Bk^{4+}) configuration for D_{8h}-Bk(COT)$_2$ and D_{2d}-Bk(hdcCOT)$_2$ (Fig. 3C and fig. S26), indicating that both are meaningfully assigned as formally Bk^{4+} 3. Figure 3C presents the compositions of the ground state wave functions for D_{8h}-An(COT)$_2$ with An = Th–Bk when expressed in the aforementioned localized orbital sets, in terms of the metal oxidation state. Following common practice for f-element complexes, the assignment of the metal oxidation state is based on occupation of the f shell and disregards donation involving 6d, 7s, or 7p shells. From Th to Cm, in particular, there is a clear preference of the central metal for the trivalent oxidation state, especially beyond Np, which is in agreement with previous studies (*20*, *53*, *54*). A sharp decrease in weight of the +3 configuration occurs between Cm(COT)$_2$ (98%) and Bk(COT)$_2$ (33%), which is reflective of a decrease in net donation from the ligands into the 5f shell as both systems increase the relative weight of the stability and chemical inertness of the $5f^7$ configuration (*20*).

To understand how the stability of a half-filled $5f^7$ shell may lead to a greater weight of the Bk^{4+} configuration, Bk(hdcCOT)$_2$ was compared with its Ce and Tb analogs. Tb(COT)$_2$ has not been observed experimentally but was described in earlier theoretical work as having a ground state dominated by an 89% weight of the ionic $(L\text{-}\delta_g)^4(L\text{-}\delta_u)^3f^8d^0$ configuration, corresponding to Tb^{3+} (*55*, *56*). This can be attributed to the large fourth ionization energy of Tb, which is similar to that of Cm (*48*, *49*), such that the Tb^{4+} $4f^7$ configuration is comparatively high in energy and not sufficiently stabilized by COT^{2-} ligands. By contrast, the overlap between 5f and ligand orbitals that is evident in the natural orbitals for Bk(hdcCOT)$_2$ (Fig. 3B) must have a stabilizing effect on the Bk^{4+} ground state. A substantial degree of 4f-shell bonding is also apparent in the natural orbitals for Ce(hdcCOT)$_2$ and Ce(COT)$_2$; however, a large amount of charge transfer into formally empty 4f orbitals (in contrast to the partially filled 5f orbitals in the Bk case) means that these complexes have dominant Ce^{3+} character (Fig. 3C). The electron populations associated with the pairs of metal-COT–localized δ_u orbitals are $(L\text{-}\delta_u)^{3.67}(f\text{-}\delta_u)^{2.33}$ and $(L\text{-}\delta_u)^{3.15}(f\text{-}\delta_u)^{0.85}$ for Bk(hdcCOT)$_2$ and Ce(hdcCOT)$_2$, respectively. This suggests that the extent of ligand-to-metal donation is far more pronounced with Ce 4f-δ_u (0.85 electrons) than with Bk 5f-δ_u (0.33 electrons); that is, the berkelocene has a dominant 4+ character.

Conclusions

The discovery and structural characterization of Bk(hdcCOT)$_2$ shows that Bk^{4+}–C bonds can be stabilized in high-valent Bk organometallics and that organometallic complexes of rare and radioactive isotopes can be isolated and fully characterized starting from <0.5 mg of metal. The experimental data provide an opportunity to test electronic structure models across both the lanthanide and actinide series. The stark differences between Bk^{4+} and its lanthanide analogs are peculiar, given that Ce^{4+} and Bk^{4+} have similar reduction potentials and that Tb^{4+} and Bk^{4+} both have half-filled f shells. However, the half-filled Bk^{4+}-$5f^7$ configuration is stabilized by the productive metal–ligand overlap afforded by more radially extended 5f orbitals.

REFERENCES AND NOTES

1. G. Wilkinson, M. Rosenblum, M. C. Whiting, R. B. Woodward, *J. Am. Chem. Soc.* **74**, 2125–2126 (1952).
2. E. O. Fischer, W. Pfab, *Z. Naturforsch. B* **7** 377–379 (1952).
3. S. G. Thompson, A. Ghiorso, G. T. Seaborg, *Phys. Rev.* **80**, 781–789 (1950).
4. S. G. Thompson, K. Street, A. Ghiorso, G. T. Seaborg, *Phys. Rev.* **80**, 790–796 (1950).
5. L. T. Reynolds, G. Wilkinson, *J. Inorg. Nucl. Chem.* **2**, 246–253 (1956).
6. H. Gilman *et al*., *J. Am. Chem. Soc.* **78**, 2790–2792 (1956).
7. A. J. Streitwieser Jr., U. Mueller-Westerhoff, *J. Am. Chem. Soc.* **90**, 7364 (1968).
8. A. Zalkin, K. N. Raymond, *J. Am. Chem. Soc.* **91**, 5667–5668 (1969).
9. A. Streitwieser *et al*., *J. Am. Chem. Soc.* **95**, 8644–8649 (1973).
10. A. J. Streitwieser Jr., N. Yoshida, *J. Am. Chem. Soc.* **91**, 7528 (1969).
11. D. G. Karraker, J. A. Stone, E. R. J. Jones Jr., N. Edelstein, *J. Am. Chem. Soc.* **92**, 4841–4845 (1970).
12. D. F. Starks, T. C. Parsons, A. Streitwieser, N. Edelstein, *Inorg. Chem.* **13**, 1307–1308 (1974).
13. A. Greco, S. Cesca, W. Bertolini, *J. Organomet. Chem.* **113**, 321–330 (1976).
14. P. G. Laubereau, J. H. Burns, *Inorg. Chem.* **9**, 1091–1095 (1970).
15. P. G. Laubereau, J. H. Burns, *Inorg. Nucl. Chem. Lett.* **6**, 59–63 (1970).
16. C. A. P. Goodwin *et al*., *Angew. Chem. Int. Ed.* **58**, 11695–11699 (2019).
17. C. A. P. Goodwin *et al*., *Nature* **599**, 421–424 (2021).
18. J. G. Brennan, J. C. Green, C. M. Redfern, *J. Am. Chem. Soc.* **111**, 2373–2377 (1989).
19. M. Pepper, B. E. Bursten, *Chem. Rev.* **91**, 719–741 (1991).
20. A. Kerridge, N. Kaltsoyannis, *J. Phys. Chem. A* **113**, 8737–8745 (2009).
21. M. L. Neidig, D. L. Clark, R. L. Martin, *Coord. Chem. Rev.* **257**, 394–406 (2013).
22. S. G. Minasian *et al*., *Chem. Sci.* **5**, 351–359 (2014).
23. G. Ganguly, D.-C. Sergentu, J. Autschbach, *Chemistry* **26**, 1776–1788 (2020).
24. A. N. Gaiser *et al*., *Nat. Commun.* **12**, 7230 (2021).
25. S. S. Galley *et al*., *J. Am. Chem. Soc.* **141**, 2356–2366 (2019).
26. M. A. Silver *et al*., *J. Am. Chem. Soc.* **139**, 13361–13375 (2017).
27. M. N. Sokolova *et al*., *Inorg. Chem.* **48**, 9185–9190 (2009).
28. D. E. Hobart, J. R. Peterson, in *The Chemistry of the Actinide and Transactinide Elements*, vol. 3, L. Morss, N. Edelstein, J. Fuger, Eds. (Springer, 2006), chap. 10, pp. 1444–1498.
29. S. G. Thompson, B. B. Cunningham, G. T. Seaborg, *J. Am. Chem. Soc.* **72**, 2798–2801 (1950).
30. M. R. Antonio, C. W. Williams, L. Soderholm, *Radiochim. Acta* **90**, 851–856 (2002).
31. J. R. Stokely, R. D. Baybarz, J. R. Peterson, *J. Inorg. Nucl. Chem.* **34**, 392–393 (1972).
32. E. Wadsworth, F. R. Duke, C. A. Goetz, *Anal. Chem.* **29**, 1824–1825 (1957).
33. M. Hiller, M. Maier, H. Wadepohl, M. Enders, *Organometallics* **35**, 1916–1922 (2016).
34. J. D. Hilgar, A. K. Butts, J. D. Rinehart, *Phys. Chem. Chem. Phys.* **21**, 22302–22307 (2019).
35. A. Streitwieser, S. A. Kinsley, C. H. Jenson, J. T. Rigsbee, *Organometallics* **23**, 5169–5175 (2004).
36. U. Kilimann, R. Herbst-Irmer, D. Stalke, F. T. Edelmann, *Angew. Chem. Int. Ed.* **33**, 1618–1621 (1994).
37. K. O. Hodgson, K. N. Raymond, *Inorg. Chem.* **12**, 458–466 (1973).
38. A. Zalkin, D. H. Templeton, S. R. Berryhill, W. D. Luke, *Inorg. Chem.* **18**, 2287–2289 (1979).
39. A. Zalkin, D. H. Templeton, W. D. Luke, A. J. Streitwieser Jr., *Organometallics* **1**, 618–622 (1982).
40. A. Avdeef, K. N. Raymond, K. O. Hodgson, A. Zalkin, *Inorg. Chem.* **11**, 1083–1088 (1972).
41. D. J. A. De Ridder, J. Rebizant, C. Apostolidis, B. Kanellakopulos, E. Dornberger, *Acta Crystallogr. C* **52**, 597–600 (1996).
42. C. J. Windorff *et al*., *Inorg. Chem.* **59**, 13301–13314 (2020).
43. D. R. Russo *et al*., *Chem. Commun.* (2025).
44. L. Pauling, *The Nature of the Chemical Bond* (Cornell Univ. Press, 1960).
45. M. L. H. Green, G. Parkin, *J. Chem. Educ.* **91**, 807–816 (2014).
46. K. N. Raymond, C. W. J. Eigenbrot Jr., *Acc. Chem. Res.* **13**, 276–283 (1980).
47. F. Ferraro, C. A. Barboza, R. Arratia-Pérez, *J. Phys. Chem. A* **116**, 4170–4175 (2012).
48. X. Cao, M. Dolg, *J. Mol. Struct. THEOCHEM* **581**, 139–147 (2002).
49. X. Y. Cao, M. Dolg, *J. Mol. Struct. THEOCHEM* **673**, 203–209 (2004).
50. G. J.-P. Deblonde *et al*., *Nat. Chem.* **9**, 843–849 (2017).
51. D.-C. Sergentu, Raw output data for "Berkelium-Carbon Bonding in a Tetravalent Berkelocene", Version v1, Zenodo, (2024); https://doi.org/10.5281/zenodo.14032783.
52. A. H. H. Chang, R. M. Pitzer, *J. Am. Chem. Soc.* **111**, 2500–2507 (1989).
53. A. Kerridge, *Dalton Trans.* **42**, 16428–16436 (2013).
54. A. Kerridge, *RSC Adv.* **4**, 12078–12086 (2014).
55. W. J. Liu, M. Dolg, P. Fulde, *Inorg. Chem.* **37**, 1067–1072 (1998).
56. W. J. Liu, M. Dolg, P. Fulde, *J. Chem. Phys.* **107**, 3584–3591 (1997).
57. T. Nishiuchi *et al*., *Aggregate (Hoboken)* **2**, e126 (2021).

ACKNOWLEDGMENTS

Funding: This work was supported by the US Department of Energy (DOE), Office of Science, Office of Basic Energy Sciences, Heavy Element Chemistry Program at Lawrence Berkeley National Laboratory under contract DE-AC02-05CH11231. J.Au. acknowledges support for the theoretical component of this study from the DOE, Office of Science, Office of Basic Energy Sciences, Heavy Element Chemistry Program, under award DE-SC0001136. We thank the Center for Computational Research (CCR) of the University at Buffalo for providing computational resources. D.-C.S. acknowledges the computing infrastructure provided by the RECENT AIR grant agreement MySMIS 127324. J.A.B. and S.N.K. acknowledge support from a DOE Integrated University Program Fellowship at the University of California, Berkeley. This research used resources of the Advanced Light Source, which is a DOE Office of Science User Facility under contract DE-AC02-05CH11231. We acknowledge T. Albrecht for providing a fraction of a $^{249}BkCl_3$ stock initially supplied by the National Isotope Development Center, which is managed by the DOE Isotope Program. **Author contributions:** Conceptualization and writing – original draft: D.R.R., A.N.G., A.N.P., D.-C.S., R.J.A., P.L.A., J.Au., S.G.M.; Formal

analysis: D.R.R., A.N.G., A.N.P., D.-C.S., X.Y., S.N.K., E.T.O., S.J.T., J.Au., S.G.M.; Funding acquisition: J.Ar., J.R.L., W.W.L., R.J.A., P.L.A., J.Au., S.G.M.; Investigation: D.R.R., A.N.G., A.N.P., D.-C.S., J.N.W., N.K., A.A.P., J.A.B., X.Y., S.N.K., E.T.O.; Methodology: D.R.R., A.N.G., A.N.P., D.-C.S., J.W., N.K.; Project administration: D.R.R., A.N.G., J.N.W., W.W.L., R.J.A., P.L.A., J.Au., S.G.M.; Resources: W.W.L., S.J.T., R.J.A., P.L.A., J.Au., S.G.M.; Supervision: J.Ar., J.R.L., W.W.L., S.J.T., R.J.A., P.L.A., J.Au., S.G.M.; Validation: D.R.R., A.N.G., A.N.P., A.A.P., J.N.W., J.A.B., S.J.T.; Writing – reviewing & editing: all authors. **Competing interests:** The authors declare that they have no competing interests. **Data and materials availability:** Crystallographic data are available free of charge from the Cambridge Crystallographic Data Centre under CCDC 2365691, 2365692, 2365694, 2366024, and 2366039. Raw outputs from the calculations are deposited at Zenodo (*51*). All other data are available in the main text or the SM.

SUPPLEMENTARY MATERIALS

science.org/doi/10.1126/science.adr3346
Materials and Methods
Figs. S1 to S30
Tables S1 to S22
References (*58*–*112*)

Submitted 27 June 2024; accepted 23 January 2025
10.1126/science.adr3346

NANOMATERIALS

Curvature-guided depletion stabilizes Kagome superlattices of nanocrystals

Siyu Wan[1]†, Xiuyang Xia[2]†‡, Yutong Gao[1], Heyang Zhang[1], Zhebin Zhang[3], Fangyue Wu[1], Xuesong Wu[1], Dong Yang[3], Tongtao Li[1]*, Jianfeng Li[3]*, Ran Ni[2]*, Angang Dong[1]*

Shape-anisotropic nanocrystals and patchy particles have been explored to construct complex superstructures, but most studies have focused on convex shapes. We report that nonconvex, dumbbell-shaped nanocrystals (nanodumbbells) exhibit globally interlocking self-assembly behaviors governed by curvature-guided depletion interactions. By tailoring the local curvature of nanodumbbells, we can precisely and flexibly adjust particle bonding directionality, a level of control rarely achievable with conventional convex building blocks. These nanodumbbells can undergo long-range ordered assembly into various intricate two-dimensional superlattices, including the chiral Kagome lattice. Theoretical calculations reveal that the Kagome lattice is a thermodynamically stable phase, with depletion interactions playing a crucial role in stabilizing these non–close-packed structures. The emergence of Kagome lattices and other unusual structures highlights the vast potential of nonconvex nanocrystals for creating sophisticated architectures.

A long-standing goal in the field of colloidal assembly is to create synthetic superstructures that mimic or even surpass the structural complexity found in natural materials (*1*–*6*). Self-assembly of colloidal nanocrystals (NCs) into superlattices provides a programmable approach to developing metamaterials with tailored optical, electronic, and catalytic properties (*7*–*9*). Achieving this requires precise control over the directionality of particle bonding, akin to the specificity observed in molecular synthesis (*10*, *11*). This level of control is particularly important for designing intricate structures such as low-symmetry, low-density lattices, which rely on highly specific and directional interparticle interactions (*12*). However, most NCs studied to date have simple convex shapes, such as spheres and polyhedral. Such high symmetry inherently limits the extent to which directional interactions can be manipulated (*13*, *14*). Surface modifications, such as generating patchiness through site-specific functionalization (*15*–*17*), can enhance interaction specificity, but attaining the desired surface characteristics is challenging. To achieve the rational design of sophisticated architectures, it is essential to develop new design principles that enable NCs to selectively recognize and flexibly bond with neighboring particles.

This study introduces nonconvex NCs, specifically nanodumbbells (NDs), as versatile building blocks that offer specific and flexible control over directional interactions through local concave-convex curvature matching. Additionally, we demonstrate that introducing depletion interactions is essential for facilitating the long-range interlocking assembly of NDs, resulting in the formation of diverse and intricate two-dimensional (2D) superlattices. These include non–close-packed architectures such as the Kagome lattice, a structure of interest in condensed-matter physics and materials science (*18*, *19*), yet notoriously challenging to create with conventional convex building blocks (*20*).

Synthesis and characterization of NDs

The NDs that we used were colloidal $NaYF_4$:Yb/Er@$NaGdF_4$@$NaNdF_4$ NCs, synthesized following a reported method (fig. S1) (*21*). The as-synthesized NDs were coated with oleic acid ligands, ensuring their high colloidal stability when dispersed in nonpolar solvents such as hexane (fig. S2). Transmission electron microscopy (TEM) tomography revealed that each ND comprised two convex heads connected by a concave waist (Fig. 1A and movie S1), and high-resolution TEM (HRTEM, Fig. 1B) and wide-angle electron diffraction (WAED, Fig. 1C) confirmed its single-crystalline nature. By optimizing synthetic conditions, we could widely tune the waist width (d) of NDs while keeping the length (L) and head width (D) relatively constant at 60 ± 8 nm and 40 ± 7 nm, respectively. We defined the concavity of NDs using the waist-to-head width ratio (d/D), with a higher ratio corresponding to reduced concavity. This parameter, continuously adjustable between 0.4 and 0.9 (fig. S3), crucially influenced the self-assembly behavior of NDs.

The selection of these NDs as nonconvex building blocks was primarily motivated by their geometric self-complementarity. Figure 1D presents the TEM images of three representative ND shapes, named ND-1, ND-2, and ND-3, corresponding to high, moderate, and low concavity, with d/D ratios of ~0.4, ~0.6, and ~0.8, respectively. These images were color-coded to delineate the local curvature (κ) along the projected contours of the NDs (fig. S4) (*22*). Further analysis revealed a consistent curvature variation profile across different particle shapes, transitioning smoothly from positive in the head regions to negative at the waist (fig. S5). Additionally, within the convex head regions, the corners tended to exhibit higher local curvature compared to the caps. Despite differences in concavity, all of the NDs exhibited self-complementarity in local curvature, which would be crucial for promoting directional interparticle interactions. The concave waist acted as a natural binding site, recognizing and interlocking with the convex head of another ND (Fig. 1E), akin to a lock-and-key process (*23*).

ND self-assembly and superlattice formation

This concave-convex curvature fitting promoted specific and stable bonding between NDs, with the bond directionality flexibly adjustable through modulation of the local curvature. To quantify the orientation between two interlocked NDs, we introduced the alignment angle (θ), defined as the angle between the extensions of their longitudinal axes. This angle reflects how NDs aligned themselves to

[1]Department of Chemistry and Shanghai Key Laboratory of Molecular Catalysis and Innovative Materials, iChEM, Fudan University, Shanghai, China. [2]School of Chemistry, Chemical Engineering and Biotechnology, Nanyang Technological University, Singapore, Singapore. [3]State Key Laboratory of Molecule Engineering of Polymers and Department of Macromolecular Science, Fudan University, Shanghai, China. ***Corresponding author. Email: agdong@fudan.edu.cn (A.D.); r.ni@ntu.edu.sg (R.N.); lijf@fudan.edu.cn (J.L.); ttli@fudan.edu.cn (T.L.)**
†These authors contributed equally to this work.
‡Present address: Arnold Sommerfeld Center for Theoretical Physics and Center for NanoScience, Department of Physics, Ludwig-Maximilians-Universität München, Munich, Germany.

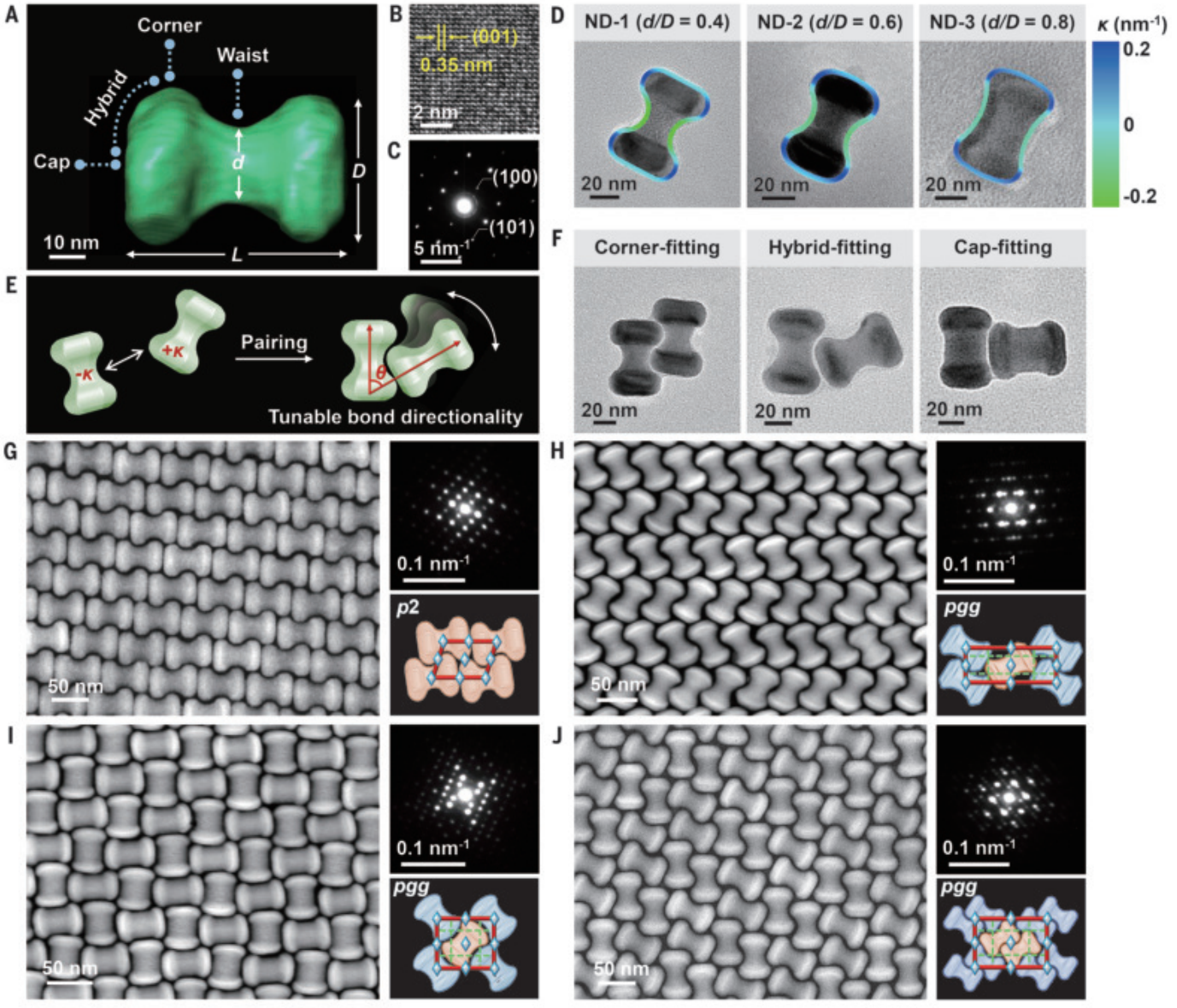

Fig. 1. Engineering the structure of 2D ND superlattices through local curvature modulation. (**A** to **C**) Structural characterization of a single ND: (A) 3D structural reconstruction, (B) HRTEM image, and (C) WAED pattern. (**D**) TEM images of NDs with three representative concavities, with their projected contours color-coded to indicate variations in local curvature (κ). (**E**) Schematic illustrating how NDs pair up through concave-convex curvature fitting, with adjustable alignment angles via curvature modulation. (**F**) TEM images of paired NDs, showing three distinct concave-convex fitting modes between NDs, dictated by their concavity. (**G** to **J**) HAADF-STEM images, SAED patterns (top right), and structural models (bottom right) of various 2D superlattices: (G) parallel, (H) herringbone, (I) chevron, and (J) bi-chevron. The structural models indicate the symmetry of the respective lattice, with different colors representing different particle orientations.

achieve optimal curvature matching during the self-assembly process.

To explore how concavity affects local particle packing, we dried a dilute hexane solution of NDs onto TEM grids and examined the pairing configurations of interlocked NDs. We identified three primary concave-convex fitting modes in ND pairs (Fig. 1F). High-concavity NDs ($d/D < 0.55$), exemplified by ND-1, favored a corner-fitting mode (fig. S6A), in which the corner of one ND fit tightly into the waist of another, forming parallel pairs with an offset in positioning. Conversely, low-concavity NDs ($d/D > 0.65$), such as ND-3, predominantly adopted a cap-fitting configuration (fig. S6C), where the cap region engaged with the waist of another ND. For NDs with moderate concavity ($0.55 < d/D < 0.65$), represented by ND-2, although corner fitting was still observed, they tended to adopt a hybrid-fitting mode (fig. S6B), involving both corner and cap regions to achieve curvature matching with neighboring NDs. These locally favored pairing configurations were primarily dictated by the degree of geometric complementarity between interlocked NDs, which tended to maximize contact between their convex and concave regions.

We hypothesized that by adjusting the concavity of NDs, we could fine-tune particle bonding directionality and thus program the structure of the resulting superlattices, provided that extended interlocking assembly of NDs was achievable. To test this hypothesis, we performed self-assembly by drop-casting a hexane solution containing NDs onto the surface of a subphase such as diethylene glycol (DEG) (*24*),

followed by controlled solvent evaporation (fig. S7). This method allowed NDs to assemble while lying flat at the liquid-air interface.

However, achieving long-range ordered assembly of NDs remained a substantial challenge (*25*). The primary obstacle stemmed from the steric hindrance associated with nonconvex particles, where NDs could become irreversibly locked by their neighbors before reaching

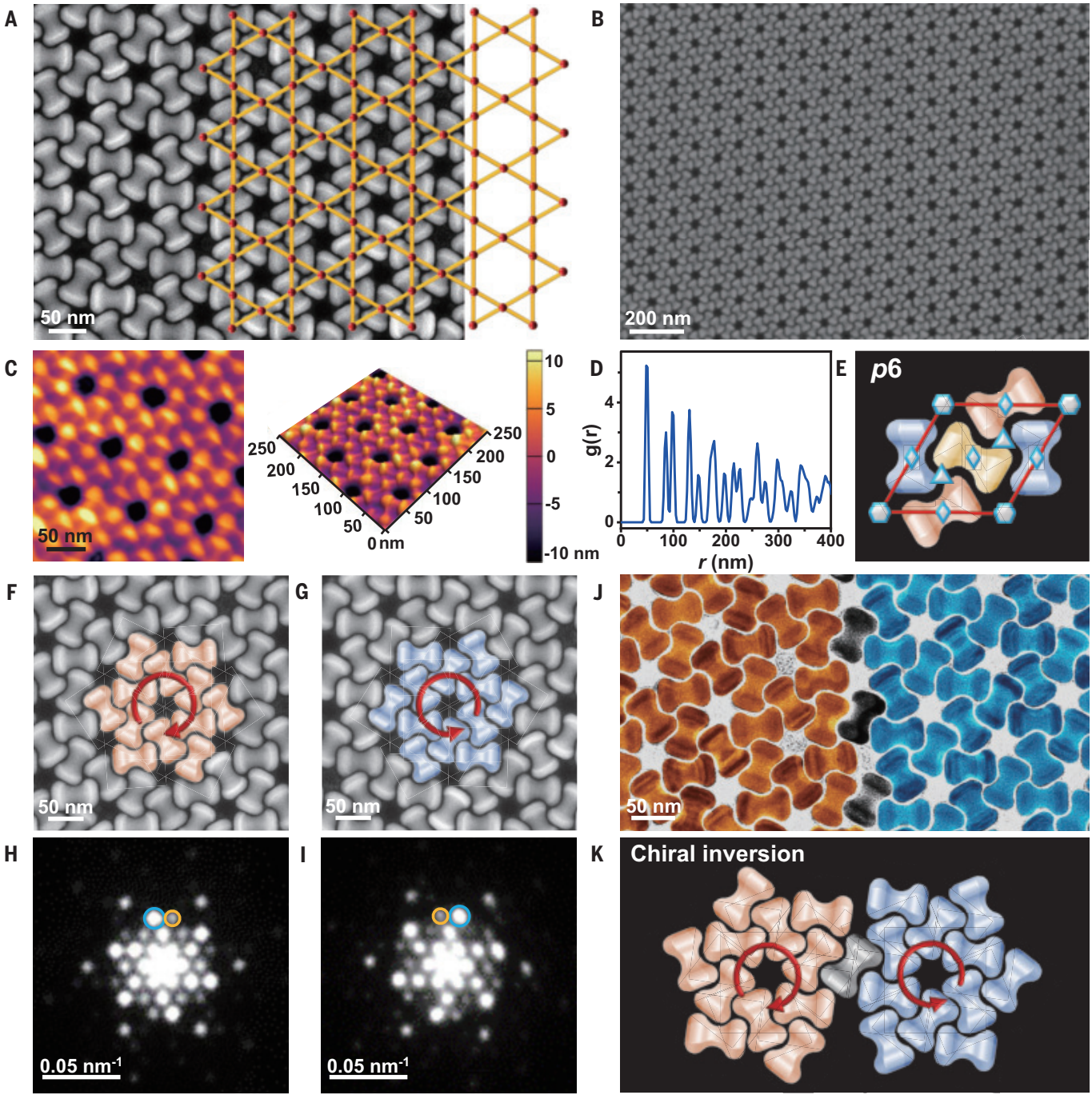

Fig. 2. Chiral Kagome lattices self-assembled from moderate-concavity NDs. (**A** to **E**) Structural characterization of Kagome lattices: (A) HAADF-STEM image, (B) SEM image, (C) AFM image and corresponding 3D topography view on the right, (D) radial distribution function computed from TEM images, and (E) structural model showing the *p*6 symmetry. The orange lines connecting the centroids (red dots) of NDs in (A) illustrate the trihexagonal motif, characteristic of the Kagome lattice. (**F** to **I**) Planar chirality of Kagome lattices: (F and G) HAADF-STEM images and (H and I) corresponding SAED patterns of two distinct chiral domains of the Kagome lattice. The colored NDs in the HAADF-STEM images highlight the gear-like superstructures formed from ND trimers, which rotate either clockwise (F) or counterclockwise (G) as indicated by the red arrows. The asymmetric diffraction spots (indicated by blue and orange circles) in the SAED patterns indicate opposite handedness of the two domains. (**J**) False-colored TEM image, showing the boundary between two distinct chiral domains of the Kagome lattice. (**K**) Schematic illustrating chiral inversion between two adjacent domains, facilitated by a single ND (colored gray) at the boundary.

equilibrium. Indeed, our initial attempts often resulted in kinetically arrested aggregates characterized by disorder or only short-range order (fig. S8). To overcome this, we exploited depletion interactions by introducing an excess of oleic acid into the ND solution. These free oleic acid molecules served as depletants, progressively inducing specific attraction between adjacent NDs as the solvent evaporated (fig. S9) (*26*, *27*).

This strategy proved highly effective in mitigating kinetic arrest and promoting the extended interlocking of NDs (fig. S8), resulting in large-area superlattice membranes upon complete solvent evaporation. Figure 1, G to J, present high-angle annular dark-field scanning TEM (HAADF-STEM) images of 2D superlattices with varying structural complexities, assembled from NDs with different concavities. Analysis of these distinct superlattices revealed a common characteristic in their local packing: Each ND provided two binding sites at its waist for interlocking with two neighboring NDs, while its two heads simultaneously engaged with the waists of two adjacent NDs. This intricate arrangement led to a globally interlocked architecture with excellent translational order, as confirmed by small-angle electron diffraction (SAED).

Further examination showed that the locally favored pairing configurations of NDs were largely maintained in the resulting superlattices, with their structure strongly influenced by the concavity of NDs. Specifically, high-concavity NDs ($d/D < 0.55$) naturally arranged into extended rows (fig. S10), where the corners of each ND fit snugly into the waists of neighboring particles. This packing motif manifested in two distinct tessellation patterns, shaped by the local curvature of the cap regions in NDs. For NDs with flat caps, such as ND-1, the rows of interlocked NDs tended to align unidirectionally, forming parallel lattices characterized by *p*2 wallpaper symmetry (Fig. 1G and fig. S11). This low-symmetry lattice was further stabilized by cap-to-cap interactions between NDs in adjacent rows. However, when the caps of NDs were more rounded, neighboring ND rows tended to alternate in orientation to create a zigzag pattern, resulting in herringbone lattices with *pgg* symmetry (Fig. 1H and fig. S12).

By contrast, the self-assembly of low-concavity NDs ($d/D > 0.65$) resulted in the formation of chevron lattices (Fig. 1I and fig. S13). These densely packed lattices, featuring *pgg* symmetry, were characterized by a V-shaped packing motif formed from two NDs interlocking through cap fitting. A notable feature of chevron lattices was the flexibility in adjusting the alignment angle between neighboring NDs without altering lattice symmetry (fig. S14). This tunability was achieved by varying the aspect ratio (L/D) of NDs, with the alignment angle decreasing as the aspect ratio increased to maintain dense packing (fig. S15). For instance, the self-assembly of ND-3 with an aspect ratio of 1.5 led to a nearly orthogonal arrangement with an alignment angle of 86° (Fig. 1I), whereas a smaller alignment angle of 69° was observed when assembling NDs with a higher aspect ratio of 1.9 (fig. S14).

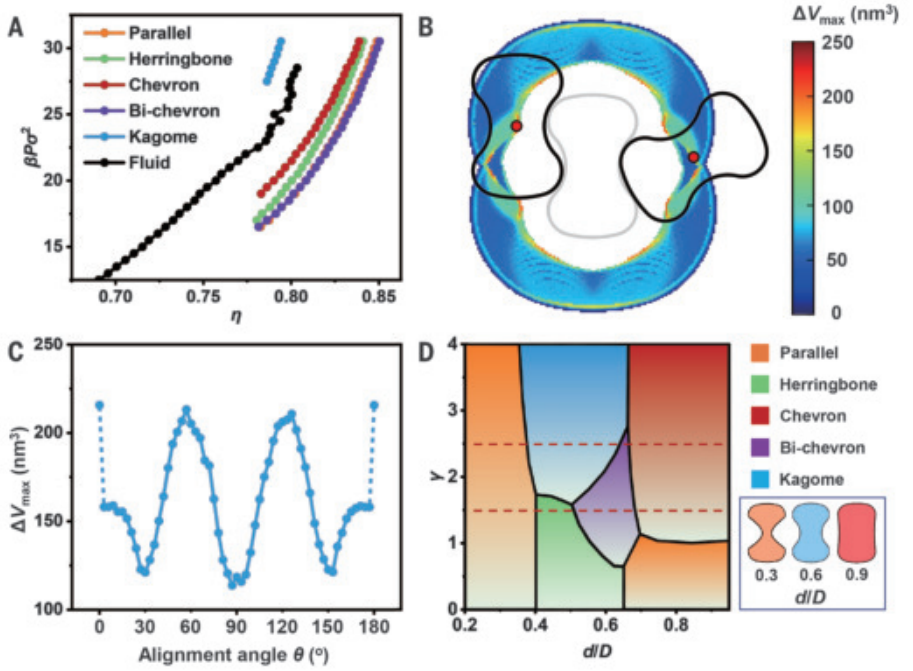

Fig. 3. Formation mechanism of Kagome lattices. (**A**) EOS of the hard-core system of ND-2, derived from simulations. Colored lines represent the expansion results for various perfect crystal structures, while the black line represents the compression of random fluid states. (**B**) Calculated ΔV_{max} for ND pairs under various particle orientations, plotted as a function of relative particle position. The two favored pairing configurations that maximize ΔV_{max} are highlighted with black NDs to indicate the optimal orientations. (**C**) Calculated ΔV_{max} for ND pairs under various particle positions, plotted as a function of relative particle orientation. (**D**) Phase diagram illustrating the phase behaviors of NDs with varying d/D ratios. The region between the two dashed lines represents the predicted phases when γ ranges from 1.5 to 2.5.

When moderate-concavity NDs ($0.55 < d/D < 0.65$) were used for self-assembly, more complex structures could be anticipated because of their tendency for hybrid fitting, which allowed for greater flexibility in tuning particle bonding. A more complex structure was illustrated by the formation of bi-chevron lattices from ND-2 (Fig. 1J and fig. S16). These close-packed lattices displayed an exotic pattern with *pgg* symmetry, in which two pairs of parallel NDs served as a repeating unit, tessellating similarly to chevron lattices. However, unlike chevron lattices, each ND in the bi-chevron lattice participated in dual pairing configurations—hybrid fitting and corner fitting—with three neighboring NDs. This packing behavior aligned with the two locally preferred fitting modes observed in moderate-concavity NDs (fig. S6B), resulting in a unit cell consisting of four NDs aligned in two orientations. The alignment angle between hybrid-fitting NDs was ~62°, as confirmed by WAED analysis (fig. S17).

Kagome lattices

The versatility of moderate-concavity NDs in constructing complex architectures was further demonstrated by the formation of Kagome lattices (Fig. 2 and fig. S18). The Kagome lattice, known for its distinctive 2D arrangement of interconnected triangles, hexagons, and voids, has attracted interest because of its specific geometric and topological properties (*28*). Although Kagome lattices have been observed previously through NC self-assembly (*29*, *30*), the resulting lattices were often low in quality or exhibited structural distortion. Here, by using moderate-concavity NDs, we achieved large-area, high-quality Kagome lattices with minimal structural defects. Figure 2A shows the HAADF-STEM image of Kagome lattices self-assembled from ND-2, the same particles used for forming bi-chevron lattices. Connecting the centroids of individual NDs led to a trihexagonal pattern featuring three distinct particle orientations and periodic voids, aligning with the geometric characteristics of a Kagome lattice. These features were further confirmed by scanning electron microscopy

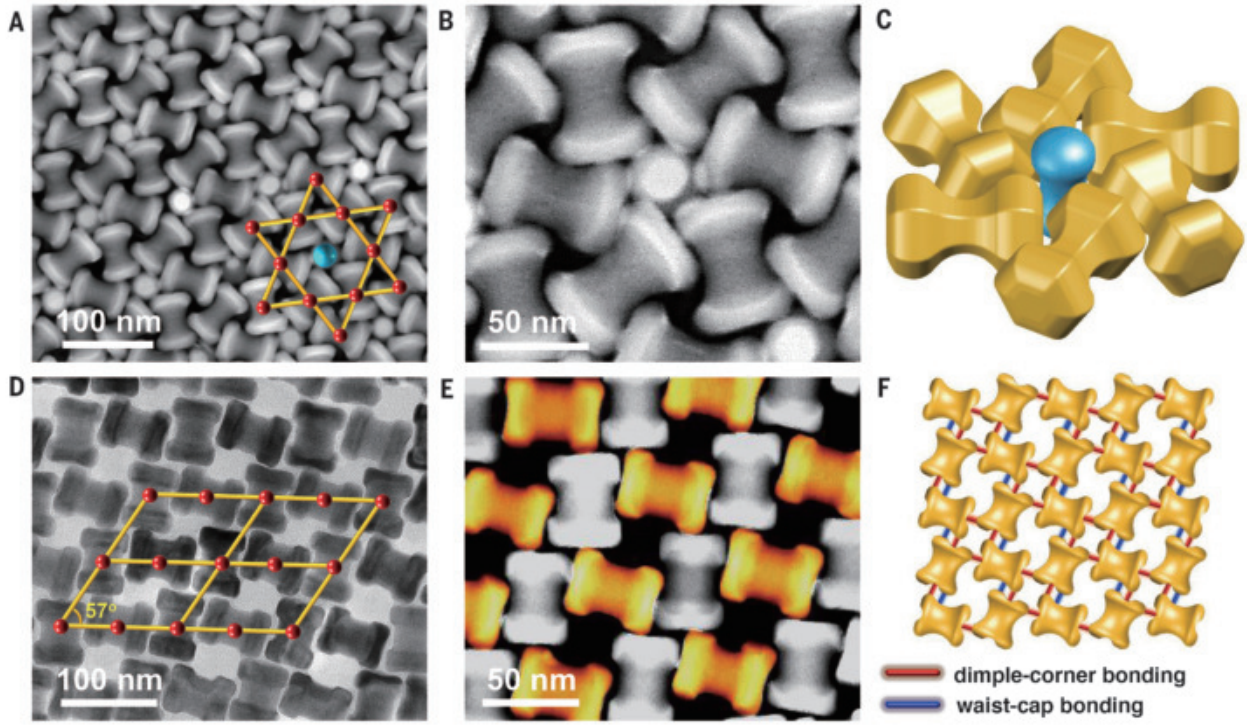

Fig. 4. Self-assembly of NDs into complex superlattices by design. (**A** to **C**) Characterization of AB_3-type binary superlattices self-assembled from two types of NDs: (A) HAADF-STEM image, (B) high-magnification HAADF-STEM image, and (C) structural schematic illustrating the arrangement of large and small NDs. The orange lines connecting the centroids (red dots) of the large NDs in (A) depict the trihexagonal motif, with the smaller ND (blue dot) occupying the void. (**D** to **F**) Characterization of open oblique lattices self-assembled from NDs though multivalent bonding interactions: (D) TEM image, (E) false-colored HAADF-STEM image, and (F) structural schematic highlighting the bonding configurations of individual NDs. The orange lines connecting the centroids (red dots) of NDs in (D) depict the oblique lattice. Half of the NDs in (E) are colored in orange to illustrate their distinct bonding configurations compared to the uncolored NDs.

(SEM, Fig. 2B) and atomic force microscopy (AFM, Fig. 2C).

The self-assembly of Kagome lattices could be reliably achieved by using various moderate-concavity NDs (fig. S19), indicating the robustness of this assembly approach. Kagome lattices often coexisted with the dense bi-chevron lattices (fig. S20), despite having a much lower packing efficiency (~65%, fig. S21). Moreover, single domains of Kagome lattices could extend up to several micrometers in lateral size (fig. S18), suggesting that their formation was under thermodynamic control. The long-range translational order of Kagome lattices was further supported by the radial distribution function (Fig. 2D and fig. S22) and grazing incidence small-angle x-ray scattering (GISAXS, fig. S23) (*31*).

Further analysis revealed that the Kagome lattice displayed *p6* symmetry (Fig. 2E), with each ND interlocking with its four nearest neighbors through hybrid fitting. This arrangement led to the formation of two vertex-sharing trimers, with an alignment angle of 60° between adjacent NDs (fig. S24). These trimers were essential for creating the Kagome pattern, as the trihexagonal motif emerged when six adjacent trimers oriented to form a gear-like superstructure (Fig. 2, F and G). Notably, these hierarchical superstructures were observed to rotate either clockwise (Fig. 2F) or counterclockwise (Fig. 2G), suggesting the development of planar chirality.

This chirality was further supported by the reciprocal space analysis (*32*, *33*), in which the diffraction spots in the SAED patterns displayed clear asymmetry in intensity (Fig. 2, H and I). The as-assembled Kagome lattice was a racemic mixture, comprising domains of both left and right handedness, which was expected given the achiral nature of NDs. An interesting observation was that at the boundary between two chiral domains, a single row of NDs was often present (Fig. 2J). These NDs, as an integral component of one domain, smoothly inverted the chirality of adjacent domains by engaging in corner fitting with NDs in the other domain (Fig. 2K). Increasing the concentration of NDs could lead to the formation of bilayer or trilayer Kagome lattices (fig. S25), with each layer maintaining consistent handedness. An interlayer offset was observed to ensure geometric complementarity between NDs across different layers (fig. S25 and S26).

Formation mechanism

The Kagome lattice, among the various superlattices observed in our experiments, likely represents the most intriguing phase, given its distinctive tessellation patterns and low packing efficiency. Previous studies on Kagome lattices assembled from triblock patchy particles suggested that vibrational entropy played a pivotal role in stabilizing these non–close-packed structures (*34*). To understand the formation mechanism of Kagome lattices assembled from NDs, we first investigated whether they could form through a purely entropy-driven process involving hard particles. To this end, we performed isobaric-isothermal floppy-box Monte Carlo (*NPT* FBMC) simulations based on a system of 960 particles, using shape parameters measured from ND-2 (supplementary text 1) (*35*, *36*). Starting from experimentally observed candidate crystal structures, including parallel, herringbone, chevron, bi-chevron, and Kagome lattices, as well as disordered fluids, we derived the equation of state (EOS) of the corresponding system.

The results indicated that, among these crystal structures, the Kagome lattice was the least favorable phase, with its packing density (η) even lower than that of glassy fluids (Fig. 3A). These findings suggested that purely hard-core interactions between NDs were insufficient to stabilize the Kagome lattice. Given these results, we proposed that depletion interactions,

which were intentionally introduced during self-assembly to overcome kinetic trapping, played a crucial role in stabilizing the Kagome lattice. We hypothesized that the depletion effect enhanced attractive interactions between concave and convex regions of adjacent NDs, guiding them into the specific arrangements needed to form the Kagome lattice. To validate this hypothesis, we conducted further calculations to examine whether depletion interactions could indeed stabilize the Kagome lattice.

The depletion attraction between two particles was proportional to both the overlapping exclusion volume (ΔV) and the number density of depletant (free oleic acid molecules) in solution (*23*). For any two surfaces, the interaction range was determined by twice the radius (r_{dep}) of the depletant molecules. To investigate the effect of depletion interactions on the local packing of NDs, we calculated ΔV for a pair of interacting NDs using a 3D particle model (supplementary text 2), with shape parameters obtained from ND-2. We sampled the local maximum ΔV (ΔV_{max}) across various particle orientations and positions using the direct Monte Carlo method. Figure 3B presents the depletion interaction landscape, represented by ΔV_{max} for various particle orientations. Notably, ΔV_{max} increased substantially when two NDs engaged in corner-fitting and hybrid-fitting modes, consistent with the two locally preferred pairing configurations observed for ND-2 (fig. S6B).

These findings suggested that during self-assembly, NDs tended to adopt concave-convex fitting modes that maximize ΔV_{max}. This mechanism was further supported by plotting ΔV_{max} across various particle positions against alignment angles, which revealed that the depletion interaction peaked at $\theta = 0°$ and nearly at $\theta = 60°$ (Fig. 3C). The calculated ΔV_{max} values for the corner-fitting and hybrid-fitting configurations, referred to as ΔV_{corner} and ΔV_{hybrid}, were ~216 and ~205 nm^3, respectively, assuming $r_{dep} = 0.75$ nm for the depletant molecules (*37*).

To further explore how depletion interactions influenced the formation of specific superlattices, we calculated the total overlapping exclusion volume (ΔV_{tot}) for individual NDs within a lattice. As an approximation, ΔV_{tot} could be considered as the sum of several local ΔV_{max} values, determined by the lattice structure and curvature-fitting modes. In the Kagome lattice, each ND interacted through hybrid fitting with four nearest neighbors (fig. S27A), thus making ΔV_{tot} approximated as four times ΔV_{hybrid}, or 820 nm^3. In the bi-chevron lattice, each ND coordinated with two nearest neighbors through hybrid fitting and one nearest neighbor through corner fitting (fig. S27B), resulting in ΔV_{tot} equal to $2\Delta V_{hybrid} + \Delta V_{corner}$, or 626 nm^3. These calculations suggested that at sufficiently high depletant concentrations, the system favored the Kagome lattice because of its stronger depletion interactions. By contrast, the bi-chevron lattice was entropically more favorable because of its higher packing density. This dual preference accounted for the frequent coexistence of these two phases within the same system.

These calculations focused on moderate-concavity NDs, but we speculated that curvature-guided depletion interactions similarly governed the extended assembly of both low- and high-concavity NDs (fig. S8). During solvent evaporation, the progressively increasing depletion interaction strengthened the binding between the concave and convex regions of neighboring NDs, allowing them to recognize and adjust their orientations for optimal concave-convex contact. This process not only helped avoid kinetic traps but also facilitated the global interlocking of NDs into the corresponding superlattice structures. Concurrently, lateral capillary forces could further enhance the concave–convex attractions at the later stage of evaporation (*38*, *39*), bringing NDs into closer proximity. As evaporation continued, van der Waals interactions between the surface ligands of adjacent NDs became increasingly dominant, effectively locking the particles in place once the solvent had fully evaporated (*40*). This transition solidified the as-assembled superlattices, ensuring their structural integrity during transfer from the liquid surface to various substrates.

Phase behavior

To construct a comprehensive phase diagram, we introduced a phenomenological parameter γ, which served to describe the relative strength of concave-convex interactions compared to convex-convex or concave-concave interactions between two NDs (supplementary text 3). This parameter reflects the degree of compatibility of local curvatures between the concave and convex patches on neighboring particles, with higher γ values indicating stronger interparticle concave-convex attractions. We investigated the system using a 2D particle model with shape parameters based on ND-2, while continuously varying the concavity (d/D ratio) from 0.20 to 0.95. Although this particle model was more coarse-grained compared to the one used for depletion calculations, it allowed us to construct a phase diagram that qualitatively captured the phase behaviors of differently shaped NDs (Fig. 3D).

By comparing the various lattice structures predicted by the phase diagram with experimental results, we estimated γ to fall within the range of 1.5 to 2.5. Within this range, the Kagome lattice could form and coexist with the bi-chevron lattice when the d/D ratio ranged from ~0.55 to ~0.65 (fig. S28), which agreed well with experimental observations. Additionally, the phase diagram predicted that for NDs with very narrow waists (e.g., $d/D = 0.3$), the stable phase was the parallel lattice, whereas for NDs with very wide waists (e.g., $d/D = 0.9$), the stable phase was the chevron lattice. These predictions were supported by experiments (fig. S29), reinforcing the validity of this phase diagram in predicting the structural outcome of superlattices assembled from NDs.

Binary superlattices and low-density superlattices

The established mechanism of curvature-guided depletion was critical, as it opened up new possibilities for creating sophisticated architectures that are otherwise unattainable with convex building blocks. For example, coassembling two types of NDs with differing dimensions led to the formation of AB_3-type binary superlattices (fig. S30). In this close-packed structure, the large NDs interlocked to form a chiral Kagome pattern (Fig. 4A), while the smaller NDs occupied the voids (Fig. 4B). To achieve optimal local curvature matching, each smaller ND aligned vertically, positioning its waist to interact with the corners of six adjacent larger NDs (Fig. 4C). Incorporating particles into the periodic voids of the Kagome lattice introduced an additional level of structural complexity, which might lead to the emergent properties stemming from the distinctive topological arrangement of the lattice (*30*, *41*).

The versatility of this curvature-guided design principle was further demonstrated by its ability to direct the assembly of low-symmetry, low-density lattices. These lattices were achieved by introducing multivalent bonding interactions through the creation of additional concave features into NDs. As a proof of concept, we synthesized NDs with two small dimples at their endcaps by modifying the reaction conditions (fig. S31). Along with the regular binding sites at the waist, these dimples provided additional sites that selectively bound with the high-convex corners of neighboring NDs through local curvature matching. This dual concave-convex interaction mode led to symmetry breaking, resulting in the formation of an open oblique lattice with an internal angle of 57° (Fig. 4D). In this low-symmetry lattice, the concave waists and dimples of half the NDs fully engaged in interlocking, whereas the other half remained uncoordinated at their waists (orange NDs in Fig. 4E). This approach led to a packing fraction of ~59% (fig. S32), which was even lower than that of the Kagome lattice. The multiple specific bonding interactions between neighboring NDs were likely responsible for stabilizing this unusual open lattice (Fig. 4F).

Conclusions

Our study demonstrates that the curvature of nonconvex NCs can be leveraged to program

directional interparticle interactions. By engineering the local curvature of NDs, we achieved precise and flexible control over particle bonding directionality, enabling the formation of diverse and intricate 2D superlattices. Our research also highlights the critical role of curvature-guided depletion interactions, which not only facilitated the global interlocking of NDs but also stabilized open structures such as Kagome lattices. With interlocked configurations and tunable lattice symmetry, these ND superlattices could have distinctive mechanical and optical properties. Additionally, this curvature-mediated design principle could serve as a general strategy for guiding the self-assembly of various nonconvex NCs (*42*). Although this work primarily focused on single-component superlattices, it paves the way for creating more complex multicomponent superlattices by coassembling NDs with appropriately shaped convex NCs.

REFERENCES AND NOTES

1. C. L. Bassani *et al*., *ACS Nano* **18**, 14791–14840 (2024).
2. L. Cademartiri, K. J. M. Bishop, *Nat. Mater.* **14**, 2–9 (2015).
3. M. R. Jones *et al*., *Nat. Mater.* **9**, 913–917 (2010).
4. M. Liu, X. Zheng, V. Grebe, D. J. Pine, M. Weck, *Nat. Mater.* **19**, 1354–1361 (2020).
5. K. Deng, Z. Luo, L. Tan, Z. Quan, *Chem. Soc. Rev.* **49**, 6002–6038 (2020).
6. Z. Xue, C. Yan, T. Wang, *Adv. Funct. Mater.* **29**, 1807658 (2019).
7. M. A. Boles, M. Engel, D. V. Talapin, *Chem. Rev.* **116**, 11220–11289 (2016).
8. X. Li, X. Liu, X. Liu, *Chem. Soc. Rev.* **50**, 2074–2101 (2021).
9. L. Z. Zornberg *et al*., *ACS Nano* **17**, 3394–3400 (2023).
10. M. S. Lee, D. W. Yee, M. Ye, R. J. Macfarlane, *J. Am. Chem. Soc.* **144**, 3330–3346 (2022).
11. R. J. Macfarlane, M. N. O'Brien, S. H. Petrosko, C. A. Mirkin, *Angew. Chem. Int. Ed.* **52**, 5688–5698 (2013).
12. W. Zhou, Y. Li, B. E. Partridge, C. A. Mirkin, *Chem. Rev.* **124**, 11063–11107 (2024).
13. J. Park *et al*., *Nat. Mater.* **3**, 891–895 (2004).
14. X. Ye *et al*., *Proc. Natl. Acad. Sci. U.S.A.* **107**, 22430–22435 (2010).
15. A. Kim *et al*., *ACS Nano* **18**, 939–950 (2024).
16. C. Yi *et al*., *Science* **369**, 1369–1374 (2020).
17. Z. Miao, C. Y. Zheng, G. C. Schatz, B. Lee, C. A. Mirkin, *Angew. Chem. Int. Ed.* **60**, 19035–19040 (2021).
18. H. Chen *et al*., *Nature* **599**, 222–228 (2021).
19. M. Qi *et al*., *J. Am. Chem. Soc.* **145**, 2739–2744 (2023).
20. Q. Chen, S. C. Bae, S. Granick, *Nature* **469**, 381–384 (2011).
21. S. Wan *et al*., *ACS Nano* **16**, 21315–21323 (2022).
22. D. A. Walker, E. K. Leitsch, R. J. Nap, I. Szleifer, B. A. Grzybowski, *Nat. Nanotechnol.* **8**, 676–681 (2013).
23. S. Sacanna, W. T. Irvine, P. M. Chaikin, D. J. Pine, *Nature* **464**, 575–578 (2010).
24. A. Dong, J. Chen, P. M. Vora, J. M. Kikkawa, C. B. Murray, *Nature* **466**, 474–477 (2010).
25. Y. Liu *et al*., *Chem. Sci.* **11**, 4065–4073 (2020).
26. K. Zhao, T. G. Mason, *Rep. Prog. Phys.* **81**, 126601 (2018).
27. E. Marino, Z. Jiang, T. E. Kodger, C. B. Murray, P. Schall, *Langmuir* **39**, 12533–12540 (2023).
28. J. L. Atwood, *Nat. Mater.* **1**, 91–92 (2002).
29. Y. Taniguchi *et al*., *ACS Nano* **11**, 9312–9320 (2017).
30. Z. Li *et al*., *Sci. Adv.* **10**, eadp3756 (2024).
31. N. Mac Fhionnlaoich, R. Qi, S. Guldin, *Langmuir* **35**, 16605–16611 (2019).
32. K. Zhao, T. G. Mason, *J. Phys. Condens. Matter* **26**, 152101 (2014).
33. H. Deng *et al*., *Nature* **632**, 775–781 (2024).
34. X. Mao, Q. Chen, S. Granick, *Nat. Mater.* **12**, 217–222 (2013).
35. J. de Graaf, L. Filion, M. Marechal, R. van Roij, M. Dijkstra, *J. Chem. Phys.* **137**, 214101 (2012).
36. D. Frenkel, B. Smit, *Understanding Molecular Simulation: From Algorithms to Applications* (Elsevier, 2001).
37. S. N. Hosseini *et al*., *Adv. Funct. Mater.* **30**, 2005491 (2020).
38. N. Bowden, F. Arias, T. Deng, G. M. Whitesides, *Langmuir* **17**, 1757–1765 (2001).
39. P. J. Yunker, T. Still, M. A. Lohr, A. G. Yodh, *Nature* **476**, 308–311 (2011).
40. F. Zhang, R. Liu, Y. Wei, J. Wei, Z. Yang, *J. Am. Chem. Soc.* **143**, 11662–11669 (2021).
41. X. Wu, D. Chakraborty, A. P. Schnyder, A. Greco, *Phys. Rev. B* **109**, 014517 (2024).
42. Q. Chen, Y. Jia, S. Xie, Z. Xie, *Chem. Soc. Rev.* **45**, 3207–3220 (2016).

ACKNOWLEDGMENTS

Funding: This work was supported by National Key Research and Development Program of China (2022YFA1503501), NSFC (52333013, 22025501, 22088101, 52202088, 52373204, 52394272, 224B1019), Science and Technology Commission of Shanghai Municipality (24TS1410200, 23JC1400100, 2024ZDSYS02, 24JD1400700), Shanghai International Science and Technology Partnership Project (23520750400), China Postdoctoral Science Foundation (2024M760493), and the Fundamental Research Funds for the Central Universities (20720220010). T.L. was supported by the Shanghai Rising-Star Program (24QA2700800). R.N. was supported by the Academic Research Fund from the Singapore Ministry of Education (RG151/23 and MOE2019-T2-2-010) and the National Research Foundation, Singapore, under its 29th Competitive Research Program (CRP) Call (NRF-CRP29-2022-0002). **Author contributions:** A.D. and T.L. conceived and supervised this work. S.W. performed the experiments and data analysis. X.X. and R.N. conducted the MC simulations and depletion interaction calculations. J.L. performed phase diagram constructions. Y.G., H.Z., and F.W. contributed to ND synthesis. Z.Z. conducted AFM characterization. X.W. and D.Y. contributed to geometric calculation and analysis. All authors participated in the writing and revision of the manuscript. **Competing interests:** The authors declare no competing interests. **Data and materials availability:** All data are available in the main text or the supplementary materials.

SUPPLEMENTARY MATERIALS

science.org/doi/10.1126/science.adu4125
Materials and Methods
Supplementary Text
Figs. S1 to S33
References (*43*–*45*)
Movie S1

Submitted 6 November 2024; accepted 9 January 2025
10.1126/science.adu4125

AGRICULTURE ECONOMICS

Too much of a good thing: Lessons from compromised rootworm Bt maize in the US Corn Belt

Ziwei Ye[1], Christina DiFonzo[2], David A. Hennessy[3], Jinhua Zhao[4], Felicia Wu[5,6], Shawn P. Conley[7], Aaron J. Gassmann[8], Erin W. Hodgson[8], Bryan Jensen[9], Janet J. Knodel[10], Bradley McManus[11], Lance J. Meinke[12], Andrew Michel[13], Bruce Potter[14], Nicholas J. Seiter[15], Jocelyn L. Smith[16], Joseph L. Spencer[17], Kelley J. Tilmon[13], Robert J. Wright[12], Christian H. Krupke[18]*

Widespread use of genetically engineered maize targeting the corn rootworm complex (*Diabrotica* species) has raised concerns about insect resistance. Twelve years of university field trial and farm survey data from 10 US Corn Belt states indicate that maize hybrids expressing toxins derived from the bacterium *Bacillus thuringiensis* (Bt maize) exhibited declining protection from rootworm feeding with increased planting while pest pressures simultaneously decreased. The analysis revealed a tendency to overplant Bt maize, leading to substantial economic losses; this was particularly striking in eastern Corn Belt states. Our findings highlight the need to go beyond the "tragedy of the commons" perspective to protect sustainable use of Bt and other crop biotechnology resources. We propose moving toward a more diversified and transparent seed supply.

Transgenic, or genetically engineered, crop technologies targeting key insect pests have revolutionized global food production, helping feed a growing population with minimal environmental harm (*1*, *2*). However, the onset of pest resistance inevitably follows increased adoption of transgenic varieties, rendering the technology less effective over time (*3*, *4*). In 2003, transgenic maize hybrids producing rootworm-active insecticidal proteins derived from the bacterium *Bacillus thuringiensis* (Bt) were introduced. These rootworm Bt maize hybrids provide protection against both western (*Diabrotica virgifera virgifera* LeConte) and northern (*Diabrotica barberi* Smith & Lawrence) corn rootworms (*5*). The western corn rootworm is the primary target because of its economic significance. The use of Bt hybrids has been extensive (fig. S1). Beginning in 2009, field studies have documented Bt resistance in rootworms, raising concerns about the long-term durability of this approach (*6*–*9*).

Pest susceptibility to rootworm Bt maize may be considered a common pool resource, prone to being exploited more than is optimal for a group (the "group optimum"): an instance of the "tragedy of the commons" (*10*–*12*). This is because individuals tend to act based upon self-interest (the "individual optimum"), intentionally or unintentionally ignoring external costs to the group. However, rootworm Bt maize may provide areawide suppression of pest populations, as seen with Bt maize hybrids targeting the European corn borer in field maize and vegetable crops (*13*, *14*) and with Bt cotton contributing to the eradication of pink bollworm (*15*). Areawide suppression may counteract the

resource overexploitation incentives for self-interest to deviate from the group interest. As a result, concerns about the "tragedy of the commons", i.e., misalignment between self- and group interests, may be misplaced, diverting policy attention from more fundamental issues that shape any overuse of rootworm Bt maize.

Combining 12 years of Bt maize field trial data and proprietary data on farmers' seed usage across the US Corn Belt, this study investigates the potential extent and economic consequences of divergence between status quo and optimal levels of rootworm Bt maize planting (supplementary text S1 and S2). We characterize the nature of this divergence by distinguishing between individual and group optima. We then propose a path forward for sustainable rootworm Bt maize deployment. Unless otherwise specified, the term "Bt" hereafter refers specifically to rootworm-active Bt toxins.

Interdisciplinary modeling approach

The western corn rootworm has an annual life cycle. Its larvae feed primarily on maize roots; severe infestations lead to considerable yield loss (*16*). Maize roots expressing Bt toxins cause larval mortality and provide yield protection in the planting year as well as population suppression in the following year. However, selection pressure over time leads to toxin resistance. The net future cost of planting Bt maize, encompassing both cost of resistance selection and benefit from pest suppression, is termed the "own-field" cost. Additionally, gravid females may disperse to neighboring maize fields in search of oviposition sites, creating a spillover cost to neighboring fields (*17*, *18*, *19*) (Fig. 1A).

We developed an interdisciplinary approach to evaluate potential overuse of rootworm Bt maize (Fig. 1A), integrating pest biology (*20*), observations of pest damage to Bt and non-Bt maize, and Bt planting levels over time. Using data from 2005 through 2016, we quantified the costs and benefits of Bt maize for individual and neighboring fields. This cost-benefit analysis determined optimal Bt planting levels for individuals and groups, comparing these with the observed status quo, and examined associated economic consequences over the 2014 to 2016 period (the most recent three-year period covered by our datasets). Optimal seed decisions weigh the yield protection benefit of a Bt hybrid relative to a non-Bt hybrid against

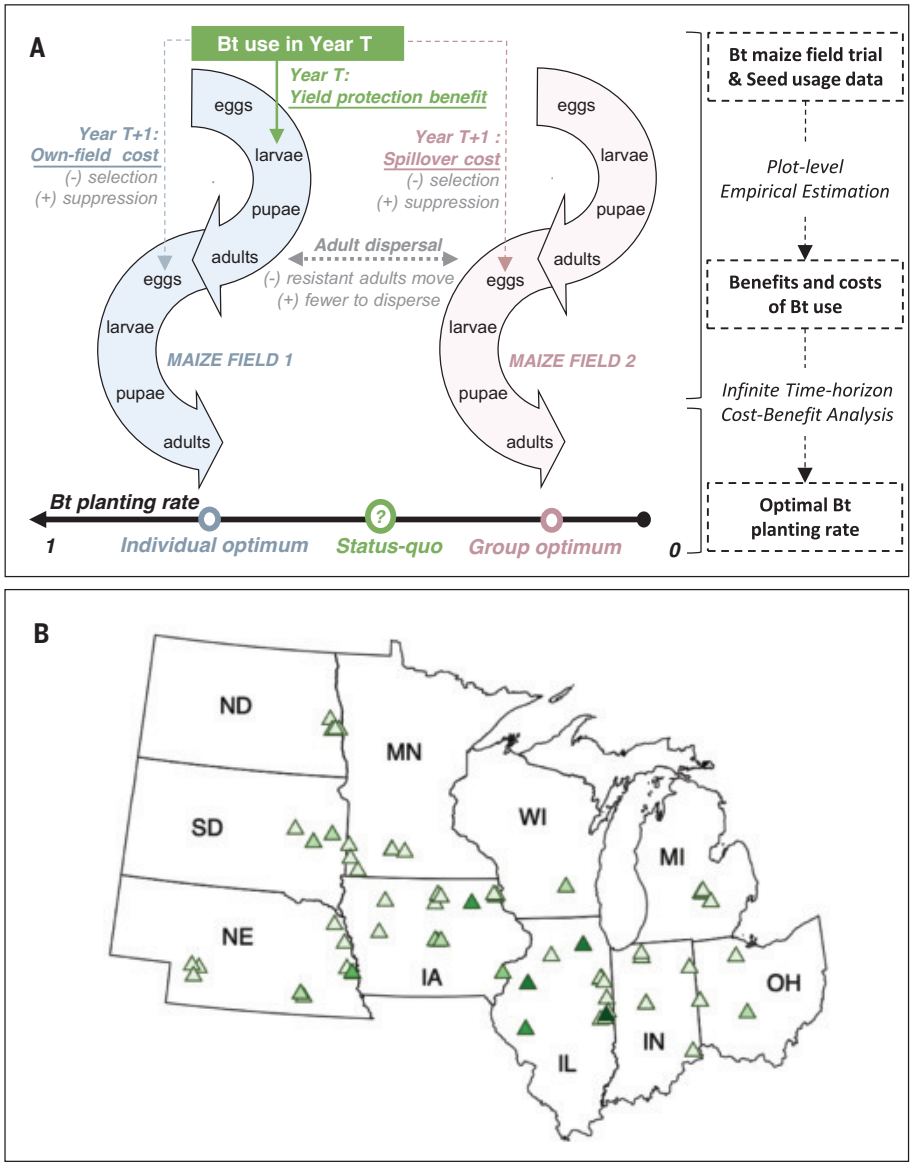

Fig. 1. Interdisciplinary modeling approach for empirical assessments of rootworm Bt maize overplanting. (**A**) Pest biology and conceptual characterization of individual and group optimum planting of rootworm Bt maize. A grower's decision to plant Bt maize in Field 1 in year T provides a yield protection benefit but incurs a future cost to the field in year T+1 (own-field cost), encompassing both the cost of resistance selection (denoted by a minus sign) and the benefit from pest suppression (denoted by a plus sign) the following season. This future cost also spills over to neighboring fields (spillover cost), represented by Field 2, through adult dispersal. The "individual optimum" refers to the optimal Bt planting rate for farmers who consider only own-field cost; the "group optimum" refers to the optimal Bt planting rate for farmers who, in addition to own-field cost, voluntarily consider the group's collective interest by incorporating the spillover cost to others' maize fields when making seed decisions. The Bt planting rate ranges from 0 to 1. (**B**) Geographical distribution of university field trials, 2005 to 2016. Triangles represent field trial sites in the sample, with a darker color indicating a greater annual number of observations at the site.

[1]School of Agricultural Economics and Rural Development, Renmin University of China, Beijing, China. [2]Department of Entomology, Michigan State University, East Lansing, MI, USA. [3]Department of Economics and Center for Agricultural and Rural Development, Iowa State University, Ames, IA, USA. [4]Charles H. Dyson School of Applied Economics and Management, Cornell University, Ithaca, NY, USA. [5]Department of Food Science and Human Nutrition, Michigan State University, East Lansing, MI, USA. [6]Department of Agricultural, Food, and Resource Economics, Michigan State University, East Lansing, MI, USA. [7]Department of Agronomy, University of Wisconsin-Madison, Madison, WI, USA. [8]Department of Plant Pathology, Entomology and Microbiology, Iowa State University, Ames, IA, USA. [9]Department of Entomology, University of Wisconsin-Madison, Madison, WI, USA. [10]Department of Plant Pathology, North Dakota State University, Fargo, ND, USA. [11]Department of Agronomy, Horticulture, Plant Science, South Dakota State University, Brookings, SD, USA. [12]Department of Entomology, University of Nebraska-Lincoln, Lincoln, NE, USA. [13]Department of Entomology, The Ohio State University, Wooster, OH, USA. [14]Southwest Research and Outreach Center, University of Minnesota, Lamberton, MN, USA. [15]Department of Crop Sciences, University of Illinois Urbana-Champaign, Urbana, IL, USA. [16]School of Environmental Sciences, Ridgetown Campus, University of Guelph, Ridgetown, ON, Canada. [17]Illinois Natural History Survey, University of Illinois Urbana-Champaign, Champaign, IL, USA. [18]Department of Entomology, Purdue University, West Lafayette, IN, USA.
***Corresponding author. Email: ckrupke@purdue.edu**

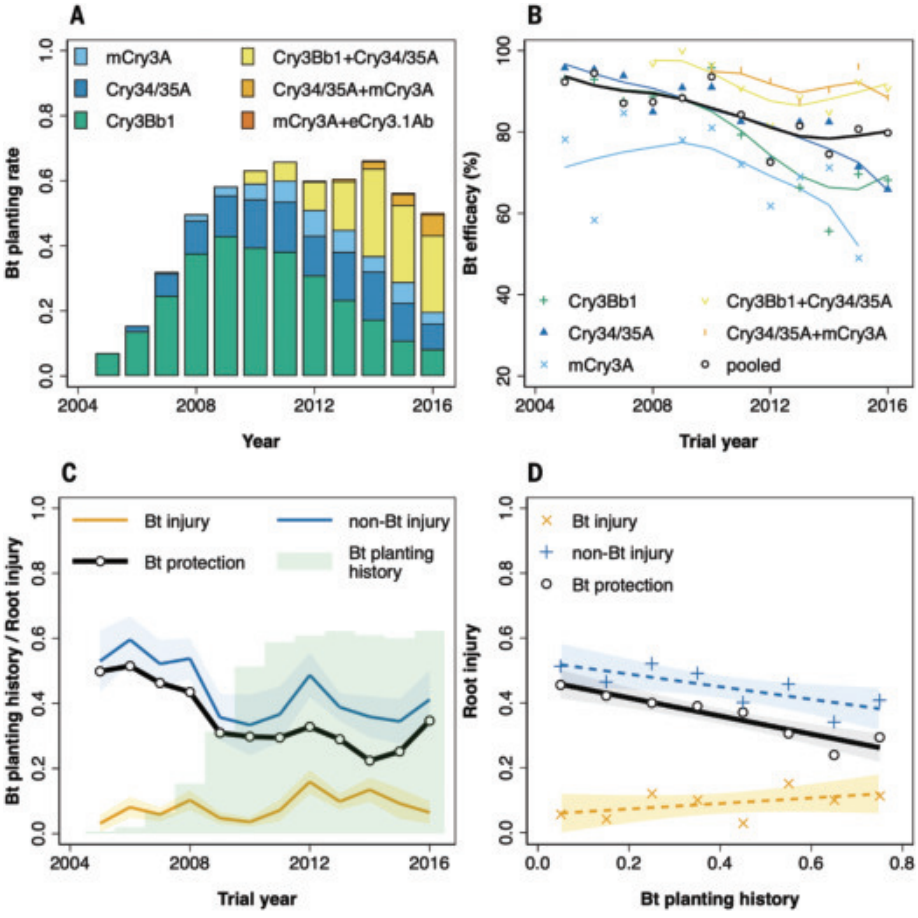

Fig. 2. Bt planting and Bt efficacy, 2005 to 2016. (**A**) Bt planting rate by the *Cry* protein expressed. The Bt planting rate is calculated as the rate of total maize acres expressing each *Cry* protein, alone or in combination. (**B**) Bt efficacy by the *Cry* protein expressed. The dots represent Bt efficacy for each *Cry* protein, alone or in combination. The curves show the smooth fit of Bt efficacy using locally weighted regression (Cleveland's tricube weighting function with bandwidth 0.8). The data for mCry3A+eCry3.1Ab were excluded due to insufficient observations. (**C**) Root injury and Bt protection overlaid on Bt planting history. Root injury data averages were taken from trials evaluating Bt and non-Bt hybrids to obtain "Bt injury" and "non-Bt injury," excluding observations treated with soil insecticides or high-rate insecticidal seed treatments. "Bt protection" is the difference between non-Bt injury and Bt injury, and "Bt planting history" is the rate of total maize acres planted to Bt hybrids in the previous year. (**D**) Linearly fitted relationships between root injury, Bt protection, and Bt planting history using ordinary least squares. The fitted slopes for Bt injury, non-Bt injury, and Bt protection are 0.09 (p = 0.217), −0.19 (p = 0.027), and −0.28 (p = 0.001), respectively (df = 7).

the additional seed cost associated with Bt maize (the "seed premium") as well as subsequent resistance selection and pest suppression. Whether farmers act according to self- or group interest distinguishes between "individual optimum" and "group optimum" (*21*). That is, individual optimum considers only the own-field cost in the future whereas group optimum also considers the spillover cost to neighbors.

Bt maize trial data were compiled from university field trial sites across 10 US Corn Belt states: Illinois, Iowa, Minnesota, Nebraska, North Dakota, South Dakota, and Wisconsin were grouped as "western states", where continuous maize is common, while Indiana, Michigan, and Ohio were grouped as "eastern states" and are generally characterized by frequent crop rotation (Fig. 1B, supplementary text S1, and fig. S2). Most sites comprised both treatment (Bt) and control (non-Bt) plots. Bt seed usage data, representative at the crop reporting district level, came from a proprietary data TraitTrak® (*22*, *23*) (supplementary text S2 and table S1).

Benefits and costs of rootworm Bt maize

Corn rootworm damage to maize plants is commonly measured using a 0 to 3 node injury scale (*24*); each root node consumed reduces yield by approximately 15% (*16*). For analysis, we standardized this on a 0 to 1 scale (supplementary text S1), termed "root injury" hereafter.

Bt maize compromised with increased planting

Our investigation began with examining changes in root injury in Bt and non-Bt hybrids, along with landscape-level changes in Bt planting between 2005 and 2016. Although the most recent growing seasons are not covered, this period was crucial for establishing a baseline and observing initial responses to selection (*6*–*8*). Many trials followed late-planted maize from the previous season to increase the attraction of gravid females and maximize rootworm detection, likely overestimating pest pressure and enabling a more conservative analysis.

Bt toxin efficacy generally declined as Bt planting increased, whether toxins were examined separately or pooled across six available trait packages: Cry3Bb1, Cry34/35A (now classified as Gpp34Ab1/Tpp35Ab1), mCry3A, Cry3Bb1+Cry34/35A, mCry3A+Cry34/35A, and mCry3A+eCry3.1Ab (Fig. 2, A and B, and table S2). Efficacy was evaluated using Abbott's formula (*25*) which, expressed as a percentage, represents the ratio of two components: the difference in root injury between non-Bt (denoted as Y) and Bt (denoted as X) maize plots—termed Bt protection—and root injury in non-Bt maize, calculated as $\frac{(Y-X)\times 100\%}{Y}$

We focused on the pooled analysis and breakdown of Bt efficacy into its two components to characterize the intertemporal selection and suppression effects. Root injury in trial year t served as a proxy for rootworm population in year t−1. The intertemporal effects can be represented by the effects of Bt planting in year t−2, or Bt planting history, on the rootworm population in year t−1. Thus the selection and suppression effects were captured, respectively, by the effects of Bt planting history on Bt protection (Y−X) and root injury in non-Bt maize (Y).

As Bt planting increased in the US Corn Belt (Fig. 2C), we observed an overall decrease in root injury in non-Bt plots (Fig. 2C and fig. S3), except for a temporary spike in 2012, likely associated with severe drought. Bt protection also declined (Fig. 2C) until the introduction of trait packages combining multiple Bt toxins in 2009 (Fig. 2A). These findings highlight the dual impacts of Bt maize, simultaneously suppressing rootworms and selecting for resistance. Figure 2D further shows a steeper fitted slope for Bt protection than for non-Bt injury, indicating that declines in Bt protection progressed more rapidly than declines in background pest pressure as Bt planting increased.

Bt maize, selection, and suppression

We fitted a plot-level fractional response model of root injury on Bt maize treatment (indicating whether a trial plot was planted to Bt or non-Bt maize), Bt planting history, their interaction term, and additional covariates. This model predicted the mean root injury for Bt and non-Bt plots planted to Bt or non-Bt maize in the preceding year (*26*) (supplementary text S3 to

Table 1. Estimated mean root injury for Bt and non-Bt maize, in fields with and without Bt history.

Mean root injury (standard errors)	Non-Bt maize [Y] (*bt* = 0)	Bt maize [X] (*bt* = 1)	Differences [Y−X]	Attributed to
No Bt history (*history* = 0)	[i] 0.55 (0.026)	[ii] 0.08 (0.014)	[v] 0.47 (0.024)	*Bt maize*
Has Bt history (*history*=1)	[iii] 0.25 (0.028)	[iv] 0.11 (0.024)	[vi] 0.14 (0.028)	*Bt maize and selection*
Differences	[vii] 0.30 (0.037)	[viii] −0.03 (0.037)	[ix] 0.33 (0.045)	
Attributed to	*Intertemporal suppression*	*Suppression and selection*	*Intertemporal selection*	

Mean root injury for Bt (or non-Bt) maize fields with (or without) Bt planting history was predicted from the fitted model at *bt* = 1 (or *bt* = 0) and *history* = 1 (or *history* = 0). For instance, cell [i] represents the estimated mean root injury for a non-Bt maize field that was planted to non-Bt maize in the preceding year, while cell [iv] represents the estimated mean root injury for a Bt maize field that was planted to Bt maize in the preceding year. Additionally, the following calculations were performed: cell [v]=[i]−[ii], [vi]=[iii]−[iv], [vii]=[i]−[iii], [viii]=[ii]−[iv], and [ix]=[v]−[vi]=[vii]−[viii].

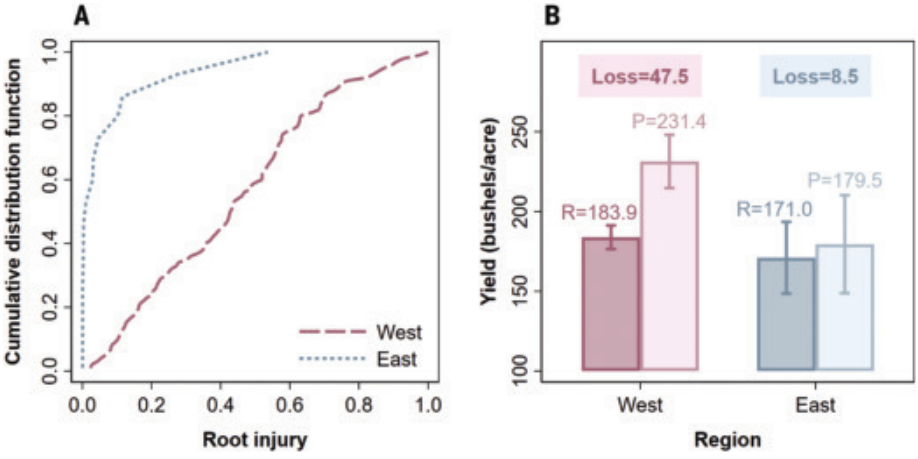

Fig. 3. Heterogeneity in rootworm incidence between western and eastern states during 2014 to 2016. (**A**) Empirical cumulative distribution functions of root injury in non-Bt trials. (**B**) Realized yield (R), yield potential (P), and annual yield losses attributed to rootworm damage (Loss). Bar plots illustrate the means of the realized yield (darker colors) and yield potential (lighter colors) across all counties in each region, with error bars representing 95% confidence intervals. The difference between yield potential and realized yield is the yield loss attributed to rootworm damage (Loss = P − R). Yield potential was determined by $P = R/(1 - 3 \times 0.15 \times \overline{rw})$, where 0.15 was the fraction of yield loss for each node of roots injured and $\overline{rw}$ denoted the county-average root injury.

S5). Differences in mean root injury were then attributed to concurrent Bt maize effects, intertemporal suppression, or resistance selection (Table 1 and table S3).

Results in Table 1 indicate that root injury was generally higher in maize fields continuously planted with non-Bt hybrids (cell [i]). Prior Bt maize cultivation in non-Bt plots reduced root injury by a considerable amount, showing intergenerational suppression of rootworms (cell [vii]). Planting Bt maize without previous Bt history achieved the highest level of root protection (cell [v]). However, with a Bt planting history, the root injury difference between non-Bt and Bt fields was reduced, suggesting a selection cost (cell [ix]) greater than the suppression benefit. Table 1 estimates remain robust to the alternative modeling approach (supplementary text S6 and tables S4 and S5) as well as additional regression analyses employing alternative specifications (supplementary text S7 and tables S3 and S6 to S10) and examining each Bt trait package separately (supplementary text S7, fig. S4, and tables S11 and S12).

The own-field cost was estimated to be 0.03 (cell [viii]) in terms of root injury. Assuming homogeneity in maize fields and equal fecundity between native and immigrating females, the ratio of spillover cost to own-field cost is determined by the ratio of immigrating females to native females. To assess the spillover cost, we calibrated the female dispersal proportion using a range of 5 to 50%, drawing from the primary literature (*17*–*19*). Our analysis revealed that resistance selection was substantially counteracted by pest suppression. Consequently, the relatively minor extent of spillover cost indicates a strong likelihood that grower self-interest closely aligned with group interest during our study period.

Cost-benefit analysis: Status quo, group optimum, and individual optimum

Heterogeneity between western and eastern states

For the 2014 to 2016 period, farm survey data show comparable seed premiums for rootworm Bt hybrids in western and eastern states, at 24.1 and 25.7 USD per acre. However, the realized yield protection benefit exhibited regional heterogeneity because it was capped when rootworm pressure was minimal (text S8). This is especially relevant for eastern states where rootworm incidence was low, from 2014 to 2016 (Fig. 3A). Estimated yield losses attributable to rootworm damage were higher in western (47.5 bushels per acre) compared with eastern states (8.5 bushels per acre) (Fig. 3B).

These findings collectively suggest that planting Bt hybrids in eastern states provided only marginal yield protection benefits compared with their costs. To illustrate, Indiana's average root injury in non-Bt maize was 0.03 in 2015, resulting in a maximum yield benefit of 9.0 USD per acre. This was calculated from avoided yield loss (0.03 × 3 × 0.15 × 179.5) multiplied by the maize cash price of 3.7 USD, where 0.15 is the fraction of yield loss per injured root node (*16*). This 9.0 USD benefit covered roughly one-third of the seed premium; the future costs were not factored in.

Bt overplanting: One-size-fits-all pest management

We empirically evaluated optimal Bt planting levels for individuals and groups, weighing the current year's payoff (yield protection benefit minus seed premium) against future payoffs that considered intertemporal costs (*27*) (supplementary text S8 and figs. S5 to S7). The future payoffs were discounted using a "discount factor" reflecting decision-makers' time-preference, or the natural inclination to undervalue future benefits (*28*); a value of 0.95 is commonly applied by economists. Despite regional heterogeneity in yield protection benefits, status quo rootworm-Bt planting rates during 2014 to 2016 were similar in western and eastern states, averaging 59% (SE = 2.3) and 50% (SE = 3.7) (Fig. 4). Within these rates, 58.5 and 49.5% comprised hybrids combining rootworm Bt with aboveground Bt and herbicide-tolerant traits, while only 0.5% were pure rootworm Bt hybrids. This underscores the tendency to opt for convenient one-size-fits-all, multitoxin Bt hybrids even in the absence of significant pest pressure.

Comparing the status quo with the group optimum (Fig. 4A and table S13) reveals differing extents of Bt maize overplanting. Western states showed a mild overplanting tendency, especially with high dispersal rates, due to higher rootworm pressure. In eastern states, overplanting was more pronounced, with group

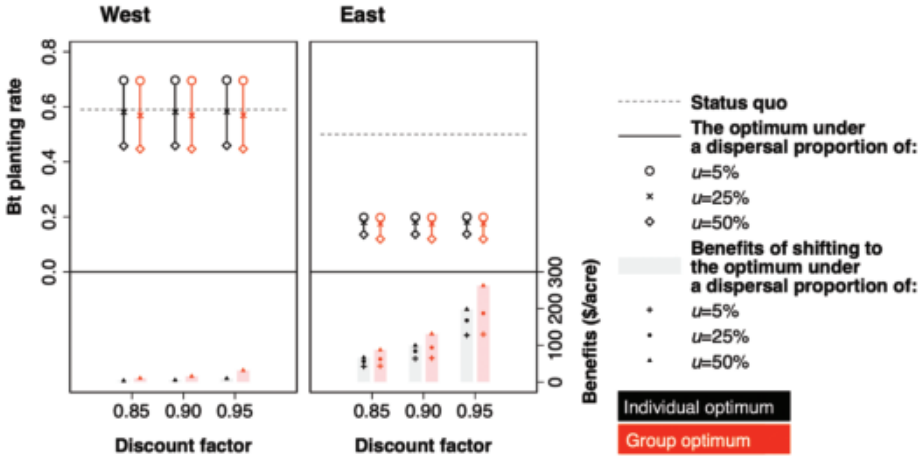

Fig. 4. Divergence between status quo and group/individual optimum Bt planting level, and economic implications for western and eastern states, 2014 to 2016. The upper panels present the individual optimum (in black) and group optimum (in red) Bt planting rate ranges under varying levels of female dispersal proportion (u) assumptions, with the dashed horizontal lines (in gray) showing the status quo Bt planting rate for comparison. The lower panels illustrate the lifetime benefits of shifting from the status quo to the individual optimum (in black) and group optimum (in red) Bt planting rates. For western states, this is shown under a 50% dispersal assumption, as the optimum exceeds the status quo at 5% dispersal and aligns closely at 25%. For eastern states, benefits are displayed across varying dispersal assumptions. The individual optimum Bt planting rate was the self-sustaining planting level best for farmers' self-interest, whereas the group optimum was best for farmers who voluntarily considered local group interests.

optimum Bt planting rates between 12 and 20%, depending on dispersal. These findings remain robust across a reasonable range of discount factor assumptions (0.85, 0.90, and 0.95) and farm heterogeneity considerations: continuous maize versus rotated maize, maize monoculture versus mixed cropping, and large field versus small field (supplementary text S9 and tables S14 to S17).

Beyond the "tragedy of the commons"

For both western and eastern states, differences between group and individual Bt planting optima were notably small. This contrasts sharply with the major discrepancy between the status quo and the individual optimum, particularly in eastern states (Fig. 4). The gap suggests that Bt hybrids were planted well beyond levels optimal to maize farmers in eastern states, whether from a self-interest or group-interest perspective. Therefore, the overplanting of Bt maize was more than could be explained by the "Tragedy of the Commons" perspective, underscoring the need for course correction toward supporting either self-interest or group interest.

Achieving the group optimum is often challenging, as coordination among growers to manage pesticide resistance remains uncommon (*29*). Our findings reveal that the individual optimum, as a second-best and feasible policy alternative, would nearly match the benefits of voluntary group coordination in preserving the technology. Our analysis demonstrates considerable benefits from shifting the Bt planting paradigm in eastern states from the status quo to the individual optimum (Fig. 4, supplementary text S10, and table S13). Between 2014 and 2016, maize was planted annually on 11.8 million acres across Indiana, Michigan, and Ohio. Farmers could have accrued one-year benefits of 99.0 million USD and lifetime benefits of 1.98 billion USD simply by reducing the Bt planting rate from 50 to 18%, while still preserving the technology (assuming a 25% female dispersal proportion and a 95% discount factor).

Our findings align with studies showing suppression of caterpillar pests by Bt maize (*13*, *14*). The overplanting of Bt maize in eastern states, where crop rotation is common, underscores recent research emphasizing the critical role of crop rotation in delaying Bt resistance (*30*). However, crop rotation is less economically rational in western states (*31*).

A way forward: Seed supply and integrated pest management

What caused the discrepancies between the status quo and the individual optimum Bt planting? The simulation reveals that the status quo for eastern states mirrored purchasing Bt seed without a premium (table S13), indicating likely misperceptions among farmers about Bt maize's costs and benefits. Supply-side trait combinations and demand-side information gaps stand out as plausible reasons.

Rootworm Bt traits are often combined with above-ground Bt and herbicide-tolerance traits (fig. S8), especially in highly desirable hybrids (*32*), effectively obscuring the individual cost of each trait (*33*). Consequently, maize farmers are more likely to purchase trait packages with rootworm Bt traits than were traits sold separately, as with many consumption goods (*34*). Moreover, uncertainty about differences in underlying genetics further complicates trait cost evaluation.

Seed companies driven by profit maximization tend to strategically combine traits and genetics (*35*). As seed industry consolidation continues, US farmers face a narrowing list of seed vendors and may be compelled to adopt varieties with unnecessary traits in order to access desired GM traits or improved genetics for other agronomic traits (e.g., drought-tolerance) (*36*). This is likely more pronounced in the smaller markets of the eastern US, where seed companies have less incentive to offer the combinations that farmers need (*37*). Despite complexities in market competition and intellectual property protection, governments could establish recognition and incentive programs that encourage seed companies to broaden trait combinations and genetic diversity in their offerings. We also propose enhancing transparency in seed marketing through labeling for trait combinations and detailing the seed premium for each trait, where possible.

On the demand side, maize farmers are likely underinformed regarding rootworm pressure and the selection costs of using Bt maize, limiting their ability to optimize out of self-interest (or group interest) (*38*). Recent research suggests that farmers often overestimate pest risks (*39*). Adherence to the fundamental principles of integrated pest management, where seed decisions are informed by regular pest monitoring, may be facilitated by drones and other novel technologies (*40*).

Bt crops are widely recognized as an environmentally benign approach to managing insect pests (*41*, *42*). However, increasing rootworm resistance to Bt maize has led to a resurgence in insecticide use that Bt hybrids were intended to replace (*43*). Moreover, with a warming climate, the range of pests targeted by current Bt crops is expected to expand (*44*), highlighting the growing importance of preserving these technologies. While our cost-benefit analysis covers 2014 to 2016 and anecdotal evidence suggests a decline in rootworm Bt adoption in recent years, we expect that the identified issues have persisted given the continued decline in Bt efficacy and rootworm pressure (*45*) (fig. S9) and relatively stable transgenic seed prices when compared to nontransgenic seeds and commodities (*46*).

The issues highlighted here extend beyond managing rootworm Bt maize, providing insights more broadly into managing the biological commons. A relevant example is the RNAi (DvSnf7) technology for rootworm management, resistance to which has been readily selected for in lab assays (*47*). This novel trait is

currently available only in combination with existing rootworm and lepidopteran Bt and desirable herbicide-tolerance traits. In areas where rootworm pressure is low, such combinations continue the trend illustrated above; pest protection benefits of the technology are minimal, while pest susceptibility to the novel technology is eroded and growers pay a premium. This research is also relevant to settings outside the United States, in particular China, which is the world's second-largest maize producer and which recently embraced commercialization of Bt maize (*48*). If current and future related innovations are managed as Bt maize hybrids have been, we risk entering a cycle of rapid obsolescence among transgenic technologies, a biotechnology version of the "pesticide treadmill" (*49*, *50*).

REFERENCES AND NOTES

1. M. Qaim, D. Zilberman, *Science* **299**, 900–902 (2003).
2. J. Huang, R. Hu, S. Rozelle, C. Pray, *Science* **308**, 688–690 (2005).
3. B. E. Tabashnik, Y. Carrière, *Nat. Biotechnol.* **35**, 926–935 (2017).
4. B. Morel, R. S. Fallow, F. Wu, E. A. Casman, in *Battling Resistance to Antibiotics and Pesticides*. R. Laxminarayan, ed. (Routledge, 2002); pp. 184–213
5. R. S. Keweshan, G. P. Head, A. J. Gassmann, *J. Econ. Entomol.* **108**, 720–729 (2015).
6. A. J. Gassmann, J. L. Petzold-Maxwell, R. S. Keweshan, M. W. Dunbar, *PLOS ONE* **6**, e22629 (2011).
7. B. E. Tabashnik, F. Gould, *J. Econ. Entomol.* **105**, 767–776 (2012).
8. A. J. Gassmann *et al*., *Proc. Natl. Acad. Sci. U.S.A.* **111**, 5141–5146 (2014).
9. V. Calles-Torrez *et al*., *J. Econ. Entomol.* **112**, 1875–1886 (2019).
10. G. Hardin, *Science* **162**, 1243–1248 (1968).
11. E. Ostrom, J. Burger, C. B. Field, R. B. Norgaard, D. Policansky, *Science* **284**, 278–282 (1999).
12. T. Dietz, E. Ostrom, P. C. Stern, *Science* **302**, 1907–1912 (2003).
13. W. D. Hutchison *et al*., *Science* **330**, 222–225 (2010).
14. G. P. Dively *et al*., *Proc. Natl. Acad. Sci. U.S.A.* **115**, 3320–3325 (2018).
15. B. E. Tabashnik *et al*., *Proc. Natl. Acad. Sci. U.S.A.* **118**, e2019115118 (2021).
16. N. A. Tinsley, R. E. Estes, M. E. Gray, *J. Appl. Entomol.* **137**, 161–169 (2013).
17. P. T. Marquardt, C. H. Krupke, *Environ. Entomol.* **38**, 176–182 (2009).
18. C. R. St Clair, G. P. Head, A. J. Gassmann, *PLOS ONE* **15**, e0237094 (2020).
19. T. W. Sappington, J. L. Spencer, *Insects* **14**, 922 (2023).
20. M. E. Gray, T. W. Sappington, N. J. Miller, J. Moeser, M. O. Bohn, *Annu. Rev. Entomol.* **54**, 303–321 (2009).
21. C. T. Bauch, A. P. Galvani, D. J. D. Earn, *Proc. Natl. Acad. Sci. U.S.A.* **100**, 10564–10567 (2003).
22. Z. Ye, F. Wu, D. A. Hennessy, *Proc. Natl. Acad. Sci. U.S.A.* **118**, e2017470118 (2021).
23. S. Lee, G. Moschini, *Am. J. Agric. Econ.* **104**, 1177–1202 (2022).
24. J. D. Oleson, Y. L. Park, T. M. Nowatzki, J. J. Tollefson, *J. Econ. Entomol.* **98**, 1–8 (2005).
25. W. S. Abbott, *J. Econ. Entomol.* **18**, 265–267 (1925).
26. L. E. Papke, J. M. Wooldridge, *J. Econom.* **145**, 121–133 (2008).
27. C. T. Bauch, D. J. D. Earn, *Proc. Natl. Acad. Sci. U.S.A.* **101**, 13391–13394 (2004).
28. K. Arrow *et al*., *Science* **341**, 349–350 (2013).
29. J. Pretty, *Science* **302**, 1912–1914 (2003).
30. Y. Carrière *et al*., *Proc. Natl. Acad. Sci. U.S.A.* **117**, 18385–18392 (2020).
31. L. J. Meinke *et al*., *PLOS ONE* **19**, e0299483 (2024).
32. C. Parisi, P. Tillie, E. Rodríguez-Cerezo, *Nat. Biotechnol.* **34**, 31–36 (2016).
33. D. Soman, J. T. Gourville, *J. Mark. Res.* **38**, 30–44 (2001).
34. M. E. Drumwright, *Mark. Lett.* **3**, 311–321 (1992).
35. G. Shi, J. P. Chavas, J. Lauer, E. Nolan, *Am. J. Agric. Econ.* **95**, 739–754 (2013).
36. Agricultural Marketing Service (AMS), US Department of Agriculture (USDA), "More and better choices for farmers: Promoting fair competition and innovation in seeds and other agricultural inputs" (USDA AMS, 2023); https://www.ams.usda.gov/sites/default/files/media/SeedsReport.pdf.
37. D. D. Reisig, *J. Integr. Pest Manag.* **8**, 9 (2017).
38. E. D. Perry, D. A. Hennessy, G. Moschini, *J. Econ. Behav. Organ.* **158**, 543–559 (2019).
39. A. N. Dean, E. W. Hodgson, A. Rieck-Hinz, M. Anderson, *J. Integr. Pest Manag.* **12**, pmab021 (2021).
40. N. Moses-Gonzales, M. J. Brewer, *J. Econ. Entomol.* **114**, 1853–1856 (2021).
41. M. Mendelsohn, J. Kough, Z. Vaituzis, K. Matthews, *Nat. Biotechnol.* **21**, 1003–1009 (2003).
42. S. Fleischer, W. D. Hutchison, S. E. Naranjo, in *Plant Biotechnology, 2nd Edition* (Springer, 2021); pp. 111–125.
43. J. D. Reinders, L. J. Meinke, *Sci. Rep.* **12**, 19221 (2022).
44. C. A. Deutsch *et al*., *Science* **361**, 916–919 (2018).
45. A. J. Gassmann, *Insects* **12**, 136 (2021).
46. J. M. MacDonald, X. Dong, K. Fuglie, "Concentration and competition in U.S. agribusiness" (Report EIB-256, USDA ERS, 2023); https://doi.org/10.32747/2023.8054022.ers.
47. C. Khajuria *et al*., *PLOS ONE* **13**, e0197059 (2018).
48. X. Yang *et al*., *Plant Biotechnol. J.* **21**, 391–404 (2023).
49. R. Van den Bosch, *The Pesticide Conspiracy* (Univ. of California Press, 1989).
50. F. Gould, Z. S. Brown, J. Kuzma, *Science* **360**, 728–732 (2018).
51. Z. Ye *et al*., datadepositor/rw_overplanting: Version 1.0 - First Public Release, Version v1.0, Zenodo (2024); https://doi.org/10.5281/zenodo.14292075.

ACKNOWLEDGMENTS

We are grateful for general assistance from S. Wechsler. Portions of the 2005 to 2014 Illinois field data were obtained from the University of Illinois' On Target summaries of insect management trials provided by M. E. Gray, K. L. Steffey, and R. E. Estes. **Funding:** This work was facilitated by the USDA-NCRA multistate research project NC246: Ecology and Management of Arthropods in Corn; and the National Natural Science Foundation of China (grants 72303230, 72141307, and 42061124002). **Author contributions:** Conceptualization: C.H.K., Z.Y., C.D., D.A.H., and F.W. Methodology: Z.Y., D.A.H., and C.H.K. Investigation: Z.Y., D.A.H., and C.H.K. Visualization: Z.Y. and C.D. Funding acquisition: C.H.K., D.A.H., F.W., and Z.Y. Project administration: C.H.K. Supervision: C.H.K., D.A.H., and F.W. Writing – original draft: C.H.K., Z.Y., C.D., D.A.H., and F.W. Writing – review and editing: Z.Y., C.H.K., C.D., D.A.H., J.Z., F.W., S.P.C., A.J.G., E.W.H., B.J., J.J.K., B.M., L.J.M., A.M., B.P., N.J.S., J. L. Smith., J. L. Spencer, K.J.T., and R.J.W. Bt trial data provided by: C.H.K., C.D., S.P.C., A.J.G., E.W.H., B.J., J.J.K., B.M., L.J.M., A.M., B.P., N.J.S., J. L. Smith, J. L. Spencer, K.J.T., and R.J.W. **Competing interests:** The authors declare no competing interests. Data and materials availability: All codes pertaining to this study will be publicly available. The TraitTrak® survey data were purchased from the GfK Kynetec company and are protected by a non-third-party disclosure agreement, but variables from the TraitTrak® survey may be obtained through crop subscription services (contact at https://www.kynetec.com/contact). Maize cash price data at the maize elevator level were purchased from GeoGrain, while the aggregated data used for analysis are available in the analysis dataset. The university field trial data were collected by authors and their collaborators, and plot-level data are made public in the analysis dataset. Precipitation and temperature data from the Parameter-elevation Regression on Independent Slopes Model (PRISM) dataset are publicly available at https://prism.oregonstate.edu/. Cropping pattern data from the Cropland Data Layer (CropScape) dataset are publicly available at https://nassgeodata.gmu.edu/CropScape/. Maize yield data and state-level genetically-engineered crop adoption data from the National Agricultural Statistics Service, United States Department of Agriculture, are publicly available at https://www.nass.usda.gov/ and https://www.ers.usda.gov/data-products/adoption-of-genetically-engineered-crops-in-the-united-states, respectively. The parameters for the fraction of yield loss for each node of roots injured and the dispersal proportion are calibrated from primary literature (*16*–*19*). The analysis dataset and codes are publicly available at (*51*).

SUPPLEMENTARY MATERIALS

science.org/doi/10.1126/science.adm7634
Materials and Methods
Figs. S1 to S9
Tables S1 to S17
References (*52*–*66*)
MDAR Reproducibility Checklist

Submitted 5 November 2023; resubmitted 6 July 2024
Accepted 6 January 2025
10.1126/science.adm7634

ORGANIC AEROSOLS

Nitrogen dominates global atmospheric organic aerosol absorption

Yumin Li[1,2,3], Tzung-May Fu[1,2,4]*, Jian Zhen Yu[3,5]*, Aoxing Zhang[1,2], Xu Yu[3], Jianhuai Ye[1,2], Lei Zhu[1,2], Huizhong Shen[1,2], Chen Wang[1,2], Xin Yang[1,2], Shu Tao[1,2], Qi Chen[6], Ying Li[7], Lei Li[8], Huizheng Che[8], Colette L. Heald[9]

Atmospheric organic aerosols (OAs) influence Earth's climate by absorbing sunlight. However, the link between their evolving composition and their absorptive effects is unclear. We demonstrate that brown nitrogen (BrN), the absorptive nitrogenous component of OAs, dominates their global absorption. Using a global model, we quantified BrN abundance, tracked its optical evolution with chemical aging, and assessed its radiative absorption. BrN contributes 76% of OAs' surface light absorption over the US and 61% of their global absorptive optical depth. Moreover, the observed variability of OAs' absorptive capacity is primarily driven by the sources and aging of BrN. BrN represents 18% of the global absorptive direct radiative effect of carbonaceous aerosols, with biomass burning being the largest contributor. Our research establishes a nitrogen-centric framework for attributing the climate impacts of OAs.

Atmospheric aerosols directly affect Earth's climate by scattering and absorbing solar radiation (*1*). Whereas black carbon (BC) is the most important light-absorbing aerosol component on a global scale (*1*), organic aerosols (OAs), typically measured by their organic carbon (OC) content, have traditionally been believed to only scatter light (*1*). Recent research has revealed that OAs can also absorb solar radiation in the near-ultraviolet to visible range, leading to a positive radiative forcing on Earth's climate (*2*, *3*). However, the absorptive properties of OAs evolve as their complex composition chemically ages in the

atmosphere, complicating the assessment and attribution of their climate impacts (*3*, *4*). Previous modeling studies have estimated the absorptive effects of OAs by dividing OC into bulk light-absorbing components (referred to as brown carbon, or BrC) and light-scattering components (referred to as white carbon, or WtC) and assuming empirical conversion rates of bulk BrC to bulk WtC to account for the changes in the absorptive properties of OAs due to atmospheric aging (*5*–*8*). These studies estimated that BrC contributes between 10 and 40% of the total absorption of carbonaceous aerosols, with global average absorptive radiative forcing estimates ranging from 0.01 to 0.6 W m^{-2} (*2*, *5*, *6*, *8*–*11*). The large discrepancies in these estimates underscore our limited understanding of OAs' specific absorptive constituents and their evolving optical characteristics in the atmosphere.

Laboratory and field studies have identified particulate organic nitrogen (ON) species as the key colored components of light-absorbing OAs, with the chemical evolution of ON being a major driver of OAs' changing absorptive properties (*3*, *4*, *12*). Known absorptive particulate ON species include nitroaromatics (NACs), N-containing polycyclic aromatic hydrocarbons (N-PAHs), N-heterocyclic compounds, imidazoles, and other imine-like compounds (*12*–*17*). These species are emitted from natural and anthropogenic sources or formed secondarily in the atmosphere (*18*). Furthermore, the mass absorption efficiencies (MAEs) of these ON species can either increase (photodarkening) or decrease (photobleaching) upon oxidation and photolysis in the atmosphere, depending on the structural changes to the ON molecules (*3*, *19*, *20*). For instance, NACs oxidized by hydroxyl radicals (OH) in the aqueous phase may undergo a doubling or nulling of MAEs, depending on whether the reaction adds an electron-donating OH functional group or cleaves the aromatic ring (*19*, *20*). Therefore, accurately quantifying the absorptive effect of OAs necessitates a comprehensive understanding of the abundance and atmospheric evolution of the ON constituents within OAs.

[1]Coastal Atmosphere and Climate of the Greater Bay Area Observation and Research Station of Guangdong Province, Southern University of Science and Technology, Shenzhen, Guangdong, China. [2]Shenzhen Key Laboratory of Precision Measurement and Early Warning Technology for Urban Environmental Health Risks, School of Environmental Science and Engineering, Southern University of Science and Technology, Shenzhen, Guangdong, China. [3]Division of Environment and Sustainability, Hong Kong University of Science and Technology, Hong Kong SAR, China. [4]National Center for Applied Mathematics Shenzhen, Shenzhen, Guangdong, China. [5]Department of Chemistry, Hong Kong University of Science and Technology, Hong Kong SAR, China. [6]State Key Joint Laboratory of Environmental Simulation and Pollution Control, BIC-ESAT and IJRC, College of Environmental Sciences and Engineering, Peking University, Beijing, China. [7]Department of Ocean Science and Engineering, Southern University of Science and Technology, Shenzhen, China. [8]State Key Laboratory of Severe Weather and Key Laboratory of Atmospheric Chemistry of CMA, Chinese Academy of Meteorological Sciences, Beijing, China. [9]Institute for Atmospheric and Climate Science, ETH Zurich, Zurich, Switzerland.
***Corresponding author. Email: fuzm@sustech.edu.cn (T.-M.F.); chjianyu@ust.hk (J.Z.Y.)**

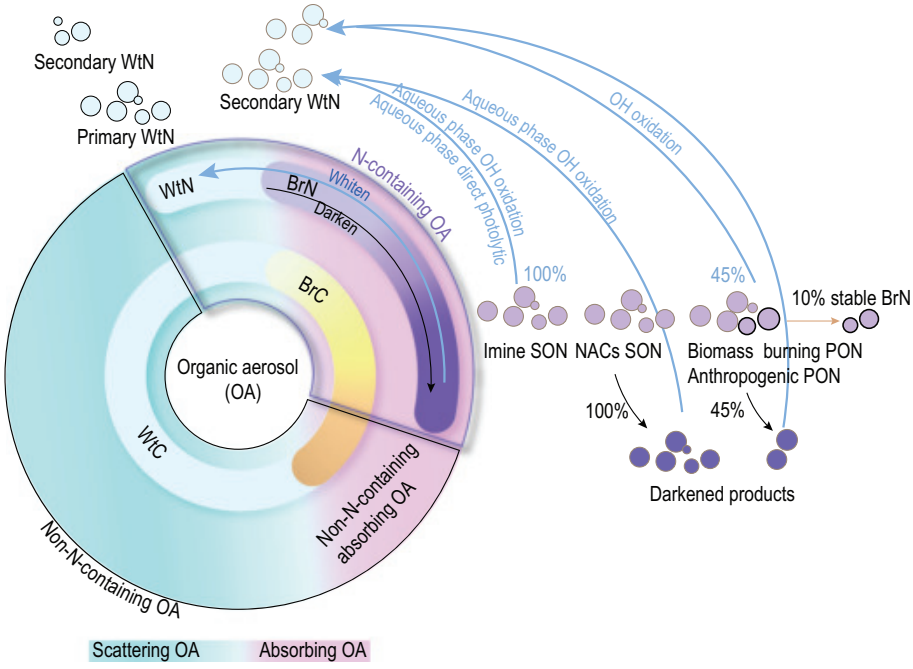

Fig. 1. Schematic representation of OA components. Total scattering OA (blue) includes WtN and WtC (light blue). Total absorbing OA (pink) includes BrC (yellow) and BrN (purple). Also shown is the chemical evolution of BrN to secondary WtN, which drives the changes in OAs' absorptive properties.

In this study, we advance the representation of OAs' absorptive effects by explicitly quantifying the abundance of absorptive ON species (hereafter referred to as brown N, or BrN) as well as their evolution to nonabsorptive ON species (referred to as white N, or WtN) (Fig. 1). We use the GEOS-Chem global model (GEOS, Goddard Earth Observing System) to simulate the primary ON (PON) emitted from anthropogenic, biomass burning, dust, marine, and biogenic sources, as well as the formation of secondary ON (SON) species, including organic nitrates, NACs, and imine-like compounds (*18*). Some PON and SON species are inherently nonabsorptive and classified as WtN. For the absorptive PON and SON species, that is, BrN, we calculated their effective MAEs and explicitly simulated their absorption and photochemical evolution to WtN (methods, table S1, and fig. S1). We evaluated our simulated BrN absorption against surface and vertically integrated measurements of BrC absorption at US and global sites (methods). Finally, we estimated the global radiative effect of BrN and quantified the factors driving the spatiotemporal variability of BrN's radiative absorption.

BrN absorption in the global surface atmosphere and the impacts of aging

Figure 2A shows our simulated BrN absorption coefficients in the global surface atmosphere, on the basis of a robust model representation of global surface ON abundances (see text S2 in the supplementary materials). Figure S2 shows the surface concentrations of total ON, including BrN from all origins, WtN that are inherently nonabsorbing, and WtN derived from photobleached BrN. Our simulated surface BrN absorption coefficients range from 0.0003 to 46 inverse megameters (Mm^{-1}), with a global average of 0.53 Mm^{-1}. Varying the effective MAEs and aging parameters within the ranges reported in literature constrains the uncertainty of global mean surface BrN absorption coefficient to be between 0.14 and 2.78 Mm^{-1} (text S3). Simulated surface BrN absorption coefficients are highest over the northern boreal forests and the tropical rain forests and savannahs, reflecting the strong emissions of BrN from wildfires in these areas (fig. S2). Simulated BrN absorption coefficients are also enhanced over regions of intense anthropogenic emissions, including the eastern and western US, Europe, and East and South Asia (fig. S2). On an annual mean basis, primary biomass burning emissions constitute the largest contributor to the simulated BrN absorption (48%), followed by primary anthropogenic emissions (29%) and secondary NACs formation (15%). Seasonally, primary biomass burning BrN make a more pronounced contribution to light absorption during April to August, whereas anthropogenic BrN dominates during September to March (Fig. 2C). Secondary BrN contributes 20 to 30% of the simulated total surface BrN absorption year-round; 40 to 80% of this absorption is attributed

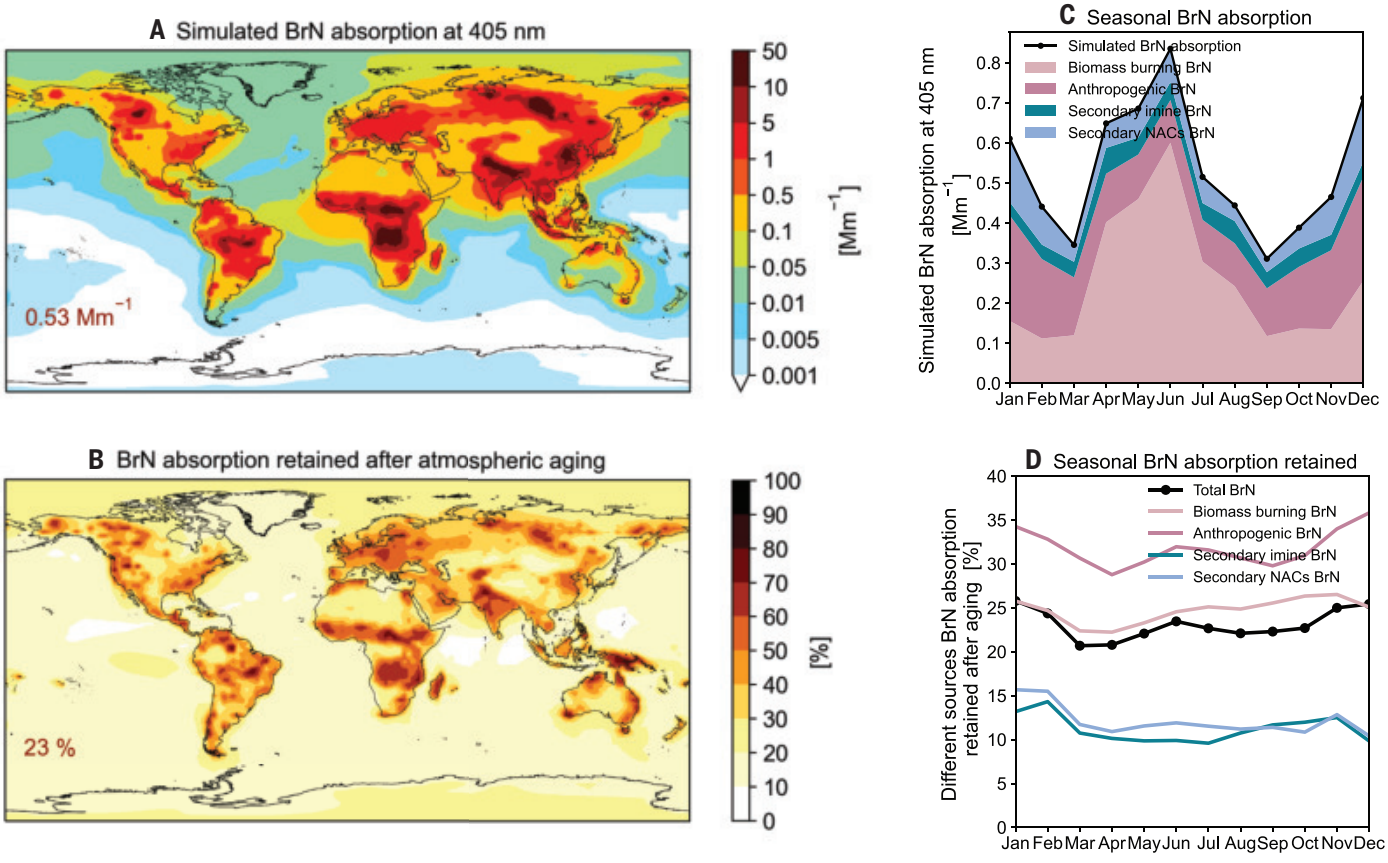

Fig. 2. Simulated global surface BrN absorption coefficients at 405 nm and the impacts of atmospheric aging. (**A**) Annual mean BrN absorption coefficients. (**B**) Percentage of BrN absorption coefficient retained after atmospheric aging. (**C**) Seasonal variation of global mean BrN absorption (black line) and the contributions from different BrN sources (colored). (**D**) Seasonal variation of the percentage of BrN absorption retained after atmospheric aging (black: total; colored lines: different sources).

to secondary NAC BrN, which has relatively low atmospheric concentrations but strong absorptive efficiencies per unit mass of N.

We further explored the impacts of atmospheric aging on BrN's absorption capacity. Figure 2B shows the fraction of global surface BrN absorption retained after atmospheric aging (f_{ret}, defined as the ratio of simulated BrN absorption coefficient with atmospheric aging relative to that without atmospheric aging). The simulated annual mean surface f_{ret} values are spatially inhomogeneous and range from 7 to 83%, with a global mean value of 23% (uncertainty range between 21 and 30%; text S3). The f_{ret} values are higher in near-source regions and lower in remote areas, reflecting the continuous conversion of BrN to WtN due to atmospheric aging. We note that, although BrN absorption coefficients are highest over the biomass burning regions, f_{ret} values are sometimes higher over regions of strong anthropogenic emissions. This is because primary anthropogenic emissions are enhanced during winter, when atmospheric aging is slower, whereas primary biomass burning usually occurs during summer, when atmospheric aging is accelerated. Atmospheric aging decreases the contribution of secondary species to total simulated BrN absorption from 38% to 20% (Fig. 2D). This decrease occurs mainly because the ring structures of secondary imine-like BrN molecules are rapidly broken when exposed to OH, resulting in 70 to 90% loss of their absorptive capacity upon aging (methods).

Evaluation of simulated surface BrN absorption against observed surface BrC absorption over the US

To evaluate our explicitly simulated BrN absorption and its contribution to total OA absorption, we compared the model results against observed BrC absorption and its spatiotemporal variability on regional and global scales. Chen *et al.* indirectly measured BrC absorption at surface sites across the contiguous US by subtracting BC absorption from the measured absorption by total carbonaceous aerosols (*7*). To the best of our knowledge, this is the only published measurement of regional BrC absorption coefficients with annual coverage. Figure 3 shows the ratio of our simulated BrN absorption versus the observed BrC absorption over the US (*7*), that is, the percentage of BrC absorption that may be accounted for by BrN absorption. On an annual mean basis, the simulated surface BrN absorption coefficients (0.01 to 1.7 Mm^{-1}; average: 0.49 Mm^{-1}) accounted for 76% of the observed surface BrC absorption (0.01 to 1.9 Mm^{-1}; average: 0.57 Mm^{-1}; Fig. 3, A and D). Additionally, simulated BrN absorption reproduces the observed spatial distribution of BrC absorption (Pearson correlation coefficient, r = 0.54) and its seasonal variation. In winter, the simulated BrN absorption coefficients (0.005 to 2.3 Mm^{-1}) represent 63% of the observed BrC absorption (0.008 to 2.8 Mm^{-1}, r = 0.60; Fig. 2, B and E). In summer, the simulated BrN absorption coefficients (0.08 to 1.2 Mm^{-1}) represent 94% of the observed BrC absorption (0.05 to 1.3 Mm^{-1}, r = 0.31; Fig. 3, C and F). These correlations demonstrate that surface BrN absorption effectively embodies the magnitudes and spatiotemporal variations of the observed surface BrC absorption over the US.

Figure 3 also shows the simulated surface ON concentrations across the contiguous US. Simulated surface ON concentrations are highest over the Rocky Mountain West and Southeast US in summer (Fig. 3C), reflecting the strong emissions of ON from the summertime

wildfires in these areas (fig. S2). In contrast, simulated ON concentrations are smaller over the northeastern US and in winter (Fig. 3, A to C), reflecting the relatively smaller ON emissions from anthropogenic sources. We find that the proportion of BrC absorption attributable to BrN does not exhibit a direct correlation with ON concentrations. This disparity is because ON species from different sources vary in their MAEs and susceptibility to photobleaching. Primary anthropogenic BrN and secondary NACs BrN from anthropogenic precursors both have higher MAEs compared with primary biomass burning BrN, whereas NACs BrN also undergo slower photobleaching.

Additionally, atmospheric oxidation substantially improves the BrN's characterization of BrC absorption properties. Without atmospheric aging, the absorptive properties of BrN do not evolve, and the resulting simulated BrN absorption overestimates the observed surface BrC absorption by 45% on an annual mean basis and by up to 128% in summer (Fig. 3 and figs. S3 and S4). This overestimation in absorption can be attributed to a combination of excessive absorption by anthropogenic BrN, biomass burning BrN, and secondary imine BrN (fig. S4). In particular, atmospheric aging decreases the contribution of secondary species to total simulated BrN absorption from 43% to 24% (Figs. 2 and 3 and figs. S3 and S4). Figure S3, A to C, shows the simulated fraction of absorption retained after aging (f_{ret}) at surface sites over the US, with an annual mean of 0.42. The values of f_{ret} are higher in the northeastern, southeastern, and Pacific coastal US and also disparate from the areas with high surface ON concentrations. Again, this spatial discrepancy between surface ON levels and retained BrN absorption is attributed to the slower photobleaching of primary anthropogenic BrN and secondary NACs BrN. Surface ON concentrations are generally higher in summer than in winter at most sites because biomass burning is more pronounced during the warm season in North America. However, the retained BrN absorption is lower in summer (mean f_{ret} = 0.35) than in winter (mean f_{ret} = 0.54) at most sites (fig. S3, A to C), indicating stronger photobleaching of BrN in the summer. In particular, the exceptionally high summertime surface ON concentrations over the US Mountain West are associated with relatively low f_{ret} (0.2 to 0.6) owing to the rapid photobleaching of BrN from biomass burning in summer. Conversely, in winter, low surface ON concentrations with high f_{ret} (>0.6) are simulated over the northeastern and Pacific coastal US, reflecting the influence of local anthropogenic emissions as well as the subdued photobleaching in winter.

Evaluation of simulated BrN absorptive aerosol optical depth (AAOD) against global observations of BrC AAOD

We extend our analyses to evaluate the extent to which OAs' atmospheric column absorption may be attributed to BrN on a global scale. Figure 4A compares our simulated BrN absorptive aerosol optical depth (AAOD) at 440 nm against observed BrC AAOD at 175 Aerosol Robotic Network (AERONET) sites worldwide (methods). Here, the observed BrC AAOD is estimated by excluding measurements affected by dust and then subtracting the estimated

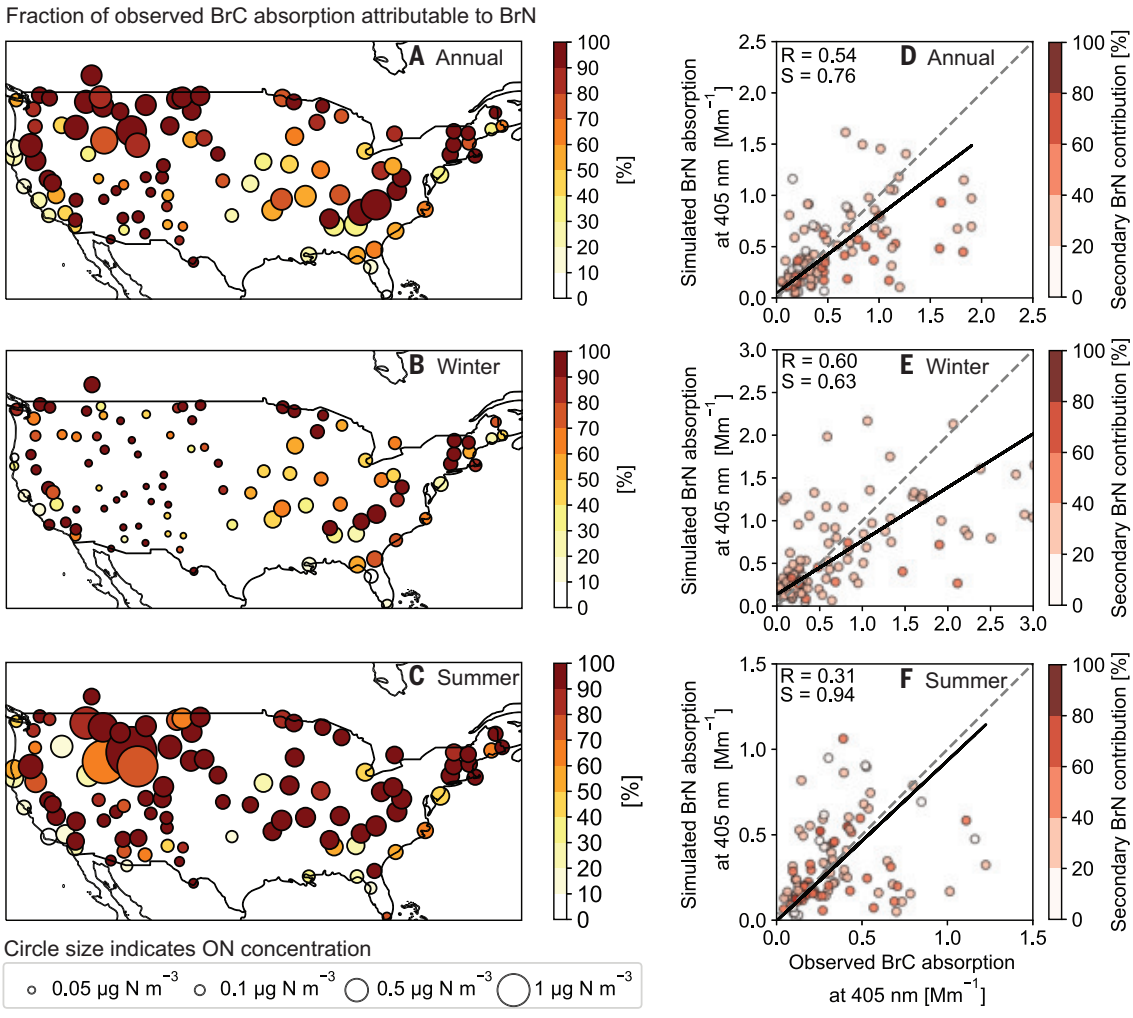

Fig. 3. Evaluation of simulated BrN absorption coefficient against observed BrC absorption coefficient at 405 nm over the contiguous US. (Left) Percentage of observed BrC absorption attributable to simulated BrN absorption with atmospheric aging (**A**) as annual mean, (**B**) in winter, and (**C**) in summer. Also shown are the simulated spatial distributions of surface ON concentrations. (Right) Scatterplots of simulated BrN absorption with atmospheric aging (**D**) as annual mean, (**E**) in winter, and (**F**) in summer. Colors indicate the secondary contribution to BrN absorption. Black lines indicate the reduced major-axis regression lines; slopes (S) and correlation coefficients (R) are inset.

absorption of BC (methods). We find that the simulated BrN AAOD accounts for 61% of the observed BrC AAOD and represents its spatiotemporal variability (Fig. 4A; r = 0.67). This finding is consistent with our analyses over the US, where BrN absorption accounts for most of the absorption of BrC. Biomass burning is the largest source of simulated BrN AAOD at global AERONET sites (39%), followed by anthropogenic sources (26%), secondary NACs (20%), and secondary imines (15%). In addition, our simulation indicates that biomass burning BrN is the main driver for the spatiotemporal variability of the observed BrC AAOD. These findings provide new insights into the relative contributions of different sources to OAs' global absorption.

We further compared the simulated ratios of BrN AAOD versus BC AAOD at 440 nm, which we refer to as R_{AAOD}, to observed values at global AERONET sites (Fig. 4B). R_{AAOD} quantifies the strength of OA absorption relative to the absorption of other carbonaceous aerosols (i.e., BC). Our simulated BC AAOD compares well with global observations (fig. S5) and therefore can be used as a reference for evaluating BrN AAOD. The AERONET-observed R_{AAOD} ranges from 12 to 68%, with a global mean of 23%. Our simulated R_{AAOD} varies from 3 to 54%, with a global mean of 16%. Several field measurements have shown the observed R_{AAOD} to be source specific (*21*–*24*). In air masses strongly affected by biomass burning, the field-measured R_{AAOD} ranged from 25 to 45% at 440 nm, depending on the completeness of combustion (*21*, *22*). Field measurements indicated that R_{AAOD} tended to be higher in samples affected by traffic emissions than those affected by residential combustion (*23*), owing to the presence of absorptive, non-N-containing PAHs from traffic sources (*25*). Our comparison shows that at times and locations strongly affected by biomass burning emissions (such as peninsular Southeast Asia, the boreal forests, and the tropical forests and savannahs of Africa and South America; fig. S6), the simulated R_{AAOD} are relatively consistent with the AERONET observations (Fig. 4B, red dots). However, over regions with substantial anthropogenic emissions (e.g., Europe, India, East Asia, and eastern North America; fig. S6), our simulated R_{AAOD} are generally <15% and systematically lower than the AERONET observations (Fig. 4B, blue dots). This disparity may suggest additional absorption from anthropogenic, non-N-containing OA constituents—such as non-N PAHs from traffic sources and other unknown light-absorbing oligomers (*25*)—which is not embodied by BrN's absorption. This disparity may also arise from potential model underestimation of anthropogenic BC and/or underestimation of effective MAEs for anthropogenic BrN. Furthermore, the AERONET AAOD observations are generally lower in areas dominated by anthropogenic emissions than in those dominated by biomass burning, making the AERONET R_{AAOD} values relatively more uncertain in areas of anthropogenic emissions (*26*, *27*).

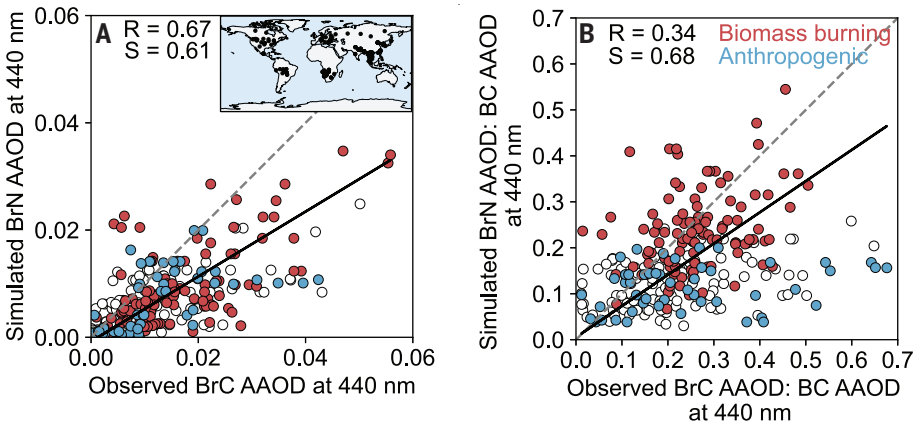

Fig. 4. Global comparison of monthly simulated BrN AAOD and AERONET-observed BrC AAOD at 440 nm. (**A**) Simulated BrN AAOD versus observed BrC AAOD. (**B**) Simulated versus observed ratios of BrN AAOD:BC AAOD (R_{AAOD}). The red and blue symbols mark sites where >50% of the simulated BrN AAOD was attributed to primary biomass burning BrN and primary anthropogenic BrN, respectively. The locations of the global AERONET sites, the slopes (S) of the reduced major-axis regression lines (solid lines), and the Pearson correlation coefficients (R) are inset. The gray dashed lines indicate the 1:1 lines.

Global absorptive radiative effect of BrN

Finally, we calculated the global absorptive direct radiative effect (DRE) of BrN and compared it with the DRE of BC. Figure 5, A and B, illustrates the simulated clear-sky absorptive DRE of BrN and BC, respectively. Our simulated global mean absorptive DRE of BC is 0.21 W m^{-2}, within the range of previous estimates (*1*). Our estimated global mean absorptive DRE of BrN is 0.034 W m^{-2} (uncertainty range: 0.008 to 0.056 W m^{-2}; text S3), also in the range of previous estimates of global mean absorptive DRE of BrC (0.01 to 0.3 W m^{-2}) (*2*). Over biomass burning areas, such as the boreal and tropical forests, the absorptive DRE of BrN exceeds 0.1 W m^{-2}. The absorptive DRE of BrN is also high over East and South Asia, reflecting the emissions of strongly absorptive BrN from anthropogenic sources. On a global average, biomass burning is the largest contributor (0.013 W m^{-2}) to BrN's absorptive DRE, followed by secondary imine BrN (0.009 W m^{-2}) and primary anthropogenic BrN (0.009 W m^{-2}) (fig. S7). This source attribution of BrN's DRE differs from the source attribution of BrN absorption coefficients at the global surface (Fig. 2), reflecting the spatial heterogeneity of BrN and shortwave fluxes in the atmosphere.

The ratio of the absorptive DRE of BrN versus that of BC, referred to as R_{DRE}, quantifies the relative importance of BrN to the total absorptive radiative effects of carbonaceous aerosols. Our simulated values of R_{DRE} range from 3 to 120%, with a global mean of 22% (Fig. 5C). Simulated R_{DRE} values are amplified over regions of substantial biomass burning, while its values are lower over regions dominated by anthropogenic emissions, such as East and South Asia. This heterogeneity arises from the dominance of anthropogenic activity as the source of BC, resulting in a substantially larger DRE from BC over East and South Asia compared with other regions (Fig. 5B). In the Southern Hemisphere, the R_{DRE} ranges from 0.1 to 0.3, with no significant regional variations, as both BrN and BC are mainly emitted from biomass burning.

Figure 5 further breaks down the global and hemispheric seasonal variations of BrN's absorptive DRE and R_{DRE}. Globally, biomass burning emission is the definitive driver for the seasonal variation of BrN's absorptive DRE, highest during May to July in the Northern Hemisphere and during August to September in the Southern Hemisphere. The global mean R_{DRE} is also notably higher during May to July than other times of the year, mainly reflecting the enhanced absorption by BrN from biomass burning emissions and secondary imines during the boreal summer.

Discussion

Our study suggests a potential positive feedback of biomass burning on climate warming through the radiative effect of BrN. Biomass burning emissions constitute the largest contributor of BrN's global absorptive DRE, which account for 60 to 70% of the radiative absorption of OAs on regional and global scales. In a future warming climate, biomass burning activities are expected to increase in frequency and severity (*28*), emitting more BrN and leading to stronger positive radiative forcing. Simultaneously, the transition away from fossil fuels as an energy source will reduce anthropogenic BrN emissions. Further investigation is necessary to fully comprehend the impacts

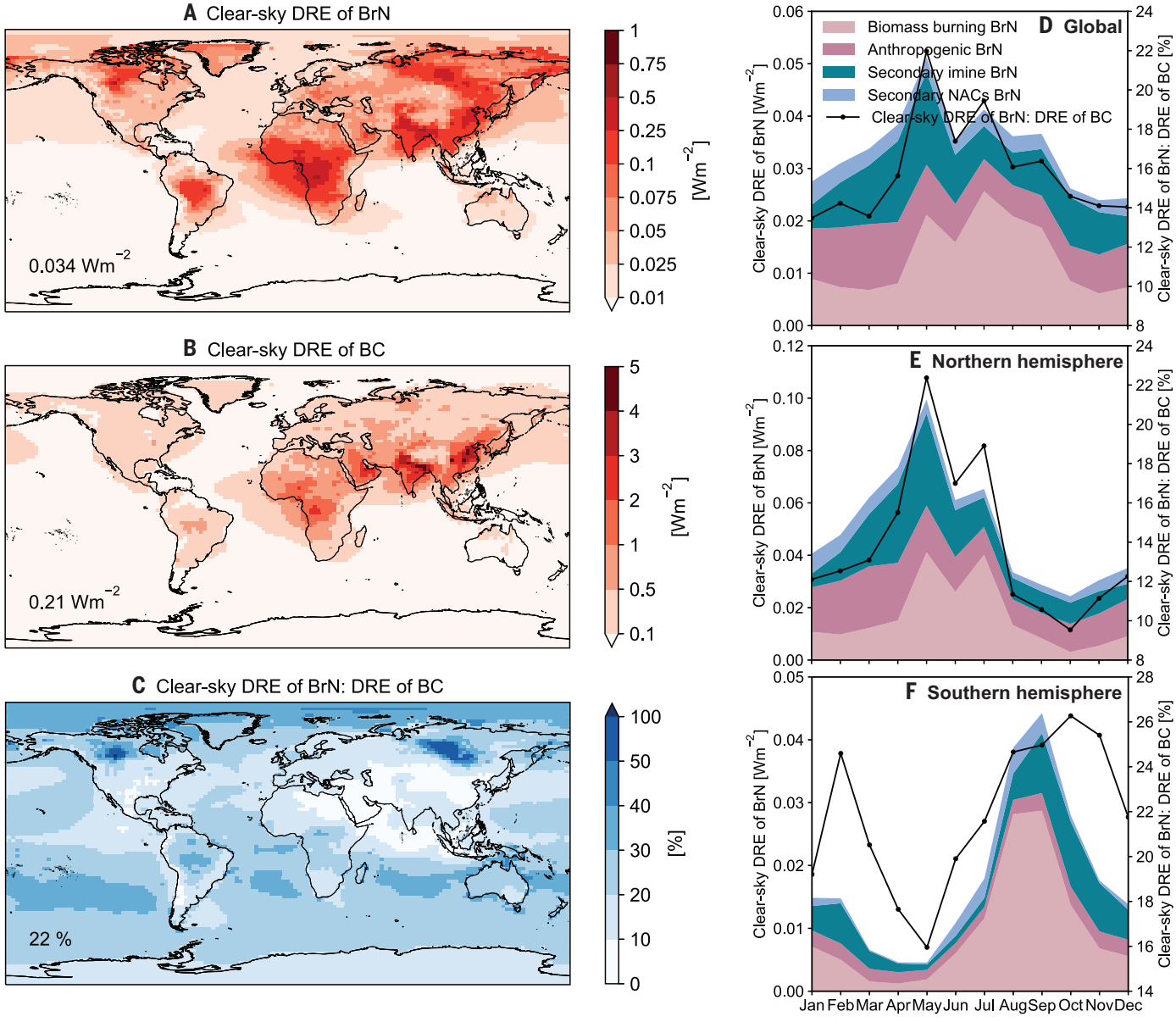

Fig. 5. Simulated global clear-sky absorptive direct radiative effect of carbonaceous aerosols and their source attributions. (**A**) Absorptive DRE of BrN, (**B**) absorptive DRE of BC, and (**C**) their ratio. Also shown are the seasonal variations of BrN's absorptive DRE, its source attributions, and its ratio relative to BC's absorptive DRE (R_{DRE}) (**D**) over the globe, (**E**) in the Northern Hemisphere, and (**F**) in the Southern Hemisphere.

of these contrasting future trends on the global radiative impacts of OAs.

Our work introduces an effective N-centric chemical framework to better attribute the climatic effects of OAs and illuminate their sensitivities to emissions and atmospheric chemistry. The simulation demonstrates that BrN from different sources, characterized by varied MAEs and aging lifetimes, significantly differs in its final absorption DRE contributions. This variability could substantially alter the attribution of OAs' climate effects, especially when considering N-species–specific information rather than a uniform treatment of bulk BrC. Guided by this framework, experimental and modeling efforts should focus on identifying the BrN species originating from biomass burning and anthropogenic activities, understanding how the optical and hygroscopic properties of those species evolve with chemical aging, and identifying other non-N-containing absorptive OA species. Ultimately, these efforts will lead to a comprehensive model elucidating OAs' climate implications in Earth's atmosphere.

REFERENCES AND NOTES

1. P. Forster *et al.* in *Climate Change 2021: The Physical Science Basis. Contribution of Working Group I to the Sixth Assessment Report of the Intergovernmental Panel on Climate Change*, V. Masson-Delmotte *et al.*, Eds. (Cambridge Univ. Press, 2021), pp. 923–1054.
2. Y. Zhang *et al.*, *Nat. Geosci.* **10**, 486–489 (2017).
3. R. F. Hems, E. G. Schnitzler, C. Liu-Kang, C. D. Cappa, J. P. D. Abbatt, *ACS Earth Space Chem.* **5**, 722–748 (2021).
4. A. Laskin, J. Laskin, S. A. Nizkorodov, *Chem. Rev.* **115**, 4335–4382 (2015).
5. A. Zhang *et al.*, *Atmos. Chem. Phys.* **20**, 1901–1920 (2020).
6. X. Wang *et al.*, *Atmos. Chem. Phys.* **18**, 635–653 (2018).
7. L. A. Chen *et al.*, *Environ. Sci. Technol.* **55**, 8561–8572 (2021).
8. R. Saleh, *Curr. Pollut. Rep.* **6**, 90–104 (2020).
9. C. L. Heald *et al.*, *Atmos. Chem. Phys.* **14**, 5513–5527 (2014).
10. T. S. Carter *et al.*, *J. Geophys. Res. Atmos.* **126**, e2021JD034984 (2021).
11. D. S. Jo, R. J. Park, S. Lee, S.-W. Kim, X. Zhang, *Atmos. Chem. Phys.* **16**, 3413–3432 (2016).
12. A. Laskin, P. Lin, J. Laskin, L. T. Fleming, S. Nizkorodov, *ACS Symp. Ser.* **1299**, 261–274 (2018).
13. P. Lin *et al.*, *Environ. Sci. Technol.* **50**, 11815–11824 (2016).
14. P. Lin *et al.*, *Environ. Sci. Technol.* **51**, 11561–11570 (2017).
15. J. Liu *et al.*, *Atmos. Chem. Phys.* **16**, 12815–12827 (2016).
16. M. Xie *et al.*, *Environ. Sci. Technol.* **51**, 11607–11616 (2017).

17. D. O. De Haan *et al.*, *Environ. Sci. Technol.* **52**, 4061–4071 (2018).
18. Y. Li *et al.*, *Natl. Sci. Rev.* **10**, nwad244 (2023).
19. R. Zhao *et al.*, *Atmos. Chem. Phys.* **15**, 6087–6100 (2015).
20. R. F. Hems, J. P. D. Abbatt, *ACS Earth Space Chem.* **2**, 225–234 (2018).
21. R. Saleh *et al.*, *Nat. Geosci.* **7**, 647–650 (2014).
22. B. Luo *et al.*, *Atmos. Chem. Phys.* **22**, 12401–12415 (2022).
23. Q. Wang *et al.*, *J. Geophys. Res. Atmos.* **127**, e2021JD035473 (2022).
24. J. Yan, X. Wang, P. Gong, C. Wang, Z. Cong, *Sci. Total Environ.* **634**, 1475–1485 (2018).
25. Q. Zhang *et al.*, *Atmos. Environ.* **166**, 234–243 (2017).
26. D. M. Giles *et al.*, *Atmos. Meas. Tech.* **12**, 169–209 (2019).
27. X. Wang *et al.*, *Atmos. Chem. Phys.* **16**, 12733–12752 (2016).
28. B. Zheng *et al.*, *Sci. Adv.* **7**, eabh2646 (2021).
29. The International GEOS-Chem User Community, geoschem/geos-chem: GEOS-Chem 12.9.3, version 12.9.3, Zenodo (2020); https://doi.org/10.5281/zenodo.3974569.

ACKNOWLEDGMENTS

Computational resources were supported by the Center for Computational Science and Engineering at the Southern University of Science and Technology. **Funding:** National Natural Science Foundation of China (42325504), National Key Research and Development Program of China (2023YFC3706205), Hong Kong Research Grants Council (R6011-18), Shenzhen Key Laboratory of Precision Measurement and Early Warning Technology for Urban Environmental Health Risks (ZDSYS20220606100604008), Shenzhen Science and Technology Program (KQTD20210811090048025, JCYJ20220818100611024), Guangdong Province Major Talent Program (2019CX01S188), High-level University Special Fund (G03050K001). **Author contributions:** Conceptualization: T.-M.F.; Funding acquisition: T.-M.F., J.Z.Y.; Investigation: Yu.Li, T.-M.F., J.Z.Y., A.Z., X.Yu, J.Y., L.Z., H.S., C.W., L.L., H.C.; Methodology: Yu.Li, T.-M.F., J.Z.Y., A.Z., J.Y., Q.C., Yi.Li; Project administration: Yu.Li, T.-M.F.; Supervision: T.-M.F., J.Z.Y.; Visualization: Yu.Li, T.-M.F.; Writing– original draft: Yu.Li, T.-M.F., J.Z.Y., A.Z., X.Yang, S.T., Q.C., Yi.Li, C.L.H.; Writing – review & editing: Yu.Li, T.-M.F., J.Z.Y., C.L.H. **Competing interests:** The authors declare that they have no competing interests. **Data and materials availability:** All data are available in the main text or the supplementary materials. The GEOS-Chem model code used in this study (GEOS-Chem v12.9.3) is permanently archived in Zenodo (*29*).

SUPPLEMENTARY MATERIALS

science.org/doi/10.1126/science.adr4473
Materials and Methods
Supplementary Text
Figs. S1 to S12
Table S1
References (*30*–*53*)

Submitted 1 July 2024; accepted 14 January 2025
10.1126/science.adr4473

COLLECTIVE MOTION

The behavioral mechanisms governing collective motion in swarming locusts

Sercan Sayin[1,2,3]*, Einat Couzin-Fuchs[1,2,3], Inga Petelski[1,2,3], Yannick Günzel[1,2,3], Mohammad Salahshour[1,2,3], Chi-Yu Lee[1,3], Jacob M. Graving[1,2,3,4], Liang Li[1,2,3], Oliver Deussen[1,5], Gregory A. Sword[6], Iain D. Couzin[1,2,3]*

Collective motion, which is ubiquitous in nature, has traditionally been explained by "self-propelled particle" models from theoretical physics. Here we show, through field, lab, and virtual reality experimentation, that classical models of collective behavior cannot account for how collective motion emerges in marching desert locusts, whose swarms affect the livelihood of millions. In contrast to assumptions made by these models, locusts do not explicitly align with neighbors. While individuals respond to moving-dot stimuli through the optomotor response, this innate behavior does not mediate social response to neighbors. Instead, locust marching behavior, across scales, can be explained by a minimal cognitive framework, which incorporates individuals' neural representation of bearings to neighbors and internal consensus dynamics for making directional choices. Our findings challenge long-held beliefs about how order can emerge from disorder in animal collectives.

Theoretical models from physics, such as the highly influential Vicsek model (*1*), describe how simple local interactions, where individuals align their movement with nearby individuals, can generate large-scale, coordinated (meaning aligned or ordered) motion in groups. This model makes the prediction that groups should exhibit a spontaneous transition between two collective states—from a disordered state (akin to a gas) to an ordered state (akin to a driven fluid)—as density increases. This concept has implications for understanding collective behavior across biological systems, from cellular aggregates to human crowds.

The results of empirical studies, including experiments with juvenile desert locusts (*Schistocerca gregaria*), have lent support to this theory. Locust swarms, which can cover vast areas and greatly impact food security (*2*), serve as a prominent example of collective motion. Laboratory findings have suggested that increasing locust density in a ring-shaped arena leads to a shift from disordered to ordered motion, appearing to validate the predicted density-dependent phase transition (*3*). Thus, despite inherent errors in individual alignment, a sufficient density of individuals is argued to enable an averaging out of noise and the emergence of coherent group movement. In general, comparison of model predictions and empirically observed collective motion has provided evidence supporting these "classical" models of collective behavior (*3*–*8*).

There exists an inherent problem with this approach, however. Given that density and order are positively correlated, it is challenging to establish cause and effect. This raises the question of whether alignment results from the averaging out of uncorrelated errors at high densities, as classical theory suggests, or whether the coherence of motion itself triggers alignment, independent of density. That is, is it the density (corresponding to the "amount" of information) or the order (the "quality" of information) that is predominantly important or rather how the two interact? Furthermore, do individuals explicitly align their direction of travel with near neighbors, as is assumed in these classic models? Addressing these questions is crucial not only for understanding the fundamentals of biological collective motion but also for gaining insights into the formation and maintenance of locust swarms, which affect human well-being (*2*).

Using a combination of field experiments with naturally occurring locust swarms and analysis of how visual interactions are mediated using immersive virtual reality (VR) (*9*, *10*), we reveal that classical models of collective behavior [such as the Vicsek model (*1*) and Couzin model (*11*–*13*)] cannot account for collective motion exhibited by locusts and that the mechanism proposed for the emergence of their collective motion needs to be corrected. We demonstrate that locusts do not explicitly align with neighbors and that their behavior is consistent with a minimal cognitive model of spatiotemporal decision-making. We argue for an approach to the study of collective behavior that moves from descriptive to generative models, with the latter taking into account that organisms are not self-propelled particles but rather probabilistic decision-making entities that base their decisions explicitly on the representation and integration of sensory information.

Field experiments

The largest East African outbreak of the desert locust in recent years began in late 2019. In February 2020, we conducted experiments on large "marching bands" of flightless juvenile

[1]Centre for the Advanced Study of Collective Behaviour, University of Konstanz, Konstanz, Germany. [2]Department of Collective Behavior, Max Planck Institute of Animal Behavior, Konstanz, Germany. [3]Department of Biology, University of Konstanz, Konstanz, Germany. [4]Advanced Research Technology Unit, Max Planck Institute of Animal Behavior, Konstanz, Germany. [5]Department of Computer and Information Science, University of Konstanz, Konstanz, Germany. [6]Department of Entomology, Texas A&M University, College Station, TX, USA.
***Corresponding author. Email: icouzin@ab.mpg.de (I.D.C.); sercan.sayin@uni-konstanz.de (S.S.)**

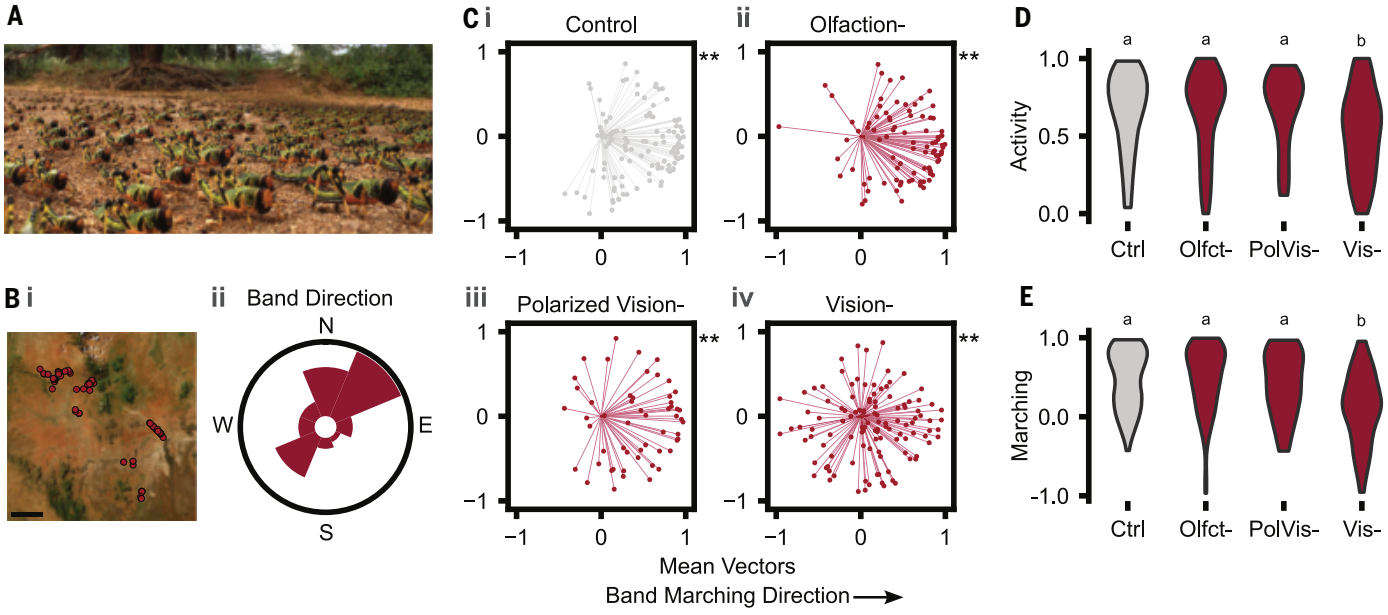

Fig. 1. Sensory deprivation experiments in the field. (**A**) A marching band of *S. gregaria* photographed in Kenya in 2020. (**B**) (i) Locust bands in a total of 112 locales between 27 February and 12 March of 2020 in the Samburu and Isiolo districts of Kenya. Scale bar: 15 km. (ii) Observed marching band directions. n = 56 bands. Histogram counts: min = 2, max = 23. (**C**) Single tagged locusts were reintroduced to a marching band after antennectomy (Olfaction−, n = 89) or visual occlusion (Polarized Vision−: dorsal eyes and ocelli, n = 54; Vision−: complete eyes and ocelli, n = 114). Control n = 110. Locust movements were reported as mean vectors. Statistical annotations on each upper right corner stand for the results of Rayleigh test for nonuniformity. (**D** and **E**) Mean binarized Euclidean distance (Activity) and mean vector magnitude in congruence with marching band (Marching) by control and treated animals. Olfct, olfaction; PolVis, polarized vision; Vis, vision. See table S2 for statistical summaries.

locusts in the Samburu and Isiolo counties of Kenya to establish the predominant sensory modalities used in coordinating motion. Swarms of locust nymphs were encountered at a large number of locations, ranging from first to sixth instar (juvenile) stages (Fig. 1, A and B). In 56 cases where we recorded marching band directions, a prominence along the north/northeast axis was noted (Fig. 1B and table S1). Consistent with previous studies (*14*), marching direction did not clearly relate to immediate weather conditions, elevation, or sun position (fig. S1).

To assess the role of different modalities used by focal locusts in maintaining coordinated group movement, we independently manipulated olfaction (by clipping antennae), polarized vision (by painting ocelli and the dorsal rim area of the compound eyes), and vision (by painting ocelli and the entirety of the compound eyes). Control insects were similarly handled but left with their senses intact. All insects were painted with an identifiable color marking on their pronotum before being returned to an undisturbed section of the marching band.

Reintroduced control locusts, anosmic locusts, and locusts deprived of polarized vision exhibited a strong, and rapid, tendency to march with, and in the direction of, conspecifics in the band (Fig. 1C, i, ii, and iii, respectively). Completely blinded insects, by contrast, moved in random directions with respect to the band direction (Fig. 1C, iv, and E). Although these blinded individuals remained mobile—likely owing to tactile cues that increase movement probability to avoid cannibalistic interactions (*15*–*17*)—in many cases, contact alone did not provide directional guidance, even in densely packed, highly directional swarms. Thus, we conclude that vision is both necessary and sufficient for individuals to coordinate motion with neighbors.

VR experiments

As noted above, there has been a confound in previous approaches to establish the mechanism by which locusts regulate their behavior in swarms because of the inherent (theoretical) positive correlation between density and order. To decouple these two factors, we enabled real locusts to interact with virtual conspecifics. Notably, our system was fully panoramic, allowing untethered, freely moving locusts to interact with visual stimuli from fully volumetric three-dimensional ("holographic") marching conspecifics with no constraints resulting from boundaries (Fig. 2, A and B).

In order to conduct a full parametric scan of density-order space, we considered independent combinations of density, from 1 to 64 locusts per m^2, and order (from 0, equivalent to randomly moving individuals, to 1, where virtual conspecifics are in perfect alignment with one another) (Fig. 2, C and D). We note that our upper and lower insect densities exceed the range tested (2 to 62 moving locusts per m^2) by Buhl *et al.* (*3*).

Locusts' alignment with the virtual swarm was found to strongly depend on the order parameter, that is, the "quality" of information presented, with no significant dependency on density (Fig. 2, E to G, and fig. S4A). With higher order, focal locusts marched longer distances in more-directed trajectories (max: 46.1 m; figs. S3 and S4A, i and ii). We note that the cumulative distances covered by focal insects were comparable between different order and density conditions (fig. S4A, iii). Clearly, if no directional cues are present, locusts have no social context on which to base their movements, but we find that even with very sparse but high-quality (i.e., ordered) information, they exhibit a strong tendency to align with the motion of others. Notably, while these results are apparently in contradiction to the data of Buhl *et al.* (*3*), a reevaluation of their data, taking into account statistical effects associated with different group sizes, reveals that collective alignment (order) is also independent of locust density in these experiments (fig. S6).

Behavioral response to optical flow

It has long been considered that coherent motion in animal groups may be mediated

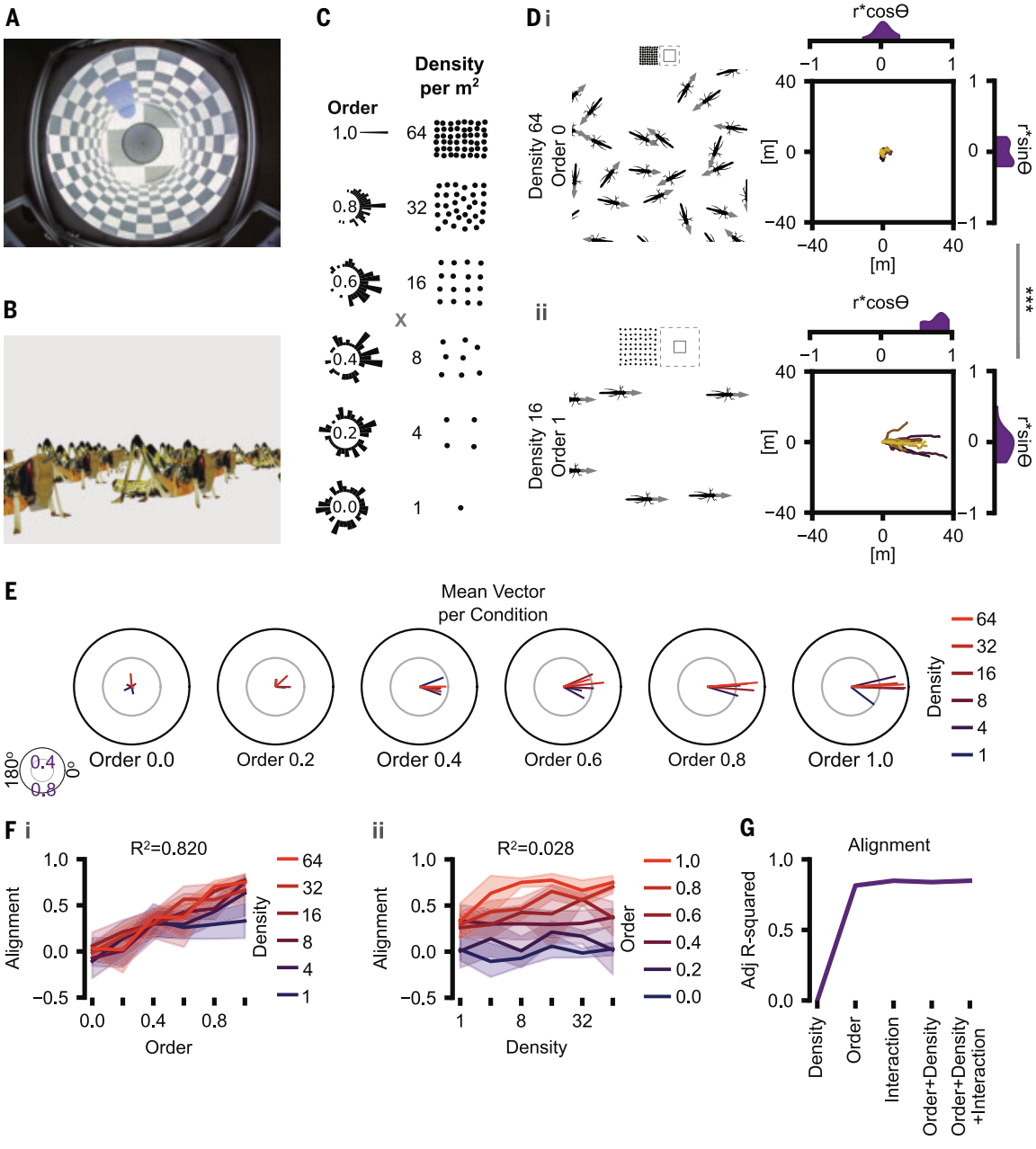

Fig. 2. Reconstructing marching in an immersive virtual reality. (**A**) Top-down view of the virtual reality system. A motion compensation system stabilizes an untethered fifth instar desert locust in position, and from this perspective, a panoramic virtual world is projected in 100-Hz high refresh rate. (**B**) Virtual marching band. The virtual reality engine draws animated juvenile desert locust visual stimuli with real-world kinematics data (fig. S2) and constant velocity. Throughout an experiment, periodic boundaries set for virtual band guarantee that the experimental focal juvenile locust is located at the virtual band's center. (**C**) Experimental design. Virtual bands were generated to vary by two parameters, order and marching band density per square meter. For a given order value, von Mises distributions constituted a marching band's coherence de novo. Focal locusts were tested once for one condition per 20 min. Completed trials equaled 421 once outliers were removed. See the methods section of the supplementary materials for details of the experimental design and the analysis pipeline. (**D**) Exemplary order and density combinations. Schematics depict virtual locust positions and directions at a given time. Above each schematic, periodic boundaries and zoomed areas are drawn with dashed and solid lines, respectively. All bands consist of 64 virtual locusts. Individual trajectories per condition are shown on the right. n = 13 for both groups. Mean vector (**r**) projections onto axes congruent with (**r***cosθ) and perpendicular to (**r***sinθ) marching band directions were used for multivariate analyses. To see all trajectories, refer to fig. S3. (**E**) Means per each condition of 64 order and density combinations. (**F**) Alignment (calculated as **r***cosθ) versus order (i) and density (ii) as primary parameters for reporting. Color codes designate secondary parameter. Coefficient of determination (R^2) scores showcase explanatory power of respective primary parameters alone. See comparison of directedness, marching, and Euclidean distances with respect to either density or order "alone" in fig. S4. See fig. S5 for clustering of all data groups. (**G**) Adjusted R^2 from ordinary least squares regression models on alignment group means for different explanatory variables used. See table S2 for statistical summaries.

by the optomotor response. If animals, such as insects or fish, are presented with coherently moving dots or stripes, they will tend to move in the direction of the resulting optical flow stimulus. Being an innate and robust behavior, optical flow is often intuitively considered an important if not essential mechanistic basis of collective motion in large mobile groups [see (*18*, *19*) for fish and (*20*, *21*) for locusts]. Yet, direct evidence in support of this hypothesis is lacking. Recently, Bleichman *et al.* (*20*) presented coherent moving dots on either side of a rigidly tethered locust and demonstrated that the motion could alter the probability of the locust moving. However, the focal locusts in this study were constrained to only be fully aligned with the stimuli and could not alter their direction in response to stimuli.

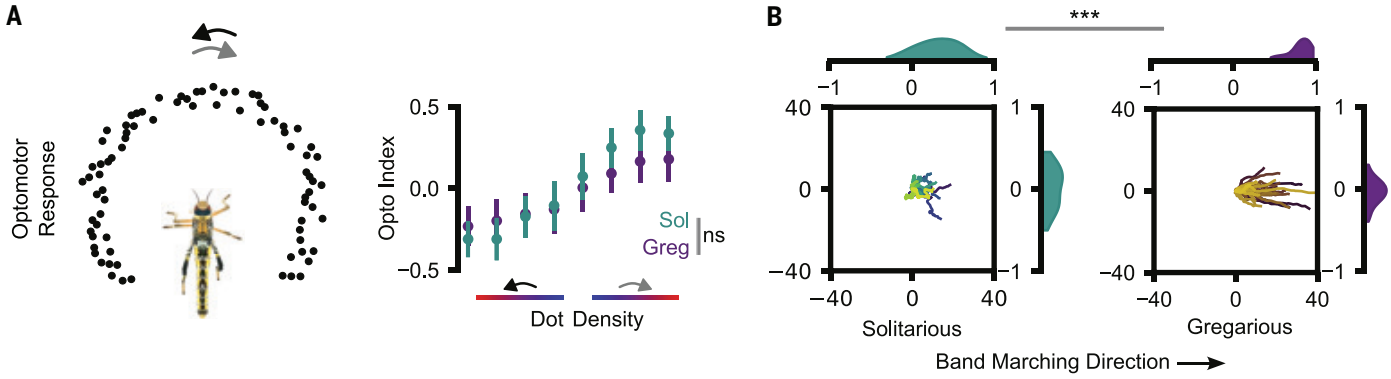

Fig. 3. Optical flow does not drive marching. (**A**) (Left) The moving-dot paradigm schematic used in the study. (Right) Optomotor responses of solitarious (Sol) and gregarious (Greg) desert locusts to moving-dot stimuli of different densities, color coded blue to red for low to high density. All stimuli have 100% coherence, meaning that the moving dots in an experiment move either counterclockwise or clockwise. The optomotor response, or opto-index, is a preference index calculated as the difference between summed absolute counterclockwise and clockwise velocities, then dividing that difference by the sum of these velocities for a given trial. *n* = 32 locusts tested. Number of dots in the density paradigm was 64, 256, 1024, and 4096. (**B**) Trajectories for solitarious locusts (*n* = 34) and gregarious control locusts (*n* = 32) within a virtual gregarious marching band (order: 1; density: 16). See table S2 for statistical summaries.

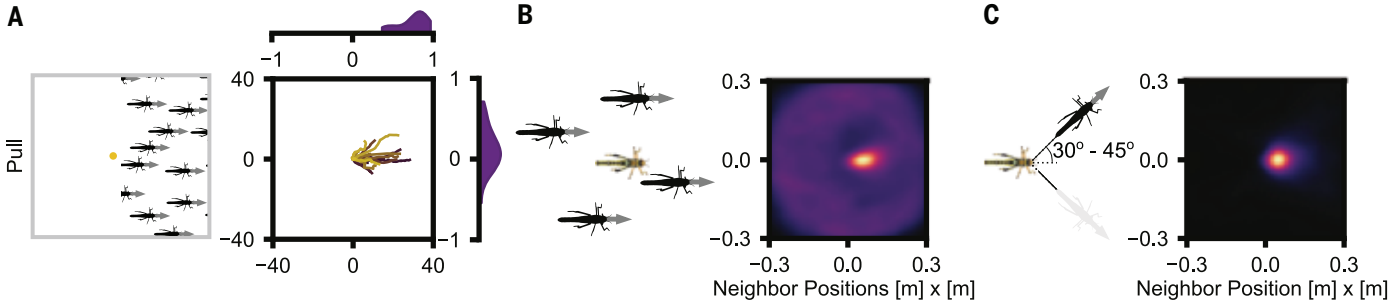

Fig. 4. Attraction to conspecifics for locust virtual bands. (**A**) Pull experimental design. A focal locust is positioned immediately behind a highly ordered marching band. *n* = 21. Periodic boundaries ensured constant distance between focal locust and marching band edge. See fig. S7 for "Push" condition. Figure S9 explores roles of order and distance in pull conditions. (**B**) Density map for egocentric neighbor positions in a highly ordered marching as in Fig. 2D. Focal heading is along +*x* axis. Focal *n* = 22. See fig. S10 for neighbor-follow duration. (**C**) Density map for neighbor positions in single virtual locust assay. A single virtual locust, with constant velocity, was positioned in front of focal locust, at 30° to 45° offset. A single trial lasted as long as the distance between follower focal locust and virtual target was maintained within a threshold distance (50 cm). Focal heading is along +*x* axis. Focal *n* = 12. Normalized densities are displayed with a color gradient from dark purple for the minimum to bright yellow for the maximum. See fig. S10 for neighbor-follow durations.

We assessed whether locusts are sensitive to optical flow under conditions where they could freely move with respect to the presented cue. In evaluating this, we took advantage of the fact that locusts exhibit extreme phenotypic plasticity, including in social behavior. If reared in isolation, locusts are sedentary insects that avoid conspecifics, a phenotype that is referred to as "solitarious" (*22*–*24*). It is only when they are reared together that they become "gregarious" and exhibit increased activity and attraction to other locusts (*22*–*24*). Should optomotor response to optical flow cues underlie the alignment among individuals in swarms, we may expect that gregarious locusts would be more responsive to such cues than are solitarious insects.

We find that this is not the case. Both solitarious and gregarious locusts exhibit a similar propensity to turn in the direction of the wide-field moving-dot stimulus, with solitarious insects exhibiting a slightly stronger response (Fig. 3A). However, when placed in a coherently moving virtual swarm, solitarious insects do not align their direction of travel with the virtual conspecifics (Fig. 3B), whereas gregarious individuals strongly do so (Figs. 2 and 3B). These results are inconsistent with the view that the optomotor response is involved in regulating social interactions in marching locusts.

The role of "pull" in swarms

Another aspect that classical collective movement models and the optical flow hypothesis do not consider is the frame of reference of focal individuals with respect to the direction of collective movement (*1*, *21*). Addressing this, later models, again relying on theoretical physics, speculated whether collective motion can be generated by collisions and escape and pursuit mechanisms (*25*, *26*). We devised a scenario to test how visual stimuli from receding swarms of virtual insects affect the behavior of focal locusts. In this condition, highly ordered marching bands at a 5-cm offset from focal positions were generated (Fig. 4A). Virtual locusts presented as moving away were sufficient to recapitulate focal locust alignment behavior with comparable distances covered as in the full virtual marching band conditions (Fig. 4B, compare with Fig. 2D, ii). Furthermore,

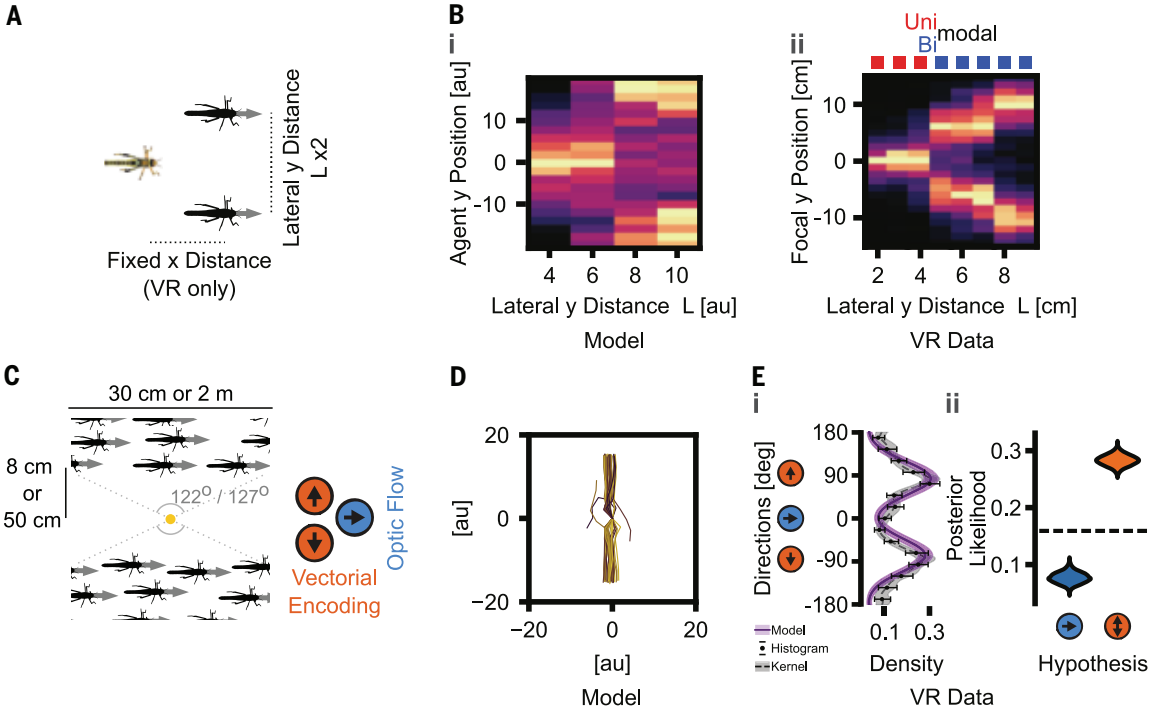

Fig. 5. Vector computations can explain individuals' response to conspecifics. (**A**) Schematic of the two conspecific "targets" scenario used in our simulation model and VR experiments. Lateral distance (along *y* axis) between two targets was set to constant at 2× *L*. In all VR trials, horizontal distance (along *x* axis) between focal locust and two targets was fixed. (**B**) (i) Model agent *y* positions when a focal agent is presented with two moving targets. au, arbitrary units. See fig. S12 for two-dimensional position histograms. *n* = 200 for all conditions. (ii) Instances in VR where focal locust followed targets depicted as a heatmap as in focal individual's *y* position versus lateral distance *L*. Dip test of unimodality is used to assess *y* position distribution (red: $P > 0.05$; blue: $P < 0.05$). Focal locust *n* = 11. Histogram range is displayed with a color gradient from dark purple for the minimum to bright yellow for the maximum. (**C**) Experimental design to evaluate the possible roles of optical flow versus vectorial representation in coordinating marching for VR experiments. At a given fixed lateral distance (8 or 50 cm) to the focal locust, two highly ordered bands move in same direction. Each virtual locust has a 100-ms life span, to preserve optical flow and positional cues but to prevent the focal locust from persistently "locking onto" a single target. (**D**) Trajectories of simulated agents. Similar to (C), an agent is placed in between two sets of targets moving in the same direction. The initial lateral distance of the agent to targets was 20 au. Trajectories plotted for the first 20 au covered by each agent. *n* = 100. (**E**) Hierarchical Bayesian model used to infer predominant movement directions in VR scenarios tested as in (C). (i) The posterior model density compared with nonparametric bootstrapped histogram density and kernel density estimates (see materials and methods for details). Lines and points show the median of the posterior or bootstrap distribution, whereas the bars and bands show the 95% interval (2.5 to 97.5%; *n* = 4000 samples per density type). (ii) Distributions of posterior likelihood scores for hypothesis testing. *n* = 4000 samples per hypothesis. Dashed line represents a random walk hypothesis as a uniform likelihood. Figure S14 offers focal locust trajectories for both conditions tested in (C). Tested locusts *n* = 50. See table S2 for statistical summaries.

our analysis of neighbor positions for locusts surrounded by conspecifics in a full marching band and in experiments when only one receding virtual locust was present showed that focal individuals closely follow neighbors (Fig. 4, C and D). As a validation of our VR experiments, quantification of locust interactions in an arena experiment with 2000 locusts revealed a similar proximal pursuit mechanism in real-world interactions as well (fig. S11). These results show that moving-away conspecifics play a strong "pulling" role in the regulation of marching behavior, consistent with a mechanism involving pursuit.

A vectorial representation of conspecifics

Our above findings show that locusts may not base decisions on simple fixed "rules." An alternative framework considers the generative process by which decisions are made; for example, Sridhar *et al.* (*10*) developed a model of spatial decision-making based on neural principles. Consistent with neurobiological studies of insects (*27*, *28*) and vertebrates (*29*), neighbors are considered to induce neural activity bumps on a "ring attractor" network, with their position on the ring reflecting their bearing with respect to the focal animal. Given that neural activity encodes both directional information (bearings) and the "strength" of influence (encoded by the magnitude of neural activity), this is a "vectorial representation" of conspecifics. Ongoing internal dynamics on the ring attractor network, defined predominantly by local excitation and long-range and/or global inhibition, facilitate the integration of these sensory inputs, generating a self-organized bump of activity on the ring (a collective neural consensus mechanism) that represents the animal's subsequent directional preference [for details, see (*10*, *30*, *31*)].

This type of cognitive model, which we refer to as the vectorial hypothesis, makes directly testable predictions with respect to behavior, and these predictions are in stark contrast to those of the optical flow hypothesis. For example, if presented with two conspecifics moving in the same direction and speed at a fixed lateral distance (*L*) (Fig. 5A), our model predicts that a follower should occupy, on average, a position directly between them, up to a critical distance above which there should exist a dynamical bifurcation in the neural dynamics, resulting in a decision to choose to follow one or the other. That is, the brain should suddenly transition between an "averaging" and a "winner takes all" dynamic (*10*). The optomotor (optical flow) hypothesis, by contrast, predicts that a focal locust should align with conspecifics irrespective of their lateral distance. In both models, there exists a further, maximal distance at which interactions become impossible owing to insufficient sensory information.

Presenting a pair of marching virtual conspecifics with different lateral distances, we see, as predicted by the vectorial hypothesis (Fig. 5B, i), a clear bifurcation in the relative position adopted by the real locust (Fig. 5B, ii). We note that in conventional laboratory

experiments with real interacting insects, it is not possible to conduct such a test of the underlying cognitive mechanism, thus highlighting an advantage of the VR approach for establishing the nature of visual social interactions.

A further, complementary experiment to test the mechanistic basis of social interactions is how a focal locust will behave if positioned directly between two coherently marching swarms. In classic models of collective behavior that include attraction, the symmetry of attractive "forces" in one direction and the other would result in them tending to cancel out, and an explicit alignment term, if present, would dominate, resulting in alignment with directional cues (see supplementary text in the supplementary materials). Similarly, the optical flow hypothesis would predict motion in alignment with swarm direction. The cognitive model, by contrast, which only considers attraction but captures the competition between conflicting directional information (owing to the presence of long-range inhibition), predicts that in this scenario, locusts should move in a direction perpendicular to the swarm motion. To evaluate these hypotheses, locusts were placed at a fixed equal distance (either 8 or 50 cm) in between two parallel virtual marching bands, both moving in the same direction (Fig. 5C). Here, optical flow is parallel to marching direction ($+x$ axis, as indicated by the blue circle), while vectors representing conspecifics are (approximately) perpendicular ($\pm y$ axis, as indicated by the orange circles) to the collective movement. For model agents (Fig. 5D) and focal locusts (Fig. 5E and fig. S14), movement direction was predominantly directly toward one marching band or the other and not in congruence with optical flow (or with classic self-propelled particle models; see supplementary text).

Our results suggest that locust marching behavior is mediated by a vectorial encoding strategy and not a strategy that uses explicit alignment. To establish whether individuals utilizing this same mechanism can account for the emergence of long-range coordinated motion in locusts, we also considered the scenario of conspecific representation as (competing) bumps on a neural ring attractor network (see supplementary materials for details), revealing that it can account for the emergence of highly ordered collective motion (fig. S15).

Conclusions

Our work suggests that, contrary to previous assertions, classical models of collective motion fail to account for the mechanism by which coherent motion is established and maintained in desert locust swarms. For example, we found no evidence that locusts explicitly align with one another nor that they use the optomotor response to mediate social interactions. Furthermore, both our data and a critical revaluation of those of Buhl *et al.* (*3*) find no evidence for a density-dependent transition from disorder to ordered swarm motion, further questioning the dominant paradigm used to study animal collectives more broadly. By contrast, we find that individual and collective locust behavior is consistent with a minimal cognitive model (a ring attractor network) in which individuals (targets) are represented as competing neural bumps. This suggests that wide-field optical flow cues (such as those used for self-motion estimation and/or wide-field landscape information) are separate from those cues used in neighbor tracking. Circuits responsible for pursuing neighbors are yet to be described for locusts. Beyond a simple detection of objects against a moving background, vectorial representation and wide-field motion necessitate competition under certain scenarios, and how global information is suppressed is yet to be explored. Revealing these circuits will enable the identification of afferent and modulatory inputs, which will be instrumental to infer causality regarding the forces that govern pursuit and collective motion. Furthermore, given the clear discrepancy between gregarious and solitarious behavior in locusts, we suggest future exploration of differential modulation or developmental regulation of visual attraction and decision-making networks. Our work argues for a refreshed perspective in the study of collective animal behavior that moves beyond the "self-propelled particle" paradigm and considers explicitly the sensory and cognitive mechanisms by which interactions are mediated.

REFERENCES AND NOTES

1. T. Vicsek, A. Czirók, E. Ben-Jacob, I. Cohen, O. Shochet, *Phys. Rev. Lett.* **75**, 1226–1229 (1995).
2. A. Steedman, *Locust Handbook* (Natural Resources Institute, 1990).
3. C. Buhl *et al*., *Science* **312**, 1402–1406 (2006).
4. J. Buhl, G. A. Sword, S. J. Simpson, *Interface Focus* **2**, 757–763 (2012).
5. D. J. T. Sumpter, R. P. Mann, A. Perna, *Interface Focus* **2**, 764–773 (2012).
6. R. Lukeman, Y.-X. Li, L. Edelstein-Keshet, *Proc. Natl. Acad. Sci. U.S.A.* **107**, 12576–12580 (2010).
7. R. P. Mann *et al*., *PLOS Comput. Biol.* **9**, e1002961 (2013).
8. Ch. Becco, N. Vandewalle, J. Delcourt, P. Poncin, *Physica A* **367**, 487–493 (2006).
9. J. R. Stowers *et al*., *Nat. Methods* **14**, 995–1002 (2017).
10. V. H. Sridhar *et al*., *Proc. Natl. Acad. Sci. U.S.A.* **118**, e2102157118 (2021).
11. I. D. Couzin, J. Krause, R. James, G. D. Ruxton, N. R. Franks, *J. Theor. Biol.* **218**, 1–11 (2002).
12. I. D. Couzin, J. Krause, N. R. Franks, S. A. Levin, *Nature* **433**, 513–516 (2005).
13. I. D. Couzin *et al*., *Science* **334**, 1578–1580 (2011).
14. P. E. Ellis, C. Ashall, *Field Studies on Diurnal Behaviour, Movement and Aggregation in the Desert Locust (Schistocerca gregaria Forskål)* (Anti-Locust Research Centre, 1957).
15. S. Bazazi *et al*., *Curr. Biol.* **18**, 735–739 (2008).
16. S. J. Simpson, G. A. Sword, P. D. Lorch, I. D. Couzin, *Proc. Natl. Acad. Sci. U.S.A.* **103**, 4152–4156 (2006).
17. H. Chang *et al*., *Science* **380**, 537–543 (2023).
18. R. Harpaz *et al*., *Sci. Adv.* **7**, eabi7460 (2021).
19. E. Shaw, B. D. Sachs, *J. Comp. Physiol. Psychol.* **63**, 385–388 (1967).
20. I. Bleichman, P. Yadav, A. Ayali, *Proc. Biol. Sci.* **290**, 20221862 (2023).
21. D. L. Krongauz, A. Ayali, G. A. Kaminka, *PLOS Comput. Biol.* **20**, e1011796 (2024).
22. M. P. Pener, S. J. Simpson, *Adv. Insect Physiol.* **36**, 1–272 (2009).
23. S. M. Rogers *et al*., *J. Insect Physiol.* **65**, 9–26 (2014).
24. H.-J. Pflüger, P. Bräunig, *J. Comp. Physiol. A* **207**, 321–326 (2021).
25. P. Romanczuk, I. D. Couzin, L. Schimansky-Geier, *Phys. Rev. Lett.* **102**, 010602 (2009).
26. D. Grossman, I. S. Aranson, E. Ben Jacob, *New J. Phys.* **10**, 023036 (2008).
27. J. D. Seelig, V. Jayaraman, *Nature* **521**, 186–191 (2015).
28. C. Lyu, L. F. Abbott, G. Maimon, *Nature* **601**, 92–97 (2022).
29. A. Sarel, A. Finkelstein, L. Las, N. Ulanovsky, *Science* **355**, 176–180 (2017).
30. L. Oscar, L. Li, D. Gorbonos, I. D. Couzin, N. S. Gov, *Phys. Biol.* **20**, 045002 (2023).
31. D. Gorbonos, N. S. Gov, I. D. Couzin, *PRX Life* **2**, 013008 (2024).
32. S. Sayin *et al*., The Behavioral Mechanisms Governing Collective Motion in Swarming Locusts [Data set], Zenodo (2025); https://doi.org/10.5281/zenodo.14353283.
33. S. Sayin *et al*., The Behavioral Mechanisms Governing Collective Motion in Swarming Locusts (Subrepository3), Zenodo (2025); https://doi.org/10.5281/zenodo.14355590.

ACKNOWLEDGMENTS

The authors thank student assistants M. C. Karakurt, J. Klein, and Z. Sener for VR data collection; E. Mamonova, H. Kübler, and N. Schwarz for tracking field data; L. Schröder and N. Schwarz for trackball data collection; F. Oberhauser for being an invaluable team member in Kenya; M. Mahmoud for contributing to VR development in its early phases; A. Bahl and K. Slangewal for implementing real-time orientation tracking in VR; and D. S. Calovi for experimental design discussions. J.M.G. thanks J. Bak-Coleman for help with model debugging and M. L. Smith for the use of his GPU. J.M.G. acknowledges support from NVIDIA Corporation's Academic Hardware Grant Program. We thank C. Buhl and K. Yates for providing Buhl *et al*. (*3*) data. We also thank C. Buhl for feedback on the manuscript. We acknowledge the use of ChatGPT, a language model developed by OpenAI, for minor suggestions with respect to the text, equations, software, and figures.
Funding: Deutsche Forschungsgemeinschaft (DFG, German Research Foundation) under Germany's Excellence Strategy–EXC 2117-422037984. To E.C.-F.: DFG GZ: CO 1758/5-1. To I.D.C.: the Max Planck Society, the European Union's Horizon 2020 Research and Innovation Programme under Marie Skłodowska-Curie Grant 860949, the DFG Gottfried Wilhelm Leibniz Prize 2022 584/22, the Struktur- und Innovationsfonds für die Forschung of the State of Baden-Württemberg, the PathFinder European Innovation Council Work Programme 101098722, and the Office of Naval Research Grant N0001419-1-2556: To G.A.S.: NSF Biology Integration Institute Program Grant DBI-2021795. **Author contributions:** Conceptualization: S.S., E.C.-F., G.A.S., I.D.C.; Formal analysis: S.S., M.S., C.-Y.L., J.M.G., L.L., I.D.C.; Funding acquisition: O.D., E.C.-F., I.D.C.; Investigation: S.S., E.C.-F., I.P., C.-Y.L., I.D.C.; Methodology: S.S., E.C.-F., J.M.G., I.D.C.; Project administration: E.C.-F., I.D.C.; Resources: Y.G., J.M.G., L.L., I.D.C.; Supervision: E.C.-F., I.D.C.; Validation: S.S., Y.G., J.M.G., I.D.C.; Visualization: S.S., J.M.G.; Writing – original draft: S.S., I.D.C.; Writing – review & editing: S.S., E.C.-F., Y.G., M.S., C.-Y.L., J.M.G., L.L., O.D., G.A.S., E.C.-F., I.D.C. **Competing interests:** The authors declare that they have no competing interests. **Data and materials availability:** The source data and material (*32*) and the analysis scripts (*33*) are available in Zenodo.

SUPPLEMENTARY MATERIALS

science.org/doi/10.1126/science.adq7832
Materials and Methods
Supplementary Text
Figs. S1 to S15
Tables S1 and S2
References (*34*–*48*)
MDAR Reproducibility Checklist

Submitted 5 June 2024; accepted 20 December 2024
10.1126/science.adq7832

MOLLUSK GENETICS

A genome-based phylogeny for Mollusca is concordant with fossils and morphology

Zeyuan Chen[1], J. Antonio Baeza[2,3], Chong Chen[4], Maria Teresa Gonzalez[5], Vanessa Liz González[6], Carola Greve[1,7], Kevin M. Kocot[8,9], Pedro Martinez Arbizu[10], Juan Moles[11,12], Tilman Schell[1,7], Enrico Schwabe[13], Jin Sun[14], Nur Leena W. S. Wong[15], Meghan Yap-Chiongco[8], Julia D. Sigwart[1,16]*

Extreme morphological disparity within Mollusca has long confounded efforts to reconstruct a stable backbone phylogeny for the phylum. Familiar molluscan groups—gastropods, bivalves, and cephalopods—each represent a diverse radiation with myriad morphological, ecological, and behavioral adaptations. The phylum further encompasses many more unfamiliar experiments in animal body-plan evolution. In this work, we reconstructed the phylogeny for living Mollusca on the basis of metazoan BUSCO (Benchmarking Universal Single-Copy Orthologs) genes extracted from 77 (13 new) genomes, including multiple members of all eight classes with two high-quality genome assemblies for monoplacophorans. Our analyses confirm a phylogeny proposed from morphology and show widespread genomic variation. The flexibility of the molluscan genome likely explains both historic challenges with their genomes and their evolutionary success.

Phylum Mollusca exhibits the widest disparity of body plans in metazoan evolution, and the interrelationships of the living lineages have been a subject of contentious debate for centuries (*1*–*3*). The eight classes of extant Mollusca are each unambiguously monophyletic, but their diverse morphologies allow many plausible sister-group combinations. The three most diverse groups are more familiar—bivalves, gastropods, and cephalopods—and the other five include worm-mollusks (Solenogastres, Caudofoveata), eight-shelled chitons (Polyplacophora), tubular infaunal predators (Scaphopoda), and headless limpets (Monoplacophora). More than 500 million years of morphological evolution have produced even more transitional forms in the fossil record, many with unclear affinities (*4*). Most studies have focused on deep phylogenetic nodes, resolving the clades Conchifera (Bivalvia, Cephalopoda, Gastropoda, Monoplacophora, Scaphopoda) and Aculifera (Caudofoveata, Polyplacophora, Solenogastres) (*2*, *5*, *6*). Resolving the topological positions of all eight clades is critical to understanding molluscan evolution (*7*), but genomic resources were limited or lacking for most classes.

Early molecular phylogenetic studies of Mollusca sometimes completely conflicted with previous morphology-based hypotheses (*8*). Phylogenomic studies using transcriptome data covered all classes but had low coverage, outdated orthology inference methods, and uncertain topological support (*2*, *6*). Results from standard genetic markers, mitochondrial genomes, transcriptomes, morphology, and the fossil record have at times seemed to be all mutually contradictory but increasingly converged toward a potential consensus (*7*, *9*). Beyond the question of resolving molluscan phylogeny, a larger issue is understanding the fundamental evolutionary factors that made it so difficult and controversial to resolve.

We present a total group phylogeny for Mollusca based on genome-wide markers comprising all metazoan Benchmarking Universal Single-Copy Orthologs (BUSCO) genes in a phylogenomic analysis that includes all major clades and multiple representatives from all eight living classes. We assembled two near-complete genomes of the enigmatic deep-sea class Monoplacophora and generated genomes for five additional taxonomic classes: Caudofoveata, Scaphopoda, Gastropoda, Bivalvia, and Polyplacophora. This dataset, combined with previously published genome assemblies, underpins our new phylogenetic analysis, which supports the origin of the phylum in the Cambrian and a rapid split into the major clades Aculifera and Conchifera (Fig. 1). Congruent with the extensive fossil record of Mollusca and phylogenetic hypotheses proposed from morphology (Fig. 2), we found that Monoplacophora is sister to the remaining Conchifera, and Cephalopoda is sister to the clade Gastropoda + Diasoma (Scaphopoda + Bivalvia).

Selecting representative data

Genome-wide data have played a pivotal role in reconstructing complex histories of the tree of life; however, genomic resources for Mollusca remain markedly underrepresented and unevenly distributed, with only 300 genomes available for more than 100,000 living species (Fig. 3A). The quality of these assemblies varies widely, in large part because of intrinsic technical difficulties that begin with challenges for sample acquisition, preservation, and DNA extraction and sequencing from animals that produce copious mucopolysaccharides (*10*). Assembly quality is further hampered by variability in genome size, heterozygosity, and repeat content, even within particular clades (Fig. 3, B to D). We generated 13 de novo genomes that fill gaps for key classes (two monoplacophorans, one caudofoveate, four chitons, one scaphopod), deeply divergent or contentious lineages (*Solemya*, *Verpa*, *Tectura*), and diverse morphologies (*Scintilla*, *Concholepas*) (fig. S1 and tables S1 and S2). We considered genome quality and phylogenetic diversity, retaining species in controversial branches even where genome quality was slightly lower (fig. S2 and table S3). This totals 77 species covering all eight classes, including two Caudofoveata, two Solenogastres, eight Polyplacophora, two Monoplacophora, 11 Cephalopoda, 22 Gastropoda, three Scaphopoda, and 27 Bivalvia.

Our phylogenomic inference relied on metazoan BUSCO genes (*11*). BUSCO represents a universal gene set that provides effective comparative power across the phylum. Because BUSCO genes are conserved regions, they are suitable for reconstructing deep divergences. Strict quality control in the selected genomes allowed us to identify a sufficient number and more even distribution of loci across species (figs. S2 and S3): Each species had an average of 897 BUSCO genes (94%) identified in the genome assemblies (table S4). To test the impact of gene occupancy on topology, we compared the metazoan BUSCO set and a reduced 96-gene dataset with 100% occupancy (figs. S3 and S4).

The balance of taxon sampling and character (gene) occupancy is a persistent dilemma, especially in deeply divergent organismal groups (*12*). High coverage of lineages, high-quality molecular markers, and sufficient molecular loci enabled us to construct the phylogeny within extant Mollusca. Coupling these factors with a more even distribution of molecular markers across species also allowed us to recover the major branches within each class

[1]Senckenberg Research Institute and Natural History Museum Frankfurt, Frankfurt am Main, Germany. [2]Department of Biological Sciences, Clemson University, Clemson, SC, USA. [3]Departamento de Biologia Marina, Universidad Catolica del Norte, Coquimbo, Chile. [4]X-STAR, Japan Agency for Marine-Earth Science and Technology (JAMSTEC), Yokosuka, Japan. [5]Instituto Ciencias Naturales "Alexander von Humboldt," Universidad de Antofagasta, FACIMAR, Antofagasta, Chile. [6]Informatics and Data Science Center, Smithsonian Institution National Museum of Natural History, Washington, DC, USA. [7]LOEWE Centre for Translational Biodiversity Genomics, Frankfurt, Germany. [8]Department of Biological Sciences, University of Alabama, Tuscaloosa, AL, USA. [9]Alabama Museum of Natural History, University of Alabama, Tuscaloosa, AL, USA. [10]German Center for Marine Biodiversity Research, Senckenberg am Meer, Wilhelmshaven, Germany. [11]Department of Evolutionary Biology, Ecology, and Environmental Sciences, University of Barcelona, Faculty of Biology, Barcelona, Spain. [12]Institut de Recerca de la Biodiversitat (IRBio), Universitat de Barcelona, Barcelona, Spain. [13]Bavarian State Collection of Zoology, München, Germany. [14]Institute of Evolution and Marine Biodiversity, Ocean University of China, Qingdao, China. [15]International Institute of Aquaculture and Aquatic Sciences, Universiti Putra Malaysia, Port Dickson, Malaysia. [16]Institute of Ecology, Evolution and Diversity, Goethe University, Frankfurt, Germany.
*Corresponding author. Email: julia.sigwart@senckenberg.de

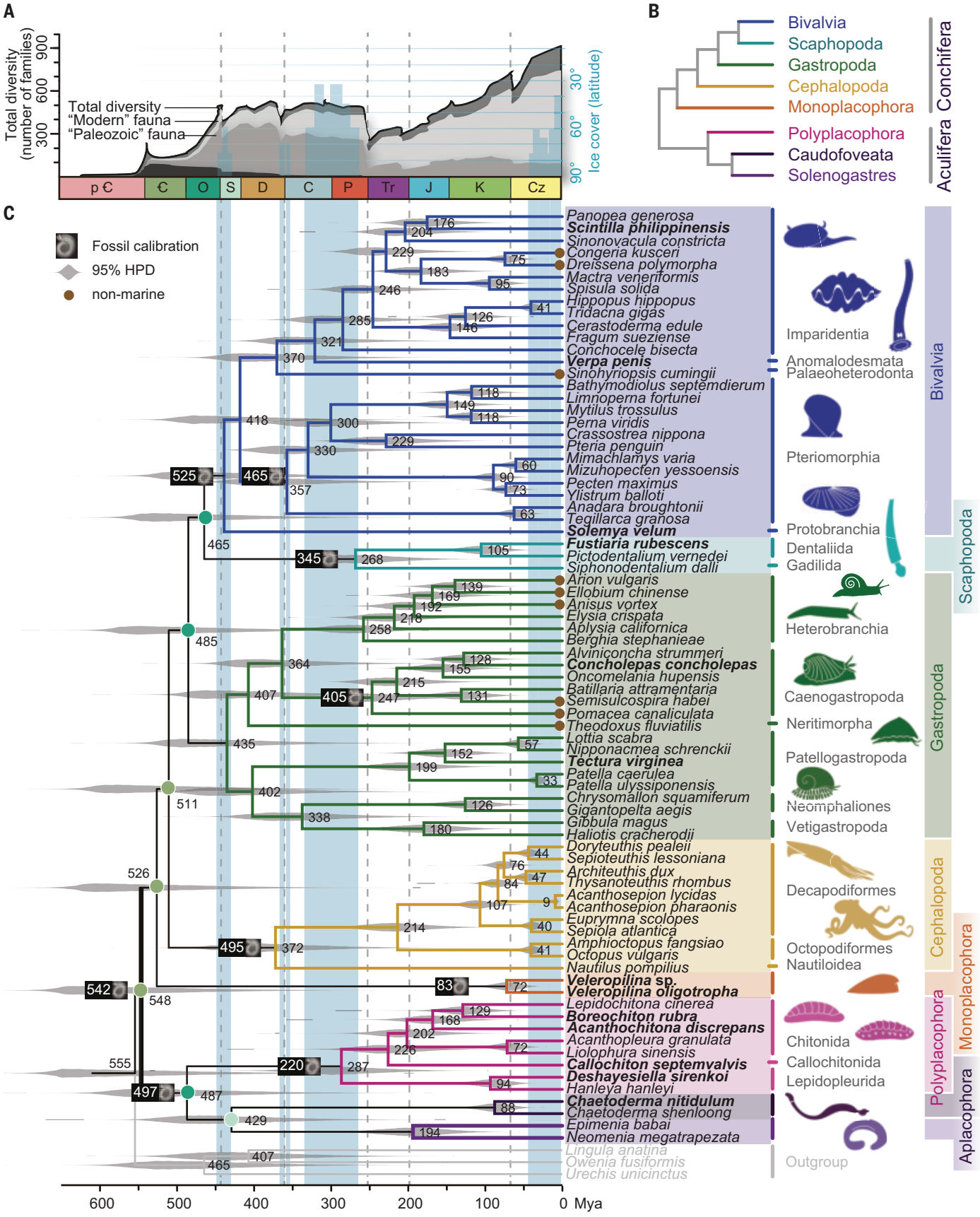
A
Total diversity (number of families)
900
600
300
Total diversity
"Modern" fauna
"Paleozoic" fauna
30°
60°
90°
Ice cover (latitude)
p Є
Є
O
S
D
C
P
Tr
J
K
Cz
B
Bivalvia
Scaphopoda
Gastropoda
Cephalopoda
Monoplacophora
Polyplacophora
Caudofoveata
Solenogastres
Conchifera
Aculifera
C
Fossil calibration
95% HPD
non-marine
Panopea generosa
Scintilla philippinensis
Sinonovacula constricta
Congeria kusceri
Dreissena polymorpha
Mactra veneriformis
Spisula solida
Hippopus hippopus
Tridacna gigas
Cerastoderma edule
Fragum sueziense
Conchocele bisecta
Verpa penis
Sinohyriopsis cumingii
Bathymodiolus septemdierum
Limnoperna fortunei
Mytilus trossulus
Perna viridis
Crassostrea nippona
Pteria penguin
Mimachlamys varia
Mizuhopecten yessoensis
Pecten maximus
Ylistrum balloti
Anadara broughtonii
Tegillarca granosa
Solemya velum
Fustiaria rubescens
Pictodentalium vernedei
Siphonodentalium dalli
Arion vulgaris
Ellobium chinense
Anisus vortex
Elysia crispata
Aplysia californica
Berghia stephanieae
Alviniconcha strummeri
Concholepas concholepas
Oncomelania hupensis
Batillaria attramentaria
Semisulcospira habei
Pomacea canaliculata
Theodoxus fluviatilis
Lottia scabra
Nipponacmea schrenckii
Tectura virginea
Patella caerulea
Patella ulyssiponensis
Chrysomallon squamiferum
Gigantopelta aegis
Gibbula magus
Haliotis cracherodii
Doryteuthis pealeii
Sepioteuthis lessoniana
Architeuthis dux
Thysanoteuthis rhombus
Acanthosepion lycidas
Acanthosepion pharaonis
Euprymna scolopes
Sepiola atlantica
Amphioctopus fangsiao
Octopus vulgaris
Nautilus pompilius
Veleropilina sp.
Veleropilina oligotropha
Lepidochitona cinerea
Boreochiton rubra
Acanthochitona discrepans
Acanthopleura granulata
Liolophura sinensis
Callochiton septemvalvis
Deshayesiella sirenkoi
Hanleya hanleyi
Chaetoderma nitidulum
Chaetoderma shenloong
Epimenia babai
Neomenia megatrapezata
Lingula anatina
Owenia fusiformis
Urechis unicinctus
Imparidentia
Anomalodesmata
Palaeoheterodonta
Pteriomorphia
Protobranchia
Dentaliida
Gadilida
Heterobranchia
Caenogastropoda
Neritimorpha
Patellogastropoda
Neomphaliones
Vetigastropoda
Decapodiformes
Octopodiformes
Nautiloidea
Chitonida
Callochitonida
Lepidopleurida
Outgroup
Bivalvia
Scaphopoda
Gastropoda
Cephalopoda
Monoplacophora
Polyplacophora
Aplacophora
600
500
400
300
200
100
0 Mya

Fig. 1. Mollusca timetree. (**A**) The timeline of global biodiversity is based mainly on the diversity of the molluscan fossil record (*55*), which is influenced by mass extinctions (gray dashed lines) and climate change with periods of extensive ice cover (*56*) (blue bars, right *y* axis). Marine invertebrate fossils, dominated by Mollusca, are divided into three successive faunas in the Sepkoski curve shown here: Cambrian, Paleozoic, and Modern (*55*). (**B**) Schematic showing the overview phylogeny of the eight living classes of Mollusca. (**C**) Phylogenetic topology was computed by ASTRAL-Pro using a set of 954 BUSCO family trees from 77 species and three outgroups. Key clades are illustrated with icons (table S7). Species from nonmarine habitats are noted with brown dots on the branch tip. Divergence time estimates were obtained with MCMCTREE using the LG + Γ_4 + F model, independent rates. Fossil calibration times are labeled at the corresponding nodes in black boxes. Solid circles at the nodes emphasize the differentiation of eight classes, with the colors representing geological eras. The age distribution violin plot (gray) for each node shows the 95% highest posterior density intervals drawn by TreeViewer. Є, Cambrian; C, Carboniferous; Cz, Cenozoic; D, Devonian; HPD, highest probability density; J, Jurassic; K, Cretaceous; Mya, million years ago; O, Ordovician; P, Permian; p-Є, pre-Cambrian; S, Silurian; Tr, Triassic.

and estimate the divergence times within the molluscan tree of life (Fig. 1).

The resulting tree recovered a topology that harmonizes key elements from former hypotheses into one topology: Aculifera, including a monophyletic Aplacophora (*2*, *6*); Conchifera with basal branching Monoplacophora; and the Gastropoda-Bivalvia-Scaphopoda (*2*, *6*, *13*, *14*) group, including Diasoma (*13*) (Fig. 2 and fig. S5).

A molluscan backbone

Morphological arguments about molluscan phylogeny historically focused on two alternative topologies, one with the clades Aculifera and Conchifera and the other with basal branching Aplacophora (vermiform mollusks) and a shelled clade "Testaria" (*9*) (Fig. 2). Early studies based on several loci recovered controversial alternative topologies with a putative sister relationship between Polyplacophora and Monoplacophora, termed Serialia, and other previously uncharacterized combinations (*8*). Later phylogenomic studies, despite low taxon sampling and data quality limitations, have mostly recovered Aculifera and Conchifera, but the relationships within Conchifera remained unresolved.

The fossil record of Mollusca provides important evidence to complement genomic data (Fig. 1A and table S5), and vice versa: In our topology, the origin of cephalopods predates Bivalvia and Gastropoda, although both appear earlier than cephalopods in the fossil record (*3*). Long-standing confusion over the affinities of univalved and bivalved small shelly fossils from the early Palaeozoic may be reinterpreted when considering a stable backbone phylogeny.

The first transcriptome-based phylogeny that included all eight classes resolved Monoplacophora as the sister to Cephalopoda (*6*), as did another recent study (*14*). This hypothesis is problematic because it is not supported by morphology or the fossil record (*9*). Adding partial genome data for a monoplacophoran resolved Monoplacophora as the sister to the remaining Conchifera, as predicted by morphological studies (*2*). Our subset analysis of a smaller gene set reproduced the Cephalopoda + Monoplacophora relationship; however, it also failed to recover a plausible ingroup topology among some bivalves (fig. S4). Cephalopoda + Monoplacophora is an anomalous result that likely arises from limited datasets.

Among Conchifera, Rostroconchia represents the ninth, extinct class of Mollusca, which appears before both gastropods and bivalves in the fossil record (*3*). Rostroconchs exhibit character combinations from bivalves and scaphopods and are important evidence supporting Diasoma (*3*, *13*). Evidence for Diasoma derives from morphology and fossils, but molecular data alone are not unequivocal. All phylogenomic studies have consistently supported a Gastropoda-Bivalvia-Scaphopoda clade. Early analyses recovered a clade [Bivalvia + (Gastropoda + Scaphopoda)], but often with relatively low support for interclass relationships (*2*, *6*, *13*, *14*). The first phylogenomic analysis that included scaphopods recovered Diasoma, which was also found here (Fig. 1). Analyses of scaphopod genomes support interpretations of incomplete lineage sorting (*13*). Molecular data show higher support for a Gastropoda-Bivalvia-Scaphopoda polytomy than either bifurcation (Fig. 2 and fig. S5). These groups likely represent the descendants of a complex and rapid radiation from a common conchiferan ancestor. This clade, here named Megalopodifera (big foot–bearing), is united by the veliger larva (although the larvae of monoplacophorans are entirely unknown), a body that can retract into the shell, a reduction in the number of foot-retractor muscles, and a large foot extending beyond the shell.

The molluscan tree of life

Internal topologies and timing within each class in the reconstructed phylogeny correspond well with established phylogenetic consensus and resolve some points of ongoing debate [see supplementary text (*15*)]. The monophyly of Aculifera is not controversial and is supported by fossil (*5*), anatomical (*16*), and molecular studies [see supplementary text (*15*)]. A

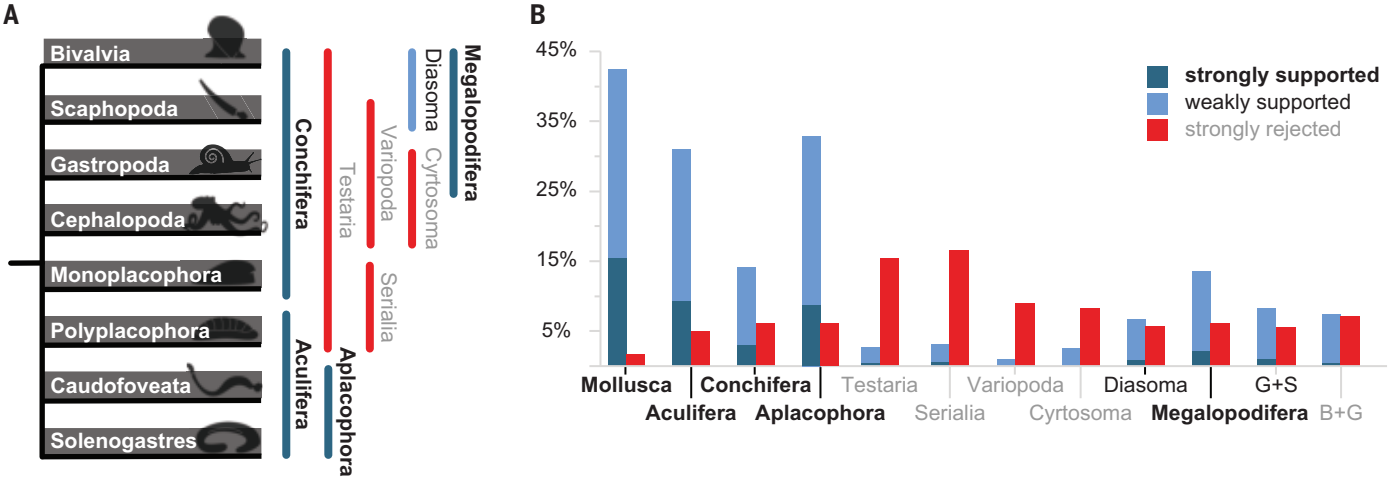

Fig. 2. Support for competing hypotheses in Molluscan relationships. (**A**) Schematic polytomy illustrating a subset of proposed molluscan ingroup relationships; colors illustrate the support. (**B**) Bar chart (*57*) comparing the proportion among 945 gene trees that support (blue) and reject (red) different proposed clades within Mollusca.

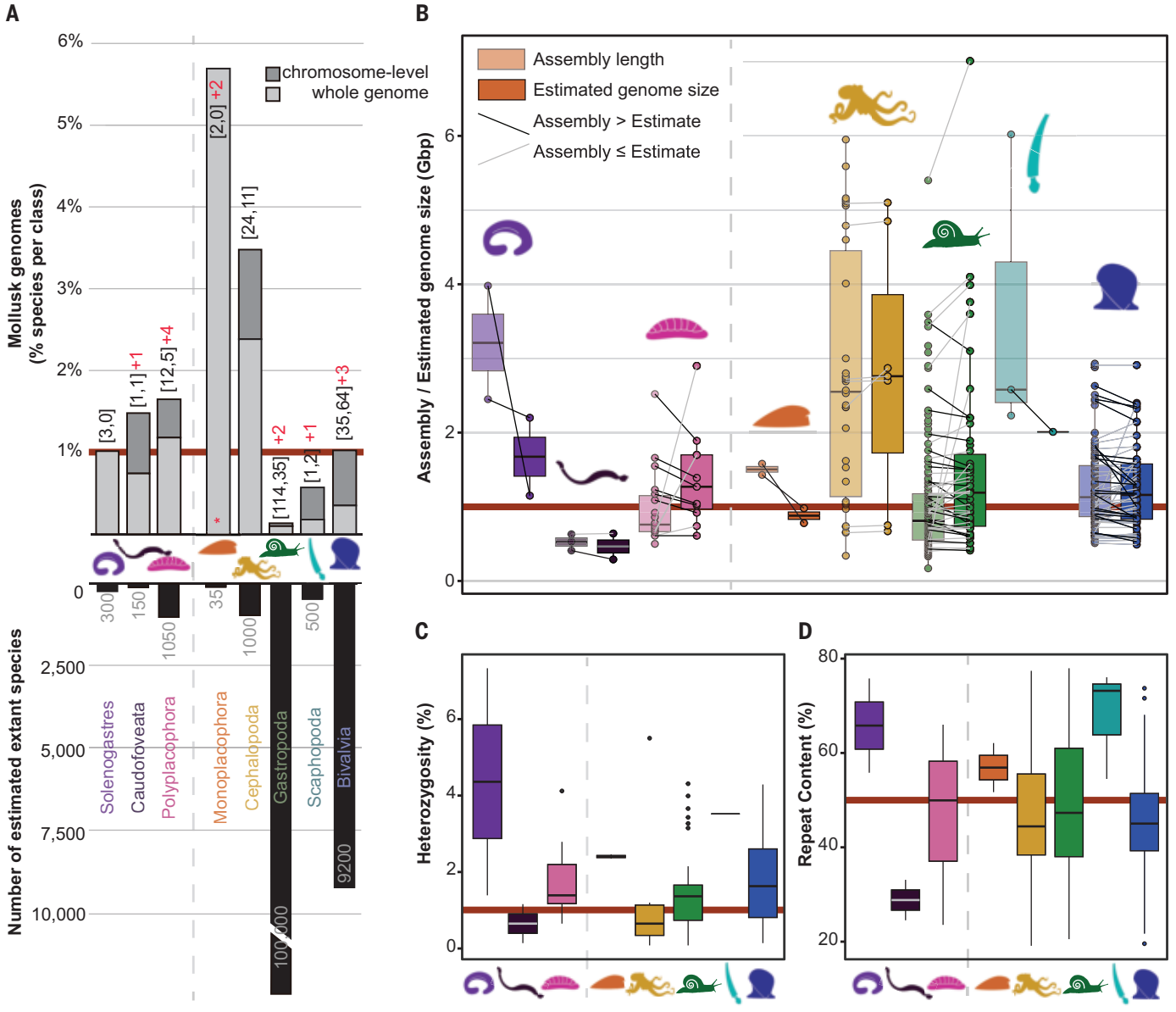

Fig. 3. Status and features of presently published molluscan genomes per class. (**A**) Variation in taxonomic richness and genome- or chromosome-level availability. The numbers in brackets show nonchromosomal assemblies (first) and chromosomal-level assemblies (second), including those in this study and all those published in National Center for Biotechnology Information (NCBI) GenBank (20 May 2024). The numbers of new genomes are indicated in red (the asterisk in monoplacophorans indicates that all available data are from the present study). A dashed line separates classes in Aculifera (left) and Conchifera (right). (**B**) Box plot summarizing reported assembly length (light colored) and estimated genome size (dark colored) median and inner quartile values for each class. Individual dots (without connecting lines) are values that are missing predicted genome-size data. Darker lines highlight the common phenomenon of assembly size being higher than genome size because of very high heterozygosity. This phenomenon is not observed in cephalopods because the high percentage of repetitive sequences makes genome assemblies incomplete, combined with redundancy caused by high heterozygosity. (**C**) Estimated genomic heterozygosity per class. (**D**) Estimated repeat content per class. For box plots, the center line represents the median, box limits are upper and lower quartiles, and whiskers are minimum and maximum values.

deep split between Solenogastres and Caudofoveata in the Silurian corresponds to a radiation of disparate fossils attributed to stem aplacophorans (*5*). Diversification within Aplacophora is difficult to calibrate because of the poor fossil record of shell-less forms; the Mesozoic splits between sampled species in each class here may indicate that biodiversity recovery after the Triassic-Jurassic extinction included a radiation in Solenogastres. The topology of sampled chitons is consistent with morphological and paleontological evidence as well as previous genetic and genomic work (*17*, *18*).

The two species used for the first full genomes of Monoplacophora include *Veleropilina oligotropha* from the Clarion Clipperton Zone and central Pacific as well as an undescribed *Veleropilina* species collected from the Aleutian Trench that was morphologically indistinguishable from *V. oligotropha* but geographically

distant (table S1). The divergence time between them was calibrated using an earlier divergence time estimate for the living monoplacophorans, which estimated the first split among living monoplacophorans in the Cretaceous (*19*). Genome data from additional monoplacophoran groups and regions will likely influence this result.

Within Cephalopoda, the phylogeny of Decapodiformes (squid and cuttlefish) has been much debated, with conflicting hypotheses from mitochondrial genomes (*20*) or nuclear transcriptome data (*21*). Our phylogeny confirms a topology proposed from a large-scale five-gene analysis (*22*). Sepiolina has a basal branching position within Decapodiformes, which also agrees with results from transcriptomes (*21*, *23*); we recognize Sepiolina as a taxonomic order, Sepiolida, on the basis of this topology. Sepiida resolved as sister to the squids (Oegopsida + Myopsida). This scenario is more parsimonious than the previous omics-based phylogenetic analyses because it suggests only a single loss of the calcareous phragmocone in the evolution of the clade. Our time-calibrated phylogeny indicates a relatively very recent radiation of Decapodiformes in the Cretaceous, in agreement with earlier work showing accelerating diversification rates in the Cenozoic (*22*). The diversification of extant coleoid cephalopods has been rapid.

Within living scaphopods, the new genome for *Fustiaria* revealed a much shallower divergence than previously predicted within Dentaliida (*24*) and for the origin of crown group Scaphopoda. Scaphopods have a long and complex fossil record with many stem lineages, and the biology of extant species remains poorly understood (*3*, *25*).

Gastropoda is divided into two fundamental clades: Psilogastropoda, which unites Patellogastropoda as sister to Vetigastropoda + Neomphaliones, and Adenogonogastropoda, which comprises Neritimorpha as sister to Apogastropoda (Caenogastropoda + Heterobranchia) [see supplementary text (*15*)]. This structure corroborates transcriptome-based studies that excluded the deep-sea subclass Neomphaliones (*26*, *27*). A subsequent transcriptome study with expanded taxon sampling recovered contradictory topologies but supported Adenogonogastropoda (*28*), first identified in an early molecular study (*29*) and later named on the basis of morphocladistic analysis (*30*). The early Cretaceous internal split in Neomphaliones also matches the scant fossil record for the group because it postdates the earliest neomphaline fossil from the Late Jurassic (*31*).

In contrast to most morphological analyses, our results indicate that Patellogastropoda is not the earliest branching clade within gastropods. A secondarily derived Patellogastropoda is recovered in most omics-based reconstructions (*27*, *32*). One recent transcriptome tree (*28*) could recover basal-branching Patellogastropoda when rapidly evolving sites representing more than half of the dataset were excluded. Incongruity between morphology and molecular results leaves the position of Patellogastropoda uncertain, or awaiting further explanation. The limpet form has evolved convergently more than 50 times among gastropods but has its largest radiation in the patellogastropods (*33*). It is well established that patellogastropods are split into two clades, Patellida + Nacellida (*3*), but divergence-time estimates in other studies vary wildly depending on the calibration points used within the clade. Our results are concordant with the fossil record, because the earliest known crown-group patellogastropod fossil is from the Triassic of Italy (*34*).

Our Caenogastropoda topology recovered Neogastropoda (*Concholepas*) nested within a paraphyletic Littorinimorpha (*Oncomelania* + *Alviniconcha*), consistent with previous findings (*35*). Our tree also supports Cerithioidea (*Batillaria* + *Semisulcospira*) clustering with hypsogastropods, which does not contradict the morphologically supported Sorbeoconcha concept (*3*). Some other studies (*36*), by contrast, unexpectedly recovered Cerithioidea as the sister to the architaenioglossan superfamily Ampullarioidea (represented here by *Pomacea*). In Heterobranchia, we recovered a monophyletic Tectipleura as sister to Ringipleura (*Berghia*). Within Tectipleura, the observed sequence of branching in Panpulmonata first gives rise to Sacoglossa (*Elysia*), then Hygrophila (*Anisus*), and finally Ellobioidea (*Ellobium*) and Stylommatophora (*Arion*), consistent with the recent consensus (*3*, *37*, *38*).

We recovered the consensus backbone phylogeny for bivalves (*39*), with Protobranchia (*Solemya*) in the earliest derived position, followed by Pteriomorphia, then Palaeoheterodonta (*Sinohyriopsis*), and Anomalodesmata (*Verpa*), sister to Imparidentia. Relationships within Pteriomorphia and Imparidentia also mostly align with other molecular and morphological results (*40*, *41*) [see supplementary text (*15*)]. One notable deviation is that the order Adapedonta (*Panopea*, *Sinonovacula*) is paraphyletic; the split between Adapedonta + Galeommatida (represented here by *Scintilla*) formed a conflicted node noted in earlier work (*39*, *42*). The reduced shells of many galeommatidans led to a poor fossil record and taxonomic uncertainty. The rich fossil record of bivalves provides a well-resolved chronology for the origin of major lineages; however, our time-calibrated tree does not account for the impact of mass extinctions and rapid bursts that shaped bivalve diversification (*43*). Within Imparidentia, all orders except Lucinida first appear in the fossil record after the end-Permian mass extinction event (*40*, *42*), as also found here. The common ancestor of crown-group Imparidentia necessarily had an origin before the end of the Permian, and the clade extends deeper in the stratigraphic record, which is not accounted for in our timetree.

Evolution of molluscan forms

The animal biomineralization toolkit predates the evolution of Mollusca (*44*). Mollusks are effective at repurposing ancient gene families in new ways (*45*). Phylogenetic relationships of phyla within Lophotrochozoa are not well resolved, and alternative hypotheses have different implications for the evolution of mineralized skeletons. Early small shelly fossils with molluscan affinity were used to calibrate the origin of Mollusca (table S5). Some putative early mollusks lack a solid shell, such as *Odontogriphus* and *Shisania* (*4*); however, the ancestor of Aculifera + Conchifera did possess a shell, and fossils lacking solid shells represent further diversity and not the condition of the common ancestor leading to Aculifera + Conchifera.

Fossil Mollusca present additional character mosaics that are not found in any living groups. The early Cambrian *Pelagiella exigua*, which had a coiled shell but flexible chaetae, was interpreted as a stem gastropod (*46*), but our timetree suggests that it is more likely a stem conchiferan. The deep divergence between Aplacophora + Polyplacophora (around 440 million years ago) is congruent with mosaic aculiferan forms in the fossil record (*Phthipodochiton*, *Kulindoplax*) from the Ordovician to Silurian (453 million to 422.9 million years ago) and much greater disparity in fossil forms in the aculiferan stem group. Character combinations underscore the flexibility of the molluscan genome to repeatedly redeploy morphological adaptations.

Body plans in living Mollusca include evidence of extensive convergence and character shifts on shorter timescales. For example, Juliidae, gastropods with bivalved shells, were once thought to be a transitional form between gastropods and bivalves but instead represent a recently derived adaptation to a specialized ecological niche (*47*). Endolithic bivalves occur in 11 separate families; *Verpa*, included here, has morphological modifications so extreme that it cannot be accommodated in morphometric comparisons (*48*), but this family has a Cenozoic origin (*49*).

Important evolutionary transitions often require the transformation of shell mineralization and associated physiology, as seen in the repeated colonization of terrestrial and freshwater environments among bivalves, gastropods, and one estuarine cephalopod. Even the few nonmarine lineages included in our study show that terrestrialization events were time independent and not directly connected to global patterns (Fig. 1). Morphological and ecological

plasticity has been a constant throughout the long history of the phylum.

Evolution of molluscan genomes

Broad taxon sampling now reveals that many molluscan genomes have extremely high heterozygosity and a high proportion of repetitive sequences (Fig. 3). These factors can result in highly fragmented assemblies, with mixed diploid sequences that are difficult to separate clearly, and multiple steps are needed for each new genome (*1*) (table S2). In Mollusca, concurrent high heterozygosity results in most assembly sizes being larger than the estimated genome size owing to the inclusion of another haplotype (Fig. 3 and tables S2 and S6). Estimates of heterozygosity for six of the eight classes are above 1%, with some species above 4%; these rates easily surpass those of other animal groups, such as Lepidoptera (butterflies and moths), where heterozygosity is considered high (*50*).

Genome features are not linearly correlated to morphological or ecological adaptations. The morphologically conserved Polyplacophora show very high rates of chromosome rearrangement (*17*). Well-conserved syntenic regions in more recent radiations of animals, such as mammals or birds, result in relatively similar genome structures, facilitating whole-genome comparisons (*51*, *52*). A new understanding of the variation in molluscan genomes provides a foundation for further work on fundamental questions of genome evolution, including the drivers of heterozygosity. Adding chromosome-level genomes for molluscan groups (e.g., Monoplacophora) is needed for comprehensive syntenic comparisons and to understand the role of chromosome rearrangements in speciation and cladogenesis. Several major lineages still have no genomes available: the bivalve clade Archiheterodonta and, at a finer scale, the bivalve orders Nuculida and Trigoniida (*Neotrigonia* is the only living member of an order known otherwise from fossils). Adding genomes for the gastropod order Cocculinida may alter, or confirm, the position of Patellogastropoda. Increased taxon sampling, especially in scaphopods, is important to fully understand molluscan topology.

Conclusions

Extensive economic and research interests have consistently held Mollusca at the forefront of diverse disciplines, including fisheries, neurobiology, ecotoxicology, and biomimetic design. However, their extraordinary diversity fundamentally hinders a confident assessment of their evolutionary history. The question of why early genetic studies struggled to recover reliable evolutionary patterns is potentially answered by the extreme variability among genomes that are now available for all classes and their major clades within the phylum. Large-scale genomic analyses across the tree of life have provided inconclusive evidence regarding the drivers of genetic diversity (*53*, *54*). These analyses are presently limited by incomplete sampling; to establish general principles of organismal phenome and genome, they must also include Mollusca, the most extensive experiment in animal body plans.

A stable topology for the total group Mollusca is fundamental for understanding the evolution of body plans and the fossil record. Based on this new phylogeny, we infer that the molluscan ancestor had a solid dorsal shell, a foot, multiple dorsal-ventral and oblique foot-retractor muscles, a radula, and no eyes. Throughout the long evolutionary history of Mollusca and continuing today, aspects of a flexible genome led to a flexible phenome: Endless forms of mollusks showcase the power of animal evolution.

REFERENCES AND NOTES

1. J. D. Sigwart, D. R. Lindberg, C. Chen, J. Sun, *Philos. Trans. R. Soc. London Ser. B* **376**, 20200161 (2021).
2. K. M. Kocot, A. J. Poustka, I. Stöger, K. M. Halanych, M. Schrödl, *Sci. Rep.* **10**, 101 (2020).
3. W. F. Ponder, D. R. Lindberg, J. M. Ponder, *Biology and Evolution of the Mollusca*, vol. 2 (CRC Press, 2020).
4. G. Zhang, L. A. Parry, J. Vinther, X. Ma, *Science* **385**, 528–532 (2024).
5. M. D. Sutton, D. E. G. Briggs, D. J. Siveter, D. J. Siveter, J. D. Sigwart, *Nature* **490**, 94–97 (2012).
6. S. A. Smith *et al*., *Nature* **480**, 364–367 (2011).
7. B. Xu *et al*., *Biol. Rev. Camb. Philos. Soc.* brv.13157 (2024).
8. I. Stöger *et al*., *BioMed Res. Int.* **2013**, 407072 (2013).
9. J. D. Sigwart, D. R. Lindberg, *Syst. Biol.* **64**, 384–395 (2015).
10. C. M. Adema, *Philos. Trans. R. Soc. London Ser. B* **376**, 20200162 (2021).
11. F. A. Simão, R. M. Waterhouse, P. Ioannidis, E. V. Kriventseva, E. M. Zdobnov, *Bioinformatics* **31**, 3210–3212 (2015).
12. J. L. Steenwyk, Y. Li, X. Zhou, X.-X. Shen, A. Rokas, *Nat. Rev. Genet.* **24**, 834–850 (2023).
13. H. Song *et al*., *Proc. Natl. Acad. Sci. U.S.A.* **120**, e2302361120 (2023).
14. X. Han *et al*., *Front. Ecol. Evol.* **12**, 1327007 (2024).
15. Materials and methods and additional supplementary text sections are available as supplementary materials.
16. M. Scherholz, E. Redl, T. Wollesen, C. Todt, A. Wanninger, *Curr. Biol.* **23**, 2130–2134 (2013).
17. J. D. Sigwart, Y. Li, Z. Chen, K. Vončina, J. Sun, *eLife* **13**, RP102542 (2024).
18. X. Liu, J. D. Sigwart, J. Sun, *Mar. Life Sci. Technol.* **5**, 525–537 (2023).
19. Y. Kano, S. Kimura, T. Kimura, A. Warén, *Zool. Scr.* **41**, 471–488 (2012).
20. J. E. Uribe, R. Zardoya, *J. Molluscan Stud.* **83**, 133–144 (2017).
21. F. E. Anderson, A. R. Lindgren, *Mol. Phylogenet. Evol.* **156**, 107038 (2021).
22. D. A. López-Córdova *et al*., *Mol. Phylogenet. Evol.* **166**, 107331 (2022).
23. A. R. Lindgren, A. Pratt, M. Vecchione, F. E. Anderson, *Org. Divers. Evol.* **23**, 91–101 (2023).
24. J. Strugnell, A. L. Allcock, in *The Timetree of Life*, S. B. Hedges, S. Kumar, Eds. (Oxford Univ. Press, 2009), pp. 239–241.
25. J. D. Sigwart, L. H. Sumner-Rooney, J. Dickey, N. Carey, *Molluscan Res.* **37**, 79–87 (2017).
26. F. Zapata *et al*., *Proc. Biol. Sci.* **281**, 20141739 (2014).
27. T. J. Cunha, G. Giribet, *Proc. Biol. Sci.* **286**, 20182776 (2019).
28. J. E. Uribe *et al*., *Syst. Biol.* **71**, 1271–1280 (2022).
29. A. G. MacArthur, M. G. Harasewych, in *Molecular Systematics and Phylogeography of Mollusks*, C. Lydeard, D. R. Lindberg, Eds. (Smithsonian Institution, 2003), pp. 140–160.
30. L. R. L. Simone, *Arq. Zool.* **42**, 161 (2011).
31. Z. Chen, M. Schrödl, *PeerJ* **10**, e13285 (2022).
32. G. J. Vermeij, *Biol. J. Linn. Soc. Lond.* **120**, 22–37 (2016).
33. C. Hedegaard, D. R. Lindberg, K. Bandel, *Lethaia* **30**, 331–335 (1997).
34. A. Kaim, in *Ancient Hydrocarbon Seeps*, vol. 53 of *Topics in Geobiology*, A. Kaim, J. K. Cochran, N. H. Landman, Eds. (Springer, 2022), pp. 323–374.
35. A. E. Fedosov *et al*., *Syst. Biol.* **73**, 521–531 (2024).
36. T. C. Goulding, E. E. Strong, A. M. Quattrini, *Mol. Ecol. Resour.* **23**, 1372–1388 (2023).
37. J. Moles, G. Giribet, *Mol. Phylogenet. Evol.* **155**, 106996 (2021).
38. R. M. Varney *et al*., *BMC Ecol. Evol.* **21**, 6 (2021).
39. S. Lemer, R. Bieler, G. Giribet, *Proc. Biol. Sci.* **286**, 20182684 (2019).
40. Y. Wang, Y. Yang, L. Kong, T. Sasaki, Q. Li, *Mar. Life Sci. Technol.* **5**, 326–336 (2023).
41. J. A. Audino, J. M. Serb, J. E. A. R. Marian, *Evolution* **74**, 2105–2120 (2020).
42. N. M. A. Crouch, S. M. Edie, K. S. Collins, R. Bieler, D. Jablonski, *Proc. Biol. Sci.* **288**, 20212178 (2021).
43. D. Jablonski, *Paleobiology* **31**, 192–210 (2005).
44. D. J. E. Murdock, *Biol. Rev. Camb. Philos. Soc.* **95**, 1372–1392 (2020).
45. J. Sun *et al*., *Nat. Commun.* **11**, 1657 (2020).
46. R. D. K. Thomas, B. Runnegar, K. Matt, *Palaeontology* **63**, 601–627 (2020).
47. N. L. W. S. Wong, J. D. Sigwart, *Mar. Biodivers.* **49**, 1997–2007 (2019).
48. K. S. Collins, S. M. Edie, D. Jablonski, *Proc. Biol. Sci.* **290**, 20221907 (2023).
49. B. Morton, *Rec. West. Aust. Mus.* **24**, 19 (2007).
50. A. García-Berro *et al*., *Mol. Ecol.* **32**, 560–574 (2023).
51. J. Damas *et al*., *Proc. Natl. Acad. Sci. U.S.A.* **119**, e2209139119 (2022).
52. J. Stiller *et al*., *Nature* **629**, 851–860 (2024).
53. J. Romiguier *et al*., *Nature* **515**, 261–263 (2014).
54. A. Mackintosh *et al*., *Nat. Commun.* **10**, 3466 (2019).
55. J. J. Sepkoski, in *Patterns and Processes in the History of Life*, D. M. Raup, D. Jablonski, Eds. (Springer, 1986), pp. 277–295.
56. T. S. Myers, *Nat. Geosci.* **9**, 803–804 (2016).
57. E. Sayyari, J. B. Whitfield, S. Mirarab, *Mol. Phylogenet. Evol.* **122**, 110–115 (2018).

ACKNOWLEDGMENTS

We thank many colleagues for their support for this work, including technical assistance, fieldwork, and fruitful discussion. We thank D. Baranski, A. B. Hamadou, and C. Gerheim of the LOEWE Translational Biodiversity Genomics (TBG) project based in the Senckenberg Research Institute and Museum, Frankfurt, for support with lab work and sequencing. We thank the staff of the laboratory of the Queen's University Marine Laboratory, Portaferry, Northern Ireland. The members of the Slug Lab (@slug_lab) are also acknowledged. K. Takai and S. Kawagucci [Japan Agency for Marine-Earth Science and Technology (JAMSTEC)] are thanked for leading and drafting the proposal for *RV Kaimei* cruise KM23-05; sampling within the Mariana Trench Marine National Monument of the United States was done under special use permit no. 12542-23001. The "AleutBio" expedition on board *RV Sonne* (cruise SO293) contributed to sampling in the Aleutian Trench and the monoplacophoran *Veleropilina* sp. We thank the Radboudumc Genome Technology Center for the use of the Sequencing Core Facility (Nijmegen, Netherlands), which provided the PacBio SMRT sequencing service on the Sequel IIe platform. We also thank the Bioscientia Institut für Medizinische Diagnostik GmbH for providing the PacBio SMRT sequencing service on the PacBio Revio platform. This is contribution number 34 of the Senckenberg Ocean Species Alliance. We are grateful to D. R. Lindberg and three anonymous reviewers for comments that improved this work.
Funding: Z.C. is supported by the Leibniz Association project PHENOME (P123/2021 to J.D.S.). This work is supported by the Natural Science Foundation of Shandong Province (ZR2023JQ014 to J.S.), Fundamental Research Funds for the Central Universities (202172002 and 202241002 to J.S.), LOEWE TBG "International Mollusc of the Year" (to J.A.B.), Programa Puente (DE 1019-2018 to J.A.B.), the National Science Foundation (DEB-1846174 to K.M.K.), the Spanish Ministry of Science and Innovation (PID2021-127037NA-I00/MCIN/AEI/10.13039/501100011033/ and by FEDER una manera de hacer Europa) (to J.M.), a generous philanthropic donation to the Senckenberg Gesellschaft für Naturforschung that funds the Senckenberg Ocean Species Alliance (to J.D.S.), Global Genome Initiative grant no. GGI-Exploratory-2016-046 (to V.L.G.), German Ministry of Education and Science BMBF (03F0707E)

funding for the EcoResponse (SO239) cruise onboard *RV Sonne* (to P.M.A.), and German Ministry of Education and Science BMBF (03G0293A) funding for the AleutBio (SO293) cruise onboard *RV Sonne* to A. Brandt (J.D.S., C.C., E.S.). **Author contributions:** Conceptualization: J.D.S., Z.C.; Methodology: Z.C., J.S., V.L.G., C.G., T.S., K.M.K.; Investigation: Z.C., J.S., V.L.G., K.M.K., M.Y.-C., J.D.S.; Visualization: Z.C.; Funding acquisition: J.D.S., J.A.B., J.M., V.L.G., K.M.K., J.S.; Project administration: J.D.S.; Supervision: J.D.S., J.A.B., C.C., V.L.G., K.M.K., J.S.; Writing – original draft: J.D.S., Z.C.; Writing – review & editing: Z.C., J.A.B., C.C., M.T.G., V.L.G., C.G., K.M.K., P.M.A., J.M., T.S., E.S., J.S., N.L.W.S.W., M.Y.-C., J.D.S. **Competing interests:** The authors declare that they have no competing interests. **Data and materials availability:** Whole-genome sequencing data and new genome assemblies generated in this study are available via the National Center for Biotechnology Information (NCBI): *Chaetoderma nitidulum* (under BioProject number PRJNA1122582); *Acanthochitona discrepans* (PRJNA1114954), *Boreochiton ruber* (PRJNA1120663), *Callochiton septemvalvis* (PRJNA1114372), *Deshayesiella sirenkoi* (PRJNA1114373), *Veleropilina oligotropha* (PRJNA1120392), *Veleropilina* sp. (PRJNA1120412), *Fustiaria rubescens* (PRJNA1120416), *Scintilla philippinensis* (PRJNA1120792), *Verpa penis* (PRJNA1120794), *Solemya velum* (PRJNA1163513), *Tectura virginea* (PRJNA1120664), and *Concholepas concholepas* (PRJNA1120782). All other data are available in the manuscript or the supplementary materials.

SUPPLEMENTARY MATERIALS

science.org/doi/10.1126/science.ads0215
Materials and Methods
Supplementary Text
Figs. S1 to S5
Tables S1 to S7
References (*58*–*269*)

Submitted 25 July 2024; accepted 5 December 2024
10.1126/science.ads0215

Post Doctoral Fellow in Dystrophic and Genetic Cardiomyopathies

The Kamdar Lab at the University of Minnesota is seeking a motivated and productive Postdoctoral Associate with expertise in gene editing and human induced pluripotent stem cells to join our dynamic research team. This position offers a unique opportunity to design and conduct NIH-funded research experiments focused on dystrophic cardiomyopathy, utilizing iPSC-derived cardiac organoids for disease modeling and gene editing. Our goal is to advance the understanding of dystrophic cardiomyopathy and explore novel therapeutic strategies.

Research Focus: This role involves experimental work on dystrophic gene editing in iPSC-derived cardiac organoids to study muscular dystrophy and genetic cardiomyopathies. The candidate will apply CRISPR/Cas9 gene editing techniques (base and prime editing) to restore dystrophin and analyze cellular and molecular outcomes.

Key Responsibilities:

- Design, execute, and analyze experiments investigating dystrophic cardiac disease models.
- Collaborate with laboratory colleagues and external scientific partners on experimental design and data interpretation.
- Maintain detailed documentation of experimental procedures, data analysis, and findings.
- Prepare and submit research manuscripts to peer-reviewed scientific journals.
- Present research findings at local, national, and international conferences.
- Provide mentorship and supervision for junior trainees in the laboratory.

Qualifications: Required

- Ph.D. in biomedical sciences, molecular biology, stem cell biology, genomics, biomedical engineering, or a related field.
- Demonstrated experience in CRISPR/Cas9 gene editing in human stem cells.
- Strong track record of publishing in peer-reviewed journals and contributing to grant writing.

Qualifications: Preferred

- Expertise in human iPSC techniques, including line derivation, cardiac differentiation, and gene editing.
- Excellent written and verbal communication skills.
- Preference will be given to applicants with demonstrated experience developing scientific protocols and scientific writing. Submit excellent letters of recommendation.

This position offers a highly collaborative and intellectually stimulating environment with opportunities for career development.

To apply, please submit a CV, cover letter, and contact information for three references to kamd0001@umn.edu.

By **Violeta J. Rodriguez**

Drowning in uncertainty

I open my application portal and see blank spaces where decisions should be. I reach out to my program and review officers at the National Institutes of Health (NIH) about my grants in the pipeline, only to hear the same response each time: "We don't have any information yet." Nearly 2 years into my assistant professorship at an R1 institution, when I should be focused on my research, I don't know where my future funding will come from. And there is the added threat that because of cuts to other government payments, the infrastructure supporting my work—grant support staff, purchasing teams, human resources staff—could also disappear. I sit in this space of waiting, fearing that years of effort, of my youth, were in vain.

When I started on the tenure track, I knew securing external funding was crucial to my success. And for health equity research, my specialty, NIH is the obvious choice. In graduate school, I spent countless hours refining my grant-writing skills, knowing that no matter how strong my research was, none of it would matter without funding to support it. I worked with mentors and researchers who invested in me, who believed in my ability to become an independent researcher. They guided me through NIH's proposal process, helping me sharpen my ideas, strengthen my applications, and navigate the often-opaque world of grant review. In my first year as an assistant professor, I was elated to be awarded the prestigious NIH Director's Early Independence Award. It was supposed to be a launch pad to accelerate my research and career.

"How do you strategize around an unpredictable funding landscape?"

But now, I submit proposals into a system where even NIH officers don't know what will happen next. Will my grants ever be reviewed? What can I research?

Every researcher understands rejection—that's academia. At least it came with a clear timeline: feedback would arrive, resubmission would be encouraged, and the next steps were relatively predictable. I used to tell myself that every unsuccessful grant was a learning experience—that even if I didn't get funded, the process of writing the proposal would help me sharpen my research questions.

The sheer ambiguity of the current situation, on the other hand, is much harder to manage. This uncertainty is affecting every aspect of my work—and my current and potential future students. Every week spent writing grant proposals that may never be reviewed is a week not spent mentoring my students, analyzing data, or publishing. As early-career researchers, we are told to be strategic in how we allocate our time—one of our most valuable resources—to make sure we are focusing on the tasks that will advance our careers. But how do you strategize around an unpredictable funding landscape? What does it mean to "work smarter" when there's no clear path forward? I recently made the difficult decision not to recruit a new graduate student for next year; given the unpredictability of my research funding, I can't justify bringing someone in when I'm not sure I'll be able to provide the stability graduate school requires.

And then there is the added layer of identity. I am a Latina scientist, an immigrant, and a non-native English speaker. I have felt the pressure of those labels throughout my career. And now, I can't help but feel that weight even more keenly. In the broader context of what is happening to my community in this country, it feels trivial to worry about my personal funding and career progression. But it's larger than me. So much of the support for minoritized scientists has come through targeted funding initiatives, mentorship programs, and institutional commitments to increasing diversity in research—opportunities that are disappearing.

Where do we go from here? I don't have an answer. I don't know what the next year will bring, what paylines will be, whether future proposals—or my research—will find a home. For now, my NIH application portal remains filled with blanks. I'll keep checking. I'll keep writing. I'll keep doing what I can to move my research forward. But I, and so many others, can't do this indefinitely. Something has to give. ■

Violeta J. Rodriguez is an assistant professor at the University of Illinois Urbana-Champaign. Send your career story to SciCareerEditor@aaas.org.

ILLUSTRATION: ROBERT NEUBECKER

myIDP ScienceCareers
INDIVIDUAL DEVELOPMENT PLAN

Features in myIDP include:

- Exercises to help you examine your skills, interests, and values.
- 20 career paths with a prediction of which ones best fit your skills and interests.
- A tool for setting strategic goals with optional reminders to keep you on track.
- Articles and resources to guide you through the process.
- Options to save materials online and print them for further review and discussion.
- A certificate of completion for users that finish myIDP.

Start planning your future today!
myIDP.sciencecareers.org

In partnership with:

FASEB Federation of American Societies for Experimental Biology
UMASS University of Massachusetts Medical School
UCSF University of California San Francisco
UIC
BURROUGHS WELLCOME FUND